



**HAL**  
open science

# Rétrodiffusion résolue en polarisation de nanoparticules atmosphériques : expériences de terrain et laboratoire

Gregory David

► **To cite this version:**

Gregory David. Rétrodiffusion résolue en polarisation de nanoparticules atmosphériques : expériences de terrain et laboratoire. Physique Atmosphérique et Océanique [physics.ao-ph]. Université Claude Bernard - Lyon I, 2013. Français. NNT : 2013LYO10225 . tel-01146445

**HAL Id: tel-01146445**

**<https://theses.hal.science/tel-01146445>**

Submitted on 28 Apr 2015

**HAL** is a multi-disciplinary open access archive for the deposit and dissemination of scientific research documents, whether they are published or not. The documents may come from teaching and research institutions in France or abroad, or from public or private research centers.

L'archive ouverte pluridisciplinaire **HAL**, est destinée au dépôt et à la diffusion de documents scientifiques de niveau recherche, publiés ou non, émanant des établissements d'enseignement et de recherche français ou étrangers, des laboratoires publics ou privés.

CLAUDE BERNARD LYON 1 UNIVERSITY

PHYSICS AND ASTROPHYSICS DOCTORAL SCHOOL

To obtain the  
DEGREE OF DOCTOR OF PHILOSOPHY

**POLARIZATION-RESOLVED BACKSCATTERING FROM  
NANOPARTICLES IN THE ATMOSPHERE: FIELD AND  
LABORATORY EXPERIMENTS**

by  
Grégory DAVID

November, 2013

Doctoral advisor: Patrick RAIROUX

Co-advisor: Alain MIFFRE

JURY:

**Reviewers:** Mr. MISHCHENKO Michael

Mr. SCHNAITER Martin

**Examiners:** Mrs. DEL FATTI Natalia

Mr. GEORGE Christian

Mr. KAHNERT Michael

Mr. KASPARIAN Jérôme

Mr. MIFFRE Alain

Mr. RAIROUX Patrick



# UNIVERSITE CLAUDE BERNARD - LYON 1

## Président de l'Université

Vice-président du Conseil d'Administration

Vice-président du Conseil des Etudes et de la Vie Universitaire

Vice-président du Conseil Scientifique

Directeur Général des Services

**M. François-Noël GILLY**

M. le Professeur Hamda BEN HADID

M. le Professeur Philippe LALLE

M. le Professeur Germain GILLET

M. Alain HELLEU

## ***COMPOSANTES SANTE***

Faculté de Médecine Lyon Est – Claude Bernard

Faculté de Médecine et de Maïeutique Lyon Sud – Charles  
Mérieux

Faculté d'Odontologie

Institut des Sciences Pharmaceutiques et Biologiques

Institut des Sciences et Techniques de la Réadaptation

Département de formation et Centre de Recherche en Biologie  
Humaine

Directeur : M. le Professeur J. ETIENNE

Directeur : Mme la Professeure C. BURILLON

Directeur : M. le Professeur D. BOURGEOIS

Directeur : Mme la Professeure C. VINCIGUERRA

Directeur : M. le Professeur Y. MATILLON

Directeur : M. le Professeur P. FARGE

## ***COMPOSANTES ET DEPARTEMENTS DE SCIENCES ET TECHNOLOGIE***

Faculté des Sciences et Technologies

Département Biologie

Département Chimie Biochimie

Département GEP

Département Informatique

Département Mathématiques

Département Mécanique

Département Physique

Département Sciences de la Terre

UFR Sciences et Techniques des Activités Physiques et Sportives

Observatoire des Sciences de l'Univers de Lyon

Polytech Lyon

Ecole Supérieure de Chimie Physique Electronique

Institut Universitaire de Technologie de Lyon 1

Institut Universitaire de Formation des Maîtres

Institut de Science Financière et d'Assurances

Directeur : M. le Professeur F. DE MARCHI

Directeur : M. le Professeur F. FLEURY

Directeur : Mme le Professeur H. PARROT

Directeur : M. N. SIAUVE

Directeur : M. le Professeur S. AKKOUCHE

Directeur : M. le Professeur A. GOLDMAN

Directeur : M. le Professeur H. BEN HADID

Directeur : Mme S. FLECK

Directeur : Mme la Professeure I. DANIEL

Directeur : M. C. COLLIGNON

Directeur : M. B. GUIDERDONI

Directeur : M. P. FOURNIER

Directeur : M. G. PIGNAULT

Directeur : M. C. VITON

Directeur : M. A. MOUGNIOTTE

Administrateur provisoire : M. N. LEBOISNE

## Thesis abstract

Atmospheric greenhouse gases and nanometer-sized particles are incriminated for their role on the Earth radiative budget and climate. This thesis relates the research performed on the polarization-resolved backscattering of these nano-sized particles and demonstrates its usefulness to address complex atmospheric processes like particles nucleation. Greenhouse gases are also studied, by coupling a spectrally broadband lidar with optical correlation spectroscopy to remotely evaluate their atmospheric content (Thomas et al., 2012, 2013a,b).

Special care has been taken to perform sensitive and accurate UV-VIS polarization lidar measurements (David et al., 2012). Hence, and as a first result, cross-polarized backscattering coefficients as low as  $(2.4 \pm 0.5) \times 10^{-8} \text{ m}^{-1} \cdot \text{sr}^{-1}$  have been measured in the troposphere, corresponding to UV-particles depolarization detection limit of 0.6 % at 4 km altitude, close to the molecular depolarization. Then, a new methodology has been developed to retrieve, in a two/three component particle external mixture, the backscattering coefficients specific to each particle component (David et al., 2013a). For that purpose, accurate knowledge on the backscattering Ångstrom exponent and depolarization ratio of each particle type must be addressed. This task is here achieved by performing either single-scattering numerical simulations using T-matrix, or alternatively by performing laboratory measurements. The inherent assumptions and the performance of the methodology are then discussed for three case studies of external mixing: i) spherical sulfate mixed with volcanic ash released from the Eyjafjallajökull 2010 eruption (Miffre et al., 2011, 2012a, b), ii) desert dust mixed with non-dust particles (Miffre et al., 2011 ; Dupart et al., 2012), iii) desert dust mixed with sea-salt and background spherical particles as an example of a three-component particle mixture (David et al., 2013a). From these field measurements, three main results have been retrieved: (a) Range-resolved particles number concentrations specific to one particle component (ash, dust) (Miffre et al., 2011, 2012b), which include the variability in the particle size distribution, the particles refractive index and possible sedimentation effects (Miffre et al., 2012b), (b) particle backscattering enhancement due to hygroscopic growth, (c) observation of new particle formation in the atmosphere using a sensitive UV polarization lidar, which is new and opens

new insights at the forefront of knowledge in atmospheric physics and chemistry (Dupart et al., 2012).

In addition, absolute particles depolarization has been for the first time measured in the exact backscattering direction ( $\theta = 180^\circ \pm 0.2^\circ$ ) for an ensemble of nanoparticles in ambient air (David et al., 2013b). The experiment is performed in the UV spectral range and fulfills the far-field single-scattering approximation. Hence, within error bars, spherical water droplets exhibit no depolarization ( $\delta_p = 0.02 \pm 0.05$  %) in agreement with Mie theory. While for sodium chloride particles, used as an example of nonspherical particles, a  $\delta_p = (4.38 \pm 0.16)$  % depolarization has been measured at the laboratory. The above studies show the need to better understand the optical properties of each particle. Hence, absolute measurements of the particle extinction cross-section have also been performed on a single dielectric ammonium sulfate or a desert dust nanoparticle having a 50 nm radius, in collaboration with N. Del Fatti and F. Vallee's group at the ILM. A discussion comparing the laboratory measurement and the theory is presented in regards to the environmental conditions.

As a conclusion, this thesis explores the optical scattering properties of a single / an ensemble of nanoparticles, addressing them in the real atmosphere, through sensitive and accurate lidar and laboratory experiments and numerical simulations, showing new outlooks on the microphysical properties of these atmospheric nanoparticles (Dupart et al., 2012, David et al., 2013b).

## Résumé de thèse

Cette thèse porte sur l'étude des gaz et nanoparticules diélectriques de l'atmosphère, fortement incriminés pour leur rôle sur le bilan radiatif terrestre et le changement climatique. Ces travaux de recherche, réalisées au sein de l'Institut Lumière Matière, traitent plus spécifiquement de la rétrodiffusion de la lumière, résolue en polarisation, par les nanoparticules de l'atmosphère, afin d'étudier la complexité des processus atmosphériques qui la composent, tels que la nucléation. En complément à cette approche particulière, les gaz à effet de serre sont également étudiés, en suivant une méthode originale, consistant à évaluer leur concentration atmosphérique, par couplage d'un télédécteur lidar possédant une large bande spectrale avec la spectroscopie optique de corrélation (Thomas et al., 2012, 2013a,b).

Une attention particulière a été portée à la réalisation de mesures sensibles et précises utilisant un lidar multi-spectral (UV, VIS), résolu en polarisation (David et al., 2012). Comme premier résultat, un coefficient de rétrodiffusion aussi faible que  $(2,4 \pm 0,5) \times 10^{-8} \text{ m}^{-1} \cdot \text{sr}^{-1}$ , a été mesuré dans l'UV en polarisation croisée à celle du laser incident dans la troposphère libre, avec une limite de détection de la dépolarisation de  $\delta_p = 0,6 \%$  (proche de la dépolarisation moléculaire), observée à plus de 4 kilomètres d'altitude. Ensuite, une méthode nouvelle a été développée pour retrouver, dans un mélange externe de particules à deux/trois composantes chimiques, le coefficient de rétrodiffusion de chacune de ces composantes. Pour ce faire, le coefficient d'Angström et la dépolarisation de chaque espèce chimique doivent être déterminés précisément. On montre dans ce travail de thèse que ces coefficients peuvent être déterminés soit par simulation numérique de la diffusion simple (algorithme T-matrix), soit directement par des mesures de laboratoire. Les hypothèses et les performances de cette méthode sont ensuite discutées dans trois cas d'étude : i) mélange externe de particules de sulfates avec les cendres volcaniques issues de l'éruption de 2010 du volcan Eyjafjallajökull (Miffre et al., 2011, 2012a, b) ii) mélange externe de poussières désertiques dans la troposphère libre (Miffre et al., 2011 ; Dupart et al., 2012) observé lors d'un épisode de tempête de sable désertique à Lyon (juillet 2010), iii) mélange externe à trois composantes : poussières désertiques, sels de mer et particules solubles dans l'eau (David et al., 2013a). Ces mesures atmosphériques ont conduit à plusieurs résultats: (a) détermination à distance de la concentration en nombre en particules volcaniques (cas i), désertiques (cas ii) (Miffre et al., 2011). Par construction, ces mesures de concentration sont spécifiques à ces particules et

intègrent les effets de taille et de sédimentation (Miffre et al., 2012b) ; (b) Evolution de la rétrodiffusion en fonction de l'hygroscopicité de ces particules ; (c) Observation de la formation de nouvelles particules dans l'atmosphère (nucléation) à partir des mesures lidar UV, résolues en polarisation. Ce résultat nouveau ouvre de nouvelles perspectives à la pointe de la recherche actuellement réalisée en physico-chimie de l'atmosphère (Dupart et al., 2012).

De manière complémentaire, la dépolarisation de nanoparticules en suspension dans l'air ambiant a été mesurée en laboratoire, pour la première fois dans la direction d'exacte rétrodiffusion ( $\theta = 180,0^\circ \pm 0,2^\circ$ ) (David et al., 2013b). Cette expérience satisfait aux conditions de diffusion simple en champ lointain et fonctionne dans le domaine spectral UV. Ainsi, en accord avec la théorie Mie, aux incertitudes de mesure près, un ensemble de nanogouttes sphériques d'eau ne manifeste aucune dépolarisation ( $\delta_p = (0,02 \pm 0,05) \%$ ), tandis que des nanoparticules de chlorure de sodium, non-sphériques, dépolarisent la lumière ( $\delta_p = (4.38 \pm 0.16) \%$ ). Ces expériences soulignent de plus le besoin de mieux connaître les propriétés optiques d'une nanoparticule individuelle. Ainsi, en collaboration avec l'équipe FemtoNano de N. Del Fatti et F. Vallée de l'ILM, des mesures absolues de section efficace d'extinction ont été réalisées sur des nanoparticules diélectriques uniques d'ammonium sulfate et de sable désertique. Une comparaison de ces mesures de laboratoire avec la théorie est présentée et discutée, en fonction des conditions environnementales.

En conclusion, cette thèse explore la diffusion optique d'un ensemble de nanoparticules et l'extinction d'une nanoparticule diélectrique unique, en les mesurant de manière très sensible et précise, en atmosphère réelle comme en laboratoire, tout en étayant cette approche expérimentale par des simulations numériques. Cette approche ouvre des perspectives nouvelles, portant sur les propriétés microphysiques de ces nanoparticules atmosphériques (Dupart et al., 2012, David et al., 2013b).

## List of variables and notations

$a$ :	spheroid's rotational symmetry axis length
$\hat{A}_p$ :	particle Ångstrom exponent
$\hat{A}_{p,\perp}$ :	cross-polarized particle Ångstrom exponent
$\hat{A}_{p,\parallel}$ :	co-polarized particle Ångstrom exponent
AFT:	aerosol flow tube
AMS:	aerosol mass spectrometer
ATD:	Arizona test dust
$b$ :	spheroid's axis length in the perpendicular direction of the rotational symmetry axis
BE:	beam expander
$c$ :	light velocity
$C_{\text{ext},p}$ :	particle extinction cross section
$C_{\text{ext},np}$ :	nanoparticle extinction cross section
$C_{\text{sca}}$ :	scattering cross section
$C_{\text{NM}}$ :	number-to-mass conversion factor
$d$ :	the distance between the particle and the observer
$d_\emptyset$ :	distance between $L_C$ and $I_r$
$d_1$ :	distance between $L_C$ and $L_1$
DB:	Dichroic beamsplitter
$D_p$ :	particle depolarization
Det <sub>L</sub> :	Lidar detector
DIAL:	differential absorption lidar
DM:	Dichroic mirror
DMA:	differential mobility analyzer
$\mathbf{E}_i$ :	incident electric field vector
$E_{i,p}$ :	components of $\mathbf{E}_i$ in the scattering plane
$E_{i,s}$ :	components of $\mathbf{E}_i$ perpendicular to the scattering plane
$\mathbf{E}_r$ :	electric field vector of the reflected wave
ECMWF:	European Centre for Medium-range Weather Forecasts
$f$ :	frequency of the spatial modulation
$f_c$ :	focal of the collecting lens $L_c$
$f_1$ :	focal of the collecting lens $L_1$
$f_2$ :	focal of the collecting lens $L_2$
$F$ :	scattering phase function
$\mathbf{F}$ :	scattering phase matrix
$F_{ij}$ :	scattering phase matrix elements
FOV:	Field of view
$G_\lambda$ :	electro-optic calibration constant
HWP:	Half waveplate
$h$ :	local hour angle of the Sun
$I$ :	first element of the Stokes vector
$I_{\text{inc}}$ :	incident light intensity
$I_l$ :	intensity spatial profile of the light beam
$I_{\text{sca},p}$ :	light intensity of the particle scattering
$I_{\text{sca},\parallel}$ :	co-polarized scattered light intensity
$I_{\text{sca},\perp}$ :	cross-polarized scattered light intensity
$\mathbf{I}_{2\lambda}$ :	backscattered photon intensity vector

$I_r$ :	detector's iris
IF:	interference filter
$\mathbf{k}_{inc}$ :	incident light wave vector
$\mathbf{k}_{sca}$ :	scattered light wave vector
K:	normalization constant of the spheroids weighting
$\ell$ :	spatial extension of the backscattering volume
L:	Latitude
$L_C$ :	collecting lens
$L_1$ :	Lens in the exact backscattering detector
$L_2$ :	Lens in the exact backscattering detector
m (subscript)	molecules
m:	refractive index
$M_{ash}$ :	ash mass concentration
$\mathbf{m}_{DB}$	matrix relating the incident electric fields to the electric fields reflected by the dichroic beamsplitter
$\mathbf{M}_{DL}$ :	lidar detector transfer matrix
$\mathbf{M}_E$ :	Mueller matrix of the emitter device
$M_{Ellip}$ :	elliptic mirror
$M_{Prim}$ :	primary mirror
$\mathbf{M}_p$ :	mueller matrix that accounting for the modification of the polarization state of the laser pulse during its propagation in the particles medium and in the air surrounding medium
$\mathbf{M}_R$ :	Mueller matrix of the receiver device
$m_O$ :	ordinary refractive index
n12:	neither ns1 nor ns2 particle component
nash:	non-ash particle (namely particles that are not ash particles)
$n_{dust}$ :	dust number density
ndust:	non-dust particle (namely particles that are not dust particles)
$n_{ndust}$ :	non-dust particle number density
np:	nanoparticle
$n_p$ :	particle number density
inc:	incident
$N_{ash}$ :	ash particle number concentration
$N_{dust}$ :	ash particle number concentration
NPF:	new particle formation
NPFG:	new particle formation and growth
ns:	nonspherical particle
ns1:	first nonspherical particle component
ns2:	second nonspherical particle component
O(z):	overlap function
OBP2:	Optical backscattering partitioning in a two-component particle mixture
OBP3:	Optical backscattering partitioning in a three-component particle mixture
OCS:	Optical correlation spectroscopy
OPC:	optical particle counter
p:	particle
P:	lidar optical signal
P	exact backscattering signal
$P_F$ :	measured background signal
$P_{inc}$ :	incident light power
$P_{trans}$ :	transmitted light power

$P_V$	small scattering volume element materialized by a point
$\mathbf{P}_{2\lambda}$ :	measured backscattering signal vector
$P_{\lambda, //}$ :	co-polarized lidar signal
$P_{\lambda, \perp}$ :	cross-polarized lidar signal
PMT:	photomultiplier tubes
PSD:	particle size distribution
Q:	second element of the Stokes vector
QWP:	Quarter waveplate
r:	particle radius
$r_{\min}$ :	minimum radius of the particle contributing significantly to the backscattering coefficient
$R_{//}$ :	parallel backscattering ratio
$R_p$ :	reflectivity coefficient for polarization in the scattering plane
$R_s$ :	reflectivity coefficient for polarization perpendicular to the scattering plane
RH:	relative humidity
RSL:	Raman scattering lidar
s:	backscattering signal
$s_0$ :	ambient air backscattering signal
SMS:	spatial modulation spectroscopy
s:	spherical particles
sca:	scattered
SMPS:	Scanning mobility particle sizer
$s_p$ :	particles backscattering signal
$S_p$ :	lidar ratio
$\mathbf{St}_p$ :	Stokes vector of the particles backscattering radiation
$\mathbf{St}_{\text{inc}}$ :	Stokes vector of the incident laser pulse emitted
ss:	sea-salt particles
T	atmospheric transmission
$T_p$ :	transmission coefficient for polarization in the scattering plane
$T_s$ :	transmission coefficient for polarization perpendicular to the scattering plane
TG:	target gas
$t_i$ :	time of the laser pulse emission
$\mathbf{u}$ :	unit vector in the z-direction
U:	third element of the Stokes vector
V:	fourth element of the Stokes vector
w:	water droplets
W:	weighting factor of the spheroids distribution
x:	size parameter
$X_{\text{ns}}$ :	fraction of ns-to-particle backscattering coefficients
$\alpha_p$ :	particle extinction coefficient
$\beta_{\text{ash}, \pi}$ :	$\pi$ -polarized ash particle backscattering coefficient
$\beta_{\text{nash}, \pi}$ :	$\pi$ -polarized non-ash particle backscattering coefficient
$\beta_{\text{dust}, \pi}$ :	$\pi$ -polarized dust particle backscattering coefficient
$\beta_{p, \pi}$ :	$\pi$ -polarized particle backscattering coefficient
$\beta_{m, \pi}$ :	$\pi$ -polarized molecular backscattering coefficient
$\beta_{\text{ndust}, \pi}$ :	$\pi$ -polarized non-dust particle backscattering coefficient
$\beta_{\text{ss}, \pi}$ :	$\pi$ -polarized sea-salt particle backscattering coefficient
$\beta_{\text{ws}, \pi}$ :	$\pi$ -polarized water-soluble particle backscattering coefficient
$\delta$ :	volume depolarization ratio

$\delta^*$ :	measured volume depolarization ratio
$\delta_{\text{NaCl}}$ :	NaCl depolarization ratio
$\delta_{\text{ash}}$ :	ash particle depolarization ratio
$\delta_{\text{dust}}$ :	dust particle depolarization ratio
$\delta_{\text{nash}}$ :	non-ash particle depolarization ratio
$\delta_{\text{ndust}}$ :	non-ash particle depolarization ratio
$\delta_p$ :	particle depolarization ratio
$\delta_{\text{ss}}$ :	sea-salt particle depolarization ratio
$\delta_{\text{ws}}$ :	sea-salt particle depolarization ratio
$\delta_w$ :	water droplets depolarization ratio
$\Delta x$ :	deviation from optics axis
$\Delta y$ :	Amplitude of the spatial modulation
$\Delta_s$ :	solar declination angle
$\Delta\lambda$ :	interferential filter bandwidth
$\Delta S$ :	collection surface of the detector
$\Delta t$ :	time interval
$\Delta\delta$ :	difference between $\delta^*/G$ and $\delta$
$\varepsilon$ :	aspect ratio
$\check{\varepsilon}$ :	width of the scattering angle detected
$\xi$ :	residual polarization of the emitted laser
$l\lambda$ :	single wavelength
$2\lambda$ :	dual wavelength
$\lambda$ :	wavelength
$\lambda/2$ :	half-waveplate
$\lambda/4$ :	quarter-waveplate
$\eta_{\lambda,\pi}$ :	electro-optic detection efficiency
$\varphi$ :	misalignment angle between the laser linear polarization and the parallel axis of the detector PBC
$\varphi_0$ :	offset-angle between the parallel laser linear polarization and the p-axis of the dichroic beamsplitter
$\pi$ :	{//,⊥} polarization components ( co- or cross-polarized)
$\emptyset$ :	diameter of the iris $I_r$
$\emptyset_c$ :	diameter of the lens $L_c$
$\emptyset_1$ :	diameter of the lens $L_1$
$\emptyset_2$ :	diameter of the lens $L_2$
$\theta$ :	scattering angle
$\theta_0$ :	offset angle between the laser linear polarization and the dichroic beamsplitter's axis in the scattering plane
$\theta_i$ :	tilt angle from normal incidence of the QWP
$\Omega$ :	solid angle
$\psi$ :	angle between the horizontal (x,z)-plane and the fast axis of the quarter waveplate
$\tau$ :	laser pulse duration
$\omega_0$ :	single scattering albedo
$(d\sigma/d\Omega)_{//}$ :	co-polarized backscattering cross-section
$\langle(d\sigma/d\Omega)_{//}\rangle$ :	mean co-polarized backscattering cross-section
$(d\sigma/d\Omega)_{\perp}$ :	cross-polarized backscattering cross-section
$\langle(d\sigma/d\Omega)_{\perp}\rangle$ :	mean cross-polarized backscattering cross-section
$(d\sigma/d\Omega)_{\text{ash}}$ :	ash particle backscattering cross-section
$\langle(d\sigma/d\Omega)_{\text{ash}}\rangle$ :	mean ash particle backscattering cross-section

# Content

<b>Thesis abstract</b> .....	<b>3</b>
<b>Résumé de thèse</b> .....	<b>6</b>
<b>List of variables and notations</b> .....	<b>8</b>
<b>Chapter 1 Introduction</b> .....	<b>15</b>
1.1 Scientific context of this work .....	15
1.2 Atmospheric aerosols .....	17
1.2.1 Atmospheric particles chemical composition .....	17
1.2.2 Particle size distribution .....	18
1.2.3 Atmospheric particle shape .....	22
1.2.4 Open questions .....	23
1.3 On the use of polarization lidar for atmospheric studies.....	24
1.4 Laboratory optical experiments on atmospheric particles.....	27
1.5 Laboratory experiment on a single particle.....	28
1.6 Outline of this thesis.....	29
<b>Chapter 2 Polarization-resolved optical backscattering</b> .....	<b>32</b>
2.1 General framework.....	32
2.2 Scattering matrix formalism.....	34
2.2.1 Polarization-resolved backscattering by mono-sized particles .....	35
2.2.2 Size-averaged polarization-resolved backscattering by a particles ensemble.....	38
2.3 Optical backscattering partitioning .....	39
2.3.1 Optical backscattering partitioning in a two-component particle mixture (OBP2)	40
2.3.2 Optical backscattering partitioning in a three-component particle mixture (OBP3)	46
2.4 Optical properties of an individual particle component .....	49
2.4.1 Field measurements .....	49

2.4.2 Laboratory measurements .....	50
2.4.3 Light scattering numerical simulations .....	51
2.5 Conclusion.....	58
<b>Chapter 3 Lidar polarization-resolved backscattering measurements .....</b>	<b>60</b>
3.1 Introduction .....	60
3.2 Lyon 2 $\lambda$ -polarization Lidar .....	62
3.2.1 Statistical errors and systematic biases .....	62
3.2.2 Lyon 2 $\lambda$ -polarization lidar experimental set-up .....	68
3.2.3 Calibration procedure for the polarization measurement .....	70
3.2.4 Polarization resolved backscattering coefficients .....	71
3.3 The Ash case: volcanic ash mixed with sulfate particles .....	75
3.3.1 Geophysical situation .....	75
3.3.2 Observation of the Icelandic volcanic ash cloud above Lyon.....	77
3.3.3 Ash and Nash backscattering retrievals .....	79
3.3.4 Applications of the OBP2-methodology .....	83
3.3.5 Ash case study summary .....	90
3.4 The Dust case study: Desert dust mixed with non-dust particles.....	91
3.4.1 Dust and ndust backscattering retrieval .....	92
3.4.2 New particle formation process (NPF-event).....	95
3.4.3 Numerical simulation of expected lidar backscattering coefficient in an NPF-event .....	97
3.4.4 Observation of new particle formation with UV polarization Lidar .....	101
3.4.5 Dust case study summary .....	104
3.5 The Sea-salt / Dust case study.....	105
3.5.1 Geophysical situation .....	105
3.5.2 Sea-salt, Dust and ws backscattering retrieval .....	107
3.5.3 Discussion .....	110

3.6 Conclusions .....	111
<b>Chapter 4 Laboratory measurements on atmospheric nanoparticles.....</b>	<b>113</b>
4.1 Polarization-resolved exact backscattering by a particles ensemble in air .....	114
4.1.1 State of the art on exact light backscattering by particles in air.....	114
4.1.2 Principle of an exact backscattering measurement for nanoparticles in ambient air .....	116
4.1.3 Experimental set-up.....	120
4.1.4 Results and discussion.....	127
4.1.5 Conclusion.....	134
4.2 Single nanoparticle experiment.....	135
4.2.1 Introduction .....	135
4.2.2 Experimental methodology .....	136
4.2.3 Results and discussion.....	141
4.3 Conclusion.....	145
<b>Chapter 5 Conclusion and outlooks.....</b>	<b>148</b>
<b>Appendix A Atmospheric gases .....</b>	<b>159</b>
A.1 Optical remote sensing methods to monitor atmospheric gases.....	159
A.2 Methodology .....	160
A.2.1 OCS-Lidar principle .....	161
A.2.2 Experimental and numerical assessment of OCS-Lidar.....	162
<b>Appendix B Sky background contribution to the polarized Lidar signal.....</b>	<b>164</b>
<b>Appendix C Depolarization ratio <math>\delta^*</math> in the presence of a dichroic beamsplitter misalignment.....</b>	<b>167</b>
<b>List of personal publications: .....</b>	<b>169</b>
<b>References: .....</b>	<b>170</b>

# Chapter 1

## Introduction

This thesis is dedicated to the study of the optical backscattering and extinction of laser light by atmospheric particles in the nanometer size range. The main concern of this work relies on accurate observation of polarization-resolved and wavelength dependence of the particles light backscattering, which makes possible to address its complex microphysical properties (chemical composition, shape and size) and concentration in the atmosphere.

### 1.1 Scientific context of this work

An aerosol is an ensemble of liquid or solid particles suspended in ambient air, which present a wide range of sizes, shapes and chemical components with interconnected distributions (Seinfeld and Pandis, 2006). Atmospheric particles are usually classified as primary particles when directly emitted from one source (desert dust, volcanic ash, soot, sea-salt or biological) then secondary aerosols, when formed by particle-to-gas conversion, such as nucleation, condensation, heterogeneous and multiphase chemical reaction (Hallquist et al., 2009).

Atmospheric aerosols strongly affect human health by giving rise to premature mortality (Pope et al, 2013; Fann and Risley 2013). For instance, 66 000 (95 % confidence interval [39 300; 84 500]) premature death per years in the USA are due to atmospheric particles (Punger and West, 2013). Moreover particles are associated with lung cancer and respiratory diseases (Katanoda et al., 2011). Indeed when aerosols are inhaled aerosols bigger than 5  $\mu\text{m}$  mostly deposit in the nose, pharynx, larynx and trachea, while aerosols smaller than 5  $\mu\text{m}$  deposit in the bronchioles and alveoli (Dockery and Pope, 1994). Dockery and Pope (1994) also underlined that the biological effect of aerosols is determined by their physical and chemical nature and especially their solubility.

In addition to this health impact, atmospheric aerosols impact the Earth's climate by modifying the optical scattering and absorption of the radiation emitted by the Earth and the Sun (direct effect) (Haywood and Boucher, 2000) and also modify the reflection of solar

radiation by changing the cloud coverage (indirect effect) (Twomey, 1977; Ramaswamy et al., 2001). Figure 1.1, derived from the IPCC report (2007), presents the global radiative forcing (RF, in  $W \cdot m^{-2}$ ) impacting the Earth's climate and underlines the role of aerosols and the remaining uncertainties concerning the direct and indirect effect of atmospheric aerosols on Earth's climate. Indeed, quantifying the climate impact of aerosols is a very difficult task as it requires the accurate determination of numerous inputs, including particle chemical composition, number concentration, size distribution, mixing state, shape and hygroscopicity, together with the particle spatio-temporal distribution (IPCC, 2007). Moreover, their optical properties such as the single scattering albedo  $\omega_0$ , the particles extinction cross-section  $C_{ext,p}$  and the particles scattering phase function  $F_{11,p}$  have to be accurately determined as function of the wavelength  $\lambda$  of the radiation and the relative humidity (RH) of the atmosphere. Another difficulty arises from complex processes and interactions between aerosols and gases, such as new particle formation which understanding is still undergoing (O'Dowd et al., 2002; Boulon et al., 2011; Kulmala et al., 2012; Dupart et al., 2012, Kyrö et al., 2013). Hence, an accurate quantifying of the atmospheric particles effect on climate and health would require a near perfect characterizing of the atmospheric particles and the processes driving their formation and aging.

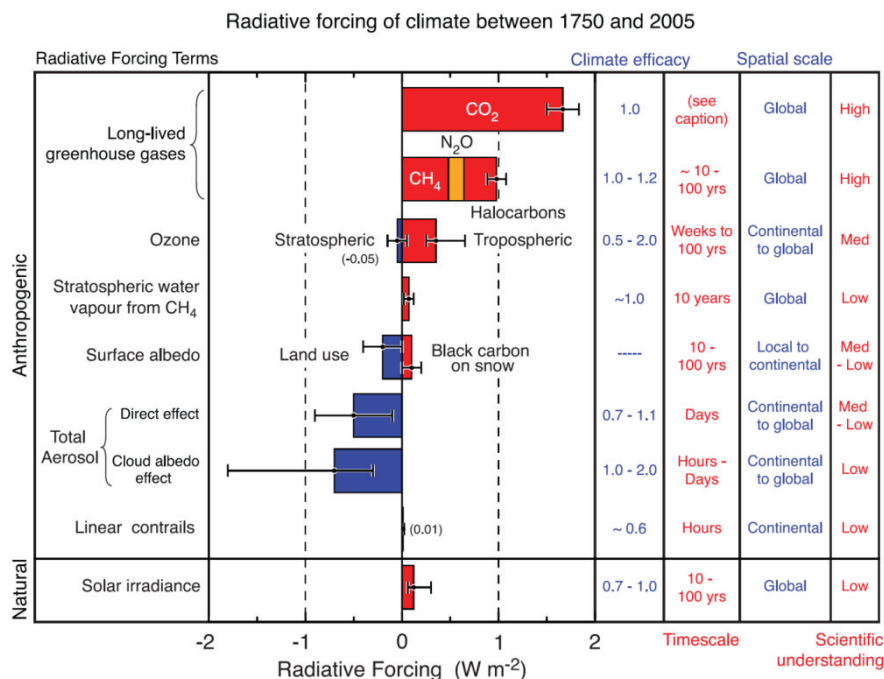


**Figure 1.1** Global mean radiative forcing (RF) from the agents and mechanisms discussed in the IPCC report (2007), grouped by agent type. The RF values, plotted in this figure, correspond to the bold values in Table 2.12 of the IPCC report (2007). The scientific understanding shown for each term is described in Table 2.11 of the IPCC report (2007). **Figure and caption from the IPCC report (2007).**

Hence, the scientific context of the Figure 1.1 settled the framework of this thesis and especially the RF uncertainties affected by aerosols. These error bars originate from the complexity of atmospheric aerosols which present a wide range of size, shape and chemical composition. In this context, we focus on the benefits brought by optical techniques: optical measurements are a key tool since they can operate under atmospheric conditions of relative humidity, temperature and pressure, which mean that, when no sampling is required during the observation, the size, the shape and the chemical composition of the aerosol are preserved. Moreover, photon-particles energy interaction relies on only few electron-volts, below ionization thresholds that would modify the aerosol. In addition, high sensibility optical detectors exist, with the ability to detect up to the photon-counting if needed. While the main concern of this work is the study of atmospheric particles optical properties, I have also performed ,through a collaborative work with my colleague B. Thomas (Thomas et al., 2012, 2013a, b), range-resolved measurements of the atmospheric water vapor content by using light absorption. This work is presented in the Appendix A.

## **1.2 Atmospheric aerosols**

In this section, we present in details the atmospheric particles, which have different chemical composition, shape and sizes. The new particle formation is also introduced. Then after recalling some remaining questions, we present the optical techniques used to study atmospheric particles through either atmospheric or laboratory experiment on an ensemble of particle or on a single particle.

### **1.2.1 Atmospheric particles chemical composition**

The chemical composition of atmospheric particles drives their physical and chemical properties such as the water uptake/solubility, scattering or absorption (Li et al., 2001; Randriamiarisoa et al., 2006; Vester et al., 2007). In the atmosphere, the predominant chemical components are sulfate, nitrate ammonium, sea-salt, mineral dust, organic compounds and black or elemental carbon. Each of these components typically contributes around 10-30 % of the total particle mass load (Pöschl et al., 2005). However these weightings may vary by one order of magnitude (Finlayson-Pitts and Pitts, 2000, Seinfeld and Pandis, 2006). These particles may exhibit hygroscopic properties. Water-soluble particles,

defined accordingly to Hess et al. (1998), include sulphate (such as  $\text{H}_2\text{SO}_4$ ,  $\text{NH}_4\text{HSO}_4$ ,  $(\text{NH}_4)_2\text{SO}_4$ ) and nitrate (such as  $\text{NH}_4\text{NO}_3$ ) particles as well as other organic water-soluble substances, while soot and soil particles are water-insoluble. Moreover, there is close link between the chemical composition and the optical properties since the particle's refractive index  $m$  drives the light scattering and absorption processes (Mishchenko et al., 2002). Hence, soot particles are sometimes considered as the second most warming component after  $\text{CO}_2$  (Jacobson, 2001), as they strongly absorb the Sun light, while sulfate particles, have a cooling effect by reflecting sun light (Mishchenko et al., 2007b). In addition, several chemical components are often mixed in the atmosphere and the corresponding particles optical properties, such as  $\omega_0$ ,  $C_{\text{ext,p}}$  or  $F_{11,p}$ , may strongly vary depending on the mixing state of these particles (Lesins et al., 2002). In the atmosphere, particle mixtures are usually observed as, either internally-mixed (when one small particle is embedded in a larger host particle) or externally-mixed (when particles are separated by a distance much greater than their size) as illustrated in Figure 1.2, inspired from Mishchenko et al. (2004b). The case of semi-external particle mixtures or aggregates is not considered in this thesis.



**Figure 1.2** Illustration of the external (a) and internal (b) mixing of atmospheric particles.

### 1.2.2 Particle size distribution

The particle size is also very important, as for instance only particles of size larger than 25-50 nm in radius are able to influence climate, although smaller particles may influence health and atmospheric chemistry (Kulmala et al., 2012). The size of atmospheric particles varies by more than four orders of magnitudes from less than 1 nm up to 100  $\mu\text{m}$ . As particles are never perfectly mono-sized, the so-called particle size distribution (PSD) is often used to characterize the size of atmospheric particles. For a particles number concentration  $N_p$ , the PSD function  $n_p(r)$ , i.e. the number of particles per  $\text{cm}^3$  in air having a radius in the range  $r + dr$ , is defined as follows (Seinfeld and Pandis, 2006):

$$N_p = \int_0^{\infty} n_p(r) \cdot dr \quad (1.1)$$

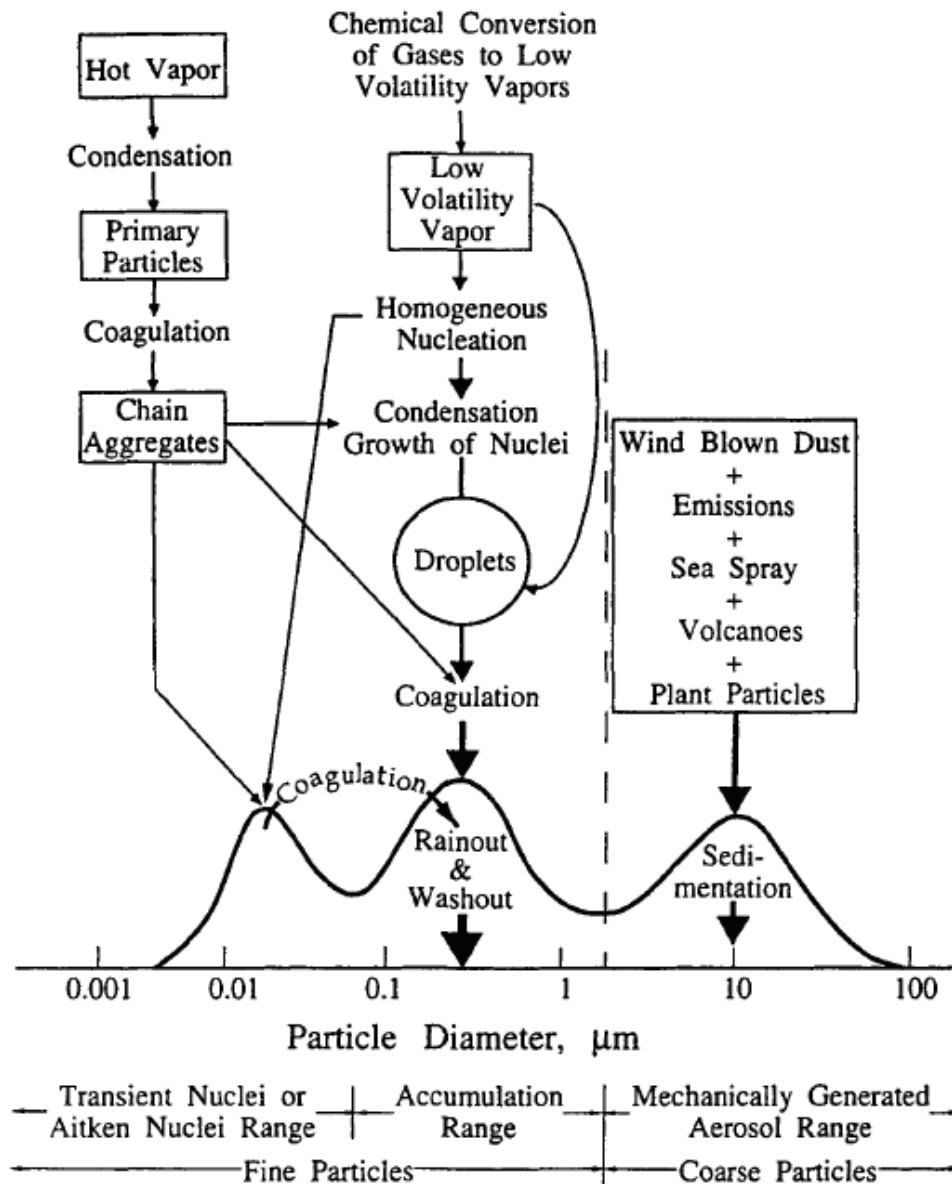
If the particles are nonspherical,  $r$  is defined as the radius of the sphere that would have the same surface or volume as the considered nonspherical nanoparticle. Hence, surface and volume  $S_p$  and  $V_p$  concentrations are also used and defined in Equation (1.2) and (1.3):

$$S_p = \pi \cdot \int_0^{\infty} r^2 \cdot n_p(r) \cdot dr \quad (1.2)$$

$$V_p = \frac{4}{3} \pi \cdot \int_0^{\infty} r^3 \cdot n_p(r) \cdot dr \quad (1.3)$$

In this thesis, if not mentioned otherwise, for non-spherical particles, the volume equivalent radius will be used.

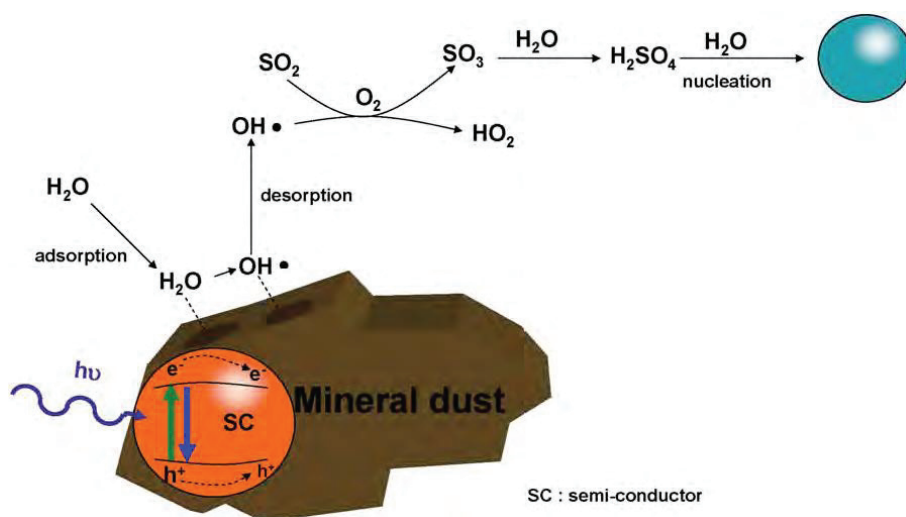
Figure 1.3 present a scheme of  $S_p(r)$  as presented by Seinfeld and Pandis (2006). The PSD exhibits three main modes: the ultrafine particles mode (around  $r = 10$  nm), the fine particles mode (around  $r = 150$  nm) and the coarse mode (around  $r = 5$   $\mu$ m). The highest surface concentration is found for fine particles, which underlines the high importance of particles having a radius in the hundred nanometer range. Ultrafine particles also have a high surface concentration. Moreover, in the particles number concentrations representation of the PSD, ultrafine particles would be the most numerous as the  $r^2$ -factor present in Equation (1.2) would then disappear. In addition, ultrafine and fine particles experience the longest lifetime in the atmosphere. Hence, some atmospheric particles may remain in the troposphere for several weeks (Robock, 2000; Overnevaide et al., 2009), which further reinforce their radiative impact.



**Figure 1.3** Idealized schematic of the distribution of particle surface area of an atmospheric aerosol (Whitby and Cantrell, 1976). Principal modes, sources, and particle formation and removal mechanism are indicated. Figure and caption from (Seinfeld and Pandis, 2006).

As detailed in Figure 1.3, to this three-mode PSD correspond several physico-chemical processes that indeed occur in the atmosphere, such as sedimentation, which usually occur on coarse particles, as during volcanic ash episodes or Saharan dust outbreaks, after long-range transport. Other processes may occur, such as condensation, coagulation, aggregation (for ultrafine particles), then homogeneous nucleation, condensation growth and coagulation in the accumulation range. These phenomena may lead to new particle formation, hereafter noted NPF. Research on NPF recently strongly involves the scientific community (O’Dowd et al., 2002; Hamburger et al., 2010; Kirkby et al., 2011; Boulon et al., 2011; Kulmala et al., 2012; Dupart et al., 2012; Kyrö et al., 2013). Laboratory experiments, performed in cloud chambers,

have settled the fundamental nucleation processes involving ions and neutral cluster (Kirkby et al., 2011). Moreover, field experiments showed that NPF can be observed everywhere in the atmosphere (Kulmala et al., 2012; Kyrö et al., 2013), such as in the Planetary Boundary Layer (PBL) (Wehner et al., 2010; Dupart et al., 2012) or in the free troposphere (Hamburger et al. 2010; Boulon et al., 2011). In this context, a recent finding is the possibility to initiate nucleation by new pathways, in the presence of mineral dust particles (Dupart et al. 2012) or volcanic materials (Boulon et al., 2011). Basically, NPF is related to the gaseous  $\text{H}_2\text{SO}_4$  in the atmosphere whereby molecular sulfuric acid formation processes are still under debate. Recent work realized on heterogeneous photochemistry shows that particulate matter presenting semi-conductor properties like desert dust containing Iron Oxide could offer a new pathway to explain the formation of  $\text{H}_2\text{SO}_4$  in the gas phase (Dupart et al. 2012). To provide details on this new pathway, it is presented in Figure 1.4.

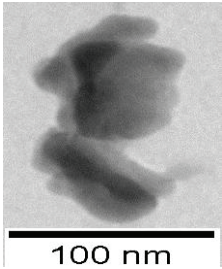


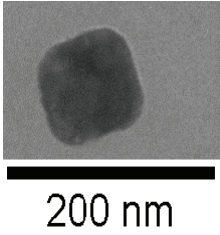
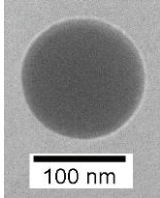
**Figure 1.4** Scheme of reaction mechanism. The semiconductor (SC) components of dust under UV irradiation are producing  $\text{OH}\cdot$  radicals that may desorb and react with  $\text{SO}_2$  in the vicinity of the dust  $\text{OH}\cdot$  radicals oxidizing  $\text{SO}_2$  in the vicinity of the surface. The produced sulfuric acid may then initiate nucleation events. Such new particle formation eventually leads to secondary particle formation. Hallquist et al. (2009) recently reviewed the formation, properties and impact of second organic particles and emphasis their complexity. In addition, Hallquist et al. (2009) pointed out numerous future research directions necessary to understand the formation, properties and impact of second organic particles, including the study of complex reactant mixture and composition, the coupling of laboratory and field studies performed under similar conditions or tools development for isolation, characterization and process studies of the water insoluble organic matter. For all these reasons, the study of fine and ultrafine particles is emphasized in this thesis, as detailed below in the thesis's outline (Figure 1.3).

### 1.2.3 Atmospheric particle shape

Among the major uncertainties involved in climate change modeling, the lack of knowledge on the atmospheric particles shape is an essential point, especially in urban polluted areas, where atmospheric aerosols may present a wide range of sizes and shapes. Applying the century-old Lorenz–Mie formalism to tropospheric particles may lead to significant errors in climate change modeling (Kahnert et al., 2005), as nonspherical particles scatter and absorb light differently from volume- or surface-equivalent spheres (Mishchenko et al., 2000). In particular, orientation averaging over an ensemble of non-spherical particles does not lead to the same scattering pattern as for spheres (Nousiainen et al., 2009). Hence, non-spherical particles are difficult to address since no general analytical solution is available, except for some specific geometry far away from the observed highly-irregular shape of atmospheric particles (Mishchenko et al., 2002). The variability in the particles size and shape is depicted in Table 1.1, where volcanic ash, desert dust and sea-salt particles are observed through electron microscope images, while water-soluble particles, like sulfate particles, are spherical.

**Table 1.1** Electron microscope images of desert dust particles, sea-salt (ss) particles and water-soluble (ws) particles (an ammonium sulphate particle is observed) taken at ILM. For volcanic ash, in the absence of measurement at the ILM, the image has been provided by O. Muñoz from Mount Spurr volcanic eruption. ws-particles are here defined accordingly to the classification of Hess et al. (1998), which include, sulphate (such as  $\text{H}_2\text{SO}_4$ ,  $\text{NH}_4\text{HSO}_4$ ,  $(\text{NH}_4)_2\text{SO}_4$ ) and nitrate (such as  $\text{NH}_4\text{NO}_3$ ) particles as well as other organic water-soluble substances.

Particle type	Label	Literature references	Electron microscope image
Volcanic ash	(ash)	Winker and Osborn (1992), Mather et al. (2003), Muñoz et al. (2004), Sassen et al. (2007), Schumann et al. (2011), Lindqvist et al., (2011), Eyjafjalljökull ACP Special Issue (Hasager et al., 2012) Miffre et al. (2012a,b)	
Desert dust	(dust)	Shimizu et al., (2004) Mallet et al. (2004) Kaaden et al. (2009) Nousiainen (2009) Veselovskii et al. (2010) Ansmann et al. (2011) Nishizawa et al. (2011) Di Girolamo et al. (2012)	

Sea-salt	(ss)	Shettle et al., (1979) O'Dowd et al. (1997) Murayama et al. (1999) Wise et al. (2005) Zhang (2008) Sakai et al. (2010)	
Water-soluble	(ws)	O'Dowd et al. (1997) Hess et al., (1998) Nishizawa et al. (2011) Di Girolamo et al. (2012)	

### 1.2.4 Open questions

The complexity of the formation, properties and impact of atmospheric particles, underline the need to address the different particle chemical component from their mixing and study the interaction between these particle components. Moreover, the optical properties (scattering and extinction) of these atmospheric particles are still under investigation and need further characterization (see Figure 1.1). In addition, the dust-climate processes due to dust transport mechanism affect adjacent continental and ocean regions (Engelstaedter et al., 2006). During transport by advection from source regions to places where intrusion episodes occur, the particle properties may also change due to processes such as sedimentation, mixing with other particles (Zhang, 2008), hygroscopic growth and possible chemical alteration (Bourcier et al., 2011; Riccobono et al., 2012). After long-range transport, these particles are hence highly dispersed and aged, and may present sizes or shapes different from those observed in the source region. One of the typical consequences is a complex vertical layering generally observed in the low troposphere at far-range remote sites, far from their source regions. Due to this complexity, new measurement methodologies and techniques have to be developed to specifically address each particle component in the particle mixtures. We here present the corresponding bibliography.

### 1.3 On the use of polarization lidar for atmospheric studies

To face the atmospheric particles complexity, laser spectroscopy is of prime importance and moreover particle light scattering and extinction are nowadays the main applied optical properties to evaluate the atmospheric particle content. Several optical properties can be addressed by laser spectroscopy, as for example the scattering phase function (Gayet et al., 1997). Laser spectroscopy can be applied to address the chemical composition of atmospheric particles, by studying their refractive index wavelength dependency (Lang-Yona et al., 2009). Laser-induced fluorescence is another methodology to access PM chemical composition also used to characterize organic and biogenic atmospheric particles (Mejean et al., 2004). Along with these laser techniques, lidar (light detection and ranging) is particularly interesting as it provides fast, reliable and range-resolved access to the optical properties of an ensemble of atmospheric particles from the ground up to several kilometers, and this under in situ atmospheric conditions of temperature and humidity (Measures, 1992; Weitkamp, 2005; Kacenenbogen et al., 2011; Di Girolamo et al., 2012). Indeed, a pulsed laser beam is sent into the atmosphere and the light backscattered by atmospheric aerosols and molecules is collected by a receiver telescope, which focus the collected light on a photo-detector. The laser excitation wavelength  $\lambda$  is often chosen in the visible (VIS) or/and in the infrared (IR) spectral range (Sugimoto et al., 2002; Mejean et al., 2004; Kacenenbogen et al., 2011) while the ultraviolet (UV) spectral range is rather seldom used (Reichardt et al., 2000; Adam de Villiers et al., 2009; Freudenthaler et al., 2009). To address the high concentrated ultrafine and fine particles with laser remote sensing, it is interesting to choose a laser excitation wavelength  $\lambda$  in the UV spectral range, where particles size parameters ( $x = 2\pi r/\lambda$  for an  $r$  equivalent sphere radius) often lead to backscattering enhancements (Mishchenko et al., 2002). This is, however, challenging since in the UV spectral range molecular scattering may overcome particles scattering. In addition, the shape of these particles can be addressed by using the light's polarization, which is defined along the direction of the light electric field. The polarization state of light can be fully defined by using the Stokes vector  $[I, Q, U, V]^T$ , where  $I, Q, U$  and  $V$  are the four Stokes parameters.  $I$  describes the light intensity, while  $Q, U$  and  $V$  fully describe the light polarization state. In this thesis, if not mention otherwise the Stokes parameters are defined with respect to the scattering plane (plane comprising the incident and scattered wave vector  $\mathbf{k}_{inc}$  and  $\mathbf{k}_{sca}$ ). As further detailed in Section 2.1, light scattering by non-spherical particles modify the polarization state of the incident laser light,

while for spherical particles, the polarization state of the laser light is preserved during the scattering process. Hence, polarization-resolved remote sensing systems can be used as a particle shape and thermodynamic phase indicator (Gobbi et al., 2004), especially in the lidar backward direction, where polarization of the scattered light is unequivocally sensitive to the particles shape (Mishchenko et al., 2002; Nousiainen et al., 2009). The polarization lidar, which equation is given in Equation (1.4) (Measures, 1992; Weitkamp, 2005), has the same principle than the regular lidar, except that before being detected the backscattered light is separated as a function of its polarization  $\pi = \{//, \perp\}$  with respect to the incident laser polarization. Hence, at altitude  $z$ , two lidar signals are obtained as function of their  $\pi = \{//, \perp\}$  polarization and are respectively called co- and cross-polarized signals:

$$P_{\pi}(\lambda, z) = \eta_{\pi}(\lambda) \cdot P_0(\lambda) \cdot \frac{O(z)}{z^2} \cdot \beta_{\pi}(\lambda, z) \cdot T^2 + P_{F,\pi} \quad (1.4)$$

$$T(\lambda, z) = \exp\left(-\int_0^z (\alpha_p(\lambda, z') + \alpha_m(\lambda, z')) \cdot dz'\right) \quad (1.5)$$

where  $\eta_{\pi}(\lambda)$  is the detection efficiency taking into account the electro-optics gain of the detector and the geometry of the telescope, while  $P_0$  is the incident laser power and  $O(z)$  is the overlap function between the laser beam and the receiver field of view (FOV).  $P_F$  is the background signal, mainly due to the backscattered sunlight.  $T$  is the atmospheric transmission, which accounts for the particles (p) and the molecular (m) extinction coefficient ( $\alpha$ ) The key point of the lidar equation is the so-called atmospheric volume backscattering coefficient  $\beta_{\pi}(\lambda, z)$ , in  $m^{-1} \cdot sr^{-1}$ , which describes the amount of backscattered light. By applying the superposition principle,  $\beta_{\pi}$  is equal to :

$$\beta_{\pi} = \beta_{p,\pi} + \beta_{m,\pi} = N_p \cdot \left\langle \left( \frac{d\sigma}{d\Omega} \right)_{p,\pi} \right\rangle + N_m \cdot \left\langle \left( \frac{d\sigma}{d\Omega} \right)_{m,\pi} \right\rangle \quad (1.6)$$

Where  $N_p$  and  $N_m$  are the particles (p) and molecules (m) number concentration (in  $m^{-3}$ ), while  $\langle (d\sigma/d\Omega)_{p,\pi} \rangle$  and  $\langle (d\sigma/d\Omega)_{m,\pi} \rangle$  is the particles and molecules co-/cross-polarized backscattering differential cross-section, averaged over their size distribution. Most of the polarization lidars use a laser linearly polarized (Sugimoto et al., 2006; Sassen et al., 2007; Freudenthaler et al., 2009; Veselovskii et al., 2010). At a far range or altitude  $z$  compared to the particles size, the magnitude of the non-zero polarization change due to the backscattering by randomly-oriented non-spherical particles is a signature of the particles sphericity

(Mishchenko et al., 2002), which is often called depolarization. In the lidar community, the volume linear depolarization ratio  $\delta$  is defined as follows:

$$\delta(\lambda, z) = \frac{\beta_{\perp}(\lambda, z)}{\beta_{\parallel}(\lambda, z)} \quad (1.7)$$

However,  $\delta$  is not a particle shape indicator as both molecules (subscript m) and particles (subscript p) contribute to  $\beta_{\pi}$  (i.e.  $\beta_{\pi} = \beta_{m,\pi} + \beta_{p,\pi}$  obtained when applying the superposition principle). Hence, the particle sphericity indicator is the so-called particle linear depolarization ratio  $\delta_p$ :

$$\delta_p(\lambda, z) = \frac{\beta_{p,\perp}(\lambda, z)}{\beta_{p,\parallel}(\lambda, z)} \quad (1.8)$$

where the particle backscattering coefficient  $\beta_{p,\pi}$  can be retrieved from the molecular backscattering coefficient  $\beta_{m,\pi}$  by applying the Klett's algorithm (1985). Moreover, with a  $\beta_{p,\parallel}$  time-altitude map, the  $\beta_{p,\pi}$ -coefficients can be used to study the complex particle layering observed in the atmosphere, as shown in Figure 1.5, where a thin filament of unusually high particle load is visible between 3 and 6 km. As detailed in Chapter 3, this filament exhibits the temporal behavior of the volcanic ash cloud. Hence, such polarization lidar measurements of  $\beta_{p,\pi}$  allow to distinguish the particle layering from the ground up to several kilometers altitude.

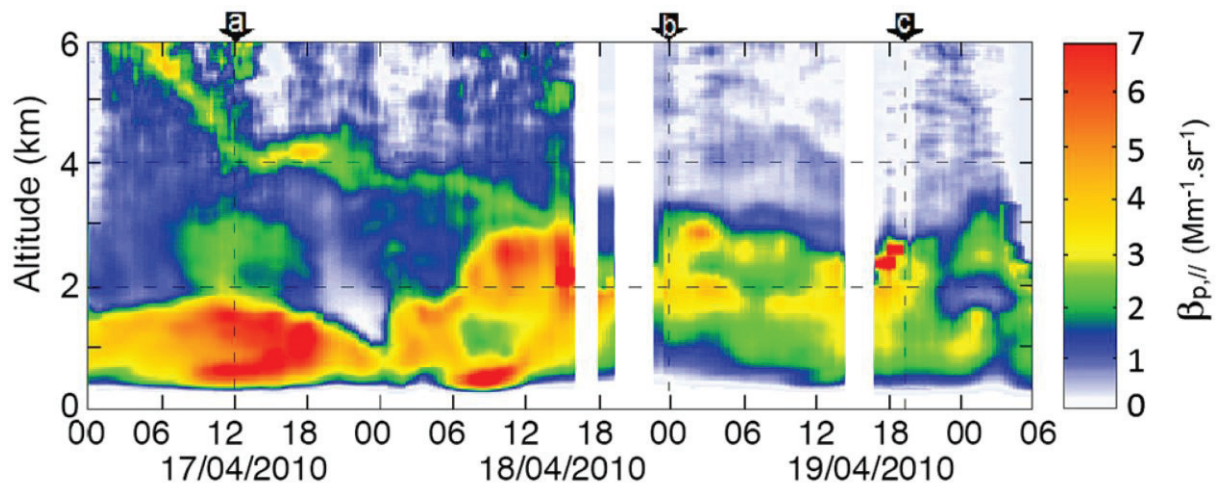


**Figure 1.5** Time altitude map of  $\beta_{p,\parallel}$  from 17<sup>th</sup> up to the 19<sup>th</sup> of April 2010. A thin filament of unusually high particle load is visible between 3 and 6 km on the 17<sup>th</sup> April.

A few lidars use a laser circularly polarized (Del Guasta et al., 2006; Roy et al., 2011; Hayman et al., 2012), which is interesting to study preferentially oriented particles (Del Guasta et al., 2006; Nicolet et al., 2012; Hayman et al., 2012). However, as shown

theoretically by Mishchenko and Hovenier (1995) and experimentally by (Del Guasta et al., 2006; Roy et al., 2011), when particles are randomly-oriented, the measurement of the linear or circular polarization leads to the same information on the particle shape as the linear and circular depolarization are linked by  $\delta_c = 2\delta_p/(1 - \delta_p)$ . Moreover, Lidar may also be used to address the PSD by using several laser wavelengths (Veselovskii et al., 2010; Di Girolamo et al., 2012) and lidar is the only remote sensing measurement allowing retrieving the range resolved vertical profile of particle concentrations (Revuelta et al., 2012).

## **1.4 Laboratory optical experiments on atmospheric particles**

To address the climate impact of atmospheric aerosols, as underlined by the IPCC report (2007), laboratory measurements are interesting, as they allow controlling the experimental conditions, such as the particle chemical composition, size and shape, which brings complementarities with atmospheric field experiments. Hence, laboratory measurements have raised new understanding on the atmospheric processes such as new particle formation (Kirkby et al., 2011). Moreover, laboratory measurements may serve as a standard for evaluating particle optical properties, such as light scattering (Munoz et al., 2004), as they account for the potential highly-irregularly shape of nonspherical particles, as well as their inhomogeneity, porosity and birefringence (Attwood and Greenslade, 2011). Therefore, coupling field with laboratory experiments, when of course performed under similar experimental conditions, considerably improves the knowledge on particles in their environment (Hallquist et al., 2009). Hence, as the presented lidar measurements are performed in the backscattering direction, we here focus on the optical laboratory measurements performed close to the backscattering direction.

Besides its quite simple geometry and its handiness for in situ applications (Ghosh et al., 2009), the backscattering direction has raised great interest as it is one of the most sensitive directions to the size and the shape of the sample (Mishchenko et al., 2002; Nousiainen et al., 2009). In addition, some experiments are polarization-resolved as they measure the elements of the scattering matrix, which relates the Stokes vector of the incident and scattered light, as developed in Chapter 2. O. Muñoz and J. Hovenier recently reviewed (2011) the existing light scattering laboratory experiments measuring one or more elements of the scattering matrix of an ensemble of particles suspended in air. Several light scattering matrix experiments have

been built and operate at high scattering angles  $\theta \geq 168^\circ$ , approaching the exact backscattering direction ( $\theta = 180^\circ$ ) (Sakai et al., 2010, Munoz and Hovenier., 2011; Schnaiter and al., 2012; Glen and al., 2013); where the scattering angle  $\theta$  is defined as the angle between the incident and scattering direction of the light. The closest value to the exact backscattering direction is  $\theta = 179.6^\circ$  (Sakai et al., 2010). To cover the exact backscattering direction, polynomial extrapolations or numerical algorithms have been proposed (Liu et al. 2003), but their inherent assumptions must be discussed and may lead to quite considerable errors, as recently discussed by M. Schnaiter et al. (2012). Hence, there is a need for laboratory scattering matrix measurements in the exact backscattering direction for an ensemble of particles in air, and this for at least two reasons. Firstly, it may help validating numerical simulations based on T-matrix or DDA numerical codes, which are never assumption-free, especially when the particles exhibit complex morphologies. Secondly, it may be also useful in passive or active lidar remote sensing field experiments, which operate in the backscattering geometry and where T-matrix computations have been coupled with polarization lidar (Veselovskii et al., 2010). However, to our knowledge, none of the existing apparatuses cover the exact backscattering direction for an ensemble of particles suspended in air and, in addition, the UV spectral range has never been explored during laboratory experiments. Moreover, from a detailed reading of the corresponding papers, it seems difficult to know if the far-field single scattering conditions are fulfilled, which is useful to benchmark with numerical simulation or passive or active lidar remote sensing field experiments.

## 1.5 Laboratory experiment on a single particle

The IPCC report (2007) underlines the need for quantitative measurements of absolute scattering and extinction cross-sections. To be performed at the scale of the atmosphere, such cross-sections must be evaluated over an ensemble of particles. In this context, it is generally assumed that the scattering and extinction cross-sections  $\overline{C_{sca,p}}$  and  $\overline{C_{ext,p}}$  of the  $N$  particles filling a volume element are obtained by summing the scattering and extinction cross-sections of the individual particles:

$$\overline{C_{ext,p}} = \sum_{i=1}^N C_{ext,i} = N \langle C_{ext,p} \rangle \quad (1.9)$$

This assumption is fulfilled if particles are in random orientation, under single-scattering approximation. Hence, there is a need for determining the scattering and extinction cross-section of one single particle. As underlined by Miles et al. (2011), the study of a single particle is necessary to avoid the ambiguity induced by the inherent averaging of particle ensemble studies, which is useful to compare models and optical properties measurements. Moreover study of single nano-crystals raised new knowledge on phenomena never expected from measurement on an ensemble (Nirmal et al., 1996). Yurt et al. (2012) recently reviewed the electrical (Fraiklin et al. 2011), mechanical (Burg et al., 2007) existing methods on single particles. Optical methods addressing a single particle have also been widely developed to measure the optical properties of a single particle, such as its extinction (Butler et al., 2007; Miles et al., 2011; Lombardi et al., 2013), scattering (Person et al., 2013) or fluorescence (Kaye et al., 2005; Heyes et al., 2007; Pan et al., 2012). These measurements have been performed on single metallic nanoparticles where the literature is abundant (Sönnichsen and Alivisatos, 2005; Lombardi et al., 2012; Li et al., 2013; Kuhlicke et al., 2013, Billaud et al., 2010; Tanabe and Tatsuma, 2012; Lee et al., 2013), but also on single semiconducting nanoparticles or quantum dots (Chung and Bawendi, 2004; Heyes et al., 2005; Person et al., 2013). However, these metallic and semi-conductor particles are rather seldom in the atmosphere. To my knowledge, measurements have never been performed on a single dielectric nanoparticle, probably due to their low refractive index, inducing lower scattering or extinction cross-sections (Yurt et al., 2012). In addition, in contrary to metallic nanoparticles, the absorption of a single dielectric nanoparticle such as a PSL (polystyrene latex sphere), an ammonium sulfate particle ( $(\text{NH}_4)_2\text{SO}_4$ ) or a desert dust nanoparticle is weak and the extinction is dominated by scattering. Miles et al. (2011) recently reviewed the existing measurements of light extinction, scattering and absorption by a single aerosols particle and underlined that *“this review is necessarily limited to measurement on coarse particles and it is crucially important that the new techniques under development aim to push the lower size limit down to the sub-micron range”*.

## 1.6 Outline of this thesis

The previous sections have enabled to identify the remaining issues that still need to be addressed. This thesis work hence proposed to address some of them, relative to the atmospheric particles characterization:

- Accurate spatial distribution and time evolution of atmospheric particles in the atmosphere is addressed (Miffre et al., 2012a; David et al., 2012).
- Backscattering of externally mixed atmospheric aerosol is accurately observed and the spatial distribution of the concentrated particles components is evaluated for several climatic situations (Miffre et al., 2011; Miffre et al., 2012b; David et al., 2013a).
- Timescale of particle size change from NPF to fine particles is evaluated (Dupart et al., 2012).
- For an ensemble of particle in ambient air, backscattering measurements in the exact backscattering direction are performed (David et al., 2013b).
- For a single dielectric nanoparticle, having a potential atmospheric interest such an ammonium sulfate nanoparticle, absolute measurement of the particles extinction cross-section are presented and discussed.

To tackle these issues, wavelength and polarization-resolved studies, either from laboratory, field experiments but also numerical simulations have been extensively used. Hence, this thesis relies on the use of polarization optics to address the backscattering and extinction properties of atmospheric particles. From a fundamental point of view, the key process is hence the interaction of light with a single / an ensemble of nanoparticles in ambient air.

The thesis work presented in this manuscript is organized as follows:

Chapter 2 begins by introducing the light scattering and especially polarization-resolved backscattering. The scattering matrix formalism is recalled to fix our notations. Then, two methodologies are proposed to retrieve, in a two or three- component particle mixture, the vertical profile of the backscattering coefficient specific to each particle component (David et al., 2013a). These two methodologies rely on the coupling of polarization-resolved backscattering measurements with optical inputs concerning the individual particle components (depolarization and backscattering spectral dependence). Hence, this chapter ends with the retrieval of these optical inputs by using either field or laboratory measurements, but also numerical simulations.

Chapter 3, lidar polarization-resolved backscattering measurements aims at presenting the experimental application of the partitioning methodologies. Hence, the UV-VIS polarization lidar used to perform polarization-resolved backscattering measurements is first presented,

with emphasis on error bar analysis (David et al., 2012). Then, the partitioning methodologies are applied to three case studies, concerning the external mixing of volcanic ash with spherical sulfates particles (Miffre et al., 2012a), the mixing of desert dust particles with water soluble particles (Miffre et al., 2011), and finally, the mixing of desert dust particles with sea-salt and water-soluble particles, as an example of a three-component particle mixture. From these retrieved backscattering coefficients, three main results are retrieved: i) Range-resolved particles number concentrations specific to one nonspherical particle component (ash, dust) are retrieved (Miffre et al., 2012b), ii) Particle backscattering enhancement due to hygroscopic growth is studied iii) New particle formation is studied in the atmosphere by using a sensitive UV-polarization lidar, which opens new insights at the forefront of knowledge in atmospheric physics and chemistry (Dupart et al., 2012).

Chapter 4 is devoted to laboratory measurements performed on generated nanoparticles, having an atmospheric impact, such as salt particles or ammonium sulfate particles. Two laboratory measurements are performed on these dielectric nanoparticles. First, a new laboratory experiment has been developed, built and optimized to observe the exact backscattering of light by an ensemble of such nanoparticles (David et al., 2013b).

This new experiment enables to measure the absolute depolarization of an ensemble of fine and ultrafine particles suspended in air, for the first time in the exact backscattering direction ( $\theta = \pi$  radian), and this with a 0.0035 radian the collection range ( $\theta = (\pi \pm 0.0035)$  radian). Secondly, a preliminary experiment on a single dielectric nanoparticle has been performed at the ILM, in collaboration with N. Del Fatti and F. Vallee's group. The absolute extinction cross-section of a fixed single aerosol dielectric nanoparticle has been measured as a function of the incident light polarization and wavelength by using a spatial modulation spectroscopy technique, as detailed in Chapter 4. The preliminary results of this new experiment are presented and discussed.

The manuscript ends with a conclusion and outlooks.

## Chapter 2

### Polarization-resolved optical backscattering

This chapter introduces the physical processes studied in this thesis, namely, the light backscattering and extinction by atmospheric particles. Moreover, a new methodology is proposed to analyze the particulate matter content of the complex atmospheric layering in the case of a two/three-component particle external mixture.

The dedicated methodology is based on coupling polarization-resolved backscattering measurements on an ensemble of external mixed particles with knowledge on the optical properties (depolarization and scattering spectral dependence) of individual particle components used as optical inputs. The chapter is organized as follows. First, we recall the light scattering and extinction phenomena to be used in the following chapters. We then focus on the scattering matrix formalism, suitable for describing polarization-resolved backscattering by an ensemble of particles. Then, the methodology to retrieve, in a two-component particle mixture, the backscattering coefficients specific to each particle component is presented. This optical backscattering partitioning in a two-component particle mixture (OBP2) is developed to address either a  $(p) = \{s, ns\}$  particle mixture, composed of spherical (s) and non-spherical (ns) particles, or a  $(p) = \{ns1, ns2\}$  particle mixture, composed of two ns-particles component. The methodology is then extended to the optical backscattering partitioning of a three-component particle external mixture (OBP3) by exploiting the spectral and polarization properties of the backscattering light (David et al., 2013a). As explained above, to apply the OBP2, OBP3-methodology, optical inputs are needed, which are determined in the last section of this chapter, based on either field or laboratory experiments, or numerical simulations.

#### 2.1 General framework

The interaction of light with a particle may lead to several effects including absorption and scattering, as explained by Mishchenko et al. (2002). The particle light absorption is defined as the incident light energy converted by the particle into other kinds of energy such as

thermal heat. The particle light scattering is defined as the incident light energy scattered in all directions without changing the light frequency, as schemed in Figure 2.1-a from Mishchenko et al. (2002). When the frequency is changing during the scattering process, non-linear or non-elastic scattering formalisms should be applied (Shen, 2003). The two last processes will be not considered in this thesis. The sum of light absorption (subscript abs) and scattering (subscript sca) is defined as the light extinction (subscript ext). From these phenomena, the corresponding particle cross-section  $C_{abs,p}$ ,  $C_{sca,p}$  and  $C_{ext,p}$  are respectively defined as the ratio of the absorbed, scattered and extinct light intensity to the incident light intensity  $I_{inc}$ . As presented in the Figure 2.1-a, the measured particle light scattering depends on the scattering angle  $\theta$ , i.e. the angle between the incident and scattered wave vectors  $\mathbf{k}_{inc}$  and  $\mathbf{k}_{sca}$ . In this thesis, the backward direction ( $\theta = 180^\circ$ ) corresponding to the backscattering direction is mainly considered (see Chapter 3 and Section 4.1). Moreover, the forward direction ( $\theta = 0^\circ$ ) is also considered by considering the particle extinction (see Section 4.2).

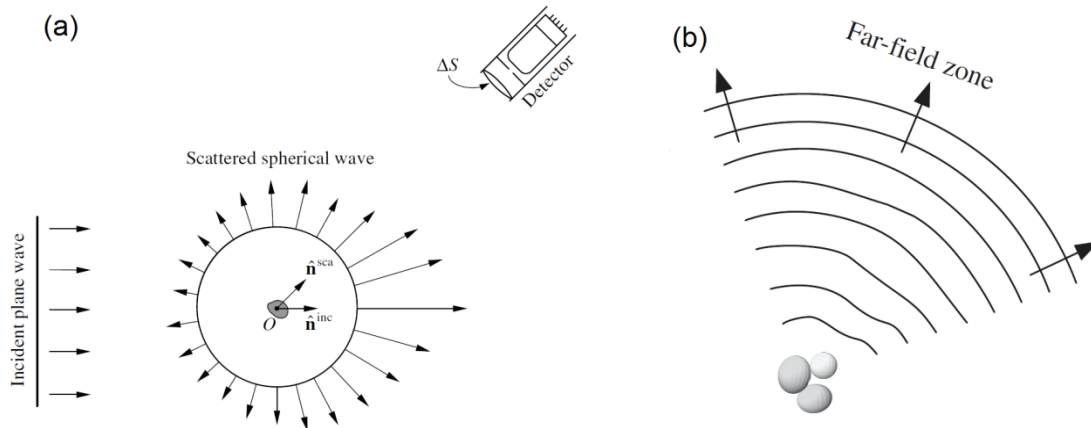


**Figure 2.1** Scheme of light scattering and its detection extracted from Mishchenko et al. (2002, 2009) (a) and representation of the far-field zone (b) where the scattered wave become spherical. Please note that the incident and scattered wave vector noted  $\hat{\mathbf{n}}^{sca}$  and  $\hat{\mathbf{n}}^{inc}$  in this figure) are respectively noted  $\mathbf{k}_{sca}$  and  $\mathbf{k}_{inc}$  in this thesis.

As presented in Figure 2.1-b, in the far-field approximation the scattered radiation becomes spherical and the scattering volume can be treated as a point source and several conditions must be fulfilled (Mishchenko et al., 2004). Firstly, the distance  $d$  from the backscattering volume to the observation point must be large compared with the particles diameter  $2r$  and with the laser wavelength  $\lambda$  (i.e.  $d \gg (2r), \lambda$ ). Secondly, the phases of the scattered partial wavelets coincide in the far-field zone only if  $d \gg k_{air} \times (2r)^2/2$ , where  $k_{air}$  is the wave vector of the light in the air surrounding medium. Thirdly, when the scattering direction changes as little as  $\pi/(2k_{air} \times (2r))$ , changes in the scattering pattern may be resolved if  $\pi/(2k_{air}(2.r)) \gg \emptyset_c/(2d)$ , where  $\emptyset_c$  is the diameter of the detector collecting lens. Finally, the position of a

particle is not affected by the presence of its neighbors when the particles are separated by a distance greater than the particles radius  $r$ .

In this manuscript, single-scattering of light in the far field approximation is assumed. In addition, the particles are assumed to be randomly-oriented, except in Section 4.2 where the particle is static. These assumptions (far-field and single scattering approximation on randomly-oriented particles) are discussed along with the performed measurements in Chapter 3 and Section 4.1. The reader may refer to (Del Guasta et al., 2006; Hayman et al., 2012; Nicolet et al., 2012) for studies on the depolarization of light by preferentially oriented particles.

## 2.2 Scattering matrix formalism

Among all scattering directions, the exact backscattering direction is one of the most sensitive to the particles microphysical properties (Mishchenko et al., 2002; Nousiainen et al., 2009). Hence, in this section, the particles optical properties (absorption; scattering and extinction) are presented by emphasis on light backscattering. These properties are textbook knowledge (Van de Hulst, 1957; Bohren and Huffman, 1983; Mishchenko et al., 2002) and recall here for the sake of clarity and to highlight our notations. Moreover, the polarization of the scattered light may differ from the polarization of the incident light depending on the particle shape (Mishchenko et al., 2002; Nousiainen et al., 2009). This polarization change can be described by using the normalized  $\mathbf{F}$ -scattering matrix (M.I. Mishchenko et al., 2002), which relates the Stokes vectors  $[I, Q, U, V]^T$  of the incident (subscript inc) and scattered light. The normalized  $\mathbf{F}$ -scattering matrix hence describes the change of the light intensity (parameter I) and polarization (Q, U and V parameters) due to the light scattering by particles. The measured light scattering by particles of arbitrary sizes, shapes, refractive index  $m$  can be described by the normalized  $\mathbf{F}$ -scattering matrix (Mishchenko et al., 2002):

$$\begin{pmatrix} I_{sca} \\ Q_{sca} \\ U_{sca} \\ V_{sca} \end{pmatrix} = \frac{C_{sca,p}}{4\pi d^2} \begin{bmatrix} F_{11,P}(\Theta) & F_{12,P}(\Theta) & F_{13,P}(\Theta) & F_{14,P}(\Theta) \\ F_{21,P}(\Theta) & F_{22,P}(\Theta) & F_{23,P}(\Theta) & F_{24,P}(\Theta) \\ F_{31,P}(\Theta) & F_{32,P}(\Theta) & F_{33,P}(\Theta) & F_{34,P}(\Theta) \\ F_{41,P}(\Theta) & F_{42,P}(\Theta) & F_{43,P}(\Theta) & F_{44,P}(\Theta) \end{bmatrix} \cdot \begin{pmatrix} I_{inc} \\ Q_{inc} \\ U_{inc} \\ V_{inc} \end{pmatrix} \quad (2. 1)$$

where the  $F_{ij}$ -matrix elements are intensive parameters which depend on the particle radius  $r$ , shape, refractive index  $m$  (which imaginary part is responsible for the absorption) and also depend on the radiation wavelength  $\lambda$  and on the scattering angle  $\theta$ .  $F_{ij}$  are equal for two particles that only differ in size if their ratios  $r/\lambda$  are the same (Muñoz et al., 2010). Hence it is useful to introduce the dimensionless size parameter  $x = 2\pi r/\lambda$ . Alternatively, an additive scattering matrix can be introduced as follows  $\overline{\mathbf{F}}_{\mathbf{p}} = C_{sca,p} \times \mathbf{F}_{\mathbf{p}}/(4\pi)$ . In this manuscript, we mainly focus on light scattering measurement in the exact backscattering direction ( $\theta = 180^\circ$ ), hence from now on, if not mentioned otherwise,  $F_{ij}$  are considered at  $\theta = 180^\circ$ . As shown by Mishchenko and Hovenier (1995), in the far-field approximation, for single-scattering by arbitrary particles in random orientation, the backscattering matrix is almost diagonal and only depends on the particle scattering matrix elements  $F_{11,p}$ ,  $F_{22,p}$ , and  $F_{14,p}$ :

$$\begin{pmatrix} I_{sca} \\ Q_{sca} \\ U_{sca} \\ V_{sca} \end{pmatrix} = \frac{C_{sca,p}}{4\pi d^2} \begin{bmatrix} F_{11,P} & 0 & 0 & F_{14,P} \\ 0 & F_{22,P} & 0 & 0 \\ 0 & 0 & -F_{22,P} & 0 \\ F_{14,P} & 0 & 0 & F_{11,P} - 2F_{22,P} \end{bmatrix} \cdot \begin{pmatrix} I_{inc} \\ Q_{inc} \\ U_{inc} \\ V_{inc} \end{pmatrix} \quad (2. 2)$$

In addition, for particles and their mirror particles in equal number and in random orientation,  $F_{14,p} = 0$  so that the scattering matrix becomes diagonal (Mishchenko and Hovenier, 1995).

## 2.2.1 Polarization-resolved backscattering by mono-sized particles

In this part, we focus on an ensemble of mono-sized particles (see Section 2.1.3 for size-averaged optical properties). Moreover we here detail how polarization-resolved backscattering measurements can be used to derive a shape and size particle indicator.

If we assume that the incident laser is linearly polarized, polarization-resolved backscattering measurements detect the backscattered light intensity  $I_{sca}$  as a function of its  $\boldsymbol{\pi} = \{//, \perp\}$  polarization with respect to the incident laser linear polarization. Hence polarization-resolved backscattering measurements separately detect  $I_{sca, //} = (I_{sca} + Q_{sca})/2$  and  $I_{sca, \perp} = (I_{sca} - Q_{sca})/2$ , while  $U_{sca} = V_{sca} = 0$ .

As shown in Figure 2.2, the light backscattered by spherical particles is only co-polarized ( $//$ ) with respect to the laser incident linear polarization, in agreement with the Lorenz-Mie theory (Mie, 1908). Hence, for s-particles,  $F_{11,s} = F_{22,s}$  and the cross-polarized backscattered intensity

$I_{\text{sca},\perp}$  is null. Meanwhile, for ns-particles, a cross-polarized backscattered intensity  $I_{\text{sca},\perp}$  appears in addition to  $I_{\text{sca},//}$ .

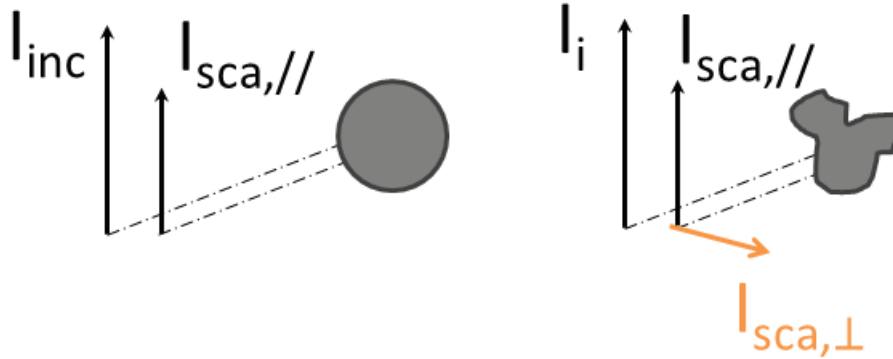


**Figure 2.2** Polarization-resolved light backscattering by a spherical particles (left scheme) then nonspherical particles (right scheme). When a linearly polarized incident light intensity  $I_{\text{inc}}$  is backscattered by a spherical particle (s), the backscattered light  $I_{\text{sca}}$  is entirely co-polarized (//) with respect to the laser linear polarization, while for a non-spherical particle, a cross-polarized backscattered intensity  $I_{\text{sca},\perp}$  appears.

The non-zero polarization change observed for ns-particles is called depolarization (Harris-Hobbs and Cooper, 1987; Baumgardner et al., 2012). The propensity of the scattering particles ensemble to depolarize laser light can be measured by the particle depolarization  $D_p$  (Gimmestad et al., 2008; Nousiainen et al., 2012):

$$D_p = 1 - \frac{F_{22,p}}{F_{11,p}} \quad (2.3)$$

Like  $F_{11,p}$  and  $F_{22,p}$ ,  $D_p$  is intensive and depends on the particle shape, size, chemical composition (through the particles refractive index  $m$ ) and on the wavelength  $\lambda$ .  $D_p$  is hence a clear indicator for deviation from particle isotropy. This shape-dependent feature arises in polarization-resolved backscattering from the interference of different parts of an anisotropic particle, although absorption may somewhat dampen this interference. Numerical simulations show that the magnitude of  $D_p$  is however not a clear indicator of the particles overall shape or morphology (Nousiainen et al., 2012). By shape, we refer to the overall shape of the particles, different from the particles' morphology which would include internal structures and porosity effects (Nousiainen et al., 2012). The particle depolarization  $D_p$  is linked to the particle linear depolarization ratio  $\delta_p$  (introduced in Chapter 1) often used in the lidar community (Cairo et al., 1999; Shimizu et al., 2004; Tesche et al., 2009; Freudenthaler et al., 2009) as well as in laboratory experiments (Sakai et al., 2010; Schnaiter et al., 2012):

$$\delta_p = \frac{F_{11,p} - F_{22,p}}{F_{11,p} + F_{22,p}} \quad (2.4)$$

Use of  $\delta_p$  or alternatively  $D_p$  is equivalent since both are an indicator for deviation from particle isotropy, both are intensive and they can be easily related as follows:  $\delta_p = D_p/(2 - D_p)$  for an incident linearly polarized laser light. I will hence preferably use the  $\delta_p$ -ratio as the depolarization observable. Additionally, polarization-resolved measurements can be performed with an incident laser circularly polarized (Hayman et al., 2012). However, since only randomly oriented particles are studied in this thesis, the use of circular polarization will not provide further information, as previously discussed (Section 1.3).

To retrieve a particle size indicator from optics, the spectral dependence of  $I_{sca}$ ,  $I_{sca, //}$  or  $I_{sca, \perp}$  have to be characterized. At a fixed radiation wavelength  $\lambda$ , the magnitude of  $I_{sca}$ ,  $I_{sca, //}$  and  $I_{sca, \perp}$  are respectively determined by the total-, co- and cross-polarized particle backscattering cross-sections, which depend on  $r$ ,  $m$  and  $\lambda$  and are defined as follows:

$$\left( \frac{d\sigma}{d\Omega} \right)_p = d^2 \cdot \frac{I_{sca}}{I_{inc}} = \frac{C_{sca,p}}{4\pi} \cdot F_{11,p} \quad (2.5)$$

$$\left( \frac{d\sigma}{d\Omega} \right)_{p, //} = d^2 \frac{I_{sca, //}}{I_{inc}} = \frac{C_{sca,p}}{4\pi} \left( \frac{F_{11,p} + F_{22,p}}{2} \right) \quad (2.6)$$

$$\left( \frac{d\sigma}{d\Omega} \right)_{p, \perp} = d^2 \frac{I_{sca, \perp}}{I_{inc}} = \frac{C_{sca,p}}{4\pi} \left( \frac{F_{11,p} - F_{22,p}}{2} \right) \quad (2.7)$$

where the  $d^2$  factor accounts for the compensation of  $I_{sca}$  with the distance  $d$  from the particle to the observer. Please note that in Equations (2.5) to (2.7), to simplify our notations, the  $\lambda$ ,  $r$  and  $m$ -dependencies of  $C_{sca,p}$ ,  $F_{11,p}$  and  $F_{22,p}$  have been omitted. In the literature, the spectral dependence of the backscattering cross-section is given in the form of the so-called Ångstrom exponent  $\mathring{A}_p$  which gives an indication on the particles size, as first shown by Sasano and Browell (1989). Note that the Ångstrom exponent considered here differs from the traditional definition which specifies the wavelength dependence of the aerosol optical depth; nonetheless both definitions indicate the particles size. Hence, for two wavelengths ( $\lambda_1$ ,  $\lambda_2$ ), we may introduce the total and co-/cross-polarized Ångstrom exponent  $\mathring{A}_{p,\pi}(\lambda_1, \lambda_2)$  to respectively address the spectral dependence of  $I_{sca}$ ,  $I_{sca, //}$  and  $I_{sca, \perp}$ :

$$\left(\frac{\lambda_2}{\lambda_1}\right)^{\mathring{A}p(\lambda_1,\lambda_2)} = \frac{I_{sca}(\lambda_2)}{I_{sca}(\lambda_1)} = \frac{\left(\frac{d\sigma}{d\Omega}\right)_p(\lambda_2)}{\left(\frac{d\sigma}{d\Omega}\right)_p(\lambda_1)} \quad (2.8)$$

$$\left(\frac{\lambda_2}{\lambda_1}\right)^{-\mathring{A}p,\pi(\lambda_1,\lambda_2)} = \frac{I_{sca,\pi}(\lambda_2)}{I_{sca,\pi}(\lambda_1)} = \frac{\left(\frac{d\sigma}{d\Omega}\right)_{p,\pi}(\lambda_2)}{\left(\frac{d\sigma}{d\Omega}\right)_{p,\pi}(\lambda_1)} \quad (2.9)$$

## 2.2.2 Size-averaged polarization-resolved backscattering by a particles ensemble

In this subsection, we account for the particles size distribution of atmospheric particles, introduced in Section 1.2.2. This approach will be found useful to interpret backscattering measurements, such as those performed with a polarization lidar (Chapter 3), or to compute size-averaged optical properties of an ensemble of particles and their extinction, as developed in Section 2.4.3.

As particles are assumed to be randomly oriented and single-scattering is considered, the optical cross sections of the particles ensemble are obtained by summing the cross sections of each individual particle (Mishchenko et al., 2002). Hence, for an ensemble of  $N$  particles, using Equations (2.5) to (2.7), the total additive particle cross-sections are defined as follows:

$$\overline{\left(\frac{d\sigma}{d\Omega}\right)_{p,\pi}} = \sum_{i=1}^N \frac{C_{sca,i}}{4\pi} \cdot \left(\frac{F_{11,i} \pm F_{22,i}}{2}\right) = N \left\langle \left(\frac{d\sigma}{d\Omega}\right)_{p,\pi} \right\rangle \quad (2.10)$$

where the sum is performed over the  $N$  particles and  $\langle (d\sigma/d\Omega)_{p,\pi} \rangle$  is the mean backscattering cross-section per particle, averaged over the particles ensemble. In this equation,  $F_{11} + F_{22}$  stands for the // -polarization, while  $F_{11} - F_{22}$  stands for  $\perp$  -polarization. As shown by (Li et al., 2001), to correctly calculate the particles ensemble optical properties, the backscattering and extinction cross-sections must be integrated over the particles size distribution (PSD) as follows:

$$\alpha_p = \int_{PSD} C_{ext,p} \cdot n_p(r) \cdot dr = N_p \langle C_{ext,p} \rangle \quad (2.11)$$

$$\beta_p = \int_{PSD} \frac{C_{sca,p}}{4\pi} \cdot \left( \frac{F_{11,p} + F_{22,p}}{2} \right) \cdot n_p(r) \cdot dr = N_p \cdot \left\langle \left( \frac{d\sigma}{d\Omega} \right)_p \right\rangle \quad (2.12)$$

$$\beta_{p,\pi} = \int_{PSD} \frac{C_{sca,p}}{4\pi} \cdot \left( \frac{F_{11,p} \pm F_{22,p}}{2} \right) \cdot n_p(r) \cdot dr = N_p \cdot \left\langle \left( \frac{d\sigma}{d\Omega} \right)_{p,\pi} \right\rangle \quad (2.13)$$

where we have introduced the particles extinction coefficient  $\alpha_p$  as well as the additive particles volume backscattering coefficient  $\beta_p$ , or its polarization-resolved equivalent  $\beta_{p,\pi}$ , which are often used in the polarization Lidar community (see Chapter 1). In Equation (2.13),  $F_{11} + F_{22}$  stands for  $\beta_{p,||}$ , while  $F_{11} - F_{22}$  stands for  $\beta_{p,\perp}$ . Moreover, by combining Equations (2.4) and (2.9) with the  $\langle (d\sigma/d\Omega)_{p,\pi} \rangle$  expression, the  $\delta_p$ -ratio and the size-averaged  $\mathring{A}_{p,\pi}$  can be deduced:

$$\delta_p = \frac{\left\langle \left( \frac{d\sigma}{d\Omega} \right)_{p,\perp} \right\rangle}{\left\langle \left( \frac{d\sigma}{d\Omega} \right)_{p,||} \right\rangle} = \frac{\beta_{p,\perp}}{\beta_{p,||}} \quad (2.14)$$

$$\left( \frac{\lambda_2}{\lambda_1} \right)^{-\mathring{A}_{p,\pi}} = \frac{\left\langle \left( \frac{d\sigma}{d\Omega} \right)_{p,\pi}(\lambda_2) \right\rangle}{\left\langle \left( \frac{d\sigma}{d\Omega} \right)_{p,\pi}(\lambda_1) \right\rangle} = \frac{\beta_{p,\pi}(\lambda_2)}{\beta_{p,\pi}(\lambda_1)} \quad (2.15)$$

Despite being size-averaged,  $\langle (d\sigma/d\Omega)_{p,\perp} \rangle$  and  $\delta_p$  remain non-null only for ns-particles. In addition, to interpret backscattering measurements such as polarization lidar measurements, the particle extinction to backscatter ratio  $S_p$  will be found useful:

$$S_p = \frac{\langle C_{ext,p} \rangle}{\left\langle \left( \frac{d\sigma}{d\Omega} \right)_p \right\rangle} = \frac{\alpha_p}{\beta_p} \quad (2.16)$$

## 2.3 Optical backscattering partitioning

In the previous part, the optical properties of an ensemble of particles have been presented. As underlined in Section 1.2, atmospheric aerosols are a complex mixture of different chemical compounds, with particles having very different sizes and shapes, especially after-long-range

transport. Hence in this section, we propose to optically partition a two component particles external mixture by retrieving the optical backscattering coefficient specific to each particle compound. This optical backscattering partitioning is then further developed to address the case of a three-component particle external mixture. Internal mixtures, such as pollutant-coated dust or internal mixture of sulfate and organic carbon, are here not considered, because they cannot be accurately treated with the light-scattering method adopted here as the mixing state must be known to accurately address this issue (Lesins et al., 2002).

### **2.3.1 Optical backscattering partitioning in a two-component particle mixture (OBP2)**

Two-component particle external mixtures were first studied by Shimizu et al. (2004), who separated dust from non-dust particles using a single wavelength ( $1\lambda$ ) polarization lidar system (noted  $1\beta + 1\delta$  in the lidar community). This methodology was then applied by Tesche et al. (2009) to address the particle extinction  $\alpha_p$  with Raman channels ( $1\alpha + 1\beta + 1\delta$ ), then further developed by Ansmann et al. (2012). Two component particle external mixtures composed of s- and ns-particles have also been studied by Veselovskii et al. (2010) and Di Girolamo et al. (2012), by measuring the  $\beta_p$ -coefficient at  $3\lambda$  with  $1\lambda$  polarization-resolved then  $\alpha_p$  at  $2\lambda$  ( $2\alpha + 3\beta + 1\delta$ ). In this paragraph, we have developed a methodology that allows to optically partition a two-component particles mixture. It is a further development of the pioneer work done by Shimizu et al. (2004) which we will apply in Chapter 3 to study volcanic ash particles mixed with spherical sulfate (Miffre et al., 2011, 2012 a,b) as well as dust mixed with non-dust particles (Miffre et al., 2012a; Dupart et al., 2012). These two experimental studies are respectively presented in Section 3.3 and 3.4. Two case studies (a) and (b) are here developed, depending on whether or not s-particles are present in the two-component particles mixture.

#### **(a) Case of nonspherical particles mixed with spherical particles**

Let us consider an external mixture of particles (subscript p), composed of both spherical (s) and nonspherical (ns) particles, having a backscattering coefficient  $\beta_p$  and a depolarization ratio  $\delta_p$ , as schemed in Figure 2.3. We here assume that ns- and s- particles are effectively present at the place where the measurements are performed. Whether these particles are

present is an issue addressed in Chapter 3. In a particles external mixture, the particles do not interact with each other. Hence, following the superposition principle, the particle backscattering coefficient  $\beta_p$  of the particle mixture is the sum of the s- and ns-particle backscattering coefficients  $\beta_s$  and  $\beta_{ns}$ , since the  $\beta_p$ -coefficient is additive. The goal of the optical backscattering partitioning in a two-component particle mixture (noted OBP2) is hence to accurately retrieve  $\beta_s$  and  $\beta_{ns}$  from  $\beta_p$ .

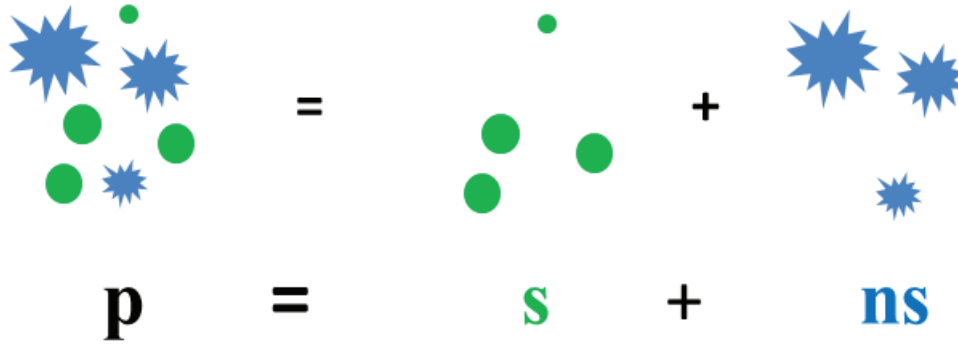


**Figure 2.3** Scheme of a two-component particle external mixture composed of spherical and nonspherical particles. The backscattering coefficient  $\beta_p$  of the particle mixture is the sum of the backscattering coefficient of each component (i.e.  $\beta_s$  and  $\beta_{ns}$ ).

The depolarization ratio of its ns-particles is denoted  $\delta_{ns}$  while for s-particles  $\delta_s$  is null. Since the  $\delta_p$ -ratio is not additive, despite  $\delta_s$  being zero, there is no reason for  $\delta_p$  to equal  $\delta_{ns}$ . However, in the literature,  $\delta_p$  is often compared to  $\delta_{ns}$  (Gasteiger et al., 2011) and the maximum value of  $\delta_p$  is sometimes used as a  $\delta_{ns}$ -measurement (Shimizu et al., 2004). Moreover, the difference between  $\delta_p$  and  $\delta_{ns}$  is not clearly stated to originate from the presence of s-particles, and the observed discrepancies between  $\delta_p$  and  $\delta_{ns}$  are sometimes attributed to imperfections originating from numerical simulations or/and experimental observations (Wiegner et al., 2009).

Here, the distinction between  $\delta_p$  and  $\delta_{ns}$  is analyzed by applying the superposition principle to the  $\beta_s$ - and  $\beta_{ns}$ -coefficients. The particles mixture backscattering coefficient  $\beta_p$  is then the sum of their s- and ns-backscattering components:

$$\beta_p = \beta_s + \beta_{ns} \quad (2.17)$$

Please note that in this section, to ease the reading, the  $\lambda$ -wavelength dependence is omitted. On the // -polarization axis, both s- and ns-particles contribute to the backscattering, while on the  $\perp$ -polarization axis only the ns-particles contribute to the backscattering, which leads to:

$$\beta_{p, //} = \beta_{ns, //} + \beta_{s, //} \quad (2.18)$$

$$\beta_{p, \perp} = \beta_{ns, \perp} \quad (2.19)$$

since  $\beta_{s, \perp} = 0$ . By combining these equations the definition of  $\beta_{p, \pi}$  (Equations (2.13)) and  $\delta_p$  (Equations (2.14)), the following relation can be retrieved:

$$\frac{1}{\delta_p} - \frac{1}{\delta_{ns}} = \frac{\overline{\left(\frac{d\sigma}{d\Omega}\right)_{ns, //}} + \overline{\left(\frac{d\sigma}{d\Omega}\right)_{s, //}}}{\overline{\left(\frac{d\sigma}{d\Omega}\right)_{ns, \perp}}} - \frac{\overline{\left(\frac{d\sigma}{d\Omega}\right)_{ns, //}}}{\overline{\left(\frac{d\sigma}{d\Omega}\right)_{ns, \perp}}} = \frac{\overline{\left(\frac{d\sigma}{d\Omega}\right)_{s, //}}}{\overline{\left(\frac{d\sigma}{d\Omega}\right)_{ns, \perp}}} \quad (2.20)$$

Hence the  $\delta_p$ -ratio of the particles mixture can be related to the depolarization ratio  $\delta_{ns}$  of its ns-particles as follows:

$$\frac{1}{\delta_p} - \frac{1}{\delta_{ns}} = \frac{N_s}{N_{ns}} \cdot \frac{\left\langle \left(\frac{d\sigma}{d\Omega}\right)_{s, //} \right\rangle}{\left\langle \left(\frac{d\sigma}{d\Omega}\right)_{ns, \perp} \right\rangle} \quad (2.21)$$

This equation has been published in Miffre et al. (2011) in a slightly different form, which explains the expression  $\langle (d\sigma/d\Omega)_{s, //} \rangle = \langle C_{sca, s} \times (F_{11, s} + F_{22, s})/2 \rangle$  and  $\langle (d\sigma/d\Omega)_{ns, \perp} \rangle = \langle C_{sca, ns} \times (F_{11, ns} - F_{22, ns})/2 \rangle$ . When s-particles are present ( $N_s \neq 0$ ), the  $\delta_p$ -ratio of a {s, ns} particle mixture is hence lower than the depolarization ratio of its ns-particles ( $\delta_p \leq \delta_{ns}$ ). Accordingly, the same conclusion can be drawn from the backscattering coefficient by combining Equations (2.13) with the above Equation (2.21):

$$\frac{1}{\delta_p} - \frac{1}{\delta_{ns}} = \frac{\beta_{s, //}}{\beta_{ns, \perp}} \quad (2.22)$$

Equation (2.21), or its lidar-equivalent Equation (2.22), shows that  $\delta_p$  equals  $\delta_{ns}$  only when there are no s-particles present ( $N_s = 0$ ). In long-range transport situations, s-particles are expected to be present in the particle mixtures which then lower  $\delta_p$  below  $\delta_{ns}$ . As a

consequence, the backscattering properties of ns-particles in {s, ns} particle mixtures cannot be easily derived from the measurement of  $\delta_p$ , because the latter is not a tracer specific to ns-particles only. A tracer for ns-particles can be derived from the cross-polarized backscattering coefficient  $\beta_{p,\perp}$ , which is specific to ns-particles (since s-particles do not depolarize light), as shown by Equation (2.19). Hence, only the cross-polarized particle backscattering coefficient  $\beta_{p,\perp}$  is a reliable tracer specific to ns-particles. When  $\beta_{ns,\perp}$  is determined, the ns-particle backscattering coefficient  $\beta_{ns}$  can be retrieved from:

$$\beta_{ns} = \beta_{ns,\perp} \cdot \left(1 + \frac{1}{\delta_{ns}}\right) \quad (2.23)$$

Hence, for accurate determination of  $\beta_{ns}$ , it is necessary to determine  $\beta_{ns,\perp}$  together with the  $\delta_{ns}$ -value. The  $\beta_s$ -coefficient can then be deduced from  $\beta_p$  and  $\beta_{ns}$ :

$$\beta_s = \beta_p - \beta_{ns} \quad (2.24)$$

To emphasize the contribution of s-particles to the  $\delta_p$ -ratio, Equations (2.20) can be rewritten by introducing the fraction  $X_{ns}$  of ns-to-particle backscattering coefficients:

$$X_{ns} = \frac{\beta_{ns}}{\beta_p} \quad (2.25)$$

Hence, by combining Equations (2.18), (2.19), (2.21) and (2.23), we get:

$$\frac{1}{\delta_p} - \frac{1}{\delta_{ns}} = \frac{1 - X_{ns}}{X_{ns}} \left(1 + \frac{1}{\delta_{ns}}\right) \quad (2.26)$$

Thus, the difference between  $\delta_p$  and  $\delta_{ns}$  can be used to determine the fraction  $X_{ns}$  of ns-particles in the two-component particle mixture:

$$X_{ns} = \frac{1 + \frac{1}{\delta_{ns}}}{1 + \frac{1}{\delta_p}} \approx \delta_p \cdot \left(1 + \frac{1}{\delta_{ns}}\right) \quad (2.27)$$

as long as  $\delta_p \ll 1$ , so that  $\delta_p$  is actually a tracer for  $X_{ns}$ . Equation (2.27), derived from the scattering matrix, agrees with Tesche et al. (2009). However, in the here developed methodology, the link with the scattering matrix formalism is explicit. Since  $\delta_p$  is sometimes assumed to equal  $\delta_{ns}$ , we plotted in Figure 2.4 the systematic bias between  $\delta_p$  and  $\delta_{ns}$  as a function of  $X_{ns}$  for three  $\delta_{ns}$ -values (10, 20 and 30%). The relative error is larger when  $\delta_{ns}$  is larger but the three curves look almost independent on  $\delta_{ns}$ .

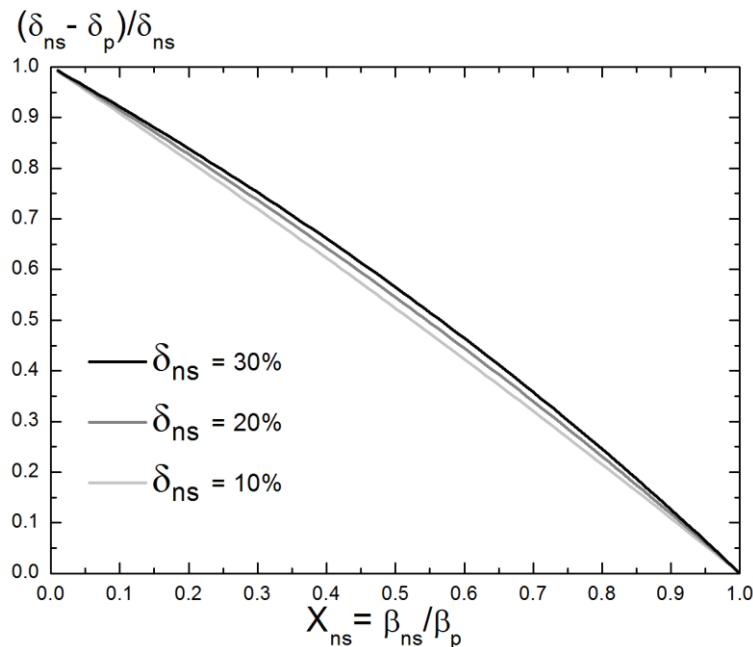


**Figure 2.4** Systematic bias on  $\delta_{ns}$  when assuming  $\delta_p$  equals to  $\delta_{ns}$  for  $\delta_{ns} = 10\%$  (light gray),  $\delta_{ns} = 20\%$  (dark gray) and  $\delta_{ns} = 30\%$  (black). This graph allows measuring the need for distinguishing  $\delta_p$  from  $\delta_{ns}$ .

Hence this part explain the optical backscattering partitioning in a two-component particle mixture (OBP2) to retrieve from a  $\{s, ns\}$  particle mixture the backscattering coefficient  $\beta_s$  and  $\beta_{ns}$  specific to the corresponding  $s$  and  $ns$ -particles.

### (b) Case of a nonpherical particle mixture

The optical backscattering partitioning in a two-component particle mixture (OBP2) methodology can also be used to partition a particle mixture composed of nonspherical particles only. Hence, we now consider a particles mixture composed of  $ns1$  and  $ns2$  particles

components with  $\delta_{ns1} \neq \delta_{ns2}$  (if  $\delta_{ns1} = \delta_{ns2}$  the two-particle component cannot be separated by using polarization-resolved backscattering). To separately retrieve the ns1 and ns2 backscattering coefficients, we offer the following set of four equations:

$$\beta_{p, //} = \beta_{ns1, //} + \beta_{ns2, //} \quad (2.28)$$

$$\beta_{p, \perp} = \beta_{ns1, \perp} + \beta_{ns2, \perp} \quad (2.29)$$

$$\delta_{ns1} = \beta_{ns1, \perp} / \beta_{ns1, //} \quad (2.30)$$

$$\delta_{ns2} = \beta_{ns2, \perp} / \beta_{ns2, //} \quad (2.31)$$

Four backscattering coefficients are hence to be determined, namely  $\beta_{p, \pi}$  with  $(p) = \{ns1, ns2\}$  and  $\pi = \{ //, \perp \}$ . This is feasible by combining  $\beta_{p, //}$  and  $\beta_{p, \perp}$  measurements with  $\delta_{ns1}$  and  $\delta_{ns2}$  values. Hence by taking into account  $\delta_{ns1}$  and  $\delta_{ns2}$ ,  $\beta_{ns1, \perp}$  is expressed as follows (Miffre et al., 2012b):

$$\beta_{ns1, \perp} = \frac{\beta_{p, \perp} - \delta_{ns2} \cdot \beta_{p, //}}{1 - \delta_{ns2} / \delta_{ns1}} \quad (2.32)$$

so that  $\beta_{ns1, \perp} = \beta_{p, \perp}$  only when  $\delta_{ns2} = 0$  as stated for  $\{s, ns\}$  particle mixtures. Equation (2.32) describes the quantitative impact of the ns2-particles depolarization ratio  $\delta_{ns2}$  on the  $\beta_{ns1}$ -backscattering coefficient, hence assuming  $\delta_{ns2} = 0$  leads to a maximum overestimation of  $\beta_{ns1, \perp}$  equal to  $\delta_{ns2} \times \beta_{p, //}$ . This maximum overestimation term is negligible when  $\delta_{ns2} \ll \delta_p$  (as  $\delta_{ns2} \beta_{p, //} = \beta_{p, \perp} \delta_{ns2} / \delta_p$ ). Moreover the difference between  $\delta_p$  and  $\delta_{ns}$  can also be interpreted for a  $\{ns1, ns2\}$  mixture in the frame of the additive scattering matrix.

$$\frac{1}{\delta_p} - \frac{1}{\delta_{ns1}} = \frac{\overline{\left(\frac{d\sigma}{d\Omega}\right)_{ns1, //}} + \overline{\left(\frac{d\sigma}{d\Omega}\right)_{ns2, //}}}{\overline{\left(\frac{d\sigma}{d\Omega}\right)_{ns1, \perp}} + \overline{\left(\frac{d\sigma}{d\Omega}\right)_{ns2, \perp}}} - \frac{\overline{\left(\frac{d\sigma}{d\Omega}\right)_{ns1, //}}}{\overline{\left(\frac{d\sigma}{d\Omega}\right)_{ns1, \perp}}} = \frac{N_{ns1} \cdot \left\langle \left(\frac{d\sigma}{d\Omega}\right)_{ns1, //} \right\rangle + N_{ns2} \cdot \left\langle \left(\frac{d\sigma}{d\Omega}\right)_{ns2, //} \right\rangle}{N_{ns1} \cdot \left\langle \left(\frac{d\sigma}{d\Omega}\right)_{ns1, \perp} \right\rangle + N_{ns2} \cdot \left\langle \left(\frac{d\sigma}{d\Omega}\right)_{ns2, \perp} \right\rangle} - \frac{N_{ns1} \cdot \left\langle \left(\frac{d\sigma}{d\Omega}\right)_{ns1, //} \right\rangle}{N_{ns1} \cdot \left\langle \left(\frac{d\sigma}{d\Omega}\right)_{ns1, \perp} \right\rangle} \quad (2.33)$$

Then after a few calculations, we get:

$$\frac{1}{\delta_p} - \frac{1}{\delta_{ns1}} = \frac{N_{ns2} \cdot \left\langle \left(\frac{d\sigma}{d\Omega}\right)_{ns2, //} \right\rangle - N_{ns2} \cdot \left\langle \left(\frac{d\sigma}{d\Omega}\right)_{ns2, \perp} \right\rangle}{N_{ns1} \cdot \left\langle \left(\frac{d\sigma}{d\Omega}\right)_{ns1, \perp} \right\rangle + N_{ns2} \cdot \left\langle \left(\frac{d\sigma}{d\Omega}\right)_{ns2, \perp} \right\rangle} \cdot \frac{1}{\delta_{ns1}} \quad (2.34)$$

which finally leads to:

$$\frac{1}{\delta_p} - \frac{1}{\delta_{ns1}} = \frac{N_{ns2} \cdot \left(1 - \frac{\delta_{ns2}}{\delta_{ns1}}\right)}{N_{ns1} \cdot \frac{\left\langle \left(\frac{d\sigma}{d\Omega}\right)_{ns1,\perp} \right\rangle}{\left\langle \left(\frac{d\sigma}{d\Omega}\right)_{ns2,\parallel} \right\rangle} + N_{ns2} \cdot \delta_{ns2}} \quad (2.35)$$

Hence, when two ns-particle components are mixed,  $\delta_p$  equals  $\delta_{ns1}$  (resp.  $\delta_{ns2}$ ) only if  $N_{ns2} = 0$  (resp.  $N_{ns1} = 0$ ). Moreover  $\delta_p$  lies between  $\min(\delta_{ns1}, \delta_{ns2})$  and  $\max(\delta_{ns1}, \delta_{ns2})$ . As a consequence, the less depolarizing particles in the mixture lowered the measured  $\delta_p$ . Equation (2.21) can be retrieved from Equation (2.35) by setting  $\delta_{ns2} = 0$ .

### 2.3.2 Optical backscattering partitioning in a three-component particle mixture (OBP3)

In the literature, three-component particle mixtures have been studied by Nishizawa et al. (2011), who considered nonspherical dust particles mixed with spherical sea-salt and water-soluble particles with a  $2\lambda$ -Lidar experiment and  $1\lambda$ -polarization-resolved ( $2\beta+1\delta$ ) to derive the particles extinction. They assumed sea-salt particles to be spherical, which may not be the case, as first shown by Murayama et al. (1999). Marengo and Hogan (2011) also analyzed a three-component mixture in the atmosphere. However, they actually include air molecules as one component which means that they actually studied a two-component particle mixture. In this section, a new optical backscattering partitioning methodology is developed to retrieve, in a three-component particle external mixture, the backscattering coefficient specific to each of the three particles components. This new methodology, hereafter called the OBP3-methodology, has been published in (David et al., 2013a). The OBP3 relies on an analysis of the spectral and polarization properties of the light backscattered by the atmospheric particles measured with  $2\lambda$ -polarization backscattering measurements ( $2\beta+2\delta$ ), such as dual-wavelength polarization lidar, which is new. To our knowledge,  $2\beta+2\delta$ -measurements have only been used to observe two-component particle mixtures (Sugimoto and Chio Hie Lee, 2006, Tesche et al., 2009). In addition, OBP3 allows taking into account the nonsphericity of each of the three particles components, which is important for radiative forcing assessments

(Kahnert et al., 2005). Examples of three-component particle mixtures are given in Chapter 3 where the OBP3-methodology is applied.

Let us now consider a three-component particle external mixture, as schemed in Figure 2.5, which is composed of two ns-particle populations (ns1 and ns2) with a third particle component (n12) belonging to neither ns1 nor ns2 particles (which may also content nonspherical particles). We here assume that ns1, ns2 and n12 particles are effectively present at the place where the measurements are performed. Whether these particles are present is an issue addressed in Chapter 3 along with the backscattering measurements. For an external mixture of ns1, ns2 and n12-particles, following the same methodology as in Section 2.2,  $\delta_p$  is below  $\max(\delta_{ns1}, \delta_{ns2}, \delta_{n12})$ , where  $\delta_{ns1}$ ,  $\delta_{ns2}$  and  $\delta_{n12}$  are respectively the depolarization ratio of the ns1-, ns2 and n12-particles depolarization ratio.

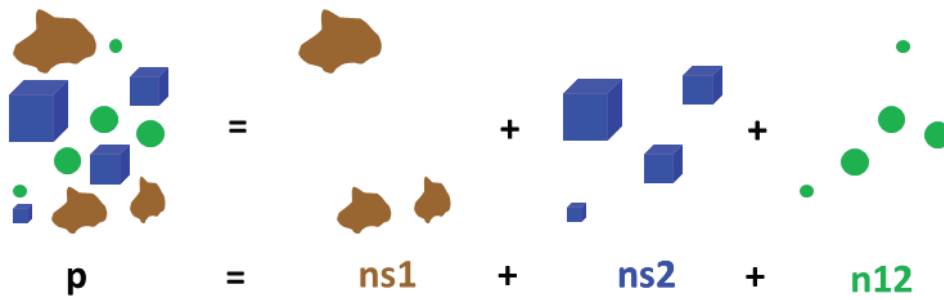


**Figure 2.5** Scheme of a three-component particle external mixture composed of ns1, ns2 and n12 particles. The backscattering coefficient  $\beta_p$  of the particle mixture is the sum of the backscattering coefficient of each component (i.e.  $\beta_{ns1}$ ,  $\beta_{ns2}$  and  $\beta_{n12}$ ).

To determine the backscattering coefficient of each particle component in the three-component mixture ( $p = \{ns1, ns2, n12\}$ ), six unknown quantities have to be determined by wavelength considered, corresponding to the three components (ns1, ns2, n12) assigned to the two polarization axes:  $\beta_{ns1,\pi}$ ,  $\beta_{ns2,\pi}$  and  $\beta_{n12,\pi}$  with  $\pi = \{//, \perp\}$ . By performing a  $1\beta+1\delta$ -backscattering measurement,  $\beta_{p,//}$  and  $\beta_{p,\perp}$  are measured, which can be coupled with the  $\delta_{ns1}$ -,  $\delta_{ns2}$ - and  $\delta_{n12}$ -values to obtain five equations only. As a consequence,  $1\beta+1\delta$ -measurements cannot be used to address a three-component particle mixture.

When dealing with  $2\beta+2\delta$ -backscattering measurements, each of these ( $\beta_{ns1,\pi}$ ,  $\beta_{ns2,\pi}$ ,  $\beta_{n12,\pi}$ ) backscattering coefficients has to be determined at the two Lidar wavelengths  $\lambda = \{\lambda_1, \lambda_2\}$ . Hence, twelve unknown backscattering coefficients have to be determined, hereafter noted  $\beta_{p,\pi}(\lambda)$ . By applying the superposition principle to the three-component particle mixture, using

the  $(\lambda, \pi)$  spectral and polarization properties, the  $\beta_{p, //}(\lambda)$  and  $\beta_{p, \perp}(\lambda)$  coefficients provide a set of four equations:

$$\beta_{p, //}(\lambda) = \beta_{ns1, //}(\lambda) + \beta_{ns2, //}(\lambda) + \beta_{n12, //}(\lambda) \quad (2.36- a,b)$$

$$\beta_{p, \perp}(\lambda) = \beta_{ns1, \perp}(\lambda) + \beta_{ns2, \perp}(\lambda) + \beta_{n12, \perp}(\lambda) \quad (2.37- a,b)$$

For the sake of clarity, we note that Equations (a) refer to  $\lambda_1$ -wavelength, while Equations (b) refer to wavelength  $\lambda_2$ . Six more equations are then provided by the ns-particle depolarization ratio at the two wavelengths  $\lambda = \{\lambda_1, \lambda_2\}$ :

$$\delta_{ns1} = \frac{\beta_{ns1, \perp}}{\beta_{ns1, //}} \quad (2.38- a,b)$$

$$\delta_{ns2} = \frac{\beta_{ns2, \perp}}{\beta_{ns2, //}} \quad (2.39- a,b)$$

$$\delta_{n12} = \frac{\beta_{n12, \perp}}{\beta_{n12, //}} \quad (2.40- a,b)$$

The last two equations are obtained by addressing the spectral behavior of the backscattering coefficient  $\beta_{ns}$ . This could be achieved by using either  $\hat{A}_{p, //}$  or  $\hat{A}_{p, \perp}$ . Here, we choose the cross-polarized Ångstrom exponent  $\hat{A}_{p, \perp}$  which takes into account the spectral dependence of  $\beta_{p, \perp}$  and represents an observable that is specific to ns-particles. Hence, by using Equations (2.15), we may write:

$$\left(\frac{\lambda_2}{\lambda_1}\right)^{-\hat{A}_{ns1, \perp}} = \frac{\beta_{ns1, \perp}(\lambda_2)}{\beta_{ns1, \perp}(\lambda_1)} \quad (2.41)$$

$$\left(\frac{\lambda_2}{\lambda_1}\right)^{-\hat{A}_{ns2, \perp}} = \frac{\beta_{ns2, \perp}(\lambda_2)}{\beta_{ns2, \perp}(\lambda_1)} \quad (2.42)$$

Hence, when dealing with a  $2\beta+2\delta$ -backscattering measurements, the twelve unknown backscattering coefficients  $\beta_{p, \pi}(\lambda)$  can be determined from the system of twelve Equations (2.36 to 2.42). As a conclusion,  $\beta_{p, \pi}(\lambda)$  can be retrieved for each particle component  $(p) = \{ns1, ns2, n12\}$  at wavelength  $\lambda_1$  and  $\lambda_2$ :

$$\beta_{ns1}(\lambda) = \beta_{ns1, //}(\lambda) + \beta_{ns1, \perp}(\lambda) \quad (2.43)$$

$$\beta_{ns2}(\lambda) = \beta_{ns2, //}(\lambda) + \beta_{ns2, \perp}(\lambda) \quad (2.44)$$

$$\beta_{n12}(\lambda) = \beta_{n12, //}(\lambda) + \beta_{n12, \perp}(\lambda) \quad (2.45)$$

Hence, four retrieved backscattering coefficients [ $\beta_{p, //}(\lambda)$ ,  $\beta_{p, \perp}(\lambda)$  with  $\lambda = \{\lambda_1, \lambda_2\}$ ], addressed in the next Chapter 3, are used in combination with eight retrieved quantities [ $\delta_{ns1}(\lambda)$ ,  $\delta_{ns2}(\lambda)$ ,  $\delta_{n12}(\lambda)$ ,  $\hat{A}_{ns1, \perp}(\lambda_1, \lambda_2)$ ,  $\hat{A}_{ns2, \perp}(\lambda_1, \lambda_2)$ ], addressed in the next Section 2.4, to determine the twelve ns-particles backscattering coefficients  $\beta_{p, \pi}(\lambda)$ , with (p) = {ns1, ns2, n12},  $\pi = \{ //, \perp \}$  and  $\lambda = \{\lambda_1, \lambda_2\}$ : the three-component particle mixture is hence optically partitioned. As a conclusion, intensive parameters such as ns-particles depolarization ratios and cross-polarized Ångstrom exponents are used in combination with  $(2\beta + 2\delta)$  polarization backscattering measurements to get the additive backscattering coefficient of each particle compound.

## 2.4 Optical properties of an individual particle component

As explained in Sections 2.3, to apply the OBP2 and OBP3 methodologies, (OPBi for Optical backscattering partitioning in a i-component particle mixture), the knowledge of the  $\delta_{ns}$ -ratio and the  $\hat{A}_{ns, \perp}$ -coefficient of each individual ns-particle component, are required. The retrieved  $\delta_{ns}$  and  $\hat{A}_{ns, \perp}$  have to be specific to each individual particle component observed at the remote site. Hence, ideally,  $\delta_{ns}$  and  $\hat{A}_{ns, \perp}$  should be retrieved for particles having the same microphysical properties (PSD, shape, refractive index) as those observed at the remote site, and this at the wavelengths of the backscattering measurement. In this section, we show that the  $\delta_{ns}$ -ratio and the  $\hat{A}_{ns, \perp}$ -coefficient can be retrieved either from field measurements, laboratory measurements or numerical simulations. However, as detailed below, each methodology has its own limitations so that the  $\delta_{ns}$  and  $\hat{A}_{ns, \perp}$ -retrieval is generally not easy to achieve. As examples of ns-particles, we here focus on volcanic ash, desert dust and sea-salt particles, to be further used in Chapter 3. From now on, the ns-subscript will hence refer to either volcanic ash (ash), or desert dust (dust), or sea-salt (ss) particles.

### 2.4.1 Field measurements

In the literature,  $\delta_{ns}$  is sometimes retrieved from the maximum value of the  $\delta_p$ -measurement (Shimizu et al., 2004). Strictly speaking, as explained in Section 2.3, this approach is valid

provided that the  $\delta_p$ -measurements are performed very close to the source region where ns-particles are the only detected particles. The Saharan Mineral Dust Experiment (SAMUM) provides measurements of  $\delta_{ns}$  and  $\hat{A}_{ns}$  for Saharan dust particles, maritime particles and smoke (Ansmann et al., 2011). SAMUM-1 and -2 took place in Southern Morocco and in Cape Verde, hence these measurements are performed close to the source region and could be used to partition the optical backscattering in a two/three component particle mixture if the observation place is itself very close to the source region. Such measurements cannot however be used to interpret measurements performed after long-range transport, since during advection up to the observation place, particles experience sedimentation, which modifies their PSD (Schumann et al., 2011, Zhang 2008). Hence, to focus on the long-range transport measurements shown in Chapter 3, field measurements of  $\delta_{ns}$  and  $\hat{A}_{ns}$  performed close to the source region cannot be used in our case studies. Field measurements of  $\delta_p$  and  $\hat{A}_p$  performed after long-range transport are usually not specific to one particle component, such as volcanic ash, desert dust or sea-salt particles. Hence in our case,  $\delta_{ns}$  and  $\hat{A}_{ns,\perp}$  cannot be easily derived from field measurements.

## 2.4.2 Laboratory measurements

To retrieve  $\delta_{ns}$  and  $\hat{A}_{ns,\perp}$ , another possibility is to use laboratory measurements in which the particle generation can be controlled. Hence, measurements can be performed on a specific particle component. For volcanic ash particles, Muñoz et al. (2004) hence performed laboratory measurements at  $\lambda = 633$  nm on samples that were mechanically sieved to remove the largest particles, to correspond with a PSD that is representative of long-range transport situations. A striking feature of Muñoz et al.'s laboratory measurements is that their measured scattering matrices for the distinct samples taken from different volcanoes look remarkably similar, despite the observed variability in the ash particle morphology. This similarity in the measured scattering matrices elements justifies the construction of a synthetic scattering matrix, which corresponds to samples taken from different volcanoes (Muñoz et al., 2004). Hence, to include the variability in the ash particle morphology, Muñoz et al.'s synthetic scattering matrix optical measurements can be used. Moreover, this synthetic scattering matrix is extrapolated up to the lidar backscattering direction  $\theta = 180^\circ$  (Liu et al., 2003). Muñoz et al. (2004) hence derived  $F_{22,ash}/F_{11,ash} = (0.423 \pm 0.030)$  at  $\lambda = 633$  nm, corresponding to  $\delta_{ash} = (40.5 \pm 2.0) \%$ . For  $\lambda = 355$  nm, due to increased size parameters,  $\delta_{ash}$

might be slightly lower (Muñoz, private communication) and  $\delta_{\text{ash}}$  may be influenced by atmospheric aging, sedimentation processes, and possible water uptake, as extensively discussed in Chapter 3 and in (Miffre et al., 2012b). A quantitative estimation of these effects is however very difficult, since it has neither been measured nor numerically simulated for volcanic ash particles. Hence, this uncertainty is difficult to evaluate.

For sea-salt and dust particles, Sakai et al. (2010) performed laboratory measurements of  $\delta_{\text{dust}}$ ,  $\delta_{\text{ss}}$  close to the exact backscattering direction ( $\theta = 179.2^\circ \pm 0.4^\circ$ ) at  $\lambda = 532$  nm. In this sub-micrometer range, they measured  $\delta_{\text{dust}} = (14 \pm 3) \%$  and  $\delta_{\text{ss}} = (8 \pm 1) \%$ . Indeed, these values are the state-of-the art literature. However, care should be taken since these measurements are not performed in the exact backscattering direction, which may lead to quite considerable errors, as recently discussed by Schnaiter et al. (2012). Otherwise, the influence of the PSD may be questioned. These two points (exact backscattering direction, possible influence of the PSD) will be further analyzed by performing a laboratory experiment in Section 4.1. Concerning the Ångström exponent, to my knowledge, no cross-polarized  $\mathring{A}_{\text{p},\perp}$ -measurement has been performed for ash, dust or ss-particles.

### 2.4.3 Light scattering numerical simulations

In complement to these field and laboratory methodologies, numerical simulations can also be used to retrieve  $\delta_{\text{ns}}$  and  $\mathring{A}_{\text{ns},\perp}$ . Using light scattering numerical simulations,  $\delta_{\text{ns}}$  and  $\mathring{A}_{\text{ns},\perp}$  can be computed in the exact backscattering direction by choosing the radiation wavelengths together with the particles PSD and shape, for a given refractive index. As indicated by Equation (2.14) and (2.15),  $\delta_{\text{ns}}$  and  $\mathring{A}_{\text{ns},\perp}$  can be computed from  $\langle (d\sigma/d\Omega)_{\text{p},\pi} \rangle$ . Hence, in this sub-section, light single-scattering numerical simulations are exploited to retrieve size-averaged backscattering cross-sections  $\langle (d\sigma/d\Omega)_{\text{ns},\pi} \rangle$  for  $\text{ns} = \{\text{ash}, \text{dust}, \text{ss}\}$ , from which  $\delta_{\text{ns}}$  and  $\mathring{A}_{\text{ns},\perp}$  are deduced. In addition, the Lidar ratios  $S_{\text{ns}}$ , defined in Equation (2.16), are also computed and will be used in Chapter 3 to retrieve  $\beta_{\text{ns},\pi}(\lambda)$ . These numerical simulations have been recently published in (David et al, 2013a).

#### (a) Numerical simulation

The optical properties of the volcanic ash, desert dust or sea-salt particles encountered in the atmosphere are difficult to simulate with numerical models, due to the complexity of these

highly irregularly shaped ns-particles. As underlined in Nousiainen (2009) and Nousiainen et al. (2012), a complete realistic modelling is difficult to simulate as it should account for these highly-irregularly shapes, as well as inhomogeneity, porosity and birefringence. Despite this complexity, it is now well-established (Dubovik et al., 2006; Veselovskii et al., 2010; Nousiainen et al., 2012) that the optical properties of size-shape distributions of such particles can be well-mimicked by size-shape distributions of homogeneous spheroids, at least when particles are not much bigger than the wavelength. For example, Dubovik et al. (2006), Veselovskii et al. (2010), Merikallio et al. (2011) demonstrated that size-shape distributions of randomly-oriented spheroids can reproduce the phase function of real dust particles. Hence, to mimic volcanic ash and mineral dust particles, we used spheroids by applying the T-matrix code developed by Mishchenko and Travis (1998). Other approaches, such as the DDA-method (Draine and Flatau, 1994), are feasible and promising but have not been performed during this thesis. The spheroids' shape is expressed by the so-called aspect ratio  $\varepsilon = b/a$ , where  $a$  is the spheroids' rotational symmetry axis length and  $b$  is its axis length in the perpendicular direction. As underlined by Merikallio et al. (2011), a distribution consisting of both oblates and prolates is a better proxy to represent atmospheric mineral dust particles. Hence, oblate ( $\varepsilon \geq 1$ ) and prolate ( $\varepsilon < 1$ ) spheroids are assumed in equal numbers (equiprobable shape distribution), as done by Dubovik et al. (2006) and Veselovskii et al. (2010). The shape distribution of the spheroids can be described by a weighting factor  $W$  following a  $n$ -power law ( $n \geq 0$ ).

$$W = K|\zeta|^n \quad (2.46- a,b)$$

where  $\zeta$  is the shape factor ( $\zeta = \varepsilon - 1$  if  $\varepsilon \geq 1$ ;  $\zeta = 1 - 1/\varepsilon$  if  $\varepsilon < 1$ ) and  $K$  is the normalization constant. Atmospheric dust samples measured in laboratory (Volten et al., 2001, Muñoz et al., 2004) are more realistically mimicked by a power-law  $n = 3$  shape distribution (Merikallio et al., 2011). This favours extreme aspect ratios at the expense of nearly spherical spheroids, but in this way, polarization effects are better taken into account. Hence to simulate desert dust and volcanic optical properties, oblate and prolate spheroids in equal numbers are used with a  $n = 3$  shape distribution. As underlined in Chapter 1, crystallised sea-salt particles exhibit a cube-like shape (below the 40 %-relative humidity crystallization point of sodium chloride (Randriamiarisoa et al., 2006)), the sea-salt optical properties are computed from cubes by using Kahnert's T-matrix algorithm (2013). This code is well-suited to compute the optical properties of particles having discrete symmetries such as polyhedral prisms or cubes. In both

of these codes (Mishchenko and Travis, 1998; Kahnert, 2013), the Maxwell's equations are solved analytically and exactly, with an analytical orientation averaging, to obtain the optical properties.

### (b) Input parameters of the numerical simulation

The computed size parameters  $x = 2\pi r / \lambda$  were chosen to be representative of atmospheric ns-particles observed after long-range transport, as in Chapter 3 case studies. Hence, as detailed in (Schumann et al., 2011), due to sedimentation effects, a cut-off radius of a few micrometers seems reasonable according to the literature. Moreover, in the case of a sea-salt and dust particle mixture, sea-salt adhering may cause the gravitational settling of dust particles to be significantly accelerated (Zhang, 2008). Accordingly, we chose  $x$ -values varying from 0.01 to 50 after long-range transport and ran the T-matrix code for volcanic ash and desert dust particles, using the  $m$ -refractive indices given in Table 2.1, for eight  $\varepsilon$ -values, varying from 1.2 up to 2.6 with 0.2 steps. This table summarizes the input parameters used in the simulations for each particle component: ash, dust, sea-salt particles.

**Table 2.1** Input parameters used in the numerical T-matrix simulation on ns-particles (ash, dust, sea-salt):  $m$ -complex refractive index at the Lidar wavelengths (UV,  $\lambda_1 = 355$  nm; VIS,  $\lambda_2 = 532$  nm), size parameter range, modelled shape, aspect ratios values and literature reference for the  $m$ -refractive index. The discrete set of  $X$ -values is  $X = 0.01, 0.02, 0.1, 0.25, 0.5, 1$ ; step of 1 for  $X = 1$  to 10, step of 2 for  $X = 10$  to 30, 35, 40, then 45, 50. For  $\varepsilon$ -values, the step is 0.2.

Ns-particle	Label	Refractive index $m$	Size parameter $X$	Shape	Aspect ratio $\varepsilon$
Volcanic ash	(ash)	$1.54 - 0.0054i$ (UV, VIS) (Winchester, 1998; Muñoz et al., 2004)	0.01 to 50	Spheroid	1.2, 1.4, 1.6, ..., 2.6
Desert dust	(dust)	$1.57 - 0.007i$ (UV, VIS) (Kandler et al., 2011)	0.01 to 50	Spheroid	1.2, 1.4, 1.6, ..., 2.6
Sea-salt	(ss)	$1.51 - 0.0004i$ (UV) $1.50 - 0.00001i$ (VIS) (Shettle et al., 1979)	0 to 20	Cubic	

### (c) Numerical simulation results

Using the respective T-matrix numerical code, we have computed  $F_{11,ns}$ ,  $F_{22,ns}$ ,  $C_{sca,ns}$  and  $C_{ext,ns}$  as a function of the particle radius  $r$  for ash, dust and sea-salt particles at the  $\lambda_1 = 355$  nm and  $\lambda_2 = 532$  nm lidar wavelengths used in the following Chapter 3. Figure 2.6 displays the retrieved particle backscattering cross-sections  $(d\sigma/d\Omega)_{ns, //}$ ,  $(d\sigma/d\Omega)_{ns, \perp}$  and  $\delta_{ns}$  as

a function of the particles radius  $r$ , by respectively using Equation (2.6), (2.7) and (2.4). For clarity, the backscattering cross-sections are plotted per unit volume of the particle to emphasize the role of the finest particles, as first done in (Veselovskii et al., 2010). The obtained curves agree with the literature on spheroids (Veselovskii et al., 2010; Mishchenko et al., 2009). In particular, the backscattering cross-sections are not monotonic with the particle radius  $r$ . Due to the homothetic scale in  $r/\lambda$ , wavelength-sized particles exhibit larger backscattering cross-sections in the UV spectral range at  $\lambda_1 = 355$  nm than in the VIS spectral range at  $\lambda_2 = 532$  nm. Hence, our sensitivity to the ultrafine and fine particles is increased in the UV. The ns-particles' depolarization ratio reaches its maximum value around  $r = 0.3$   $\mu\text{m}$  in the UV ( $0.5$   $\mu\text{m}$  in the VIS). Above this maximum, the dependence of  $\delta_{\text{ns}}$  with  $r$  exhibits weak secondary maxima, but is otherwise almost constant when increasing the particles radius. Up to  $r = 0.5$   $\mu\text{m}$ ,  $\delta_{\text{ns}}$  rapidly increases with  $r$  and depolarization ratios as high as 50 % are reached so that ns-particles in the fine mode may also depolarize laser light. Such high depolarization ratios may then be experimentally observed with polarization-resolved backscattering measurements, such as polarization lidar. However,  $\delta_{\text{ns}}$  cannot be used as a particle size-meter since it also depends on  $m$  and  $\varepsilon$  (Mishchenko et al., 1995b).

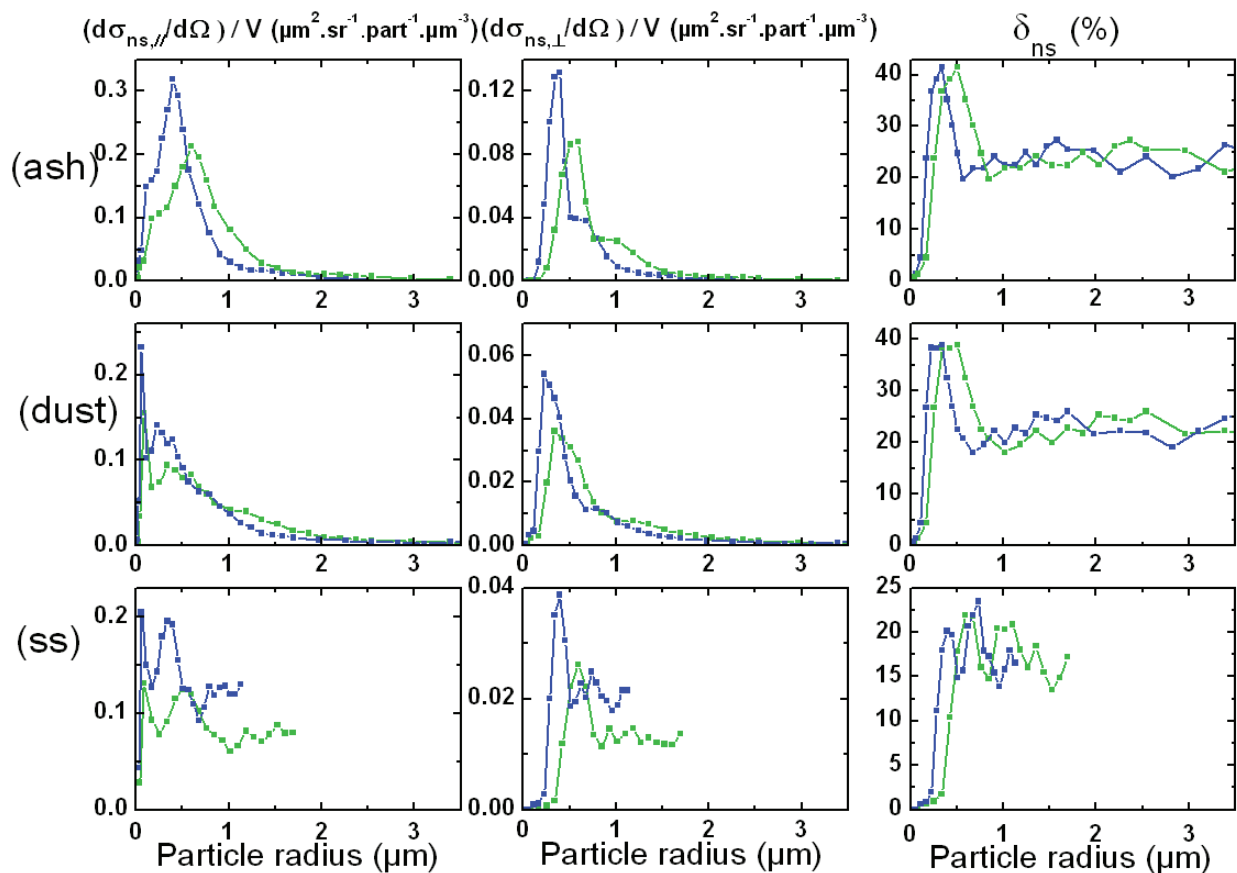


**Figure 2.6** Ns-particle backscattering cross-section  $(d\sigma/d\Omega)_{ns,\parallel}$  and  $(d\sigma/d\Omega)_{ns,\perp}$  per particle volume and ns-particle depolarization ratio  $\delta_{ns}$  as a function of the particle radius  $r$  in the UV (blue,  $\lambda_1 = 355$  nm) and in the VIS (green,  $\lambda_2 = 532$  nm) for each ns-particle type (ash, dust and sea-salt (ss)).

For a particles ensemble, the optical properties have to be integrated over the PSD and shapes.

Ideally, the PSD of each particle component should be accurately known. However, this information cannot be sufficiently precisely addressed from backscattering measurements. In the absence of complementary measurements, we used PSD's reported from the literature on volcanic ash, dust and sea-salt, after long-range transport as a proxy, with the criteria of ensuring specificity to the considered particle component, since our numerical simulations are built for that purpose. As an example, for volcanic ash, we used the PSD reported by Muñoz et al. (2004), since it is ash-particle specific, while being representative of long-range transport, as discussed in detail in Chapter 3 and in Miffre et al. (2012b). For dust particles, we chose Mallet et al.'s PSD (2004), who isolated the dust contribution by performing measurements after long-range transport, close to Lyon (France). We hence ensure dust particles specificity after long-range transport. Other literature references are of course possible, provided that the given PSD is representative of long-range transport and dust particles specific. The chosen PSD for the ns-particle types considered are displayed in Figure 2.7.

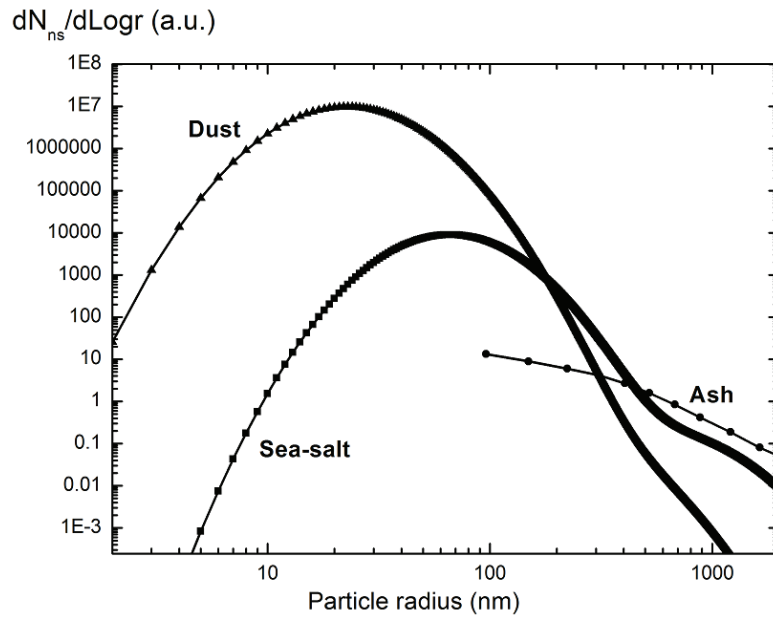


**Figure 2.7** Selected ns-particle size distributions (PSD) introduced in numerical calculations for volcanic ash (Muñoz et al., 2004), desert dust (Mallet et al., 2004) and sea-salt particles (ss, O'Dowd et al., 1997).

By integrating  $(d\sigma/d\Omega)_{ns,\parallel}$ ,  $(d\sigma/d\Omega)_{ns,\perp}$  over the PSD, we plotted co and cross-polarized size-averaged particle cross-sections  $\langle(d\sigma/d\Omega)_{ns,\parallel}\rangle$  and  $\langle(d\sigma/d\Omega)_{ns,\perp}\rangle$  as a function of the wavelength in Figure 2.8. For volcanic ash and desert dust particles, with this choice of PSD,

$\langle(d\sigma/d\Omega)_{ns,\perp}\rangle$  is higher in the UV spectral range than in the VIS-spectral range, while the opposite behavior is observed for sea-salt particles. The wavelength-dependence of  $\delta_{ns}$  is also displayed. The observed dependence agrees with the literature as for desert dust (Veselovskii et al., 2010). However, the ash particle depolarization ratio  $\delta_{ash}$  is different from those found in the literature (Muñoz et al., 2004, Lindqvist et al., 2011). The discrepancy may originate from surface roughness, which is more important for larger particles and is not accounted for in our spheroid model: indeed, in contrast to simulations based on spheroids, laboratory measurements show a tendency of increasing  $\delta_{ns}$  with effective radius (Nousiainen et al., 2009). The depolarization ratios predicted with spheroids for large volcanic ash particles may thus be underestimated. It follows that spheroids may have difficulties in predicting large particle depolarization ratios correctly. A DDA-approach (Lindqvist et al., 2011) might be a fruitful complementary approach; however extensive DDA simulations have not been performed in this thesis. Hence, for volcanic ash, we will use Muñoz et al.'s laboratory measurements  $\delta_{ash} = 40.5$  %-value (2004). Nonetheless, whatever the chosen  $\delta_{ash}$ -value, the behavior of  $\beta_{ash}$  vertical profile is still retraced, as shown in Equation (2.23) and further confirmed with the experimental results in Section 3.3.

The Lidar ratios  $S_{ns}$  are computed and displayed in Figure 2.8 as a function of the wavelength. The obtained  $S_{ns}$ -values agree with the literature, derived from Raman Lidar measurements. For example, at  $\lambda_1 = 355$  nm,  $S_{ash}$  equals  $(60 \pm 5)$  sr measured by Ansmann et al. (2012), while for dust particles, Veselovskii et al. (2010) numerically computed  $S_{dust} = 68$  sr. Sea-salt particles exhibit  $S_{ns}$ -values around 20 sr consistent with Ansmann et al. (2011). The Figure 2.8 error bars are the results of a sensitivity study, aimed at addressing the issue of size and shape variability. The size-sensitivity has been tested by varying the particles radius by  $\pm 10$  %, while for the shape-sensitivity, the  $n = 3$  shape distribution was replaced with the  $n = 0$  equi-probable shape distribution ( $n = 1$  and  $n = 2$  led to similar results as the original  $n = 3$  shape distribution). To provide the Figure 2.8 error bars that combine this size and shape sensitivity, the Table 2.2 numerical outputs have been computed by using the  $n = 0$  shape distribution and this for all particles radii. Note also that our sensitivity study has been performed for dust and sea-salt particles only, since, as explained above, the T-matrix numerical model has difficulties in correctly simulating the depolarization of volcanic ash. For volcanic ash particles, the interested reader may refer to Miffre et al. (2012b) where a detailed error analysis has been performed on the chosen particles size distribution.

Finally, by using this spectral dependence of  $\langle (d\sigma/d\Omega)_{ns,\perp} \rangle$  with Equation (2.15), we calculated  $\hat{A}_{ns,\perp}(\lambda_1, \lambda_2)$  for volcanic ash, desert dust and sea-salt particles corresponding to the chosen ns-PSD.

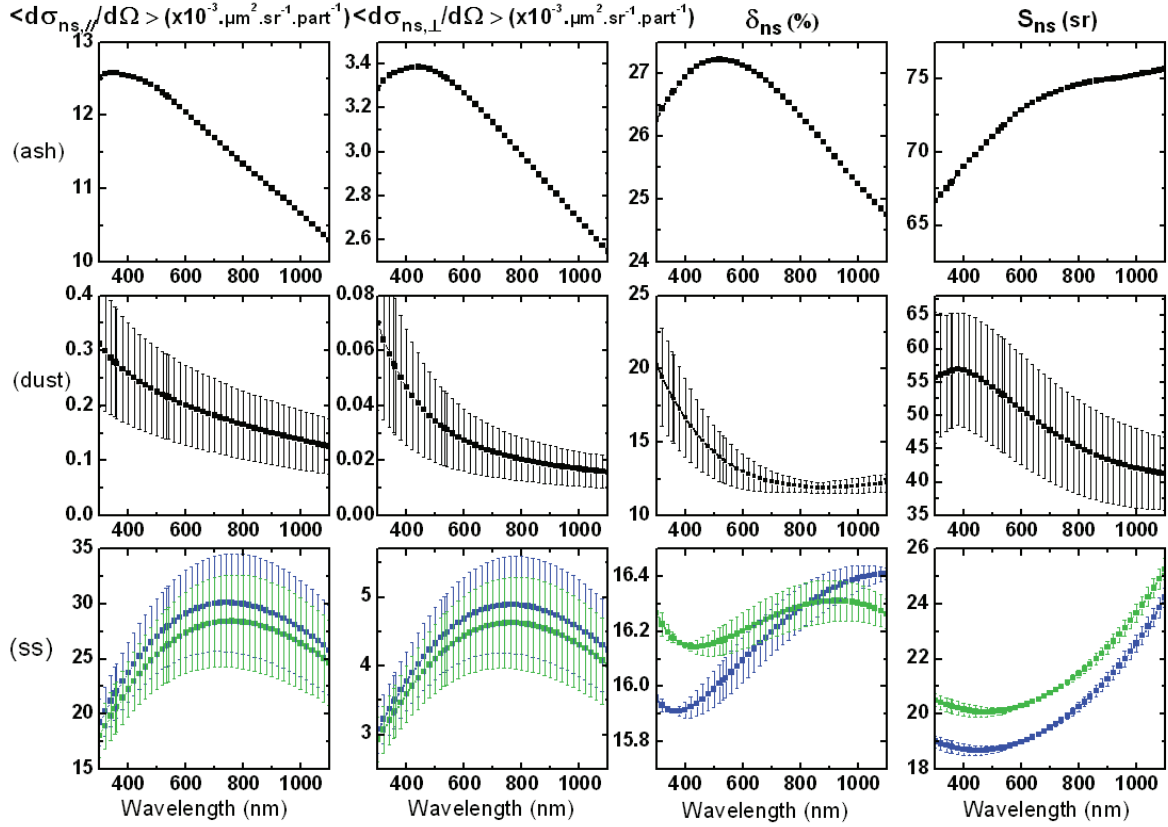


**Figure 2.8** Ns-particle backscattering coefficients, particle depolarization ratios  $\delta_{ns}$  and Lidar ratios  $S_{ns}$  as a function of the  $\lambda$ -wavelength, for each ns-particles type: volcanic ash, desert dust and sea-salt (ss). For ss-particles, two curves are represented, one for each refractive index given in Table 2.

Table 2.2 summarizes the results of our light-scattering simulations to be used in Sections 3.3, 3.4 and 3.5 where the methodology developed in Sections 2.2 and 2.3 are applied. For each ns-particle component considered, the depolarization ratio  $\delta_{ns}$  averaged over the corresponding PSD is given at the two Lidar wavelengths, together with the cross-polarized Ångstrom exponent  $\hat{A}_{ns,\perp}(\lambda_1 = 355 \text{ nm}, \lambda_2 = 532 \text{ nm})$  and the Lidar ratios  $S_{ns}$  needed for the Klett inversion (1985). The sign of  $\hat{A}_{ns,\perp}$  (UV, VIS) underlines our chosen PSD: dust (resp. sea-salt) particles backscatter more light in the UV (resp. VIS) spectral range than in the VIS (resp. UV) spectral range.

**Table 2.2** Results of the T-matrix simulations: depolarization ratios  $\delta_{ns}$  averaged over the corresponding PSD, cross-polarized Ångstrom exponents  $\hat{A}_{ns,\perp}(\lambda_1 = 355 \text{ nm}, \lambda_2 = 532 \text{ nm})$  and Lidar ratios  $S_{ns}$ , for each ns-particle component: volcanic ash, desert dust, sea-salt (ss) at  $\lambda_1 = 355 \text{ nm}$  (UV), at  $\lambda_2 = 532 \text{ nm}$  (VIS).

Ns-particles	Label	$\delta_{ns}(\text{UV})$ [%]	$\delta_{ns}(\text{VIS})$ [%]	$\mathring{A}_{ns,\perp}(\lambda_1 = \text{UV}, \lambda_2 = \text{VIS})$	$S_{ns}(\text{UV})$ [sr]	$S_{ns}(\text{VIS})$ [sr]
Volcanic ashes	(ash)	26.7	27.2	0.015	53.6	56.3
Desert dust	(dust)	$18.1 \pm 3.1$	$13.8 \pm 1.6$	$1.326 \pm 0.086$	$56.7 \pm 8.7$	$53.2 \pm 8.6$
Sea-salt	(ss)	$15.9 \pm 0.1$	$16.2 \pm 0.1$	$-0.478 \pm 0.034$	$18.8 \pm 0.2$	$20.1 \pm 0.2$

## 2.5 Conclusion

This chapter is related to the optical formalism applied in this thesis. After recalling the basic physical processes of scattering and extinction to be applied in the next chapters, this chapter focuses on polarization-resolved backscattering which relies on the scattering matrix formalism. The novelty of this chapter is related to the development of a new methodology allowing the optical backscattering partitioning of a three-component particles external mixture into its individual spherical and nonspherical components.

Hence, the issue addressed in this chapter is how to retrieve, from polarization-resolved and mutliwavelength backscattering measurement on an ensemble of external mixed particles the backscattering coefficient specific to each spherical (s) and nonspherical (ns) particle component, The polarization-resolved backscattering of a particle external mixture has first been analyzed for the following mixtures: (p) = {s, ns}, composed of spherical (s) and non-spherical (ns), then (p) = {ns1, ns2}, composed of two ns-particles components. It has been shown that the particle mixtures' depolarization ratio  $\delta_p$  differs from the nonspherical particles' depolarization ratio  $\delta_{ns}$ , due to the presence of spherical particles or less depolarizing particles in the mixture. Hence, by identifying a tracer for nonspherical particles based on the cross-polarized backscattering coefficient, a new methodology has been developed to retrieve, in a two-component particle mixture, the backscattering coefficients specific to each particle component. This optical backscattering partitioning is based on coupling a single wavelength polarization-resolved backscattering measurement ( $1\beta + 1\delta$ ) with the depolarization ratio of each particle component.

The optical backscattering partitioning in a two-component particle mixture (OBP2-methodology) has then been extended to the case of three-component particle external mixture (OBP3) by retrieving the backscattering coefficient specific to each of the three

particles components. OBP3 is based on coupling dual-wavelength polarization-resolved backscattering measurement ( $2\beta + 2\delta$ ) with the  $\delta_{ns}$ -value of the three particle component and the cross-polarized backscattering Ångstrom exponent  $\hat{A}_{ns,\perp}$  of two particle components. The novelty of this OBP3 methodology is twofold: firstly, a methodology had never been developed to retrieve from a three-component particle mixture, the backscattering coefficient specific to each particle component; secondly the nonsphericity of each of the three particle components is, taken into account.

To apply the OBP2 or OBP3 methodologies, optical inputs specific to each ns-particle component, are needed, i.e. the  $\delta_{ns}$ -ratio and the  $\hat{A}_{ns,\perp}$ -coefficient, which have been determined by using either field measurements, laboratory measurements or numerical simulations. Field measurements are suitable provided that they are specific to one ns-particle component, i.e. performed close to the source region, where atmospheric particles are dominated by one ns-particle component. Laboratory measurements are useful as the particles generation can be controlled and as the complex morphologies of the particles are taken into account, but to operate the OBP-methodologies, these measurements must be performed in the exact backscattering direction and at the appropriate radiation wavelength. To my knowledge, laboratory measurements of cross-polarized  $\hat{A}_{ns,\perp}$ -exponent have never been performed. Finally, by applying the Mishchenko T-matrix's code (Mishchenko et al., 1998), we performed light single-scattering numerical simulations to provide the  $\delta_{ns}$ -ratio and the  $\hat{A}_{ns,\perp}$ -coefficient for volcanic ash and desert dust particles in the exact backscattering directions as a function of the radiation wavelength, using the refractive index and the PSD that are specific to one ns-particle component. To account for the cubic shape of sea-salt particles, Kahnert's code (2013) has been used. The obtained values are in good agreement with the reference literature, except for volcanic ash for which the retrieved  $\delta_{ns}$  with spheroids is lower, perhaps due to surface roughness effects. These results are to be used in the following chapters, Chapter 2 opening new insights for both field measurements, to be studied in Chapter 3, as well as laboratory measurements, to be studied in Chapter 4.

## Chapter 3

### Lidar polarization-resolved backscattering measurements

The physical and chemical processes involved during transport by advection from a source region to a place where intrusion episodes occur was underlined in the general introduction. To briefly recall that point, the particle properties may change due to processes, such as sedimentation, mixing with other particles (Zhang, 2008), hygroscopic growth and possible chemical alteration (Bourcier et al., 2011; Riccobono et al., 2012). Hence, after long-range transport, one of the typical consequences is a complex vertical layering of the aerosols generally observed in the low troposphere.

#### 3.1 Introduction

In this chapter, the atmospheric particle vertical layering is retrieved together with its temporal evolution by using the Lyon UV-VIS polarization lidar (David et al., 2012). In the literature, multiwavelength lidar are currently used to retrieve  $\beta_p$  at several wavelengths (Del Guasta et al, 1994; Sugimoto et al, 2006; Freudenthaler et al., 2009; Veselovskii et al, 2010; Di Girolamo et al., 2012). As shown in Chapter 2, when dual wavelength ( $2\lambda$ ) measurements are polarization-resolved ( $2\beta+2\delta$ -measurements), they are suitable to apply the OBP3 methodology, which increase the knowledge on the optics of the particles layering in the atmosphere. Among the chosen  $2\lambda$ , the UV spectral range is favored in lidar measurements to address the highly concentrated ultrafine and fine particles. Hence, the  $1\beta+1\delta$ -measurements are performed with a UV-polarization lidar, while the  $2\beta+2\delta$ -measurements are performed with a UV-VIS polarization lidar.

In this context, three case studies, and further analyzed to objectively show the precision and the performance of the OBP-methodologies. To apply these methodologies, the single or dual-wavelength polarization backscattering measurements ( $1\beta+1\delta$  or  $2\beta+2\delta$ ) have to be performed and knowledge on particle chemistry present in the atmospheric particle mixture should be gathered by applying a complementary methodology, different from the lidar methodology. In

this context, air masses trajectories have been used as an indicator on the sources of the atmospheric particles.

Therefore, two cases studies, corresponding to different geophysical situations, have been studied by applying the OBP2 methodology, namely:

- *The Ash case*, in which volcanic ash particles are mixed with sulfate particles, as an example of a two-component particle external mixture that occurred at Lyon between 17<sup>th</sup> and 19<sup>th</sup> of April 2010, during the Eyjafjallajökull volcanic eruption. After more than 2 500 kilometres of transport by advection, the volcanic ash particles entering Lyon's atmosphere might have mixed with other particles, most likely to be hydrated sulfates, produced by SO<sub>2</sub>-oxydation (Mather et al., 2003), giving rise to a two-component external mixture. In this case study,  $\beta_{\text{ash}}$  and  $\beta_{\text{non-ash}}$  are simultaneously retrieved and the robustness of the OBP2 methodology is also discussed. Then, vertical profiles of volcanic ash mass/number concentrations are retrieved and analyzed from the  $\beta_{\text{ash}}$ -retrieval, which is new. Moreover, a nice comparison is found between the polarization lidar measurement and the FLEXPART ash particles numerical dispersion model and sulfate hygroscopicity is discussed.
- *The Dust case* is a two-component particle external mixture of desert dust with non-dust particles, observed at Lyon during a Saharan dust outbreak that occurred on July 09<sup>th</sup> 2010 after thousands kilometers of advection. In this cases study,  $\beta_{\text{dust}}$  and  $\beta_{\text{non-dust}}$  are simultaneously retrieved. Moreover,  $\beta_{\text{non-dust}}$  is interpreted in the context of new particle formation, hereafter called NPF, introduced in Chapter 1 in the context of mineral dust particles. It is generally considered that NPF cannot be observed with a lidar. Here, a numerical simulation of the backscattering coefficient corresponding to a typical NPF event is performed to demonstrate that observation of NPF events based on polarization lidar is feasible. This numerical simulation gives the features of the backscattering coefficient corresponding to a typical NPF.

Finally, we applied the OBP3 methodology to the following case study:

- *The Sea-salt/dust case* is an example of three-component particle external mixture. On October 18<sup>th</sup> 2011, a Saharan dust outbreak occurred at Lyon with particles entering the Lyon troposphere after several thousand kilometres of transport by advection above the Atlantic Ocean, during which mineral dust particles mixed with sea-salt (ss) and water-soluble (ws) particles in the troposphere over Lyon. In this case,  $\beta_{\text{dust}}$ ,  $\beta_{\text{ss}}$  and  $\beta_{\text{ws}}$  are

simultaneously retrieved. The robustness of the OBP3-methodology is analyzed and the retrieved  $\beta_{\text{dust}}$ ,  $\beta_{\text{ss}}$  and  $\beta_{\text{ws}}$  are interpreted.

This chapter is hence organized as follows. First, the statistical errors and systematical biases affection the Lyon  $2\lambda$ -polarization lidar are presented. Then, the Lyon UV-VIS polarization lidar setup is described with emphasis on the key points to reduce these statistical errors and systematical biases so as to perform sensitive and accurate measurements. Then, the  $(\beta_{p,\pi}, \delta_p)$ -retrieval from the  $2\lambda$ -polarization lidar measurements is detailed. Finally, the three above case are presented and analyzed in details with emphasis on the above cited applications, such as NPF.

## 3.2 Lyon $2\lambda$ -polarization Lidar

In this section, the Lyon dual-wavelength and polarization-resolved lidar is presented and used to perform the backscattering measurements ( $2\beta+2\delta$ ). Such measurements are based on efficiently separating the backscattered light with respect to its  $(\lambda,\pi)$ -spectral and polarization optical properties. This approach implies an ability to perform sensitive depolarization measurements: from low  $\delta_p$ -values, below the percent range, close to the molecular depolarization, up to high  $\delta_p$ -values, in the several tens percent range. Therefore, a precise analysis of the statistical errors and systematical biases is necessary. Consequently, an experimental setup-up has been developed reaching a drastic improvement of these statistical errors and systematical biases. The section is organized as follows:

- (1) Statistical errors and systematic biases
- (2) Lyon  $2\lambda$ -polarization lidar experimental set-up
- (3) Calibration procedure for the polarization measurement
- (4) Polarization resolved backscattering coefficients

### 3.2.1 Statistical errors and systematic biases

This error analysis relies on the opto-electronic components used in the lidar device depicted below in Figure 3.3. Statistical errors on the Lidar signal are due to the laser fluctuations (power, polarization) and to the detector noise. The latter includes the electronic noise and the shot noise induced by the laser backscattered photons and the sky background detected light.

To minimize these statistical errors, we minimized the sky background contribution to the cross-polarized lidar signal  $P_{\perp}$ , whose intensity is low (in the range of 100 times lower than  $P_{//}$ ). Appendix B contains the sky background information, which has been simulated and measured to minimize its contribution on the cross-polarized lidar signal.

An atmosphere having a depolarization ratio  $\delta$  (defined in Equation (1.7)) is hence considered as an input. This  $\delta$ -ratio originates from both atmospheric molecules and aerosols, which both depolarize laser light. Both statistical errors and systematic biases a priori affect the  $\delta$ -measurement so that the measured depolarization  $\delta^*$  a priori differs from  $\delta$ . In the absence of these undesirable errors and biases, the measured depolarization  $\delta^*$  is linked to  $\delta$  in the following way:

$$\delta^*(\lambda, z) = \frac{P_{\perp}(\lambda, z)}{P_{//}(\lambda, z)} = \frac{\eta_{\perp}(\lambda)}{\eta_{//}(\lambda)} \frac{\beta_{\perp}(\lambda, z)}{\beta_{//}(\lambda, z)} = G(\lambda) \cdot \delta(\lambda, z) \quad (3.1)$$

where  $P_{\pi}(\lambda, z)$  are the polarization-resolved lidar signals measured at altitude  $z$  (above mean sea-level, ASL) and  $G = \eta_{\perp}/\eta_{//}$  is the electro-optics gain calibration constant, which depends on the reflectivity and the transmission of the detector optical components and the detector electronic gain. Four systematic biases are here analyzed (see Figure 3.1):

- (a) Imperfect linear polarization of the light emitted in the atmosphere
- (b) Imperfect separation of polarization components (polarization cross-talk)
- (c) Misalignment between the transmitter and receiver polarization axes
- (d) Misalignment of the dichroic beamsplitter used for the  $\lambda$ -separation

In each case, to perform a sensitivity study, relations between  $\delta^*/G$  and  $\delta$  are provided through  $\Delta\delta/\delta = (\delta^*/G - \delta)/\delta$ . the corresponding  $\Delta\delta/\delta$  are plotted for each bias in Figure 3.1 for  $\delta$ -values in the percent range.

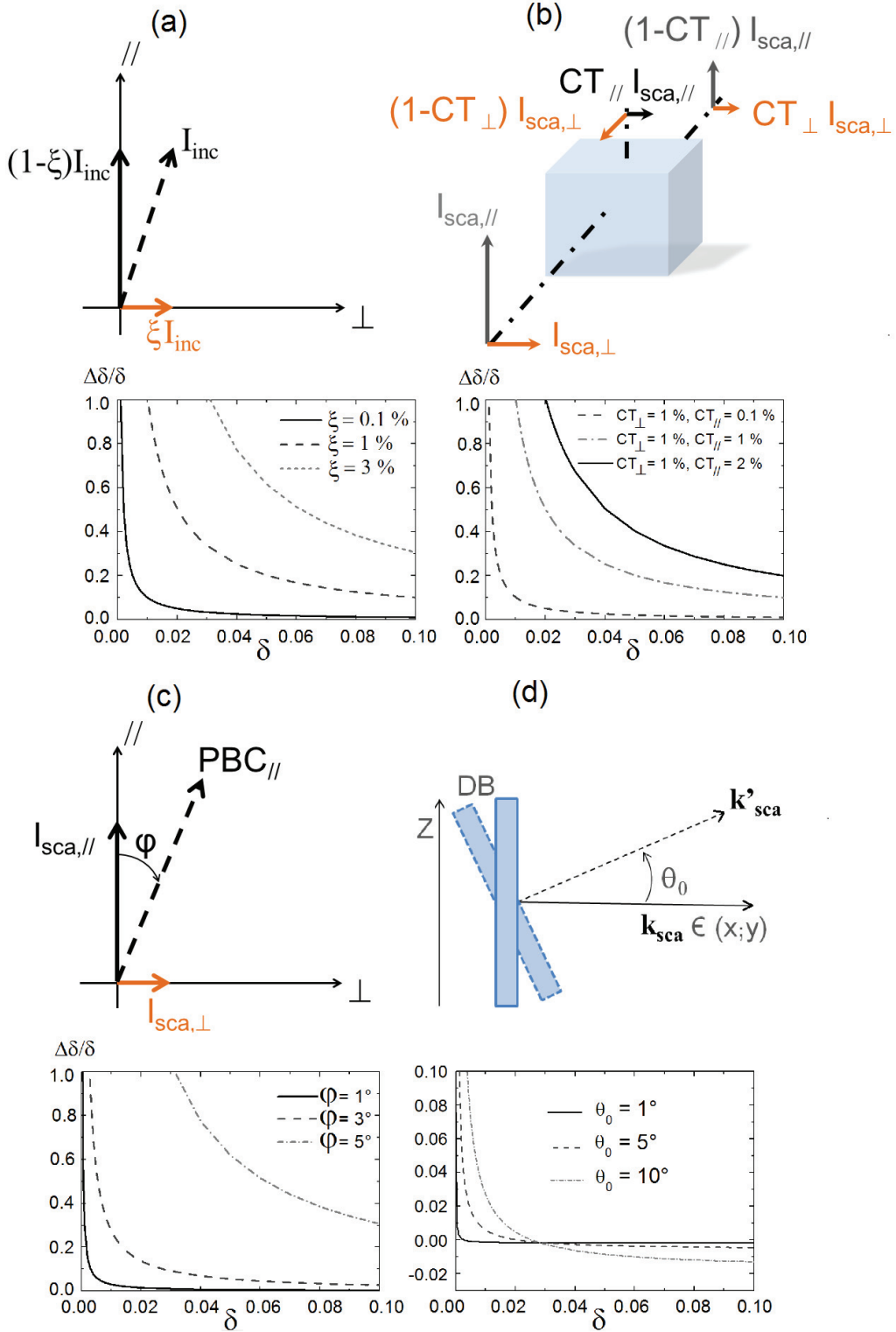


**Figure 3.1** Four systematic biases affecting the depolarization measurements: influence of a non-perfect linear polarization of the light emitted in the atmosphere (a), imperfect separation of polarization component, namely polarization crosstalk between  $\perp$  and  $\parallel$  detection channels (b), misalignment between the linear polarization of the emitted light and the PBC  $\parallel$  axis of the lidar detector (c) and misalignment of the dichroic beamsplitter used for  $\lambda$  separation (d).

### (a) Imperfect linear polarization of the light emitted

Here, we quantify the effect of a small unpolarized component in the emitted laser polarization on the  $\delta$ -measurement, as displayed in Figure 3.1-a where a residual polarization  $\xi = I_{i,\perp} / I_i \ll 1$  is introduced with  $I_{sca} = I_{sca, //} + I_{sca, \perp}$ . This emitted residual polarization  $\xi$  may originate from the laser degree of linear polarization or / and from polarization-sensitive reflective mirrors from the emission optics. In this case, even in a non-depolarizing atmosphere ( $\delta = 0$ ), the polarization state of the backscattered wave will have a depolarized component, leading to a non-zero measured depolarization  $\delta^*$ , i.e.  $\delta^*/G \geq \xi$ . The parallel Lidar intensity  $I_{sca, //}$  is contaminated by the induced non-zero  $\beta_{\perp} I_{inc, \perp}$  term; while the perpendicular lidar intensity  $I_{sca, \perp}$  is contaminated by the term  $\beta_{//} I_{inc, \perp}$ . Hence, after a few calculations from Equation (3.1),  $\delta^*$  can be expressed as a function of  $\delta$  and  $\xi$ , the bias parameter, as follows:

$$\frac{\delta^*}{G} = \frac{(1-\xi) \cdot \delta + \xi}{(1-\xi) + \xi \cdot \delta} \quad (3.2)$$

When  $\delta = 10 \%$ , a residual polarization  $\varepsilon = 1 \%$  induces a measured depolarization  $\delta^* = 11 \%$ . As shown in Figure 3.1-a plotting the Equation (3.2) by the quantity  $\Delta\delta/\delta = (\delta^*/G - \delta)/\delta$ , care should be taken when measuring low depolarization ratios, in the 1 %-range: for  $\delta = 1 \%$ , the required  $\xi$ -value to ensure that  $\delta^*$  differs from  $\delta$  by no more than 1 %, is only equal to 0.01 %. As shown bellow in our experimental set-up,  $\xi$  is below 0.0001.

### (b) Imperfect separation of polarization components: polarization cross-talk

When separating two  $\pi$ -polarization components of the backscattered light, defined with respect to the laser linear polarization, some leakage between the two polarization detection channels may occur, leading to an imperfect polarization separation leading to so called cross-talk effects (Figure 3.1-b). To calculate the allowed leakage for measuring  $\delta$ -values in the few percents range, we introduce a cross-talk coefficient  $CT_{//}$  to characterize the leakage of the // -polarization light into the  $\perp$ -polarization channel. As shown in Figure 3.1-b, the parallel Lidar intensity  $I_{sca, //}$  is contaminated by the contribution from perpendicular channel, having a  $CT_{\perp}$ -efficiency, while removing the leakage contribution into the perpendicular channel, which

occurs at a  $CT_{//}$ -efficiency. Hence, the measured parallel Lidar intensity  $P_{//}$  is given by:  $P_{//} = \eta_{//} [(1 - CT_{//})I_{sca, //} + CT_{\perp}I_{sca, \perp}]$ . Symmetrically, the perpendicular Lidar intensity can be written as  $P_{\perp} = \eta_{\perp} [(1 - CT_{\perp}) I_{sca, \perp} + CT_{//} I_{sca, //}]$ , as obtained from the  $P_{//}$ -expression by simply exchanging the  $//$  and  $\perp$ -subscripts, to satisfy photon energy conservation, hence introducing the  $CT_{\perp}$  cross-talk coefficient, characterizing the leakage of the  $\perp$ -polarization channel into the  $//$ -polarization channel. Hence,  $\delta^*$  is linked to  $\delta$  via the bias parameters  $CT_{//}$  and  $CT_{\perp}$  as follows:

$$\frac{\delta^*}{G} = \frac{(1 - CT_{\perp}) \cdot \delta + CT_{//}}{(1 - CT_{//}) + CT_{\perp} \cdot \delta} \quad (3.3)$$

For a  $\delta = 10\%$  atmospheric input depolarization, a bias parameter of  $CT_{//} = CT_{\perp} = 1\%$  leads to  $\delta^* = 11\%$ . Again, as shown by Equation (3.3) and in Figure 3.1-b, care should be taken when measuring low depolarization ratios, in the 1 %-range: for  $\delta = 1\%$ , the same residual leakage induces a measured depolarization  $\delta^*$  of 2 %, which represents a 100 %-relative error. As shown below in our experimental set-up,  $CT_{//}$  and  $CT_{\perp}$  are below than  $10^{-7}$ .

### (c) Misalignment between transmitter and receiver polarization axes

The backscattered photons polarization is analyzed by projection on the lidar detector polarization axes, assumed to implicitly match with the laser linear polarization, so that the polarization plane of the transmitter and the receiver are in perfect alignment. When a systematic offset-angle  $\varphi$  exists between the incident laser linear polarization and the detector polarization axes (see Figure 3.1-c), as first described by Alvarez et al. (2006), the measured depolarization  $\delta^*$  can be expressed as a function of  $\delta$  and the  $\varphi$ -angle as follows:

$$\frac{\delta^*}{G} = \frac{\delta + \tan^2(\varphi)}{1 + \delta \cdot \tan^2(\varphi)} \quad (3.4)$$

The relative error on  $\delta$  is plotted in Figure 3.1-c for different  $\varphi$  angles. When  $\delta = 10\%$ , a residual offset angle of  $3^\circ$  leads to  $\delta^*/G = 10.03\%$  only. For  $\delta = 1\%$ , when  $\varphi = 1^\circ$  (resp.  $3^\circ$ ),  $\delta^*/G = 1.03\%$  (resp.  $1.27\%$ ). Varying the offset angle  $\varphi$  can also be used to calibrate our

depolarization measurements by determining  $G$ , as proposed by Alvarez et al. (2006) and as detailed in Section 3.2.3.

As shown bellow, in our experimental set-up  $\varphi$  is below  $0.5^\circ$ , which means the induced  $\Delta\delta/\delta$  is below 4 % when  $\delta \geq 0.2$  % and below 0.1 % when  $\delta \geq 0.8$  %.

#### (d) Misalignment of the dichroic beamsplitter used for the $\lambda$ -separation

In dual-wavelength polarization Lidar detectors, a dichroic beamsplitter (DB) is often introduced to differentiate the backscattered photons at the two laser wavelengths. In this paragraph, we analyze the possible bias introduced by such a DB on the  $\delta$ -measurement. To our knowledge, such a systematic study has never been reported in the literature, where the DB is assumed to be polarization-insensitive.

Let us consider a dichroic beamsplitter having  $R_p$ ,  $R_s$ -reflectivity coefficients, defined with respect to the dichroic beamsplitter incidence plane (a similar discussion could be held on the corresponding transmission coefficients ( $T_p = 1 - R_p$ ,  $T_s = 1 - R_s$ )). As a consequence of Fresnel's formula,  $R_p$  generally differs from  $R_s$  ( $R_p < R_s$ ), so that the reflection on the DB may modify the polarization state of the backscattered photons. When the linear polarization of the laser correspond either to the s or p axis of the DB ( $\varphi_0 = 0$  or  $90^\circ$ ),  $\delta^*$  is proportional to  $\delta$  so that the corresponding proportionality coefficient  $R_s/R_p$  can be included in the polarization calibration procedure. However, when a systematic offset-angle  $\varphi_0$  exists between the laser linear polarization axis and the p-axis of the dichroic beamsplitter (see Figure 3.1-d), polarization cross-talks appear, which cannot be compensated during the polarization calibration procedure. We quantified the effect of a non-zero offset angle  $\varphi_0$  on the measurement of a low atmosphere depolarization ratio  $\delta$ . The corresponding calculations are detailed in appendix C.

$$\frac{\delta^*}{G} = \frac{a^2 \cdot \cos^2(\varphi_0) \cdot \sin^2(\varphi_0) + \delta \cdot (b - a \cdot \cos^2(\varphi_0))^2}{(b - a \cdot \sin^2(\varphi_0))^2 + \delta \cdot a^2 \cdot \cos^2(\varphi_0) \cdot \sin^2(\varphi_0)} \quad (3.5)$$

where the two coefficients  $a = \sqrt{R_p} - \sqrt{R_s}$  and  $b = \sqrt{R_p}$  are determined by the  $R_p$ ,  $R_s$ -reflectivity coefficients, as detailed in Appendix C. The relative error bar on  $\delta$  is plotted in Figure 3.1-d for different offset angles  $\varphi_0$ , using  $R_p = 72$  % and  $R_s = 94$  %.

### 3.2.2 Lyon 2 $\lambda$ -polarization lidar experimental set-up

The UV-VIS polarization lidar experimental setup developed in this PhD has a home-built detector to minimize the statistical errors and systematical biases developed in Section 3.2.1. The UV spectral range has been chosen to increase the sensitivity to the ultrafine and fine particles, while the VIS spectral range has been chosen to probe coarser particles in the micron range (see Figure 2.6). Our set-up, described in Figure 3.2, uses a doubled and tripled Nd:YAG laser emitting pulses of 15 and 30 mJ respectively in the UV ( $\lambda = 355$  nm) and the VIS ( $\lambda = 532$  nm) spectral ranges. An emission polarizing beamsplitter cubes (PBC) is used to ensure that laser emission is linearly polarized with a degree higher than 10000:1. A half-wave-plate ( $\lambda/2$ ) is used to align the linear polarization of the laser with the PBCs' axis of lidar detector ( $\text{Det}_L$ ), with better than  $0.5^\circ$  uncertainty. A 2.5x beam expander (BE) reduces the laser divergence down to 0.4 mrad. The UV and VIS lasers are combined on the same optical pathway through a dichroic mirror DM to probe the same atmospheric particles. The light backscattered by atmospheric particles and molecules (subscript m) is collected with a 200 mm f/3-Newtonian telescope. The 2.5 mrad field of view (FOV) of the telescope is determined by a 3 mm-diameter pinhole inserted at the telescope's focus, and was chosen to minimize multiple scattering and solar sky background contributions to the lidar signals. As shown by Tatarov et al. (2000) for FOV below 8 mrad, the multiple-scattering contribution is almost negligible. Moreover, the pinhole diameter was determined with the constraint to achieve lowest possible geometric compression, defined as the overlap function  $O(z)$  between the laser beam divergence and the receiver FOV. Hence by choosing a 3 mm-diameter pinhole, the overlap function  $O(z)$  is equal to unity for z-altitudes around 500 meters above ground, as can be seen on the lidar signals in Figure 3.5. After being collected by the telescope, the backscattered light is then ( $\lambda, \pi$ )-separated by the lidar detector  $\text{Det}_L$ , as schemed in Figure 3.3. Each polarization channel is composed of two PBC to ensure a precise polarization separation. Very narrow interference filters IF ( $\Delta\lambda = 0.35$  nm) are used to ensure there is no wavelength crosstalk. Moreover, the IFs minimize the sky background contribution as well as molecular backscattering. The backscattered light is finally focalized, by using a lens (L2), on the 6 mm effective diameter of a photomultiplier tubes (PMT). Each PMT's signal  $P_\pi(\lambda)$  is then sampled by a Licel TR-20 MHz, leading to 75 m-vertical range resolution

after noise filtering and range-averaging.  $P_{\pi}(\lambda)$  statistical noise is further reduced by averaging the signals over 4000 shots (less than 7 min) before range averaging and noise filtering.

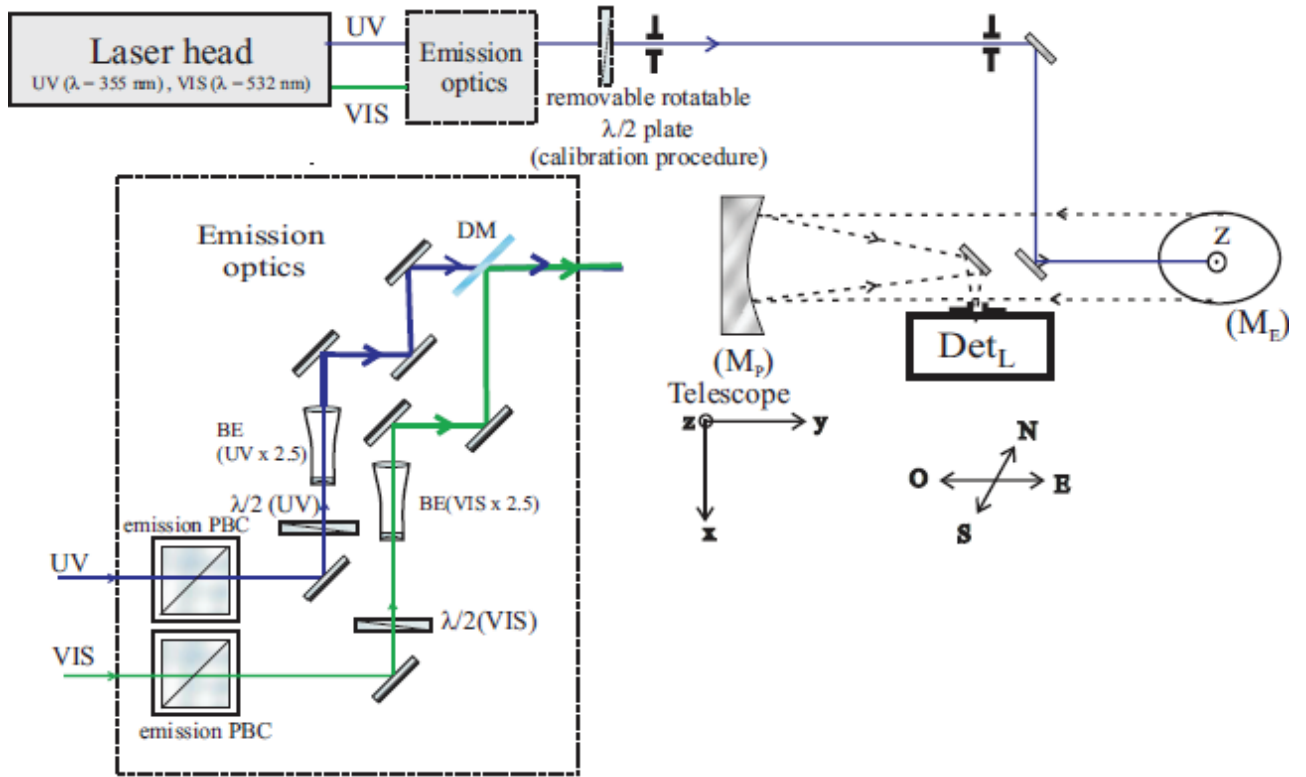


**Figure 3.2** Top view of the lidar experimental set-up. Double (532nm) and triple (355nm) Nd:YAG laser pulses are combined through the emission optics before propagating through the atmosphere along z axis, after reflection on an elliptic mirror ( $M_E$ ). The light backscattered by the atmospheric aerosol and molecules is collected by a  $f/3$  primary mirror  $M_P$ . Before entering the lidar detector  $Det_L$ , a 3 mm pinhole is used to reduce the field of view of the telescope to 5 mrad. The emission optics is composed for each wavelength of a polarizing beamsplitter cubes (PBC), to ensure a high polarization rate of the laser light (higher than 10000:1), a half-waveplate ( $\lambda/2$ ), to align the linear polarization of the laser with  $Det_L$ , a beam expander BE (2.5x) to reduce the laser divergence and reduce the laser power density and then a dichroic mirror DM is used to combine both 355 and 532 nm laser pulses.

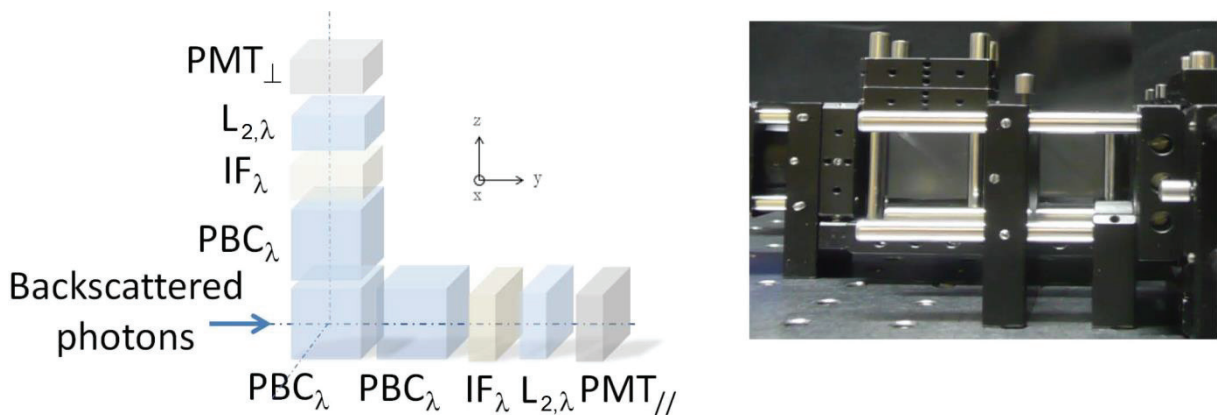


**Figure 3.3** Exploded view of each polarization channel (left panel) composed of two PBC, an interferential filter (IF), a lens ( $L_2$ ) and a photomultiplier tubes (PMT). Photograph of the UV cross-polarized lidar polarization channel composed of two PBC (right panel)

To sum up, the polarization and wavelength separation efficiency of the detector can be evaluated by writing the lidar detector transfer matrix  $\mathbf{M}_{DL}$  which relates the backscattered photon intensity vector  $\mathbf{I}_{2\lambda} = [I_{UV, //}, I_{UV, \perp}, I_{VIS, //}, I_{VIS, \perp}]$  to the measured backscattering signal vector  $\mathbf{P}_{2\lambda} = [P_{UV, //}, P_{UV, \perp}, P_{VIS, //}, P_{VIS, \perp}]$ . During a previous thesis work (Abou Chacra, 2009), the detector has been characterized on a dedicated test bench to measure the detector transfer matrix. A striking feature is that, with better than  $10^{-7}$  uncertainty, polarization and wavelength crosstalk are fully negligible, as shown by the diagonal transfer matrix:

$$\begin{bmatrix} P_{UV, //} \\ P_{UV, \perp} \\ P_{VIS, //} \\ P_{VIS, \perp} \end{bmatrix} = \begin{bmatrix} 0.99 \cdot \eta_{UV, //} & 0 & 0 & 0 \\ 4 \times 10^{-8} \cdot \eta_{UV, \perp} & 0.72 \cdot \eta_{UV, \perp} & 0 & 0 \\ 0 & 0 & 0.87 \cdot \eta_{VIS, //} & 0 \\ 0 & 0 & 0 & 1 \cdot \eta_{VIS, \perp} \end{bmatrix} \begin{bmatrix} I_{UV, //} \\ I_{UV, \perp} \\ I_{VIS, //} \\ I_{VIS, \perp} \end{bmatrix} \quad (3.6)$$

where  $\eta_{\lambda, \pi}$  is the electro-optic detection efficiency of the corresponding detector channel, which depends on the reflectivity and the transmission of the DB and the PBCs, the IF-transmission and the gain of the PMT at the applied voltages.

### 3.2.3 Calibration procedure for the polarization measurement

Since the relation between the PMT gain and the applied voltage is not precisely known, a calibration procedure is necessary to determine the electro-optical calibration constant  $G = \eta_{\perp} / \eta_{//}$  corresponding to the  $\lambda$ -channel. Since the detector transfer matrix is diagonal, a robust calibration procedure can be performed which consists in determining the multiplicative electro-optics gain calibration constant  $G$  for each laser wavelength. In the literature, different calibration methods exist (Behrendt and Nakamura, 2002 ; Alvarez et al. 2006; Freudenthaler et al., 2009). Behrendt and Nakamura (2002) proposed to use an atmosphere where only molecules are present, as the depolarization in this atmosphere equals  $\delta_m$ . For instance, our molecular depolarization ratios  $\delta_m(355) = 3.7 \times 10^{-3}$  at  $\lambda = 355$  nm and  $\delta_m(532) = 3.6 \times 10^{-3}$  at  $\lambda = 532$  nm, have been computed by taking into account the IF bandwidth  $\Delta\lambda = 0.35$  nm (Behrendt and Nakamura, 2002). Freudenthaler (2009) uses an angle  $\varphi = \pm 45^\circ$ , which leads to  $P_{\perp} = P_{//}$  and  $\delta^* = G$  as shown in Equation (3.4). Finally, Alvarez et al., (2006) introduce a control amount of polarization cross-talk by varying the  $\varphi$ -angle to perform an accurate calibration procedure, by relying on several  $\varphi$ -values. Hence they measure  $\delta^*$  as a function of  $\varphi$  and use Equation (3.4) to retrieve  $G$  from the  $\delta^*$  measurements.

To reduce the statistical noise of the calibration, we chose to apply the methodology proposed by Alvarez et al. (2006) with a dozen points to calibrate ( $\delta^*$  is measured for twelve  $\varphi$ -values). This methodology avoids assumption about the atmospheric particle content. In addition, in our case, the precision of the  $\varphi = \pm 45^\circ$  calibration is limited by the possibility to have an exact  $90^\circ$  rotation control between the  $\varphi = +45^\circ$  and  $\varphi = -45^\circ$  measurements. Moreover, the  $\varphi = \pm 45^\circ$  calibration may lead to possible PMT-saturation during the calibration procedure, as for  $\delta = 1\%$ ,  $P_\perp$  is multiplied by 50. Hence, to retrieve  $G$ ,  $\delta^*$  is first measured for twelve  $\varphi$ -angles as shown in left panel of Figure 3.4. Then,  $\delta^*$  is averaged between 0.8 and 2.0 km (the average value is here after noted  $\langle\delta^*\rangle$ ), where atmospheric conditions are stable as the vertical profiles of  $\delta^*$  remain almost constant for each  $\varphi$ -angle. Finally, these  $\langle\delta^*\rangle$ -values are used to fit the Equation (3.4) and retrieved  $G$  as shown in right panel of Figure 3.4, which represents  $\langle\delta^*\rangle$  as a function of  $\varphi$ . Hence, the retrieved  $G$  is known with less than 2 % error for both wavelengths ( $G(\text{UV}) = 29.16 \pm 0.22$  and  $G(\text{VIS}) = 16.69 \pm 0.23$ )

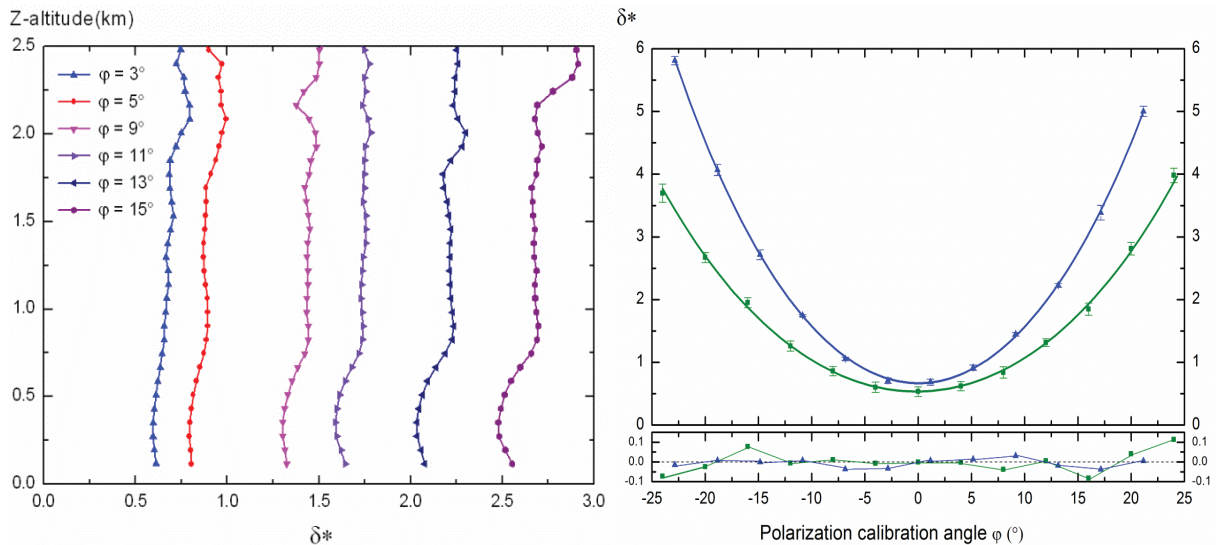


**Figure 3.4** Vertical profiles of  $\delta_\lambda^*$  for different value of misalignment angle  $\varphi$  between the laser linear polarization and the parallel axis of the detector PBC.

### 3.2.4 Polarization resolved backscattering coefficients

Here, we present the methodology used to retrieve the particle backscattering coefficient  $\beta_{p,\pi}$  from the lidar signals  $P_\pi$ . Three examples of  $P_\pi(\lambda)$  lidar signals measured with the above setup are plotted in Figure 3.5 respectively for the *dust case* (left panel), the *ash case* (middle panel), and *sea-salt/dust case* (right panel). The given statistical error bars are very low, as

drastically reduced by laser shot averaging, noise filtering and range averaging. Except for the  $P_{\perp}$ (UV)-signal on July 09<sup>th</sup>, the maximum value is reached in the Planetary Boundary Layer (PBL), where usually most aerosols are located (Miffre et al., 2010a; Winker et al., 2013), while an unusually high particle load is observed between 2 and 6 km.

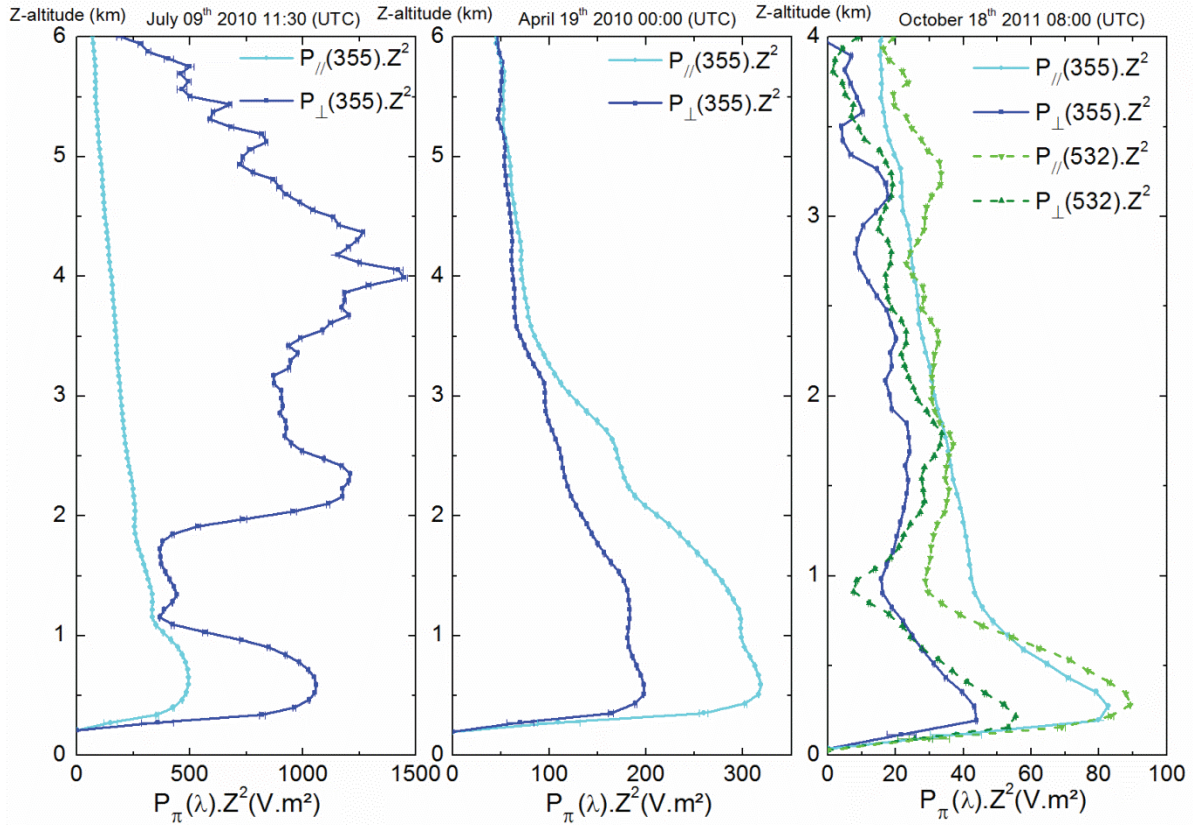


**Figure 3.5** UV polarization-resolved lidar signals  $P_{\pi}(355)$  on July 09<sup>th</sup> 2010 (left panel) and April 19<sup>th</sup> 2010 (middle panel) and UV-VIS polarization-resolved lidar signals  $P_{\pi}(\lambda)$  on October 18<sup>th</sup> 2011 (right panel) and. Blue and cyan full lines represents  $P_{\perp}(355)$  and  $P_{\parallel}(355)$ . Green and olive dashed curves represents  $P_{\perp}(532)$  and  $P_{\parallel}(532)$ .

As both molecules and particles contribute to the lidar signals  $P_{\pi}(\lambda)$ , the particles backscattering contribution must be retrieved by introducing the contrast  $R_{\parallel} = 1 + \beta_{p,\parallel}/\beta_{m,\parallel}$  of the molecular-to-particle backscattering, called the parallel backscattering.  $R_{\parallel}$  has been computed by applying the Klett's inversion algorithm (1985), which uses the lidar  $S_p$ -ratio, to correct for particle extinction in the lidar equation recalled in Chapter 1. To apply the Klett's algorithm, a predefined value for  $S_p$  is needed as well as a starting point  $Z_0$  for the inversion algorithm, generally chosen at high altitudes (above 7 km). The choice of  $S_p$  will be explained for each case study in the corresponding case study Section 3.3, 3.4 and 3.5. Error bars on  $R_{\parallel}$

are calculated by using the maximum and minimum values of  $S_p$  in the Klett's algorithm. Then  $\beta_{p,\parallel}$  and  $\beta_{p,\perp}$  are retrieved by using  $R_{\parallel}$  and the calibrated  $\delta$ -measurement as follows:

$$\beta_{p,\parallel} = (R_{\parallel} - 1) \times \beta_{m,\parallel} \quad (3.7)$$

$$\beta_{p,\perp} = (R_{\parallel} \delta - \delta_m) \times \beta_{m,\parallel} \quad (3.8)$$

The vertical profile of  $\beta_{m,\parallel}$  is computed from reanalysis model of the European Centre for Medium-range Weather Forecasts (ECMWF), by taking into account  $\Delta\lambda$  of the IF (Miles et al., 2001; Behrendt and Nakamura, 2002). Finally, by using  $R_{\parallel}$  and  $\delta$ , the particle depolarization ratio  $\delta_p$  can be retrieved from Equation (3.9), as first proposed by Winker and Osborn (1992) :

$$\delta_p = \frac{R_{\parallel} \delta - \delta_m}{R_{\parallel} - 1} \quad (3.9)$$

Equation (3.9) can be simply retrieved from the ratio of Equation (3.8) and Equation (3.7). Figure 3.6 displays the retrieved vertical profiles of  $\beta_{p,\parallel}$ ,  $\beta_{p,\perp}$  and  $\delta_p$  for each case study. For the ash and dust cases, measurements have only been performed in the UV, as a single-wavelength measurement can be used to apply the OBP2 methodology developed in Section 2.3. For the sea-salt/dust case,  $2\lambda$ -polarization measurements are performed, since dual-wavelength measurements are required to apply the OBP3 methodology.

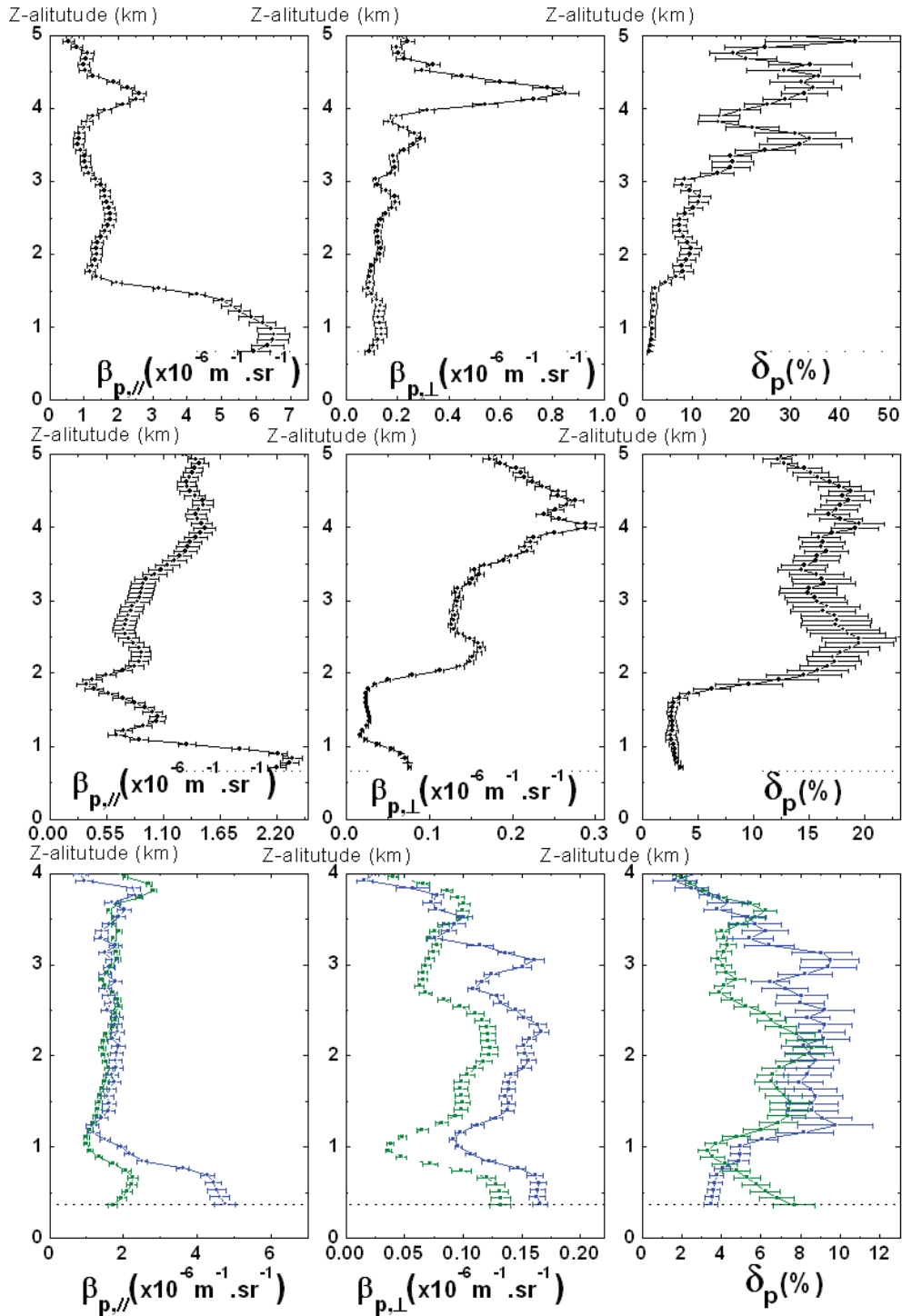


**Figure 3.6** Vertical profiles of particle backscattering coefficient  $\beta_{p,\parallel}$  and  $\beta_{p,\perp}$  and  $\delta_p$  for each of the three case studies. Ash case on April 19<sup>th</sup> at 0 h UTC (upper row) and dust case on July 9<sup>th</sup> at 12h UTC (middle row) are measured in the UV, while sea-salt/dust case on October 18<sup>th</sup> 2011 (bottom row) is measured in the UV (blue line) and VIS (green line). Error bars on  $\beta_{p,\perp}$  (resp.  $\delta_p$ ) are determined by using Equation 3.8 (resp. Equation 3.9). Due to the overlap function, the lidar signals start from 0.6 km altitude.

In the PBL, particles depolarize light with  $\delta_p$ -values in the percent range. Hence, within error bars, the particle depolarization in the PBL should be considered as different from zero. The

achieved sensitivity enables to measure with accuracy very low depolarization ratios, as low as only a few percent. In the UV (resp. VIS), at  $z = 600$  meters altitude (resp.  $z = 3800$  m), we measured  $\delta_p$  (UV) =  $(4.2 \pm 0.3) \%$  (resp.  $\delta_p$  (VIS) =  $(3.1 \pm 0.3) \%$ ) at 14h45. Hence, our detection limit is  $2 \times 0.3 \% = 0.6 \%$ , a value comparable to the molecular depolarization. As a conclusion, the Lyon  $2\lambda$ -polarization lidar has the ability to measure particles depolarization ratios over two orders of magnitude, from  $0.6 \%$  (detection limit very close to the molecular depolarization), up to  $40 \%$ , as observed during volcanic ash episodes. Moreover, in the cross-polarized channel, whose importance has been underlined in Chapter 2, very small  $\beta_{p,\perp}$ -values, as low as  $(2.4 \pm 0.5) \times 10^{-8} \text{ m}^{-1} \cdot \text{sr}^{-1}$  are measured.

### **3.3 The Ash case: volcanic ash mixed with sulfate particles**

We first introduced the geophysical situation and then, the optical analysis is performed by applying the OBP2-methodology, with emphasis on the potential applications. Moreover, from the OBP2-methodology, a new method for determining range-resolved number and mass concentrations specific to volcanic ash particles is proposed. This work has been published in (Miffre et al., 2010b, 2011, 2012a,b).

#### **3.3.1 Geophysical situation**

Volcanic eruptions release particles and gases such as sulfur dioxide ( $\text{SO}_2$ ) into the atmosphere that have implications on global climate. For example, Pinatubo's eruption in 1991 injected large quantities of  $\text{SO}_2$  into the stratosphere, which caused an anomalous cooling of the Earth's surface (Ramaswamy et al., 2001). Volcanic aerosols emitted in the troposphere affect climate through both direct and indirect effects, however this topic is still subject to large uncertainties (Robock, 2000). To quantify the impact of volcanic ash, the evaluation of ash mass, ash number, and even surface concentration is necessary (Ravishankara 1997). Ash number concentrations are often measured by filtration and sampling using either optical particle counters (Kaaden et al. 2009; Schumann et al. 2011) or inverse modeling of measured aerosol optical thicknesses (Tsanev and Mather 2007). Such measurements are, however, sensitive to an ensemble of particles and are not generally specific to volcanic ash particles, so that the retrieved number concentrations must be

carefully analyzed. Moreover ash mass concentrations are useful for airspace closures (the aviation safety limit is  $2000 \mu\text{g}\cdot\text{m}^{-3}$ ).

The Eyjafjallajökull volcano (63.63N, 19.62W, Iceland) started to erupt on March 20th 2010, before entering an explosive phase on April 14th 2010 lasting for several days, followed by further explosive eruptions during May 2010. In the initial explosive phase in April 2010, the eruption ejected volcanic ash to altitudes as high as 9 km above sea level (ASL), as reported by the Institute of Earth Sciences (IES, <http://www.earthice.hi.is>). On April 15th and 16th, the volcanic activity and ash generation continued, with reduced activity from April 16th. IES chemical analyses of ash samples revealed eruptive products with a silica content of 58% by weight, alumina  $\text{Al}_2\text{O}_3$  (15%), and oxides ( $\text{FeO}$ ,  $\text{CaO}$ , <10%).  $\text{SO}_2$  fluxes of  $3 \text{ kt day}^{-1}$  were reported by the Icelandic METOffice (<http://en.vedur.is/>), comparable with the annual flux of  $\text{SO}_2$  normally emitted by the whole Icelandic volcanic region (Halmer et al., 2002). As shown by MODerate resolution Imaging Spectrometer MODIS (<http://modis.gsfc.nasa.gov/>) on April 15th, the volcanic cloud emitted by the strong initial eruption on 14th April was transported eastwards and subsequently spread over northern Europe before reaching the South of France, leading to a six-days closure of the airspace for aviation over western Europe due to possible hazards to aircraft (Prata and Tupper, 2009). During their transport, irregularly-shaped volcanic ash particles larger than about 20 micrometers diameter are rapidly removed from the volcanic cloud by gravitational settling. In contrast, finer ash particles and secondary aerosols such as hydrated sulfates, formed by  $\text{SO}_2$ -oxidation, may remain in the troposphere for several weeks (Ovadnevaite et al., 2009). Hence after long-range transport, non-ash particles (here after noted nash) are present in the volcanic cloud and likely to be spherical hydrated sulfates (Mather, 2003; Schumann, 2011). Hence, a two-component particle mixture of volcanic ash mixed with ash particles is observed after long-range transport. Our remote site of Lyon is located at the border of the air traffic closure area, with particles that were highly dispersed and aged, after more than 2,600 km transport by advection. A precise chemical analysis has not been performed during the experiments carried out. Instead, we used 7-days air mass back-trajectories (Stohl et al., 1995) to identify the origin of the nonspherical particles present at the remote site, as shown in Figure 3.7. According to these back-trajectories, Saharan dust can be excluded as a source of particles over Lyon during the observation period. During this event, RH-values range between 50 and 75 % close to the ground to reach 70 % near 3 km-altitude. However, in the air masses coming from Iceland around 4-5 km, very low (10-25%) RH-values are observed.

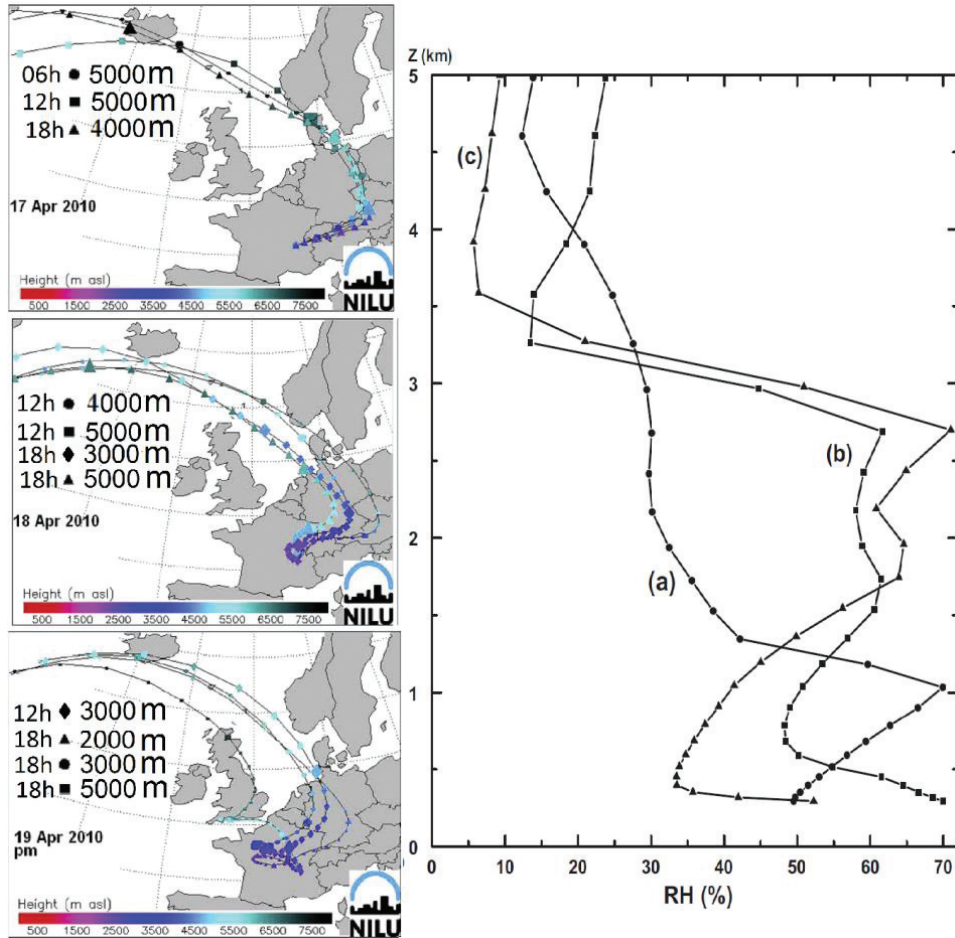


**Figure 3.7** NILU FLEXTRA 7-days air mass back-trajectories on April 17<sup>th</sup>, 18<sup>th</sup> and 19<sup>th</sup>, and relative humidity RH on April 17<sup>th</sup> at 12 h UTC (circles) (a), April 19<sup>th</sup> at 0 h UTC (squares) (b) and April 19<sup>th</sup> at 19 h UTC (triangles) (c).

### 3.3.2 Observation of the Icelandic volcanic ash cloud above Lyon

We analyzed the lidar signals recorded during this ash episode to analyze  $\beta_{p,\pi}$ -coefficients for the *ash case* study. We used  $S_p = 55 \pm 5$  sr in the Klett algorithm to retrieve the  $\beta_{p,\pi}$  and  $\delta_p$ , in agreement with Table 2.3 and the literature (Ansmann et al., 2012). The retrieved time-altitude map of  $\beta_{p,\pi}$  is potted in Figure 3.8, where, between 3 and 6 km an unusually high particle load is visible on April 17<sup>th</sup> and 18<sup>th</sup> in a thin filament. In this filament,  $\beta_{p,\pi}$ -values vary between 2 and 5  $\text{Mm}^{-1}.\text{sr}^{-1}$ . The filament tilts from 6 to 4 km above sea level (asl) on April 17<sup>th</sup> at 12 h, and then at 3 km asl on April 18<sup>th</sup> in the evening before mixing into the PBL. On April 19<sup>th</sup>, measured particle backscattering coefficients are lower because of less direct atmospheric transport and decreased volcanic activity (Schumann et al., 2010).  $\beta_{p,\pi}$ -values do not exceed 3.5  $\text{Mm}^{-1}.\text{sr}^{-1}$ , except for the 3 km altitude cloud seen on April 19<sup>th</sup> at 18h.

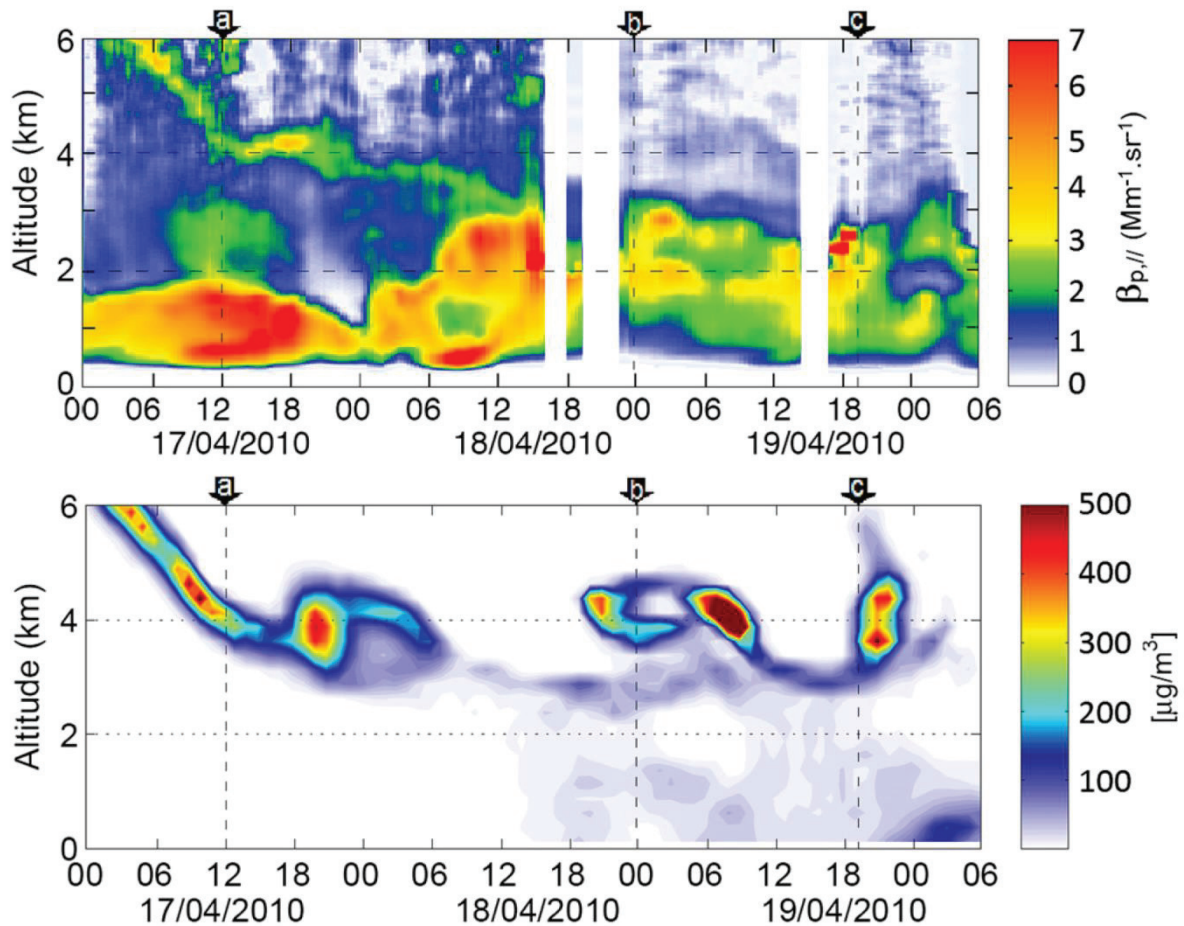


**Figure 3.8** Top graph: Parallel UV-particle backscattering coefficient (in  $\text{Mm}^{-1} \text{sr}^{-1}$ ) at Lyon as a function of time (in UTC units) from April 17th to 20th 2010. Bottom graph: FLEXPART time-height section of the ash tracer at Lyon. Letters from (a) to (c) correspond to vertical profile's times, to be analyzed in the next Section 3.4.3, 3.4.4 and 3.4.5.

In the lower part of Figure 3.8, we plotted the time-altitude plots retrieved from FLEXPART ash numerical dispersion model, in collaboration with the group headed by A. Stohl who simulated the volcanic ash transport from Iceland to Lyon. The lidar-observed filament structure (top of Figure 3.8) nicely agrees with the FLEXPART simulated ash layers within the vertical and time resolutions of both methodologies. This agreement is observed even for some small-scales features, for instance the maximum on April 17th at 18 h at 4 km. The comparison between the simulated and observed ash layers relies on the proportionality between  $\beta_{p,||}$  and the particles number concentration. The filament structure suggests that the ash layers remained highly stratified even after long-range advection. On April 17th, the observed layers below the filament (2-3 km) correspond to air masses originating from the East of Europe and are, thus, of non-volcanic origin. When volcanic particles mix into the PBL on April 18th, parallel backscattering enhancement relies on the volcanic ash particles intrusion, as shown by FLEXPART, and on possible sulfate hygroscopic growth. On April

19th,  $\beta_{p, //}$ -values decrease caused both by the reduced volcanic activity after the initial eruption and less direct transport to the measurement site. An interesting feature occurs between 3 and 5 km altitude where, in agreement with back-trajectories, new ash layers are simulated by FLEXPART in high mass concentrations. By the same time, low  $\beta_{p, //}$ -values are observed on Figure 3.8, dedicated to scattering on the parallel polarization channel. As shown in the next paragraphs, it is necessary to include the  $\beta_{p, \perp}$  profiles to further address the ash particles content. In addition, the ash particle content, deduced from backscattering measurements, is necessary to further interpret the comparison to the FLEXPART ash dispersion model.

### 3.3.3 Ash and non-ash (nash) backscattering retrievals

We here apply the OBP2-methodology introduced in Section 2.3 to the *ash case study* to simultaneously retrieve  $\beta_{ash}$  and  $\beta_{nash}$ , as illustrated in Figure 3.9 in the form a diagram showing the different necessary steps. As explained in Section 2.3,  $\delta_{ash}$  and  $\delta_{nash}$  have to be known and, as discussed in Section 2.4, to ensure ash specificity, we chose  $\delta_{ash} = (40.5 \pm 2.0) \%$ , derived from laboratory measurements on volcanic ash particles performed by Muñoz (2004). For nash (non-ash) particles,  $\delta_{nash} = 0 \%$  is used, as nash-particles are likely to be spherical hydrated sulfates.

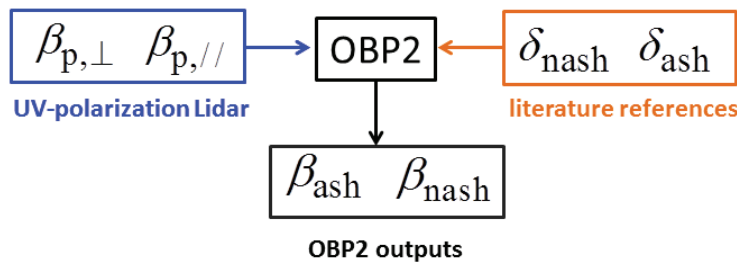


**Figure 3.9** Flowchart of the OBP2 methodology highlighting the inputs and outputs for ash and nash particles. Concerning the inputs,  $\beta_{p, //}$  and  $\beta_{p, \perp}$  are measured with UV-polarization Lidar,  $\delta_{ash} = (40.5 \pm 2.0) \%$  has been measured by Muñoz et al. (2004) and  $\delta_{nash} = 0 \%$  is used, as nash-particles are likely to be spherical sulfate.  $\beta_{ash}$  and  $\beta_{nash}$  are the retrieved outputs, from which the fraction of ash-to-particle backscattering  $X_{ash}$  (Equation (2.27)) as well as  $X_{nash}$  can be deduced.

As for  $(\beta_{p, //}, \beta_{p, \perp})$ -vertical profiles, we chose those from April 19<sup>th</sup> 2010 at 00h UTC (see Figure 3.8) which correspond to the (b)-profile on the time-altitude map displayed in Figure 3.8. Note that the  $\beta_{p, //}$  and  $\beta_{p, \perp}$  profiles are different, as both spherical and non-spherical particle contribute to  $\beta_{p, //}$  (Equation 2.18), while only nonspherical particles contribute to  $\beta_{p, \perp}$  (Equation 2.19). If the particle mixture was only composed of non-spherical ash particles,  $\delta_p$  would be equal to  $\delta_{ash}$  everywhere. However, the presence of nash-particles lowers the

observed  $\delta_p$ -values, which are always below  $\delta_{ash}$  within our error bars. Consequently, far from the source region,  $\delta_{ash}$  cannot be directly retrieved from  $\delta_p$  without care (Miffre et al., 2011). To ease the understanding, we also display the  $\beta_{ash, //}$ -profile in Figure 3.10 ( $\beta_{ash, //} = \beta_{ash, \perp} / \delta_{ash}$  since  $\beta_{ash, \perp} = \beta_{p, \perp}$ ). Hence, when  $\beta_{ash, //}$  equals  $\beta_{p, //}$ , there are no nash-particles and  $\delta_p$  reaches  $\delta_{ash}$  as observed around 4 km ASL within our error bars, in agreement with Equation (2.21). When  $\beta_{ash, //}$  deviates from  $\beta_{p, //}$ , nash-particles are present and we observe lowered  $\delta_p$ -values, in agreement with Equations (2.21). We hence explain the observed behaviour of  $\delta_p$  with z-altitude. Contrary to the  $\delta_p$ -profile, only ash particles contribute to the  $\beta_{p, \perp}$ -vertical profile, as discussed in Chapter 2. Thus, the vertical dispersion of the volcanic ash cloud in the low troposphere of Lyon can be retraced by the  $\beta_{p, \perp}$ -vertical profile: within our error bars, the achieved sensitivity allows distinguishing several successive volcanic ash layers at about 1.5, 3.0, 4.0, 4.5 km altitudes. As shown by the comparison of the  $\beta_{p, \perp}$  and  $\delta_p$ -vertical profiles, depolarization does not necessarily correlate with the backscattered power. The observed 1 km altitude difference between the  $\beta_{p, \perp}$  and the  $\delta_p$ -maxima is hence due to the presence of spherical nash particles.

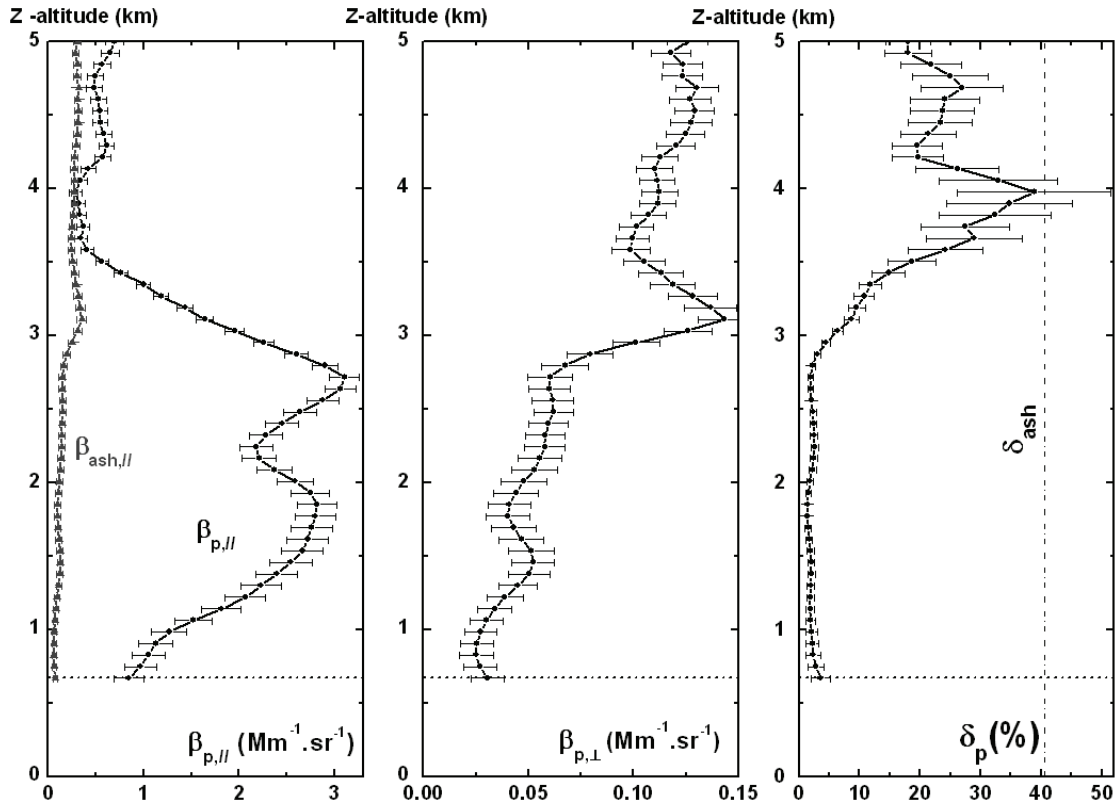


**Figure 3.10** Vertical profiles of backscattering coefficients  $\beta_{p, //}$ ,  $\beta_{p, \perp}$ , depolarization ratio  $\delta_p$ , and  $\beta_{ash, //}$  retrieved in the mixed {ash, sulfate} particle cloud on April 19<sup>th</sup> 2010 at 00h UTC at Lyon. With  $\beta_{ash, //} = \beta_{ash, \perp} / \delta_{ash} = \beta_{p, \perp} / \delta_{ash}$  (also assuming  $\delta_{nash} = 0$ ). The experiment is performed in the UV ( $\lambda = 355$  nm). Due to the overlap function, the lidar signals start from 0.6 km asl.

Then, the  $\beta_{p,\parallel}$  and  $\beta_{p,\perp}$  vertical profiles plotted in Figure 3.10 and the  $\delta_{\text{ash}}$ - and  $\delta_{\text{nash}}$ -value are used as inputs in the OBP2 methodology to determined  $\beta_{\text{ash}}$  with Equation (2.19) and (2.23) and  $X_{\text{nash}}$  with Equation (2.27). Figure 3.11 displays the hence retrieved vertical profiles of  $\beta_{\text{ash}}$  and  $X_{\text{nash}}$ . The corresponding error bars on  $X_{\text{ash}}$  and  $\beta_{\text{ash}}$  are range-dependent since the vertical profile of  $\beta_{p,\perp}$  is itself range-dependent. Its error bar includes the error bar on  $\delta_{\text{ash}}$  ( $(40.5 \pm 2.0) \%$ ) derived in Section 2.4.2 from Muñoz et al. measurements (2004). In agreement with Equation (2.27), the  $X_{\text{ash}}$ -profile follows the  $\delta_p$ -profile (Figure 3.10), which confirms that  $\delta_p$  can be considered in our case as a tracer for  $X_{\text{ash}}$ .

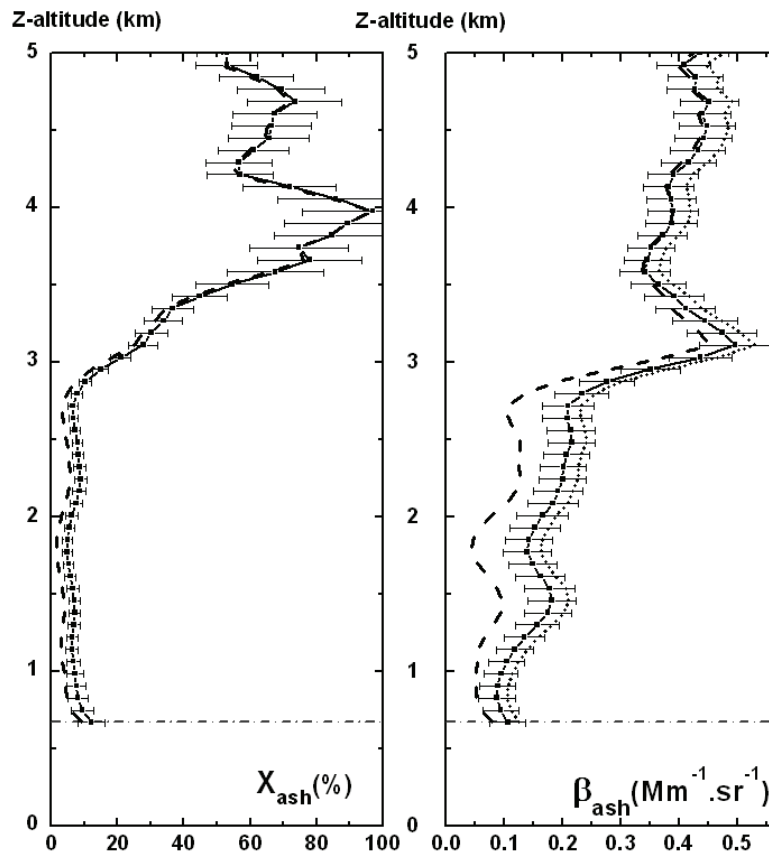


**Figure 3.11** Vertical profiles of  $X_{\text{ash}}$  and  $\beta_{\text{ash}}$  in the mixed {ash, sulfate} particle cloud on April 19h 2010 at 00h UTC at Lyon, for  $\delta_{\text{nash}} = 0$  and  $S_p = 55 \pm 5$  sr (full lines). Within our error bars, these profiles are slightly influenced by  $S_p$  (dotted lines, for  $S_p = 40$  sr) and by the sulfate depolarization  $\delta_{\text{nash}}$  (dashed lines, for  $\delta_{\text{nash}} = 1 \%$ ) at altitudes where back-trajectories confirm the presence of volcanic ash particles.

To discuss the robustness of  $\beta_{\text{ash}}$ -retrieval OBP2-methodology, we here discuss two arguments:

- First, we changed the  $S_p$ -value used in the Klett algorithm. As shown in Figure 3.11, the influence of the  $S_p$  is very low, as using  $S_p = 55$  sr (full line curves in Figure 3.11) or

$S_p = 40$  sr (dotted line curves in Figure 3.11) leads to negligible difference in the retrieved  $\beta_{\text{ash}}$  within our error bars.

- Secondly, the assumption of ash particles being the main depolarizing source may also be questioned. Nash particles may slightly depolarize light and contaminate the  $\beta_{p,\perp}$  measurement. Therefore, we need to correct the contaminated coefficient  $\beta_{p,\perp}$  for the background depolarization ratio  $\delta_{\text{nash}}$ . Hence, by applying Equation (2.32), we may write:  $\beta_{\text{ash},\perp} = (\beta_{p,\perp} - \delta_{\text{nash}} \beta_{p,\parallel}) / (1 - \delta_{\text{nash}} / \delta_{\text{ash}})$ . The dashed line curve plotted in Figure 3.11 corresponds to  $\delta_{\text{nash}} = 1\%$ , as measured by Sakai et al. (2010) for sulfate particles.  $\beta_{\text{ash},\perp}$  is then used in Equations (2.24) to retrieve  $\beta_{\text{ash}}$ . As can be seen from Equation (2.32), by assuming  $\delta_{\text{nash}} = 0\%$ , the maximum overestimation term on  $\beta_{\text{ash},\perp}$  is equal to  $\delta_{\text{nash}} \beta_{p,\parallel}$ , which is negligible when  $\delta_{\text{nash}} \ll \delta_p$  (as  $\delta_{\text{nash}} \beta_{p,\parallel} = \beta_{p,\perp} \delta_{\text{nash}} / \delta_p$ ). Hence, at altitudes where back-trajectories confirm the presence of volcanic ash particles, the background depolarization  $\delta_{\text{nash}} = 1\%$  has negligible influence on the retrieved vertical profiles of  $\beta_{\text{ash}}$ . As a consequence, our  $\beta_{\text{ash}}$ -retrieval is very robust since the influence of  $S_p$  and  $\delta_{\text{nash}}$  is negligible in the volcanic ash layers. Hence, we are confident that the retrieved  $\beta_{\text{ash}}$ -profiles are ash-specific, which is new.

In addition, the OBP2-methodology provides the  $\beta_{\text{nash}}$ -coefficient, obtained by simply noting that  $\beta_{\text{nash}} = \beta_p - \beta_{\text{ash}}$ . Figure 3.12 displays the vertical profiles of  $\beta_{\text{nash}}$  and  $\beta_{\text{ash}}$ , together with the relative humidity (RH).  $\beta_{\text{ash}}$ -value and  $\beta_{\text{nash}}$ -value respectively as low as  $(4.9 \pm 3.7) \times 10^{-8} \text{ m}^{-1} \cdot \text{sr}^{-1}$  and  $(0.129 \pm 0.125) \times 10^{-8} \text{ m}^{-1} \cdot \text{sr}^{-1}$  have been retrieved on April 19<sup>th</sup> 0h UTC at 3.7 km asl and at 0.9 km altitude. Hence the achieved  $\beta_{\text{ash}}$  and  $\beta_{\text{nash}}$  detection limits are below  $0.049 \times 10^{-8} \text{ m}^{-1} \cdot \text{sr}^{-1}$  and  $0.129 \times 10^{-8} \text{ m}^{-1} \cdot \text{sr}^{-1}$ . In addition, two main features are observed in Figure 3.12:

- First,  $\beta_{\text{nash}}$  seems to be higher when RH is high. For instance on April 19<sup>th</sup>,  $\beta_{\text{nash}}$  almost follows the RH vertical profile. Since nash particles are most likely to be sulfate, the nash-particle hygroscopic growth can explain the similarity between  $\beta_{\text{nash}}$  and RH.
- The second feature observed is a negative-correlation between  $\beta_{\text{nash}}$  and  $\beta_{\text{ash}}$ . This negative correlation cannot be explained by the OBP2 methodology applied to retrieve  $\beta_{\text{ash}}$  and  $\beta_{\text{nash}}$  (as this negative-correlation is already observed between  $\beta_{p,\perp}$  and  $\beta_{p,\parallel}$ ). One possible explanation to the negative-correlation between ash and nash particles is the new particle formation (NPF), which is most likely to occur when low particle surface concentration is available (Wehner et al. 2010). Hence ash particles act as a

growing condensational sink which stops the new particle formation and growth (NPGF). Such NPGF is also addressed and carefully studied in the case a desert dust outbreak episode (Section 3.4)

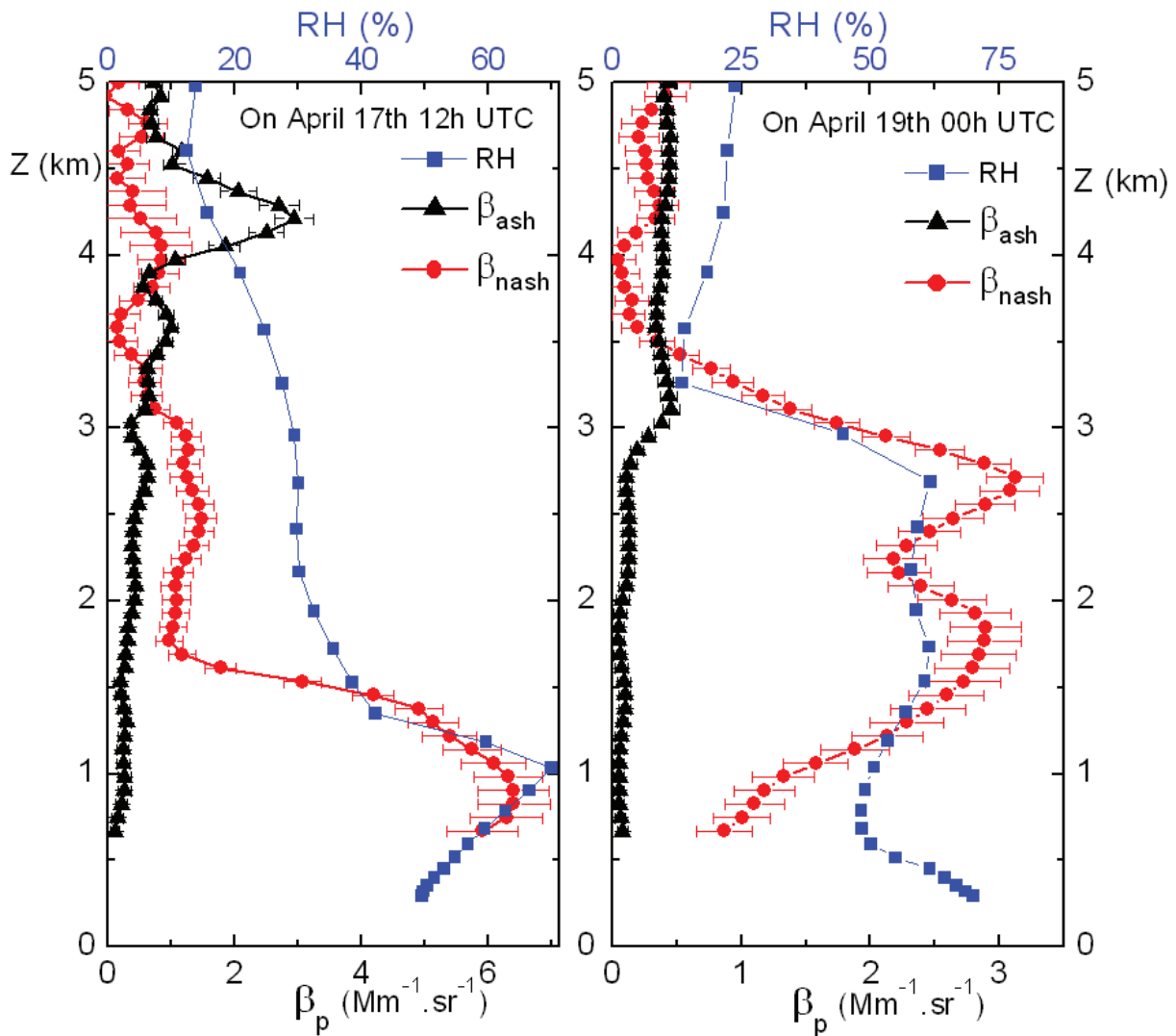


**Figure 3.12** Vertical profiles of  $\beta_{ash}$  (black triangles),  $\beta_{nash}$  (red circles) and RH (blue squares) on April 17<sup>th</sup> at 12 h UTC (left panel) and April 19<sup>th</sup> at 0 h UTC (right panel).

### 3.3.4 Applications of the OBP2-methodology

In this subsection, two applications of the OBP2 methodology are proposed. Starting from the separate retrieval of  $\beta_{ash}$  and  $\beta_{nash}$ , we provide a new methodology to retrieve the ash number concentration. This methodology is then further used to retrieve the ash mass concentration, which is compared with the ash mass computed with FLEXPART particle dispersion model.

### (a) Ash number concentration retrieval

In the literature to my knowledge, remote sensing have only been used to retrieve the ash mass concentrations (Schumann et al., 2011; Gasteiger et al., 2011; Hervo et al., 2012; Markowicz et al., 2012; Revuelta et al., 2012; Wiegner et al., 2012). Our here proposed methodology proposes to retrieved ash number concentration by discriminating  $N_{\text{ash}}$  from  $N_{\text{nash}}$ , which is new and has been published in Miffre et al. (2012b).  $N_{\text{ash}}$  is retrieved from the definition of the backscattering coefficient in Equation (2.12), namely:

$$N_p = \frac{\beta_p}{\left\langle \left( \frac{d\sigma}{d\Omega} \right)_p \right\rangle} \quad (3.10)$$

where  $\langle (d\sigma/d\Omega)_{\text{ash}} \rangle$  has been computed by averaging  $(d\sigma/d\Omega)_{\text{ash}}(r)$  over the ash-PSD.  $(d\sigma/d\Omega)_{\text{ash}}(r)$  is computed by using T-matrix numerical simulations presented in Section 2.4.3 using the parameters indicated in Table (2.1). The corresponding  $\langle (d\sigma/d\Omega)_{\text{ash}} \rangle$  averaged over Muñoz et al.'s ash-PSD (2004) is plotted as a function of the wavelength in Figure 2.8. Nonetheless, the choice of the ash-PSD may be questioned, as ash-PSD is changing during the explosive and ascending phases of the volcanic eruption, while complex physical and chemical processes are occurring, as pointed out by several authors (Delmelle, 2005; Schumann, 2011). During advection, the ash-PSD undergoes several modifications with possible scavenging, sedimentation and water adsorption on ash particles surface (Lathem, 2011). Because these processes are complex, a quantitative in-situ observation of the change in the volcanic ash PSD has never been reported in the literature from the source region down to the observation region. Hence ideally, the ash-PSD should be accurately known. However, in the absence of complementary measurements, the robustness of the retrieved  $\langle (d\sigma/d\Omega)_{\text{ash}} \rangle$  has been studied by using three different ash-PSD reported in the literature, which are plotted in Figure 3.13. Two PSD's are derived from the literature on the Eyjafjallajökull eruption, either close to the source region (Ilyinskaya, 2011) or after long-range transport (Schumann, 2011) and we also added Muñoz's ash PSD as a recognized reference for volcanic ash particles. Ilyinskaya et al. (2011) measurement has been performed a few kilometers outside of Island providing measurement close to the source and as a consequence most probably ash specific. Schumann et al. (2011) performed their measurement on volcanic cloud over Germany, providing long-range-transport measurement in the volcanic cloud.

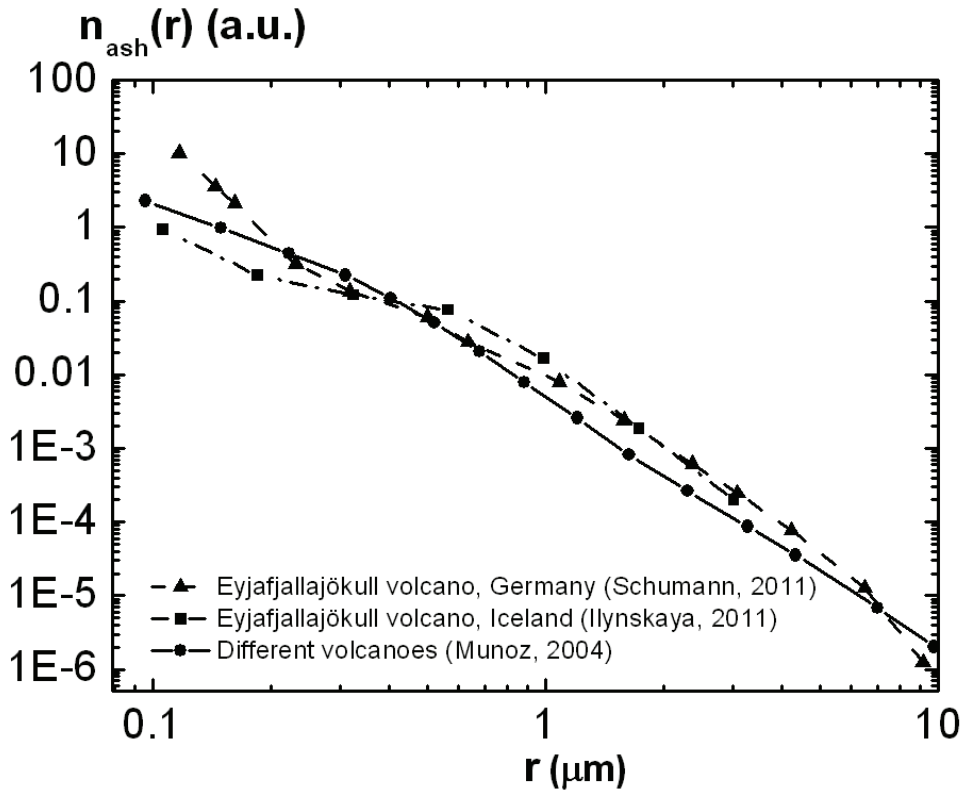


**Figure 3.13** Normalized volcanic ash number density  $n_{ash}$  as a function of  $r$  radius (in  $\mu\text{m}$ ) derived from (Muñoz et al., 2004, full line with circles); (Schumann et al., 2011, dashed lines with triangles); (Ilyinskaya et al., 2011, dashed dotted lines with squares). Muñoz’s ash particles PSD was derived from samples collected near the ground close to the volcano, mechanically sieved to remove the largest particles. Ilyinskaya’s PSD was derived at 15 km from the Eyjafjallajökull’s volcano. Schumann’s PSD was evaluated in the atmosphere above Leipzig (North-East of Germany) after long-range transport from the Eyjafjallajökull Icelandic volcano.

$\langle(d\sigma/d\Omega)_{ash}\rangle$  derived by averaging  $(d\sigma/d\Omega)_{ash}$  over the three corresponding PSD is summarized in Table 3.1.

**Table 3.1** Summarize of  $\langle(d\sigma/d\Omega)_{ash}\rangle$  computation by using the PSD presented in Muñoz et al. (2004), Ilyinskaya et al. (2011) and Schumann et al. (2011). The main features of the measured PSD are also indicated.

Reference	Volcano	Location	Characteristics	$\langle(d\sigma/d\Omega)_{ash}\rangle$ ( $10^{-10} \text{ cm}^2 \cdot \text{part}^{-1}$ )
Muñoz et al. (2004)	different volcanoes	laboratory	long-range transport ash specificity	1.59
Ilyinskaya et al. (2011)	Eyjafjallajökull	Iceland	short-range transport ash specificity	2.16
Schumann et al. (2011)	Eyjafjallajökull	over Germany	long-range transport absence of ash specificity	1.65

To compute the  $\langle(d\sigma/d\Omega)_{ash}\rangle$  used to retrieve  $N_{ash}$ , we chose Muñoz’s PSD to be both ash particles specific (instead of Schumann’s PSD) and representative of long-range transport

(instead of Ilynskaya's PSD). Nonetheless, the  $\langle(d\sigma/d\Omega)_{ash}\rangle$ -computation may be influenced by several effects, namely i) ash water uptake, ii) aging of ash particles and iii) ash particles sedimentation. We here analyze these three items:

i) Water up-take on ash particles should be considered in  $\langle(d\sigma/d\Omega)_{ash}\rangle$ -calculations. However, ash particles practically do not contribute to water-uptake, as first shown by P. Delmelle (2005) and as recently confirmed by C. Lathem (2011) for the specific case of the Eyjafjallajökull volcanic eruption. Quantitatively, it is found that for RH = 90 %, the hygroscopic growth for ash particles is between 2 and 5 % (ash particles are found to be 35 times less hygroscopic than sulfates). Hence, ash hygroscopic growth should be considered only for relative humidity approaching condensation levels, which does not occur under the considered clear-sky conditions in this case (see RH profiles in Figure 3.7).

ii) The effect of atmospheric aging on the ash PSD can be seen by comparing Ilynskaya's, and Schumann's PSD, under the assumption that Schumann's PSD is ash specific as Ilynskaya's PSD.

iii) The quantitative role of sedimentation processes has been intensively studied by Schumann et al. (2011) who discussed how the ash-PSD is modified by sedimentation processes during the Eyjafjallajökull eruption. For a given plume age, sedimentation processes act as a low-pass size filter for the ash-PSD so that *“the plumes of ages larger than 2 days should be free of particles for diameter larger than 15 mm due to sedimentation”*. The cut-off radius is determined by the square root of the fall distance (see Schumann et al.'s Eq. (3)). From this equation, we determined the modification of the ash-PSD and computed the corresponding  $\langle(d\sigma/d\Omega)_{ash}\rangle$  to include the sedimentation processes. Table 3.2 presents the retrieved cutoff radius on April 19th at 18h UTC close to the end of the volcanic episode. As cut-off radii are above 6  $\mu\text{m}$ , the corresponding size parameters are above  $x = 106$  for  $\lambda = 355 \text{ nm}$ . We could not compute such high  $x$ -values with T-matrix numerical simulations. Hence to simulate the effect of sedimentation on  $\langle(d\sigma/d\Omega)_{ash}\rangle$ , ash particles were assumed to behave like projected-surface-area-equivalent spheres and we computed  $\Delta\langle(d\sigma/d\Omega)_{ash}\rangle$  as follows:

$$\Delta\left\langle\left(\frac{d\sigma}{d\Omega}\right)_{ash}\right\rangle = \frac{\left\langle\left(\frac{d\sigma}{d\Omega}\right)_{ash} (cutoff\ radius)\right\rangle - \left\langle\left(\frac{d\sigma}{d\Omega}\right)_{ash}\right\rangle}{\left\langle\left(\frac{d\sigma}{d\Omega}\right)_{ash}\right\rangle} \quad (3.11)$$

Where  $\langle(d\sigma/d\Omega)_{ash} (cut-off\ radius)\rangle$  accounts for the cut-off radius in contrary to  $\langle(d\sigma/d\Omega)_{ash}\rangle$  which is computed over the entire ash-PSD. The computed  $\Delta\langle(d\sigma/d\Omega)_{ash}\rangle$  are

summarized in Table 3.2. As a conclusion, sedimentation processes induce less than 4% variations on the retrieved  $\langle(d\sigma/d\Omega)_{\text{ash}}\rangle$ , leading to the same relative uncertainty on  $N_{\text{ash}}$ . We here assume that the cut-off radius induced the same error on  $\langle(d\sigma/d\Omega)_{\text{ash}}\rangle$  computed with spheroids than on  $\langle(d\sigma/d\Omega)_{\text{ash}}\rangle$  computed with surface-area-equivalent spheres. Hence the 4% variations have been included in  $N_{\text{ash}}$  error bars.

**Table 3.2** Influence of sedimentation processes on the ash particle size distribution (cutoff radius) and corresponding  $\Delta\langle(d\sigma/d\Omega)_{\text{ash}}\rangle$  at different altitudes for two times up to the end of the volcanic episode. The cutoff radius has been calculated by assuming a 10-km plume top height (Schumann et al. 2011).

April 18 <sup>th</sup> 2010 at 12h UTC (3 days aged plume)			
Altitude Z asl (km)	3	4	5
Cutoff radius ( $\mu\text{m}$ )	8.2	7.6	7.0
$\Delta\langle(d\sigma/d\Omega)_{\text{ash}}\rangle$ (%)	-1.3	-1.9	-2.5
April 19 <sup>th</sup> 2010 at 18h UTC (4 days aged plume)			
Altitude Z asl (km)	1.7	3	5
Cutoff radius ( $\mu\text{m}$ )	7.7	7.1	6.0
$\Delta\langle(d\sigma/d\Omega)_{\text{ash}}\rangle$ (%)	-1.9	-2.4	-3.7

Figure 3.14 displays the  $N_{\text{ash}}$  vertical profile retrieved from  $\beta_{\text{ash}}$  and  $\langle(d\sigma/d\Omega)_{\text{ash}}\rangle = 1.59 \times 10^{-10} \text{ cm}^2 \cdot \text{part}^{-1}$  (Table 3.1) on April 19<sup>th</sup> at 00h UTC. This  $N_{\text{ash}}$ -retrieval methodology, because it is by construction ash-specific, reveals the dispersion behavior of the volcanic ash cloud. Quantitatively, on April 19<sup>th</sup> at 00h UTC, the ash number concentration reaches a few tens  $\text{part} \cdot \text{cm}^{-3}$ . Because in-situ measurements specific to volcanic ash particles do not exist in the literature, it is difficult to provide a correlative measurement. During the Eyjafjallajökull eruption, the measurements performed by Schumann et al. (2011) after long-range transport appear to be the most appropriate reference, since the air masses that they studied in the North East part of Germany passed over Lyon a few hours after, as confirmed by Figure 3.7 back-trajectories. Their measured number concentrations are in agreement within error bars with our  $N_{\text{ash}} = (17.7 \pm 5.4) \text{ part} \cdot \text{cm}^{-3}$  for particles in the 0.25 – 1  $\mu\text{m}$  size range. Hence, particles number concentration compare well when ash particles radii around 0.5  $\mu\text{m}$  are considered. This size represents the particles size at which our 355 nm-lidar measurements are among the most sensitive as confirmed by Figure 2.6. Comparison of our  $N_{\text{ash}}$  with particles counters (Schumann, 2011) should however be done with care as our new  $N_{\text{ash}}$ -retrieval methodology is volcanic ash particles specific in contrary to these optical particle counters. To become quantitative, further specific in-situ comparison measurements at the lidar location are needed.

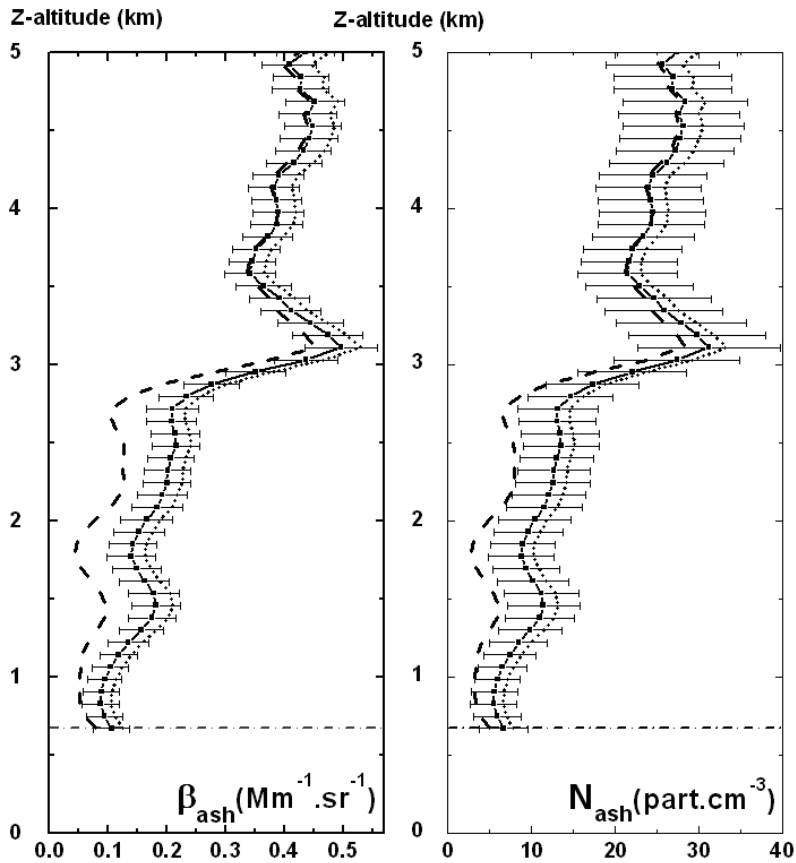


**Figure 3.14** Vertical profiles of  $\beta_{\text{ash}}$  and  $N_{\text{ash}}$  in the mixed {ash, sulfate} particle cloud on April 19h 2010 at 00h UTC at Lyon, for  $\delta_{\text{nash}} = 0$  and  $S_p = 55 \pm 5$  sr (full lines). Within our error bars, these profiles are slightly influenced by  $S_p$  (dotted lines, for  $S_p = 40$  sr) and by the sulfate depolarization  $\delta_{\text{nash}}$  (dashed lines, for  $\delta_{\text{nash}} = 1$  %) at altitudes where back-trajectories confirm the presence of volcanic ash particles.

At altitude  $z$ , the uncertainty on  $N_{\text{ash}}$  depends on the uncertainty on our lidar measurements, on the  $\langle (d\sigma/d\Omega)_{\text{ash}} \rangle$ -computation uncertainty and on the depolarization ratios  $\delta_{\text{ash}}$  and  $\delta_{\text{nash}}$ . Thanks to our sensitive and accurate polarization measurement, the error bar on  $N_{\text{ash}}$  slightly depends on the uncertainty on the  $\beta_{p,\perp}$ -lidar measurement. For the  $\langle (d\sigma/d\Omega)_{\text{ash}} \rangle$  uncertainty, use of Schumann's PSD instead of Muñoz's PSD would lead to a 3 % lower  $N_{\text{ash}}$ -value. The uncertainty on  $\delta_{\text{ash}}$  ( $\delta_{\text{ash}} = (40.5 \pm 2.0)$  %), leads to a 3.5 % relative error on  $N_{\text{ash}}$ , which is included in Figure 3.14. The effect of a possible bias and higher uncertainty in the  $\delta_{\text{ash}}$ -laboratory value can be evaluated by using Equation (2.32) and (2.23). The exact value of a possible bias is difficult to determine, but to fix the way the errors propagate, one can note that the relative error on  $N_{\text{ash}}$  grows to 6.7 % for  $\delta_{\text{ash}} = (50.0 \pm 5.0)$  %. Such a 10 %-bias appears to be high under our operating conditions (use of accurate Muñoz et al.'s laboratory scattering measurements). This however confirms that the proposed methodology can only be applied if accurate laboratory scattering matrix measurements are available.

In complement to this approach, numerical simulations using DDA instead of T-matrix might be interesting to develop for precise evaluation of  $\langle(d\sigma/d\Omega)_{\text{ash}}\rangle$ . However, the complexity resulting from the numerical simulation of randomly oriented vesicular and non-vesicular ash particles (Lindqvist, 2011) may lead to higher bias and uncertainties in the retrieved  $N_{\text{ash}}$ -number concentration. Finally, within our error bars, Figure 3.11  $N_{\text{ash}}$ -vertical profiles are slightly dependent on the exact  $\delta_{\text{nash}}$ -value at altitudes where the volcanic cloud is present. Hence, our new  $N_{\text{ash}}$ -retrieval methodology is volcanic ash particles specific and very robust: it is practically not affected by possible non-ash particles depolarization.

### (b) Ash mass concentration retrieval

Ash mass concentrations  $M_{\text{ash}}$  can be evaluated from  $N_{\text{ash}}$  by using the number-to-mass conversion factor  $C_{\text{NM}} = 1.88 \times 10^{-6} \mu\text{g}\cdot\text{part}^{-1}$ , deduced from the volcanic ash density assumed equal to  $2600 \text{ kg}\cdot\text{m}^{-3}$  (Gasteiger et al., 2011) and the mean particle volume  $\langle V_p \rangle$  of Munoz's PSD defined in Equation (3.12) with the volume particle concentration  $V_p$  which is integrated over the PSD (Equation (1.3)):

$$\langle V_p \rangle = V_p / N_p \quad (3.12)$$

Vertical profiles of  $M_{\text{ash}}$  are displayed in Figure 3.15. All retrieved mass concentrations are well below the limit value of  $2\,000 \mu\text{g}\cdot\text{m}^{-3}$  chosen for airport closures. In the PBL, the low ash concentration is comparable with  $10$  to  $50 \mu\text{g}\cdot\text{m}^{-3}$  PM10 concentration measured at ground level in urban polluted areas (Miffre et al., 2010). The highest  $M_{\text{ash}}$ -value,  $(346 \pm 87) \mu\text{g}\cdot\text{m}^{-3}$ , is observed on April 17<sup>th</sup> at 12h (figure 7a) in the volcanic layer around 4.5 km altitude ( $M_{\text{ash}}$ -values are not evaluated under 4 km as air masses do not originate from the volcano), in excellent agreement with FLEXPART ash simulation. In Figure 3.15 profiles (b) and (c) exhibit lower  $M_{\text{ash}}$ -values for the new ash intrusions, and when particles mix into the low troposphere,  $M_{\text{ash}}$ -values are even lower, in agreement with FLEXPART. The observed discrepancy above 3 km between FLEXPART and Lidar ash mass concentrations may be due to the air masses hanging around in Europe moving back and forth as suggested by Figure 3.7 back-trajectories; rain further complicates the situation.

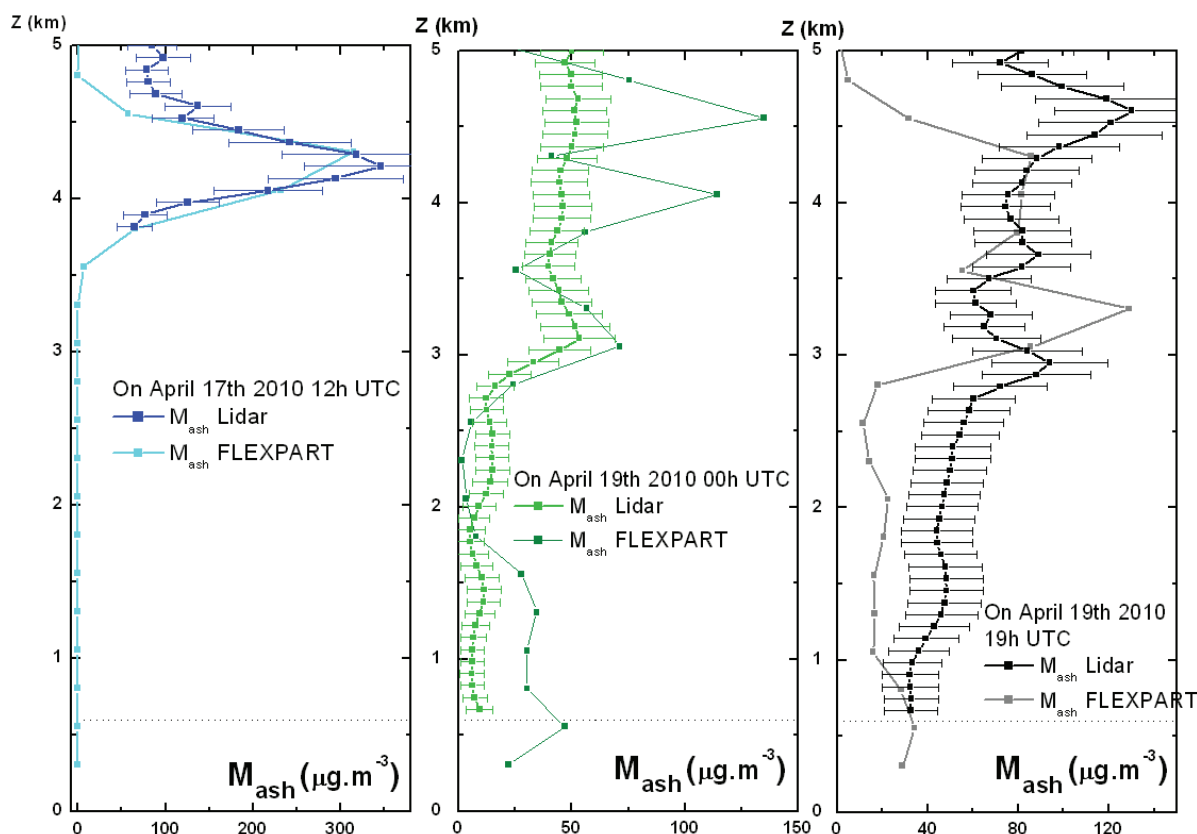


**Figure 3.15** Vertical profiles of volcanic ash mass concentration on April 17th at 12 h UTC (left panel), on April 19th at 0 h UTC (middle panel) and on April 19th at 19h UTC (right panel). FLEXPART ash mass concentrations vertical profiles are added for quantitative comparison.

### 3.3.5 Ash case study summary

As a summary on the *Ash case study*, the OBP2-methodology has been successfully applied to the mixing of nonspherical volcanic ash particles with spherical sulfates, as observed at Lyon during the mid-April 2010 Eyjafjallajökull eruption. Starting from the lidar measured  $\beta_{p//}$ ,  $\beta_{p\perp}$ , and  $\delta_p$ -coefficients derived from our sensitive and accurate UV-polarization measurements, we discriminated nonspherical volcanic ash particles from non-ash particles in the volcanic cloud mixture to retrieve the volcanic ash backscattering coefficient  $\beta_{ash}$ . The accuracy of the OBP2-methodology depends on the accuracy of the UV-polarization measurements. In agreement with Section 2.3, the measured  $\delta_p$  has been found to differ from  $\delta_{ash}$ , as non-ash particles are present in the volcanic cloud after long-range transport. The robustness of the  $\beta_{ash}$ -retrieval has been studied by changing the  $S_p$  and the  $\delta_{nash}$ -value, while the uncertainty in  $\delta_{ash}$  is already included in the error bars. The influence of both  $S_p$  and  $\delta_{nash}$  is negligible within our error bars within the volcanic ash layers. Hence, the achieved  $\beta_{ash}$  and  $\beta_{nash}$  detection limits are below  $0.049 \times 10^{-8} \text{ m}^{-1} \cdot \text{sr}^{-1}$  and  $0.129 \times 10^{-8} \text{ m}^{-1} \cdot \text{sr}^{-1}$ . In addition, the

retrieved  $\beta_{\text{nash}}$  follows the RH vertical profile due to the nash particles hygroscopic growth. Hence, polarization optics, when used in the context of the OPB2 methodology has the ability to enhance physic-chemical processes such as nash hygroscopicity which can then be studied by using optics, through sensitive, non destructive and accurate measurements. Finally, two applications of the OPB2 methodology have been proposed, which further reinforces its novelty and usefulness. First, by using  $\beta_{\text{ash}}$ , the vertical profile of ash number concentration  $N_{\text{ash}}$  in the troposphere is retrieved, by combining the polarization lidar experiment with a T-matrix numerical simulation of the ash particles mean backscattering cross-section  $\langle(d\sigma/d\Omega)_{\text{ash}}\rangle$ . The  $N_{\text{ash}}$ -retrieval is robust, as almost insensitive to sedimentation effects, as well as change in the chosen ash-PSD or to water uptake. Finally, ash mass concentrations have been retrieved in good agreement with FLEXPART ash particles numerical dispersion model.

### **3.4 The Dust case study: Desert dust mixed with non-dust particles**

In this section, *the Dust case study* is analyzed by applying the OBP2-methodology, following the same methodology as for the *Ash case study*. As underlined by Engelstaedter et al. (2006), the dust-climate processes due to dust transport mechanisms affect adjacent continental and ocean regions. In addition, during desert dust episodes, non-dust particles, such as water soluble particles (Wang et al., 2005) or sea salt (Zhang et al., 2008), are often mixed with dust particles. In this section, the mixing of desert dust with non-dust (ndust) particles during a Saharan dust outbreak that occurred on July 2010 is studied. The  $\beta_{\text{dust}}$  and  $\beta_{\text{ndust}}$ -coefficients are retrieved from their mixing by applying the OBP2-methodology and are further used to interpret the atmospheric particle content. The main novelty of this section is the observation of new particle formation (NPF) event in the atmosphere by using a UV polarization lidar, as published in PNAS (Dupart et al., 2012), in collaboration with C. George's and H. Herrmann's chemical groups. From the OBP2-methodology, the potential observation of new particle formation with a polarization lidar is discussed by performing a numerical simulation, based on Dupart et al.'s measurements (2012). It is shown that, indeed, an NPF event can be observed with a polarization lidar, provided that the polarization lidar instrument (see Section 3.2) reaches a sensitivity and an accuracy similar to ours.

### 3.4.1 Dust and ndust backscattering retrieval

During the July 9<sup>th</sup> 2010 dust episode, ns-particles were attributed to highly-irregularly shaped dust particles, as confirmed by Figure 3.16, where 7-days FLEXTRA back-trajectories provide the Saharan dust origin of the observed air masses, for altitudes between 3 and 6 km asl. After long-range transport by advection, coarse particles were removed from the dust cloud by gravitational settling and the particle cloud was composed of both dust and non-dust (ndust) particles with humidity conditions detailed in Figure 3.16. Ndust particles are likely to be small-sized ammonium sulfates and aged carbonaceous particles (Kaaden et al., 2009). Hence  $\delta_{\text{ndust}} = 0\%$  is assumed.

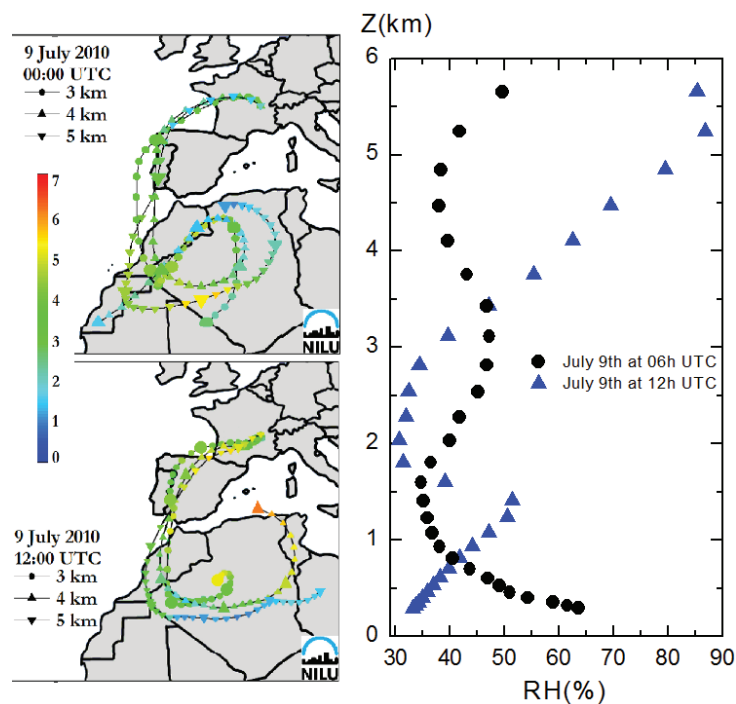


**Figure 3.16** NILU FLEXTRA 7-days air mass back-trajectories and relative humidity RH on July 9<sup>th</sup>.

Figure 3.17 displays the time-altitude maps of  $\beta_{p,\parallel}$ ,  $\beta_{p,\perp}$  and  $\delta_p$  measured above Lyon on July 09<sup>th</sup> 2010 in the UV spectral range together with the  $\beta_{\text{dust}}$ ,  $\beta_{\text{ndust}}$  and  $X_{\text{dust}}$  ( $X_{\text{dust}} = \beta_{\text{dust}} / \beta_p$ ) mapping obtained by applying the OBP2-methodology. Hence, for the first time to my knowledge, UV time-altitude maps of  $\beta_{\text{dust}}$  and  $\beta_{\text{ndust}}$  are plotted, which allow to address the spatio-temporal distribution of these particle components. Moreover from  $\beta_{\text{dust}}$ , the dust number concentration  $N_{\text{dust}}$  can also be computed by using the methodology described in Section 3.3.4 as for volcanic ash particles. Further information on  $N_{\text{dust}}$  can be found in (Miffre et al., 2011), where the retrieved dust particles number concentrations compare with the reference literature (Klein et al., 2010). Here, the OBP2-methodology has been applied to

the  $\beta_{p,\parallel}$  and  $\beta_{p,\perp}$  maps with the following input parameters:  $\delta_{\text{ndust}} = 0 \%$  and  $\delta_{\text{dust}} = 21 \%$ , in agreement with our T-matrix numerical simulation presented in Table 2.2, which agree with (Veselovski et al. 2010). The highest value of  $\delta_{\text{dust}} = 21 \%$  is used to account for the polarization properties of light backscattered by dust particles, by using the  $n = 3$  shape distribution (Merikallio et al., 2011). For retrieving the  $\beta_{p,\parallel}$ ,  $\beta_{p,\perp}$  and  $\delta_p$  maps, a lidar ratio  $S_p = (68 \pm 5) \text{ sr}$  has been used, derived from Table 2.2 in agreement with the literature (Veselovski et al. 2010; Tesche et al., 2011).

Between 2 and 6 km asl, a high  $\beta_{p,\parallel}$  and  $\beta_{p,\perp}$ -values layer is observed. According to the back-trajectories (Figure 3.16), this layer can be attributed to dust particles. On the  $\beta_{p,\parallel}$  time altitude map, a particle layer between 2 and 3 km is observed from 2 h 30 to 6 h 00, which can be attributed to spherical particles since this layer is not observed on the  $\beta_{p,\perp}$ -map. This observation justifies the assumption of  $\delta_{\text{ndust}} = 0 \%$ . The  $\delta_p$  and  $X_{\text{dust}}$ -maps are remarkably similar, as observed in the volcanic ash and sulfates mixture, in agreement with Equation (2.27). The highest  $\beta_{\text{ndust}}$ -values and consequently the highest ndust particles concentration are mainly observed in the PBL. The particles layer between 2 and 3 km from 2 h 30 to 6 h 00 is only composed of ndust particles, since it is observed on  $\beta_{p,\parallel}$ , on  $\beta_{\text{ndust}}$  but not on the  $\beta_{\text{dust}}$ . Meanwhile, the particles layer between 3 and 6 km is mostly composed of dust particles, as suggested by the back-trajectories. N dust particles are mainly located at the border of the dust layer, as can also be seen at 5 km at 1h UTC. Around 12 h, a high particle depolarization ratio is observed. Combined with a high RH-value of 85 %, it may lead to the formation of ice crystals. This hypothesis however needs to be further discussed and analyzed. To further interpret the observed time-altitude maps, we analyzed the state-of-the art literature on laboratory experiments performed on mineral dust particles. In particular, an alternate pathway of NPF (Figure 1.10), occurring in low dust particle concentration, has been recently identified (Dupart et al., 2012): a high dust concentration reduces such NPF, as dust particle act as a condensational sink. Here, our ndust particles are observed at the border of the dust layer which means that their concentration is low so that ndust particles may have been induced by such an NPF-event. It is the subject of the next paragraph to analyze this hypothesis in detail. We first describe this new particle formation process.

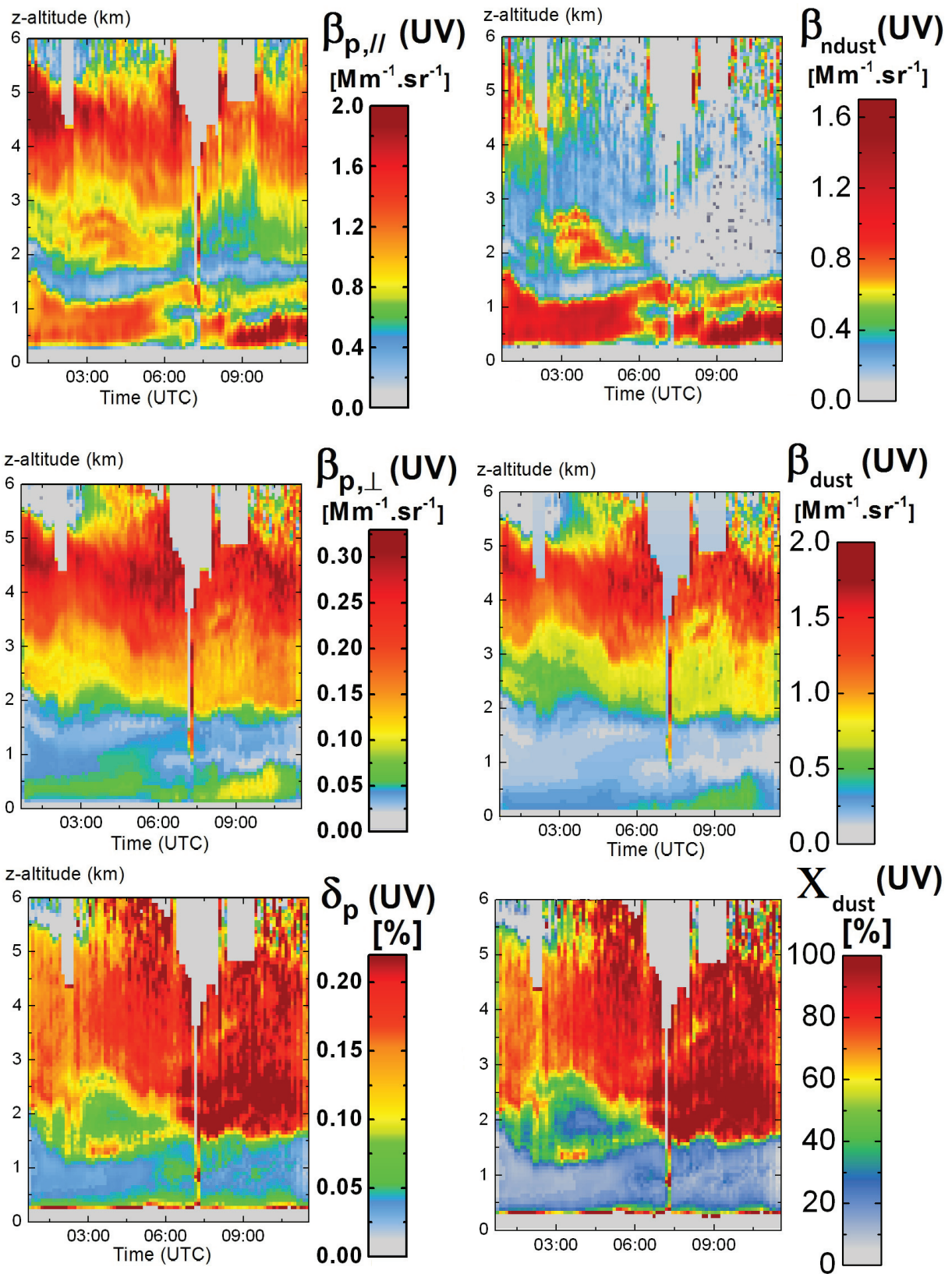


**Figure 3.17** Time-altitude maps of  $\beta_{p,\parallel}$ ,  $\beta_{p,\perp}$ ,  $\delta_p$ ,  $\beta_{\text{ndust}}$  and  $\beta_{\text{dust}}$  in the UV on July 09<sup>th</sup> 2010 at Lyon obtained by applying the OBP2-methodology. The grey bands above 4000 meters correspond to clouds which prevented retrieving  $\beta_{p,\parallel}$ ,  $\beta_{p,\perp}$ ,  $\delta_p$ ,  $\beta_{\text{ndust}}$ ,  $\beta_{\text{dust}}$  and  $X_{\text{dust}}$ .

### 3.4.2 New particle formation (NPF) process

NPF is basically related to the gaseous  $\text{H}_2\text{SO}_4$  in the atmosphere whereby molecular sulfuric acid formation processes are still under debate. Laboratory experiments in cloud chambers could settle the fundamental nucleation processes involving ions and neutral clusters (Kirkby et al., 2011). Moreover, field experiments showed that NPF can be observed everywhere in the atmosphere (Kulmala et al., 2012; Kyrö et al., 2013), such as in the PBL (Wehner et al., 2010; Dupart et al., 2012) or in the free troposphere (Hamburger et al. 2010; Boulon et al., 2011). Moreover, NPF can also be initiated in the presence of volcanic materials (Boulon et al., 2011) and very recently in the presence of mineral dust particles (Dupart et al. 2012). Into more details, recent laboratory findings, achieved on heterogeneous photochemistry (Dupart et al. 2012), have identified a new chemical pathway in which mineral dust photochemistry induces nucleation events in the presence of  $\text{SO}_2$ . This new mechanism has been detailed in Figure 1.10, which means that mineral dust containing Iron Oxide offers a new pathway to explain the appearance of an NPF event of sulfuric acid ( $\text{H}_2\text{SO}_4$ ) promoted in the gas phase.

As an introduction to this important part of the thesis, a brief presentation of the laboratory experimental results obtained by Dupart et al. (2012) is proposed to highlight the main features of such an NPF-event occurring in the presence of mineral dust particles. Figure 3.18 and Figure 3.19 summarized the experimental results obtained by Dupart et al. (2012). In a few words, an aerosol flow tube was equipped with lamps to provide continuous UV-irradiation (from 300 to 420 nm-wavelengths) and the injected dust particles had variable residence times. As shown in Figure 3.18 and Figure 3.19, the interaction of  $\text{SO}_2$  with dust particles and water vapor under UV-light systematically resulted in NPF. These dust-induced nucleation events were clearly observed only in the presence of water vapor, gaseous  $\text{SO}_2$ , and UV irradiation. The absence of any one of these parameters inhibited nucleation. The nucleated particles number concentration increased with increasing the UV-photon flux (Figure 3.18) and a similar trend was observed with increasing the relative humidity (RH) then the  $\text{SO}_2$ -concentration. On the other hand, the particle number concentration decreased with increasing the injected dust particles number concentration and with increasing the dust residence time (Figure 3.19), which is consistent with a growing condensational sink. Hence, the three main features of NPF retrieved from this laboratory experiments are:

(a) The formed particle number concentration increases when increasing the UV-irradiance.

- (b) Mineral dust particles in the presence of water vapor, gaseous  $\text{SO}_2$ , and UV-irradiation are necessary to obtain NPF.
- (c) The formed particle number concentration decrease when increasing the dust particle concentration and the residence time of dust particle in the NPF location.

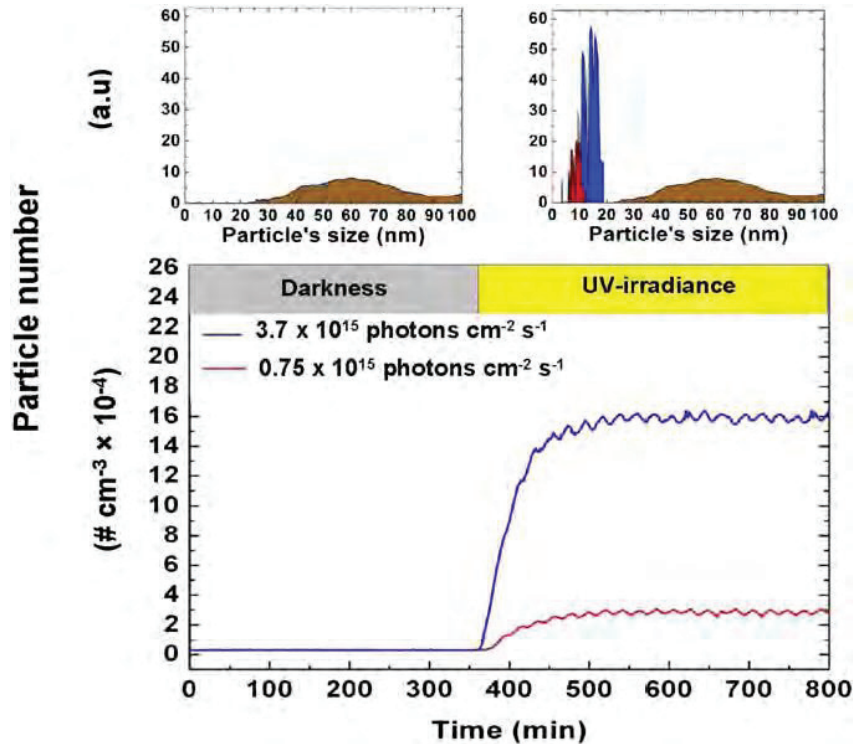


**Figure 3.18** Data from Dupart et al. (2012). Evolution of the particle number and size distribution in the aerosol flow tube during the laboratory experiment with ATD (UV irradiance at 300 ppbv of  $\text{SO}_2$  and  $3,000 \text{ cm}^{-3}$  of Arizona Test Dust particles (ATD) injected). Under UV-illumination (red and blue lines correspond to two different photon fluxes), particle-number concentration increases strongly, together with the appearance of small particles ( $<20 \text{ nm}$ ).

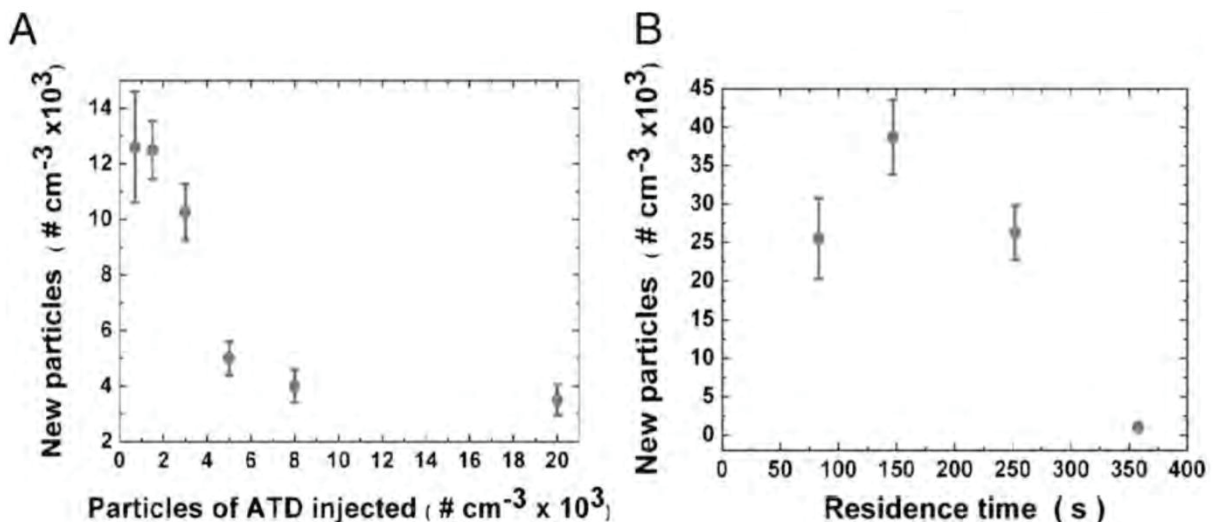


**Figure 3.19** Data from Dupart et al. (2012). Dependence of the number concentration of new particles on ATD-dust particles particle-number concentration injected into the aerosol flow tube (A) and residence time in the aerosol flow tube (B). These experiments are performed with an UV-irradiance of  $2.2 \times 10^{15}$  photons per square centimeter per second, a  $\text{SO}_2$  concentration of 170 ppbv, an RH of 50%, a residence time of 110 s, and ATD number seed-particle concentration of  $3,000 \text{ cm}^{-3}$  (except when varied systematically)

### 3.4.3 Numerical simulation of expected lidar backscattering coefficient in an new particle formation event

The observation of a new particle formation and growth event (NPF) is usually achieved by measuring the time evolution of the PSD, to retrieve the so-called “banana plots” (Kulmala et al., 2012). Such a PSD is usually measured with a differential mobility particle sizer, a particle size magnifier, a neutral cluster and air ion spectrometer, a diethylene glycol-scanning mobility particle sizer, an air ion spectrometer, a balanced scanning mobility analyzer and condensation particle counter (Kulmala et al., 2012). Such apparatuses allow performing an accurate PSD-measurement, but cannot be used to remotely detect NPF as these are not range-resolved. Use of a lidar to detect NPF would hence lead to new observation possibilities, which raises the following issue: whether or not NPF can be observed with a lidar, and especially with our lidar. We have performed numerical simulations to compute the  $\beta_p$ -coefficient corresponding to the NPF observed in the atmosphere. These numerical simulations are used to identify the  $\beta_p$ -features corresponding to NPF. In the literature, it is generally considered that ultrafine particles cannot be observed with optical scattering based on a Lidar. Let us recall that  $\beta_p$  is obtained by integrating  $n_p(r) \times (d\sigma/d\Omega)_p(r)$  over radius  $r$  as shown by Equation (2.12). Hence, ultrafine particles, despite their very low sizes, may strongly contribute to optical scattering when they are numerous, as implied by atmospheric molecular scattering responsible for the blue color of the sky.

In the absence of complementary number density  $n_p(r)$  measurements, to compute  $\beta_p$ , the PSD has been taken from the literature. Figure 3.20-a shows the PSD time evolution during a NPF that occurred in China during an intensive field campaign: strong nucleation events initiated on mornings following strong dust events, while dust particle concentrations are still present (Dupart et al, 2012). NPF was marked by the appearance of the so-called “banana shaped plots” in the measurement as can be seen from 08 h 00 to 20 h 00 in Figure 3.20-a2, which is due to the induced enhancement of particles number concentration in the ultrafine mode and the particle size increase in the fine mode (Boulon et al, 2011; Dupart et al., 2012). Moreover, in the literature (Ansmann et al., 2012; Dupart et al., 2012), for particles radii  $r$  below  $0.5 \mu\text{m}$ , dust particles practically do not contribute to the PSD, while for particles radii  $r$  above  $0.5 \mu\text{m}$ , dust particles are often assumed to be the main contributor to the PSD (Ansmann et al., 2012; Dupart et al., 2012). Hence  $n_p(r,t)$  derived from the PSD's in Figure

3.20-a2 can be considered as  $n_{\text{dust}}$ -specific and hereafter noted  $n_{\text{dust}}(r,t)$  while the particle number density  $n_{\text{dust}}(r,t)$  retrieved from the PSD in Figure 3.20-a1 is assumed to correspond to dust particles.

Equation (2.12) is used to operate the numerical simulation whose outputs  $\beta_{\text{dust}}$  and  $\beta_{\text{ndust}}$  are given in Figure 3.20-b. The newly formed particles are assumed to be  $\text{H}_2\text{SO}_4$ , as usually done for NPF-events (Kulmala et al, 2012). Consequently the Mie theory, suited for spherical particles, has been used to compute the  $(d\sigma/d\Omega)_{\text{ndust}}(r,\lambda)$  with the  $\lambda$ -dependent refractive index  $m$  measured by Hummel et al. (1988) for  $\text{H}_2\text{SO}_4$ . Palmer and Williams (1975) also reported similar results for  $m\text{-H}_2\text{SO}_4$  values as a function of  $\lambda$ ; we however used Hummel et al.'s reference which extends down to 200 nm. As a first output, we plotted the time evolution of  $\beta_{\text{ndust}}(t)$  in Figure 3.20-b at  $\lambda = 355$  (UV, blue curve), 532 (VIS, green curve) and 1064 nm (IR, red curve) wavelengths, corresponding to three spectral ranges currently used in lidar experiments (Alvarez et al., 2006; Sugimoto et al, 2006; Freudenthaler et al., 2009; Veselovskii et al, 2010; David et al, 2012). For the dust particles,  $\beta_{\text{dust}}(t)$  has been computed in the UV spectral range from Equation (2.12) by using the  $n_{\text{dust}}(r,t)$ -PSD and the  $(d\sigma/d\Omega)_{\text{dust}}$  retrieved in Section 2.4.3 with a  $n = 3$  shape distribution of spheroids.

As can be seen in Figure 3.20-b,  $\beta_{\text{ndust}}(t)$  increases from 9h to 12h and from 18h and 19h when particle size grows due to the NPF for the three spectral ranges. These  $\beta_{\text{ndust}}(t)$  increase is stronger in the UV ( $+0.76 \text{ Mm}^{-1}.\text{sr}^{-1}$  between 09 and 12h and  $+3.1 \text{ Mm}^{-1}.\text{sr}^{-1}$  between 18 and 19h30), than in the VIS (resp.  $+0.33 \text{ Mm}^{-1}.\text{sr}^{-1}$  and  $+1.3 \text{ Mm}^{-1}.\text{sr}^{-1}$ ) and in the IR (resp.  $+0.11 \text{ Mm}^{-1}.\text{sr}^{-1}$  and  $+0.46 \text{ Mm}^{-1}.\text{sr}^{-1}$ ) spectral ranges. This is not surprising since as underlined by Mishchenko and Sassen (1998), UV is more sensitive to ultrafine and fine particles. Hence, to observe the  $\beta_{\text{NPF}}(t)$  enhancement, a lower detection limit is necessary in the UV spectral range than in the VIS and IR. By following the procedure to be discussed in Section 3.3, we retrieve a below  $0.22 \text{ Mm}^{-1}.\text{sr}^{-1}$  detection limit for the  $n_{\text{dust}}$ -particles backscattering coefficient. It follows that the two observed simulated  $\beta_{\text{ndust}}$  increase (between 9h to 12h then between 18h and 19h) are detectable with our UV-polarization lidar set-up, which means that, indeed, NPF event can be observed with our UV-polarization lidar.

In addition, Figure 3.20-b also displays the time evolution of  $\beta_{\text{dust}}$ , which is important since dust particles act as a condensation sink (Dupart et al., 2012; Kulmala et al., 2012; Wehner et al, 2010). As shown in Figure 3.20-b, the simulated  $\beta_{\text{ndust}}$  increase observed between 09 to

12h then 18 to 19h occurred after a  $\beta_{\text{dust}}$ -decrease (and the  $\beta_{\text{ndust}}$  decrease starts after  $\beta_{\text{dust}}$  increased strongly by more than 70 %, between 11 and 12h). Moreover, a striking feature is the negative correlation observed between  $\beta_{\text{ndust}}(t)$  and  $\beta_{\text{dust}}(t)$ . By negative correlation, we intend that when  $\beta_{\text{ndust}}$  decreases from 12 to 18h (-33 % in the three spectral range),  $\beta_{\text{dust}}$  increases (+19 %) during the same time.

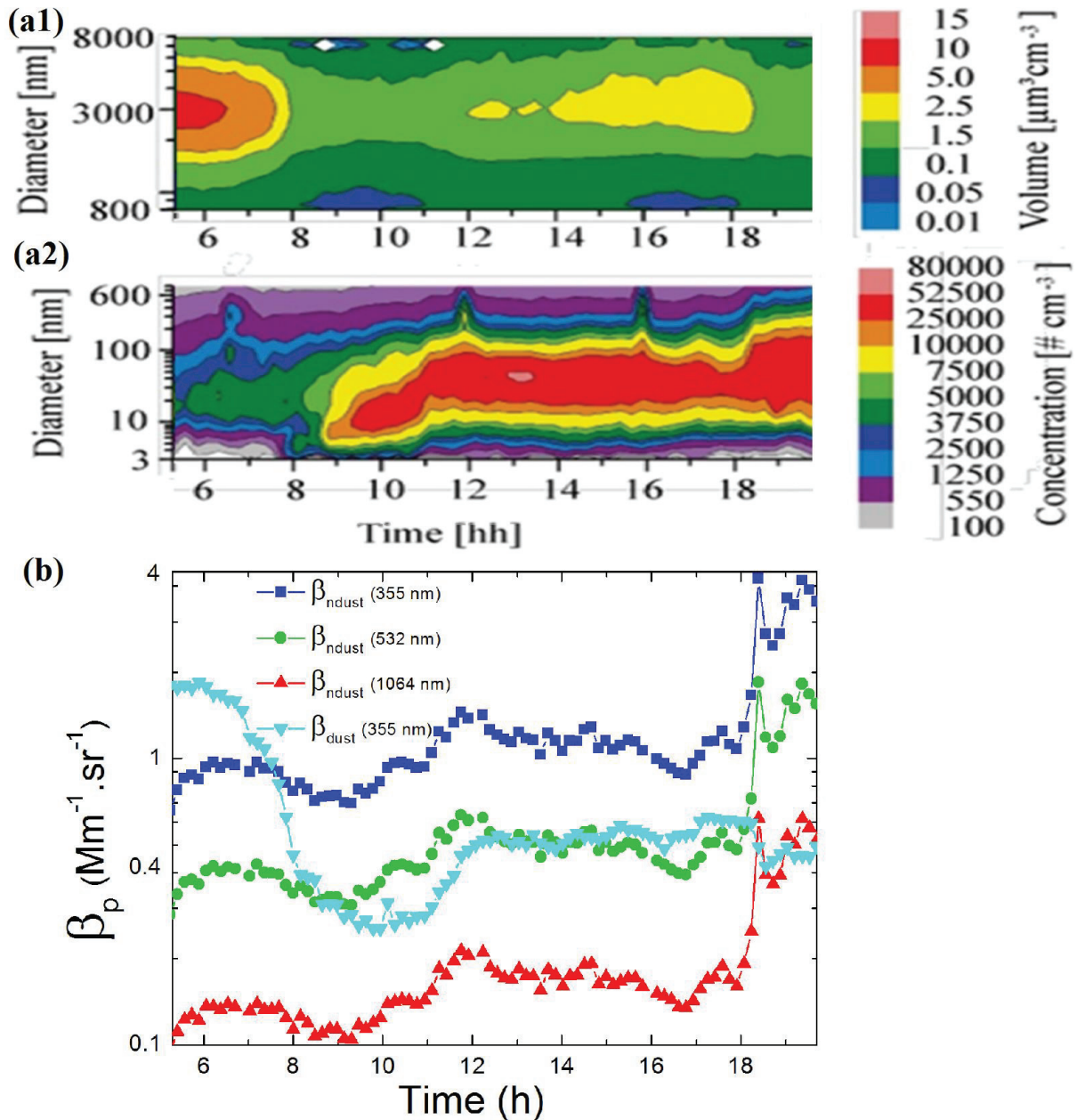


**Figure 3.20** Panel (a) displays ground-based in situ measurements conducted at the Wuqing meteorological station, China (39°23'9"N, 117°1'26"E), on March 13<sup>th</sup> 2009 during a NPF event. Panel (a1) shows particle-volume distribution in the size range between 0.8–8 μm, indicating the presence of coarse particles; and panel (a2) shows particle-number concentrations for particle diameters between 3 and 800 nm as a function of local time of day (x axis) and the particle diameter (y axis). Panel (b) displays the time evolution of simulated backscattering coefficient  $\beta_{\text{ndust}}$  and  $\beta_{\text{dust}}$ , corresponding respectively to the PSD displays in panel (a1) and (a2) for ultrafine-fine particles and coarse particles.

Before the occurrence of the NPF-event, no negative correlation is visible: both  $\beta_{\text{ndust}}(t)$  and  $\beta_{\text{dust}}(t)$  reach a maximum around 06h before decreasing around 07h30. As a conclusion, for a dust NPF-event to be observed with a lidar, the following features are to be pointed out:

- i) A  $\beta_{\text{ndust}}$ -enhancement due to the NPF is observable provided that our lidar is polarization-resolved so that the detection limit be sufficiently low, once the optical partition has been performed to efficiently separate dust from ndust-particles
- ii) UV should be preferably used to observe NPF as this enhancement  $\beta_{\text{ndust}}$  is more than two times stronger in the UV than in the VIS (more than six times stronger in the UV than in the IR)

The occurrence of the NPF-event is identified by the negative correlation between  $\beta_{\text{ndust}}$  and  $\beta_{\text{dust}}$  during the NPF event: while no negative-correlation is observed before.

Let us now discuss on the contribution to  $\beta_{\text{ndust}}$  of each particle size. Ultrafine particles are very numerous but their cross-sections are small while fine particles have a smallest number concentration but have higher backscattering cross-sections. Hence, the good optical observable is the integrand of  $\beta_{\text{ndust}}$ , namely  $n_{\text{ndust}}(r, t = t_0) \times (d\sigma/d\Omega)_{\text{ndust}}(r, \lambda)$ , at a fixed time  $t_0$ . Figure 3.21 plots  $n_{\text{ndust}}(r, t_0) \times (d\sigma/d\Omega)_{\text{ndust}}(r, \lambda)$  as a function of  $\lambda$  and  $r$  (panel (a)) together with its PSD-integrated value  $\beta_{\text{ndust}}(\lambda, t_0)$  (panel (b)), where the PSD  $n_{\text{ndust}}(r, t_0)$  is retrieved from the PSD measured in Figure 3.20-a2. Hence the plotted  $n_{\text{ndust}}(r, t_0) \times (d\sigma/d\Omega)_{\text{ndust}}(r, \lambda)$  indicates for a given particle size its contribution to  $\beta_{\text{ndust}}(\lambda, t_0)$ . In the UV-spectral range, a high  $n_{\text{ndust}}(r, t_0) \times (d\sigma/d\Omega)_{\text{ndust}}(r, \lambda)$  value is observed for almost all particles between 25 nm to 400 nm which hence contribute to  $\beta_{\text{ndust}}$ . In the IR spectral range, only particles around 170 nm contribute to  $\beta_{\text{ndust}}(\lambda, t_0)$ . As shown in Figure 3.21-a, the particles minimal radius  $r_{\text{min}}$  significantly contributing to  $\beta_{\text{ndust}}$  increases with increasing  $\lambda$ : it is around 20 nm at  $\lambda = 240$  nm and reaches around 150 nm at  $\lambda = 1200$  nm. An NPF-event begins by nucleation of clusters with a few nanometers radius or even smaller (Kulmala et al., 2012). Clearly, such small particles cannot be detected with a polarization Lidar, at least in the UV. Nonetheless, when  $r$  is a few tens of nanometers large, particles more significantly contribute to the backscattered light if UV spectral range is used. We hence explain the several petals shape observed in Figure 3.21-a, which is mainly due to the  $(d\sigma/d\Omega)_{\text{ndust}}(r, \lambda)$  behavior, which is not monotonously increasing with increasing the particle radius  $r$ .

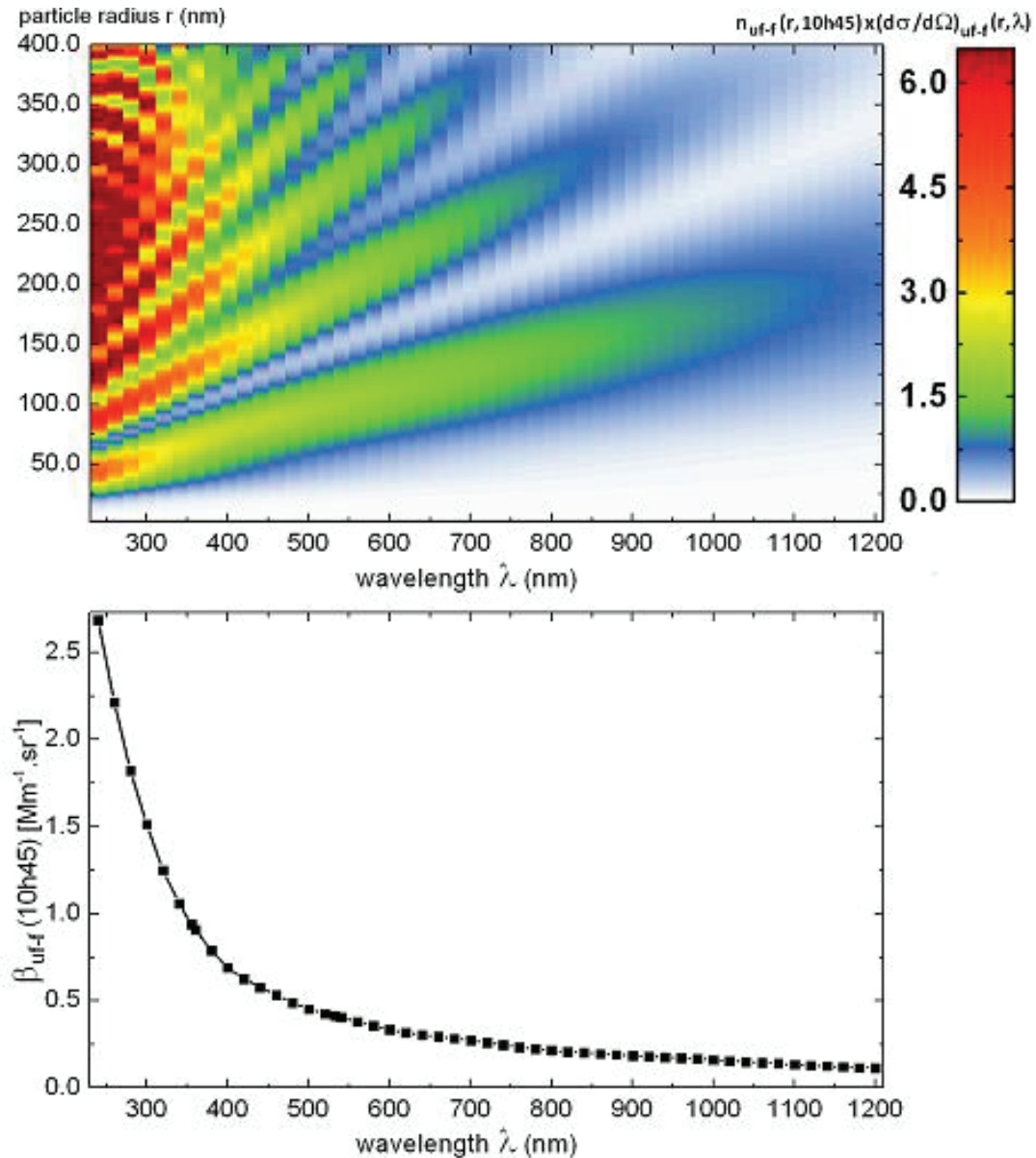
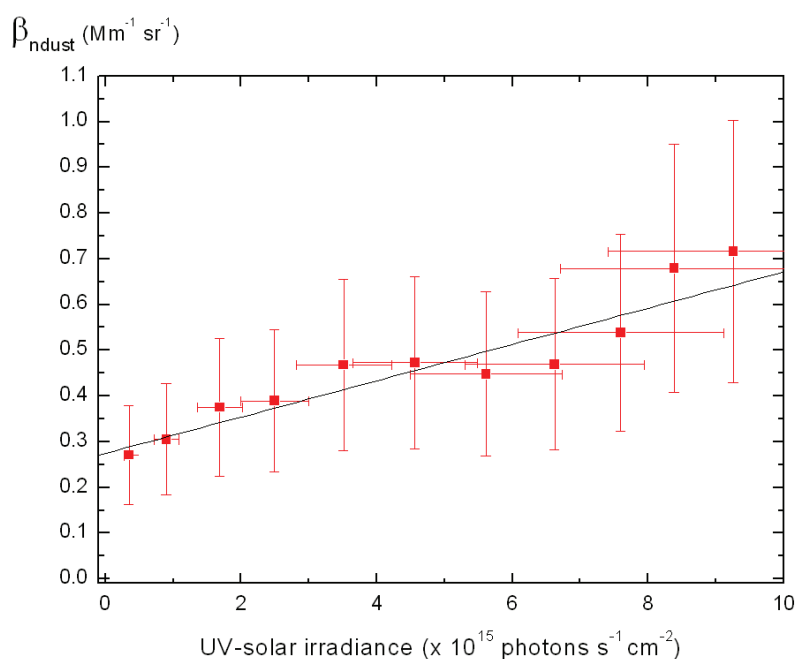


**Figure 3.21** Backscattering cross section multiplied by the particle number density  $n_{\text{ndust}}(r, t_0 = 10\text{h}45) \times (d\sigma/d\Omega)_{\text{ndust}}(r, \lambda)$  as function of the optical wavelength and particle radius (panel (a)).  $n_{\text{ndust}}(r, t_0 = 10\text{h}45)$  is retrieved from the 10h45 PSD in Figure 3.20-a2.  $\beta_{\text{ndust}}(\lambda)$  is deduced from panel (a) by integrated  $n_{\text{ndust}}(r, t_0 = 10\text{h}45) \times (d\sigma/d\Omega)_{\text{ndust}}(r, \lambda)$  over the particle radius  $r$  (panel(b)).  $t_0 = 10\text{ h}45$  is the chosen time, to be representative of the NPF-event which extends from about 9h to 12h.

### 3.4.4 Observation of new particle formation with UV polarization Lidar

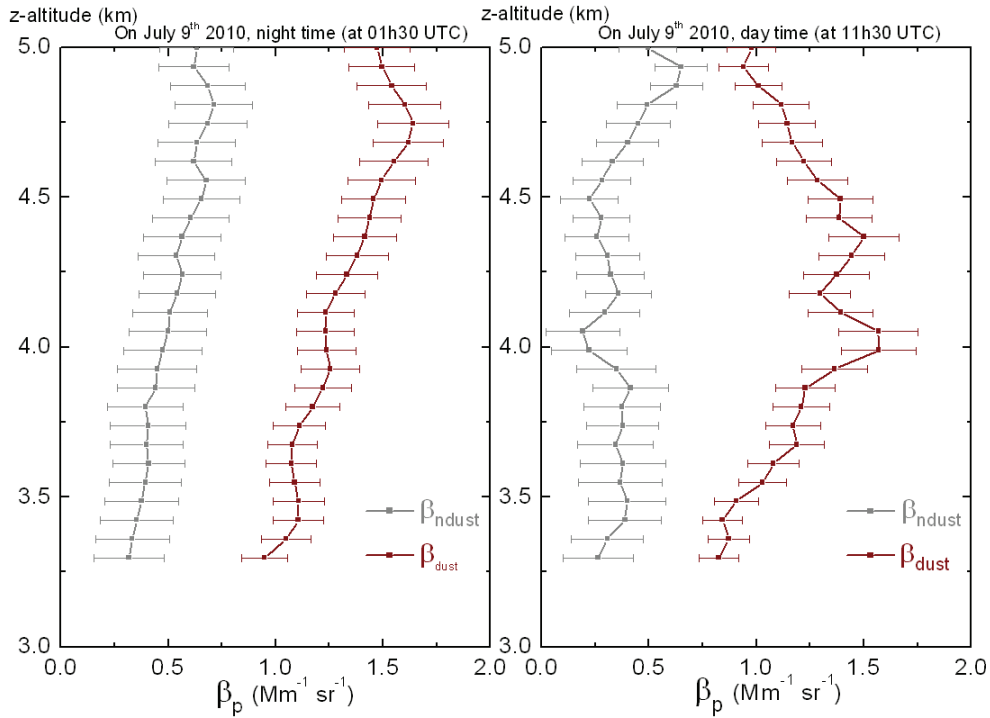
In this section, the identified NPF-event features are used to interpret the lidar measurement presented in Section 3.5.1 to determine whether or not NPF can be observed with our UV-polarization Lidar. Each NPF-feature identified in the Dupart's et al.'s laboratory measurement (see Section 3.4.2) or numerical simulations (see Section 3.4.3) is compared with the measured  $\beta_{\text{dust}}$  and  $\beta_{\text{ndust}}$ , as presented in Figure 3.17.

Figure 3.22 plots the lidar-retrieved  $\beta_{\text{ndust}}$ -coefficient at 2.8 km altitude, on July 9, 2010 during sunrise as a function of the solar UV-irradiance. The  $\beta_{\text{ndust}}$ -values have been retrieved from the Figure 3.17 time altitude map at a 2.8 km altitude between 2h30 and 3h40 UTC. The solar UV-irradiance has been computed in the spectral range that provoked NPF in the laboratory experiment (300 to 420 nm). The UV-irradiance (in photons per second per square centimeter) illuminating the dust particles at a 2.8 km altitude has been evaluated by considering the Sun as a blackbody, applying the single-scattering atmosphere radiative-transfer formalism to consider the solar light extinction from the top of the atmosphere to the dust particles altitude. This extinction depends on the solar zenith angle and, consequently, on the local solar angle. Figure 3.22 shows that, for UV irradiances slightly lower than to those observed in the laboratory,  $\beta_{\text{ndust}}$  increases with increasing solar UV-irradiance. Moreover, the  $\beta_{\text{ndust}}$  enhancement ( $+0.45 \text{ Mm}^{-1}.\text{sr}^{-1}$ ) measured with our UV-polarization lidar is in the same range as the  $\beta_{\text{ndust}}$  enhancement ( $+0.75 \text{ Mm}^{-1}.\text{sr}^{-1}$ ) simulated from the NPF measured in China and presented in Section 3.5.3.



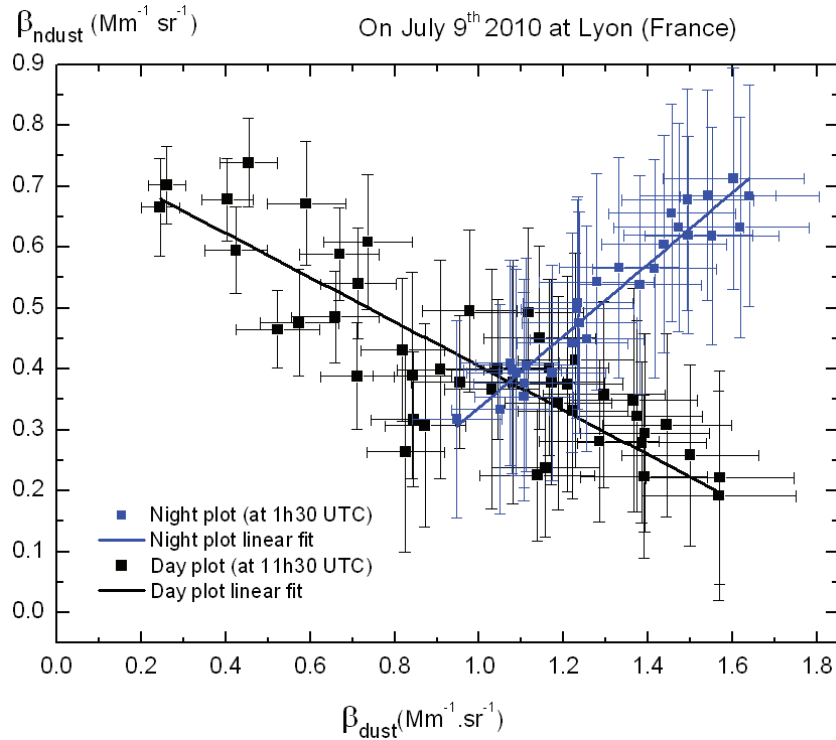
**Figure 3.22**  $\beta_{\text{ndust}}$  as a function of the solar UV irradiance during sunrise (between 2h30 and 5h40 UTC).

Figure 3.23 represents the  $\beta_{\text{dust}}$  and  $\beta_{\text{ndust}}$  lidar vertical profiles on July 9<sup>th</sup> 2010, at Lyon during nighttime (1h30 UTC) and daytime (11h30 UTC), for altitudes between 3.3 and 5 km asl, derived from the Figure 3.17 time-altitude maps. A positive correlation between  $\beta_{\text{ndust}}$  and  $\beta_{\text{dust}}$  is seen during nighttime, while a negative-correlation is observed during daytime.



**Figure 3.23** lidar vertical profiles of  $\beta_{ndust}$  (in gray) and  $\beta_{dust}$  (in brown) during the July 9, 2010, Saharan dust episode, during nighttime (left profiles at 01h30 hours UTC) and daytime (right profiles at 11h30 hours UTC).

This positive/negative correlation is best seen in the form of a scatter-plot showing  $\beta_{ndust}$  as a function of  $\beta_{dust}$  for the daytime (blue squares) and nighttime (black squares) lidar profiles as plotted in Figure 3.24: within our error bars, under / without solar UV-irradiance, a positive/negative correlation scatter-plot is observed. The daytime-observed negative correlation does not originate from our retrieval methodology: despite  $\beta_{ndust} = \beta_p - \beta_{dust}$ , at a given z-altitude,  $\beta_{ndust}$  evolves independently of  $\beta_{dust}$  which is not constant with the altitude, so that there is no reason for  $\beta_s$  to be in an opposite behavior with  $\beta_d$  (as can be seen on the night profile in Figure 3.23). Secondly, a careful analysis of the  $\beta_{p,||}$  and  $\beta_{p,\perp}$  already showed evidence of negative correlation between polarization-resolved optical signals, and this prior our  $\beta_{ndust}$  and  $\beta_{dust}$  retrieval, obtained by applying the OBP2-methodology. To interpret these positive/negative correlation plots, in the absence of complementary measurements and literature on these new Lidar-observed photo-induced processes, in addition to NPF-process and  $H_2SO_4$  condensation on dust surface, coagulation and hygroscopicity growth should be considered. However, RH is almost constant and moreover, such processes do not explain the different behavior observed during night and daytime.



**Figure 3.24** Scatter plot of the  $\beta_{\text{ndust}}$  as a function of  $\beta_{\text{dust}}$  showing negative correlation during daylight hours (black) and positive correlation during nighttime hours (blue). The plotted point correspond to the point plotted in Figure 3.23.

The combined laboratory, numerical simulations and field observations presented here provide strong arguments in favor of the identified new chemical pathway for dust particles to promote nucleation: indeed, semiconductor properties of atmospheric dust particles lead to new chemical properties affecting aerosol formation, associated with dust, in the troposphere. All the features retrieved from laboratory measurement and numerical simulations (except the  $\text{\AA}_p$  measurement) have been retrieved on our lidar measurements. We are hence confident that NPF event has been observed on July 9<sup>th</sup> 2010 with our UV-polarization lidar.

### 3.4.5 Dust case study summary

In this section, the mixing of dust and non-dust (ndust) particles has been studied. First the optical backscattering coefficients  $\beta_{\text{dust}}$  and  $\beta_{\text{ndust}}$  specific to dust and ndust particles have been retrieved simultaneously by using the OBP2 methodology developed in Section 2.3.1. In the free troposphere, the ndust particles are located at the border of the dust layer. Such an observation may be consistent with NPF formation (Dupart et al., 2012). To support this hypothesis, numerical simulations of  $\beta_{\text{ndust}}$  corresponding to an NPF event have been performed based on Dupart et al.'s measurements (2012). These numerical simulations shown

that NPF event can be observed with the detection limit of our UV polarization lidar and also demonstrated that during a NPF event almost all the particles from 30 and up to 400 nm contribute to  $\beta_{\text{ndust}}$  in the UV. Moreover several features have been pointed out from these simulations and have all been retrieved on the lidar measurement of  $\beta_{\text{ndust}}$ :

- i) An enhancement of the  $\beta_{\text{ndust}}$  backscattering coefficient due to the NPF can be observed and UV should be used for this as the  $\beta_{\text{ndust}}$  enhancement is two times higher in the UV than in the VIS (five times higher in the UV than in the IR).
- ii) The nucleated particles number concentration increases with increasing UV-irradiance.
- iii)  $\beta_{\text{ndust}}$  enhancement is negatively-correlated with  $\beta_{\text{dust}}$  during the NPF event, while no negative-correlation is observed before the NPF-event.

For all these reasons, we hence are confident that NPF event has been observed on July 9<sup>th</sup> 2010 with our UV-polarization lidar.

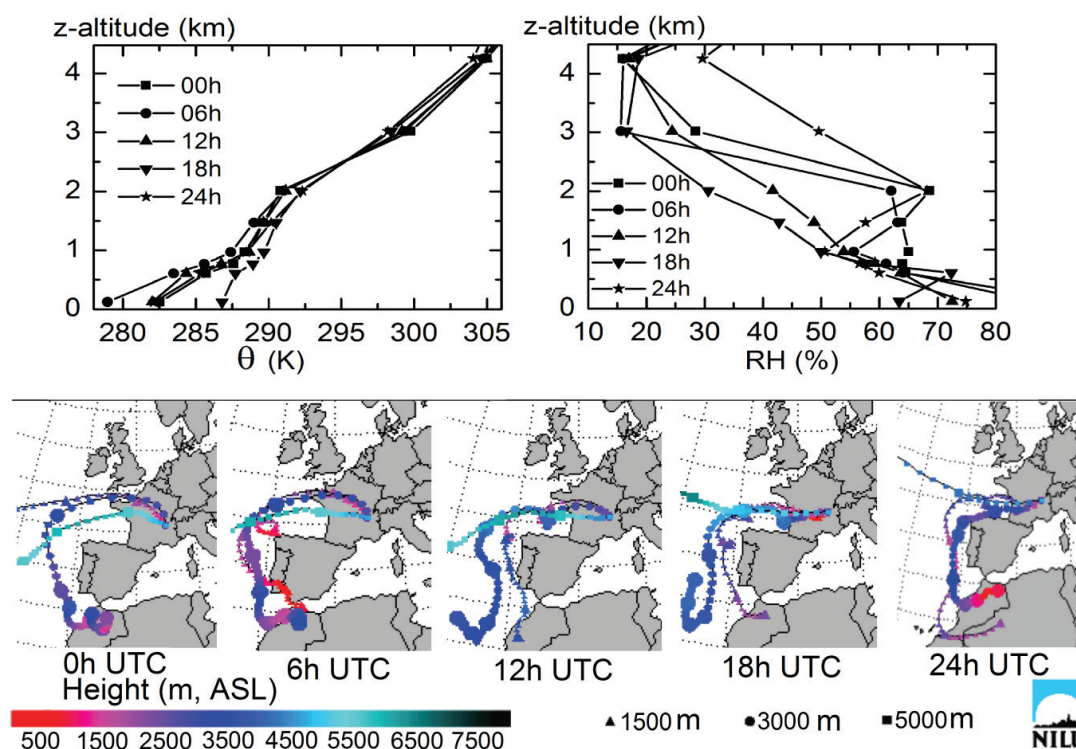
### **3.5 The Sea-salt / Dust case study**

Three-component particle mixtures are also encountered in the atmosphere: for example, during the 2011 eruption of the Eritrean Nabro volcano, volcanic ash particles encountered desert dust particles in the troposphere while also water soluble particles were present. In this section, we analyse the vertical layering in a three-component particle external mixture with the new OBP3-methodology to retrieve the backscattering coefficients specific to each particle component.

#### **3.5.1 Geophysical situation**

A mixture of dust (dust) with sea-salt (ss) and other particles (n12) particles occurred at Lyon on October 18<sup>th</sup> 2011 due to favourable meteorological conditions after more than 2,500 km advection from the Saharan dust source region. As shown by the back-trajectories in Figure 3.25, in the morning of October 18<sup>th</sup> 2011, the air masses passing above the lidar station about 1.5 km altitude were originating from a ss source region and around 3 km from a dust source region. In the evening, the two layers were inverted, with air masses originating from a dust source region around 1.5 km and from a ss region around 3 km. Hence, a possible mixing of ss and desert dust particles occurred during daytime in the low troposphere. Moreover, after more than 2,500 km advection these dust and ss particle are probably mixed with other ws

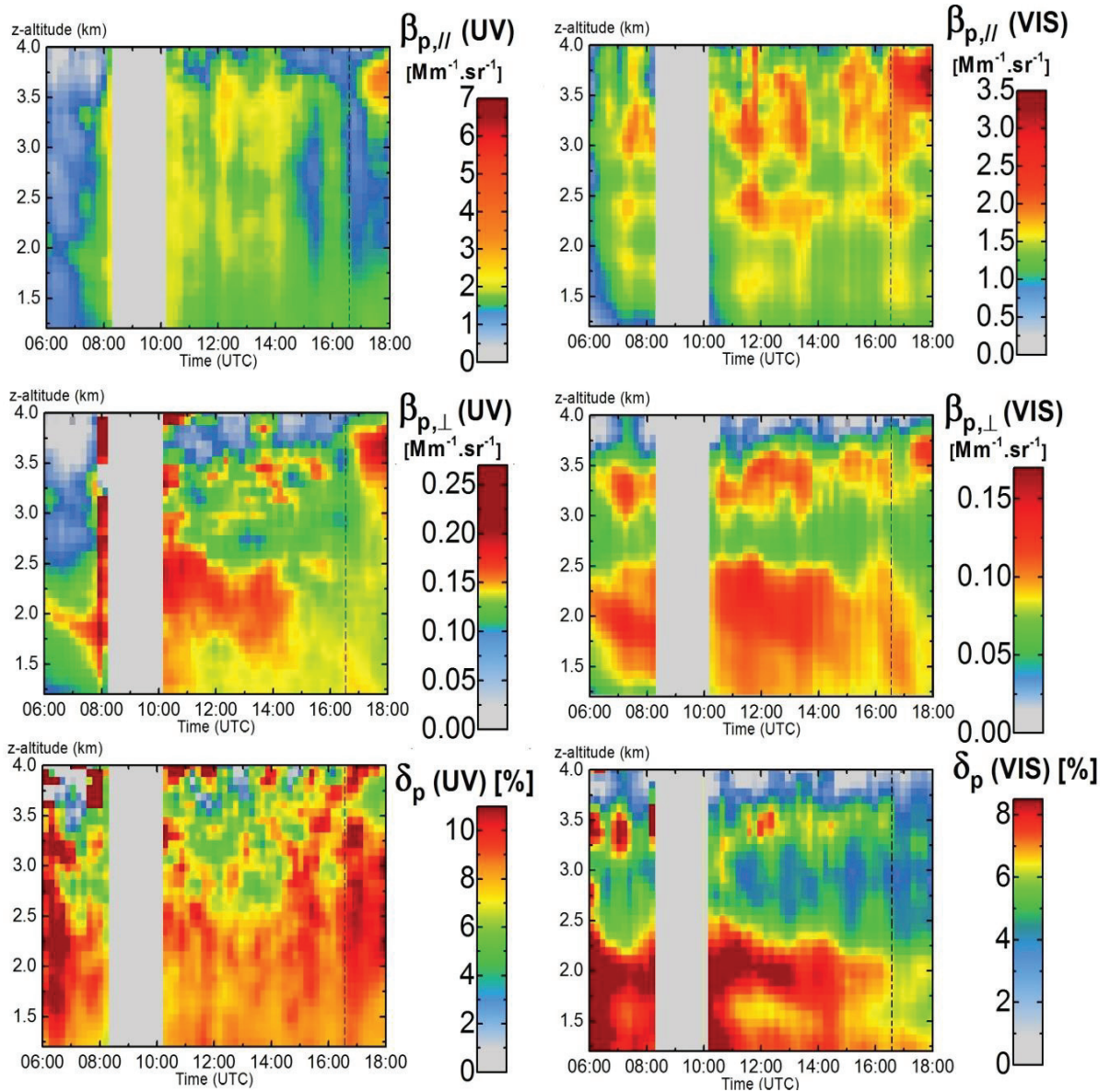
particles. The 1.5 and 3 km layers are delimited by temperature inversion layers, as can be seen in the vertical profiles of potential temperature in Figure 3.25, showing that the troposphere was stably stratified. As can be seen in Figure 3.25 for altitudes above 2 km, RH was below 40 %, which is the sodium chloride crystallization point. Hence in agreement with Section 2.4, the cubic shape model is applicable for sea-salt particles for altitudes above 2 km. The n12 particles are likely to be water-soluble (ws) particles defined accordingly to the classification of Hess et al. (1998), which include, sulfate (such as  $\text{H}_2\text{SO}_4$ ,  $\text{NH}_4\text{HSO}_4$ ,  $(\text{NH}_4)_2\text{SO}_4$ ) and nitrate (such as  $\text{NH}_4\text{NO}_3$ ) particles as well as other organic water-soluble substances. The efflorescence of  $\text{H}_2\text{SO}_4$ ,  $\text{NH}_4\text{HSO}_4$  and  $\text{NH}_4\text{NO}_3$  particles is kinetically inhibited (Cziczo and Abbatt, 2000; Li et al., 2001), while  $(\text{NH}_4)_2\text{SO}_4$  particles effloresce for RH below 32 % (Onasch et al., 1999). However, as published by Wise et al. (2005) and Sakai et al. (2010),  $(\text{NH}_4)_2\text{SO}_4$  crystals have a rounded shape and nearly spherical shapes. Consequently ws particles are assumed to be spherical ( $\delta_{\text{ws}} = 0\%$ ). The section is organized as follows. First  $\beta_{\text{p},//}$ ,  $\beta_{\text{p},\perp}$  and  $\delta_{\text{p}}$  are retrieved on October 18<sup>th</sup> 2011 using our UV-VIS polarization lidar measurements. Then  $\beta_{\text{dust}}$ ,  $\beta_{\text{ss}}$  and  $\beta_{\text{ws}}$  are retrieved by applying the OPB3-methodology, where for the first time, both sea-salt and dust particles are treated as nonspherical, which is justified due to the observed low relative humidity. Afterwards, the OPB3-inherent assumptions and the robustness of this new methodology are discussed.



**Figure 3.25** Upper panel: Relative humidity (RH) and potential temperature ( $\theta$ ) vertical profiles on October 2011 18<sup>th</sup> at Lyon (Météo France). Lower panel: FLEXTRA 7-days air mass back-trajectories showing the history of air masses arriving in the Lyon atmosphere on 2011 October 18<sup>th</sup>.

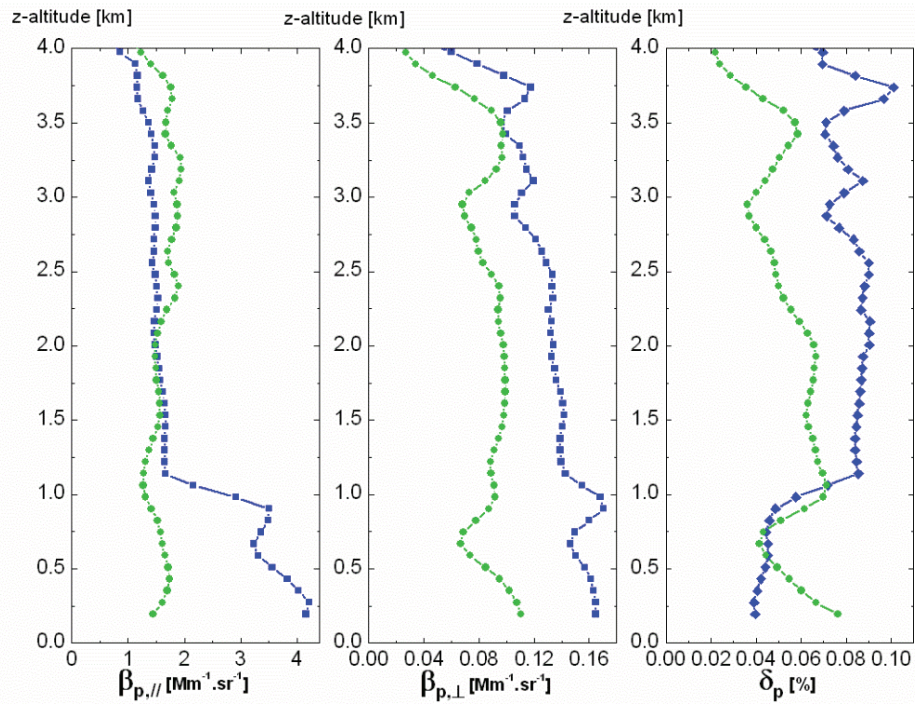
### 3.5.2 Sea-salt, Dust and ws backscattering retrieval

Figure 3.26 displays the time-altitude maps of  $\beta_{p,\parallel}$ ,  $\beta_{p,\perp}$  and  $\delta_p$  measured above Lyon on October 18<sup>th</sup> 2010 in the UV and the VIS spectral ranges. As the mixing of dust with sea-salt is studied, to obtain these maps, we chose  $S_p(\text{UV}) = 50 \pm 5$  sr and  $S_p(\text{VIS}) = 60 \pm 5$  sr in the free troposphere, in agreement with the literature (Murayama et al., 1999). In addition, these values are between the computed values for dust and sea-salt indicated in Table 2.2. Here the PBL content is not analyzed as it is not only composed of a dust, ss and ws mixture due to the local emission of particles (A. Miffre et al., 2010). Please note that since we use the Klett's algorithm (1985), the  $S_p$ -value used in the PBL does not change the retrieved  $R_{\parallel}$ -values in the free troposphere and consequently it does not change the  $\beta_{p,\pi}$  and  $\delta_p$ -values either. Consequently, we can focus only on the free troposphere without any assumption on the PBL content, as done in the Figure 3.26. Each time-altitude map has adjusted colour scales to emphasize the temporal behaviour of two main atmospheric layers having different thicknesses, located between 1.5 and 2.5 km and between 3.0 and 3.5 km. This layering is clearly visible in the UV and VIS  $\beta_{p,\perp}$  maps, which are ns-particles specific. The particle depolarization ratio maps exhibit maximum  $\delta_p$ -values equal to 11 % at  $\lambda_1 = 355$  nm and 9 % at  $\lambda_2 = 532$  nm, well below the  $\delta_{ns}$ -values computed for ss or dust particles (see Table 2.2), due to the presence of ws particles, in agreement with Section 2.4.3.



**Figure 3.26** Time-altitude maps of  $\beta_{p,\parallel}$ ,  $\beta_{p,\perp}$  and  $\delta_p$  in the UV ( $\lambda_1 = 355$  nm, left three vertical panels) and in the VIS ( $\lambda_2 = 532$  nm, right three vertical panels) on October 18<sup>th</sup> 2011 at Lyon. The grey band corresponds to clouds which prevented retrieving the  $\beta_{p,\parallel}$ ,  $\beta_{p,\perp}$ ,  $\delta_p$ -coefficients. Dashed lines correspond to Figure 3.27-case study, at 16h15 UTC.

Figure 3.27 displays the retrieved vertical profiles of  $\beta_{p,\parallel}$ ,  $\beta_{p,\perp}$  and  $\delta_p$  on October 18<sup>th</sup> at 16h15 UTC, obtained by applying the OBP3-methodology. At that time, as shown in Figure 3.25, for altitudes above 2 kilometres, the relative humidity is below the 40 % RH sea-salt crystallization point, allowing sea-salt particles to depolarize. The nonsphericity of both dust and sea-salt particles must hence be taken into account. Then the  $2\beta + 2\delta$  algorithm to solve the set of 12 Equations (Equations (2.32) to (2.38)) has been run to separately retrieve  $\beta_{\text{dust}}$ ,  $\beta_{\text{ss}}$  and  $\beta_{\text{ws}}$  as a function of the altitude plume on October 18<sup>th</sup> at 16h15 UTC. Figure 3.28 displays the retrieved vertical profiles of  $\beta_{\text{dust}}$ ,  $\beta_{\text{ss}}$  and  $\beta_{\text{ws}}$ , together with the fraction of each component ( $X_{\text{dust}}$ ,  $X_{\text{ss}}$ ,  $X_{\text{ws}}$  defined in Equation 2.25) in the particles mixture.



**Figure 3.27** Vertical profiles of  $\beta_{p,\parallel}$ ,  $\beta_{p,\perp}$ ,  $\delta_p$  on October 18<sup>th</sup> 2011 at 16h15 UTC at Lyon (France), addressed in the UV ( $\lambda_1 = 355$  nm, blue squares) at and in the VIS ( $\lambda_2 = 532$  nm, green circles).

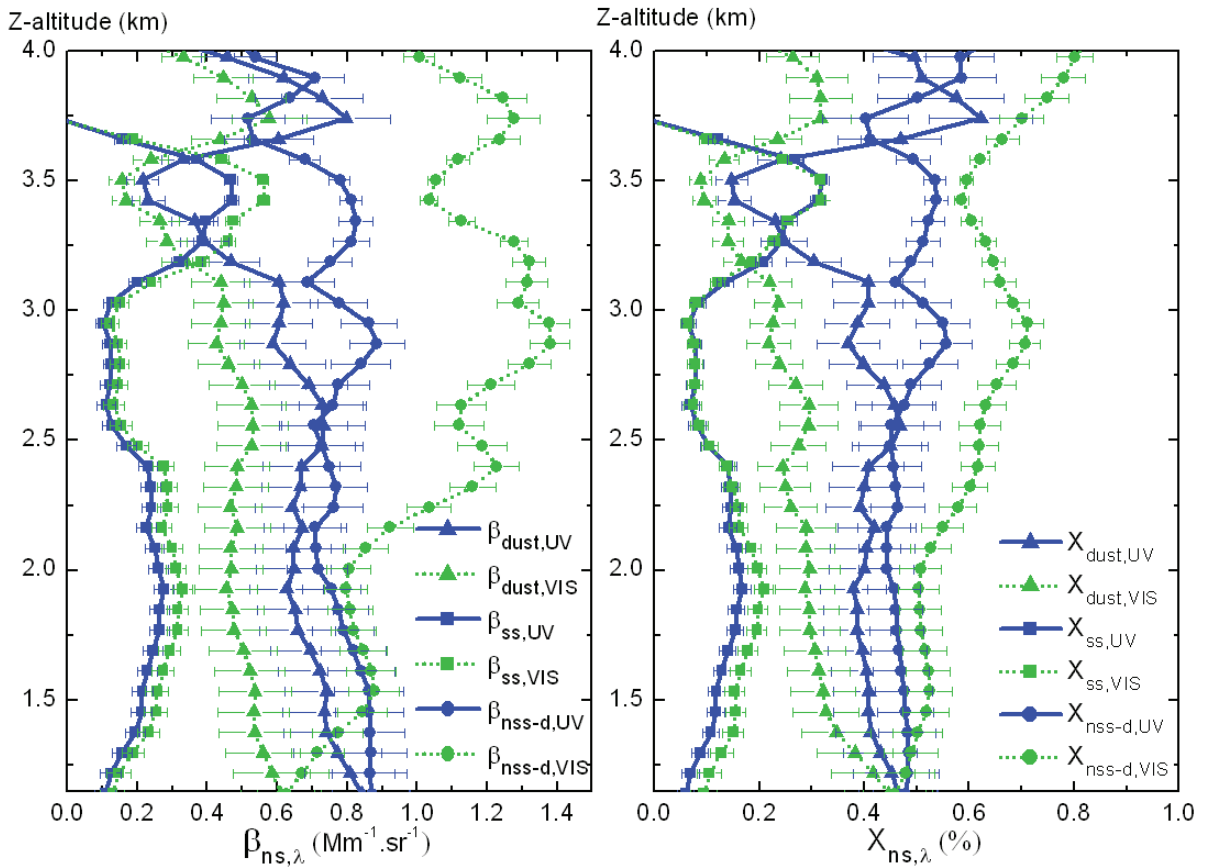


**Figure 3.28** Vertical profiles of  $\beta_{\text{dust}}$  (triangles),  $\beta_{\text{ss}}$  (squares) and  $\beta_{\text{ws}}$  (spheres) and fraction of ns-particles (dust, ss) and s-particles (ws) in the three-component mixture on October 18<sup>th</sup> 2011 at 16h15 UTC at Lyon (France), addressed in the UV ( $\lambda_1 = 355$  nm, blue full lines) at and in the VIS ( $\lambda_2 = 532$  nm, green dotted lines).

### 3.5.3 Discussion

Because the optical properties of the particle mixture are not the optical properties of each distinct particle component, a quantitative evaluation of the spatial distribution of each distinct particle component needs the (complex) methodology presented here. Because of its novelty, it is yet to be validated in the atmosphere by independent co-located measurements. We here discuss the possible influence of computed numerical values of  $\delta_{ns}$  and  $\dot{A}_{ns,\perp}(\text{UV}, \text{VIS})$  for dust and ss-particles (see Table 2.2 for the used numerical values) on the retrieval results. To test the robustness of our new methodology, we used somewhat arbitrary, test values for  $\delta_{ss}$  and  $\dot{A}_{ns,\perp}(\text{UV}, \text{VIS})$  :

- As shown by Equation (2.23), the effect of a different  $\delta_{ns}$ -value is to shift the corresponding  $\beta_{ns}$ -profile. Therefore, the behavior of  $\beta_{ns}$  with altitude is still retraced for all  $\delta_{ns}$ -value considered. Quantitatively, when using  $\delta_{ss} = 33\%$  instead of  $10\%$ ,  $\beta_{ss}$  decreases by a factor of almost 3 ( $11/4$  exactly), which in turn may increase the observed  $\beta_{ws}$ -value, depending on the corresponding  $\beta_{dust}$ -value observed. Note that that an assumption of  $\delta_{ss} = 0\%$  results in a singularity in Equation (2.23). Very close to  $\delta_{ss} = 0\%$ , we noted that the retrieved  $\beta_{ss}$  and  $\beta_{ws}$ -values were very different from those observed in Figure 3.28 and that negative values of  $\beta_{ss}$  and/or  $\beta_{ws}$  were observed. Hence negative values are retrieved if only one particle component is considered as non-spherical, which underlines the importance of taking into account the dust and ss-particle nonsphericity.
- The computed cross-polarized Ångstrom exponent  $\dot{A}_{ns,\perp}(\text{UV}, \text{VIS})$  may also be questioned. In agreement with Section 2.4, Figure 3.28 shows that dust particles contribute more to particle backscattering at the UV spectral range than in the VIS, while sea salt-particle backscattering is stronger in the VIS spectral range. The  $\dot{A}_{dust,\perp}(\text{UV}, \text{VIS})$  and  $\dot{A}_{ss,\perp}(\text{UV}, \text{VIS})$  values can be considered as convergence criteria in our algorithm, since for very different values of  $\dot{A}_{dust,\perp}(\text{UV}, \text{VIS})$  and  $\dot{A}_{ss,\perp}(\text{UV}, \text{VIS})$ , negative particle backscattering coefficients were retrieved. Hence, to obtain accurate retrievals of dust, sea-salt and ws-particles backscattering coefficients, care should be taken on the choice of PSD when applying our new OBP3-methodology.

To be quantitative, we have run our OBP3 algorithm by including the Table 2.2 error bars on the cross-polarized Ångstrom exponent and the UV-VIS ns-particles depolarization ratios. The corresponding errors are plotted as error bars in Figure 3.28. The error bars on the retrieved particle backscattering coefficients are quite low, which shows the robustness of our

new methodology. The model variability induces an uncertainty on the retrieved  $\beta_{\text{dust}}$  (UV),  $\beta_{\text{dust}}$  (VIS),  $\beta_{\text{ss}}$  (UV),  $\beta_{\text{ss}}$  (VIS),  $\beta_{\text{ws}}$  (UV) and  $\beta_{\text{ws}}$  (VIS) which is respectively below 20 %, 24 %, 24 %, 23 %, 21% and 12 %. These error bars are almost independent of the laser wavelength, except for the ws-particles. Moreover, by using UV-VIS laser light, we have increased our sensitivity to particles in the fine particles mode.

Figure 3.28 shows the vertical profiles of dust, sea-salt and ws-particles revealing the complex vertical layering of the Lyon troposphere. In contrast to what is observed in the two-component methodology, due to the presence of ws-particles, the  $\beta_{\text{dust}}$ -vertical profile is not complementary of the  $\beta_{\text{ss}}$ -vertical profile. Up to 3.0 kilometres altitude, where a temperature inversion is observed, in the 1.5 km layer, dust (resp. sea-salt) particles contribute to nearly 40% (resp. 10%) to the total particle backscattering coefficient. The vertical profile of ws-particles is much more complicated to describe, except when  $X_{\text{ss}}$  is constant such as between 2.7 and 3.0 km altitude, in which case  $X_{\text{dust}}$  and  $X_{\text{ws}}$  are in opposite phases with respect to altitude. Despite its complex behavior, the  $\beta_{\text{ws}}$ -vertical profile closely follows the  $\beta_{\text{p,}}$ -vertical profile, into which s-particles mainly contribute. Above 3.0 kilometres altitude, in the 3 km layer, the fractions of dust, ss and ws-particles in the total particle backscattering vary with altitude revealing a very complex vertical layering. A very interesting point is to be seen around the extrema observed at a 3.5 kilometres altitude where, in the UV, the  $\beta_{\text{dust}}$  and  $\beta_{\text{ws}}$  vertical profiles are in opposite phases to the  $\beta_{\text{ss}}$  variation with respect to altitude. As recently shown in Dupart et al. (2012) and discussed in Section 3.4, this behavior may be related to new particles formation events, where ss particle may act, as well as dust, as a condensation sink. This observation indicates that the proposed methodology is able to reveal very complex particle microphysical behaviour.

### 3.6 Conclusions

In this Chapter, we have applied the optical backscattering partitioning OBP2/OBP3 to retrieve the backscattering coefficients specific to each particle component of externally mixed aerosols. The polarization-resolved particle backscattering coefficients  $\beta_{\text{p},\pi}$ , required to apply the OBP2 and OBP3 methodologies, are here measured with a UV-VIS polarization lidar to allow studying the vertical layering of these atmospheric particles. The statistical errors and systematical biases affecting the polarization lidar measurement have been analyzed in detail. Then, the Lyon UV-VIS polarization lidar experimental setup has been

detailed by focusing of the key points to reduce the systematical biases affecting the dual-wavelength polarization lidar measurements. In particular, we efficiently separate the backscattered light with respect to its  $(\lambda, \pi)$ -spectral and polarization optical properties with a fully negligible cross-talk (less than  $10^{-7}$ ). Then, by achieving a robust calibration (less than 2 %-error) and by applying the Klett's algorithm, we retrieved the polarization particles backscattering  $\beta_{p,\pi}$  coefficients, then successfully applied the OBP2/OBP3-methodology to three case studies, namely, *the Ash case* (volcanic ash particles mixed with sulfates particles), the *Dust case* (desert dust particles mixed with non-dust particles), then the *Sea-salt/dust case* study (desert dust particles mixed with sea-salt and water soluble particles).

For each case study, we analyzed the robustness of the OBP2 methodology by changing the lidar ratio  $S_p$  used in the Klett algorithm and the  $\delta_{ns}$ -depolarization ratio chosen as input parameters of these methodologies. A negligible influence on the retrieved backscattering coefficient  $\beta_{ns}$  was found, which allowed developing several applications for the *Ash case* as well as for the *Dust case*. We hence developed a new methodology to retrieve the range-resolved particles number and mass concentrations specific to one particle component (ash, dust) (Miffre et al., 2011, 2012a, b), which include the variability in the particle size distribution and possible sedimentation effects (Miffre et al., 2012b). In addition, the retrieved  $\beta_{nash}$  has a good agreement with the relative humidity (RH) vertical profile, which could be used to study the hygroscopic growth of the nash particles.

Additionally, we also discussed the inherent assumptions and demonstrated the performance of the OBP3-methodology in the case study of external mixing of desert dust with sea-salt and water-soluble particles. Indeed the input parameters variability induces on the retrieved backscattering coefficient, less than 24 % uncertainty. However, to further interpret the retrieve backscattering coefficients, the methodology now needs to be validated in the atmosphere by independent co-located measurements.

Finally, using the OBP2-methodology, we evaluated the ability of polarization lidar to measure NPF. Laboratory measurement and numerical simulation of NPF have been used to retrieve the feature of the  $\beta_{ndust}$  corresponding to NPF. Several features have been pointed out from laboratory measurements and numerical simulations, which have all been retrieved on the lidar measurement of  $\beta_{ndust}$ . We hence demonstrated that NPF can be observed with a UV polarization lidar, as the  $\beta_{ndust}$  enhancement due to the NPF event is higher than the  $\beta_{dust}$  detection limit of our UV polarization lidar.

## Chapter 4

### Laboratory measurements on atmospheric nanoparticles

This fourth chapter presents the laboratory experiments performed in the frame of this thesis. To apply the OBP2/OBP3-methodology to study two- or three-component particle mixtures, accurate particles backscattering measurements performed in the exact backscattering direction and specific to each particles component are required as optical inputs, namely the ns-particles depolarization ratio  $\delta_{ns}$  and the cross-polarized ns-particles Ångstrom exponent  $\tilde{A}_{ns,\perp}$  (see Chapter 2). In this context, laboratory measurements are interesting as they account for the highly-irregularly ns-particles shapes, inhomogeneity, porosity or birefringence (Attwood and Greenslade, 2011). In addition, laboratory measurements are interesting to benchmark the numerical simulations. Hence, the first goal of this chapter is to present the principle, the design and the optimization of a laboratory experiment designed to measure the particles depolarization ratio  $\delta_p$  of an ensemble of particles in ambient air, for the first time in the exact backscattering direction. A measurement of the  $\delta_p$ -ratio for water droplets and salt particles suspended in air is presented, as a case study respectively for spherical and nonspherical particles. We believe this result may be useful for comparison with the existing numerical models and for remote sensing field applications in radiative transfer and climatology. This work has been published in (David et al., 2013b).

In addition, to retrieve the optical properties of a particles ensemble, the optical properties of each individual particle have to be addressed. Numerous studies have shown the interest to study of a single particle to avoid the ambiguity induced by the inherent averaging present in particles ensemble studies (Nirmal et al., 1996; Lombardi et al., 2012), which is necessary to compare optical models with optical properties measurements (Miles et al., 2011). For particle size in the nanometer range, numerous studies exist in the literature, but only for metallic and semiconductor particles, which are very seldom in the atmosphere. In this chapter, for the first time to our knowledge, an absolute measurement of the extinction cross-section of a single dielectric nanoparticle has been performed, on an ammonium sulfate nanoparticle, then on a mineral dust nanoparticle having a  $r = 50$  nm radius. This measurement has been achieved in collaboration with N. Del Fatti and F. Vallee's group at the Institute of Light and Matter

(ILM). A discussion is then proposed to compare the results of this new and preliminary laboratory measurement with theory in regards to the environmental conditions.

## **4.1 Polarization-resolved exact backscattering by a particles ensemble in air**

This section presents the laboratory experiment designed to measure the exact backscattering of light by an ensemble of particles suspended in ambient air (David et al., 2013b). This experiment operates in the far-field single scattering approximation (see Chapter 2), covers the exact backscattering direction with accuracy ( $\theta = \pi \pm \xi$  where  $\xi = 3.5 \times 10^{-3}$  radian is the width of the scattering angle detected) and efficiently collects the particles backscattering radiation, while minimizing any stray light. The section is organized as follows. First, the state-of-the-art on exact backscattering measurements is presented. Then, the principle of our laboratory exact backscattering measurement is presented, followed by the corresponding experiment setup. Finally, the experimental signals are presented and the retrieved particles depolarization is discussed.

### **4.1.1 State of the art on exact light backscattering by particles in air**

Besides its quite simple geometry and its handiness for in situ applications (Ghosh et al., 2009), the backscattering direction has raised great interest as it is one of the most sensitive directions to the particles size and shape (Mishchenko et al., 2002; Nousiainen et al., 2009). Although more than a century has now elapsed since G. Mie presented his theory (1908), even though measurements of water clouds do not contradict the Mie theory, it is surprising that its experimental proof has never been achieved in the exact backscattering direction for an ensemble of particles in air, such as spherical water droplets, while, in the literature, a considerable number of papers apply the Mie theory, as for environmental purposes, such as in remote sensing and radiative transfer applications. Hence, there is a need for laboratory scattering matrix measurements in the exact backscattering direction for an ensemble of particles in air, for at least two reasons. Firstly, it may help validating numerical simulations based on T-matrix or DDA numerical codes, which are never assumption-free, especially when the particles exhibit complex morphologies. Secondly, it may be also useful in active lidar remote sensing field experiments, which operate in the backscattering geometry and where T-matrix computations have been coupled with polarization lidar (Veselovskii et al.,

2010; David et al. 2013a). For instance, to efficiently partition particles backscattering in a two/three-component ambient air mixture with a precise UV-VIS polarization lidar, it is necessary to specifically address the depolarization properties of each particles component composing the particles mixture (see Chapter 2). It is feasible if optical inputs (laboratory measurements and or numerical simulations) exist for each particles ensemble in air that cover the exact backscattering direction. Ideally, such data should be representative of the far-field single scattering approximation, to ease the comparison with both the numerical simulations and the field experiments.

When measuring the scattering of light by a particles ensemble at high scattering angles, close to the backscattering direction ( $\theta = 180^\circ$ ), two main difficulties arise, which have been identified by J.W. Hovenier et al. (2003). The first intricacy is relative to the finite size of the detector, which may block the incident radiation in the backscattering geometry. The insertion of a beamsplitter, as often performed for condensed matter phases (Studinski and Vitkin, 2000; Vitkin and Studinski, 2001; Kuga and Ishimaru, 1984; Silverman et al, 1996; Wiersma et al., 1995), usually limits the accuracy of the backscattering measurement because its specifications are generally imperfectly known and represent an important artifact, source of systematic error in the backscattering measurement (Wiersma et al., 1995). In addition, inserting a beamsplitter plate may create some stray light, affecting the particles backscattering signal, as for solid biological tissues (Studinski and Vitkin, 2000). The second intricacy is relative to the intensity of the backscattering signal itself, which might be low for an ensemble of particles in air, so that any stray light might overcome the particles backscattering signal. To overcome this difficulty, for condensed matter phases, lock-in detection is usually applied on continuous incident radiation (Studinski and Vitkin, 2000; Vitkin and Studinski, 2001; Silverman et al, 1996). Hence, the observation at the exact backscattering angle  $\theta = 180^\circ$  has only been overcome in experiments related to condensed matter phases, such as solid GaAs crystals (Wiersma et al., 1997), solid biological tissues (Studinski and Vitkin, 2000; Vitkin and Studinski, 2001), liquid water (Kuga and Ishimaru, 1984), PSL spheres in liquid water (Kuga and Ishimaru, 1984; Silverman et al, 1996) or, more recently, for liquid animal blood (Wang et al., 2012). However, up to now to our knowledge, no laboratory measurement exists that covers the exact backscattering angle for an aerosol, an ensemble of suspended particles in air. Muñoz and Hovenier recently reviewed (2011) the existing light scattering laboratory experiments measuring one or more elements of the scattering matrix. Several light scattering matrix experiments have been built and operated at

high scattering angles ( $\theta \geq 168^\circ$ ), approaching the exact backscattering direction. Table 4.1 presents their principal characteristics for an ensemble of particles in ambient air by giving the scattering angle range, the wavelength  $\lambda$  of the radiation, the nature (continuous/pulsed) of the laser source and the detector field of view (FOV). The closest value to the exact backscattering direction is  $\theta = 179.6^\circ$  (Sakai et al., 2010). To cover the exact backscattering direction, polynomial extrapolations or numerical algorithms have been proposed (Liu et al. 2003). Nonetheless, their inherent assumptions must be discussed and may lead to quite considerable errors, as recently discussed by M. Schnaiter et al. (2012). Moreover, from a detailed reading of the corresponding papers, it rather seems difficult to know if the far-field single scattering conditions are fulfilled.

**Table 4.1** Existing light scattering experiments for particles in air, close to the exact backscattering direction. The scattering angle  $\theta$ , the wavelength of the radiation  $\lambda$  and the field of view FOV are given, together with the corresponding sample and the continuous / pulsed character of the chosen laser source. Our work provides laboratory measurements in the exact backscattering direction, with a high signal-to-noise ratio.

Authors and reference	Sample	$\theta$ (deg)	$\lambda$ (nm)	Laser source	FOV (mrad)
A. Glen et al. (2013)	Single dust particle	$172.0 \pm 4.0$	680	Laser diode	–
T. Sakai et al. (2010)	NaCl, water	$179.2 \pm 0.4$	532	Pulsed laser	2.8
O. Muñoz and J.W. Hovenier (2011)	Ash, dust, water, NaCl particles	up to 177	483, 488, 520, 568, 647	CW laser with chopper	35
M. Schnaiter et al. (2012)	Ice crystals	178.2	488	CW laser	1.5
This work	Water droplets, Salt (NaCl) particles	$180.0 \pm 0.2$	355	Pulsed laser	1.0

#### 4.1.2 Principle of an exact backscattering measurement for nanoparticles in ambient air

In this subsection, we present the principle of our exact backscattering measurement for nanoparticles in ambient air, which operates in the far-field single scattering approximation. These approximations are respectively discussed in Sections 4.1.4-c and 4.1.3-c.

Figure 4.1 is a 3D-scheme showing the principle of our particles backscattering measurement (see Section 4.1.3 for a detailed description of our experimental set-up). We overcome the

first intricacy by inserting a polarizing beamsplitter cube (PBC) on the optical pathway from the laser source to the particles scattering medium. In this way, the particles backscattering radiation is detected after retro-reflection on a PBC, (for specifications and acceptance angle see Sections 3.2 and 4.1.3). Moreover, the particles backscattering radiation is discriminated from the background stray light by realizing time resolved measurement.

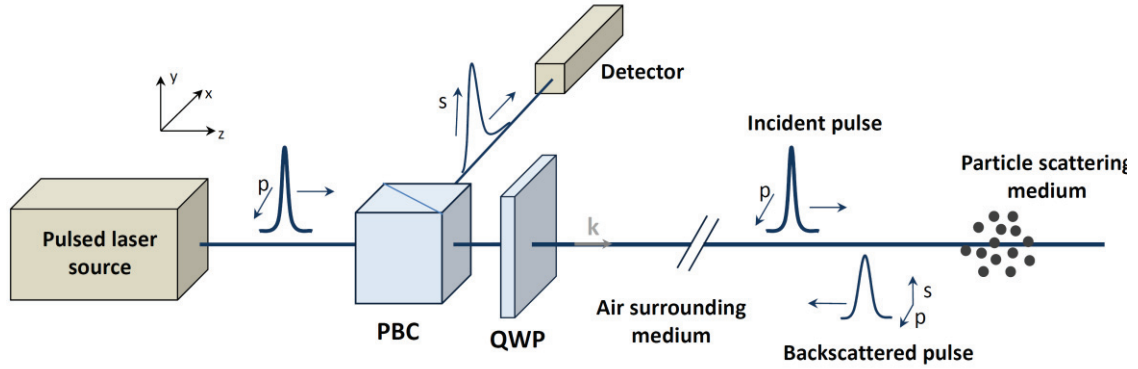


**Figure 4.1** Principle of an exact backscattering measurement for an ensemble of nanoparticles in ambient air: the particles backscattering radiation is discriminated from the background stray light by measuring the time interval  $\Delta t = 2d/c$  taken by a laser pulse to reach the detector, after retro-reflection on a polarizing beamsplitter cube (PBC). The polarization (p, s) of the backscattered light is related to the particle scattering medium in the laboratory ambient air and to the quarter-wave plate (QWP) used to modulate the incident laser linear polarization (p).

As underlined by M.I. Mishchenko et al. (2009), any measurement of particles scattering consists in a two-stage procedure: the scattering signal  $\mathcal{P}$  is first measured in the absence of the particles (in which case,  $\mathcal{P} = \mathcal{P}_0$ ), then, in their presence. The particles backscattering signal  $\mathcal{P}_p$  is then basically deduced by subtracting  $\mathcal{P}_0$  from  $\mathcal{P}$ :

$$\mathcal{P}_p = \mathcal{P} - \mathcal{P}_0 \quad (4.1)$$

The  $\mathcal{P}_0$  signal is due to ambient air backscattering and to the partial reflection of the incident laser pulse on optical components (see Section 4.1.4). When the laser pulse is emitted at a time  $t_i$ , the particles backscattering signal  $\mathcal{P}_p(t)$  is always null, except for  $t = t_i + \Delta t$ , where  $\Delta t = 2d/c$  represents the time-of-flight of the laser pulse from the laser cavity to the detector, located at a distance  $d$  from the particles. When the laser pulse duration  $\tau$  is taken into account, backscattering occurs along the  $z$ -propagation direction over a length  $\ell = c\tau/2$ , which defines the spatial extension of the backscattering volume in the  $z$ -direction. Accordingly, the particles backscattering signal  $\mathcal{P}_p(t)$  extends over a time interval close to  $\tau$ . In the framework

of the Mueller matrices, in the far-field single scattering approximation, the Stokes vector  $\mathbf{St}_p$  ( $= [I_{sac,p}, Q_{sac,p}, U_{sac,p}, V_{sac,p}]^T$ ) of the particles backscattering radiation at time  $(t_i + \Delta t)$  relates to the Stokes vector  $\mathbf{St}_{inc}(t_i)$  ( $= [I_{inc}, Q_{inc}, U_{inc}, V_{inc}]^T$ ) of the incident laser pulse emitted at time  $t_i$  as follows:

$$\mathbf{St}_p(t_i + \Delta t) = \eta P_0/d^2 \mathbf{M}_p \mathbf{St}_{inc}(t_i) \quad (4. 2)$$

Where  $d$  is the distance from the particles to the detector and  $\eta/d^2$  accounts for the collection solid angle ( $\eta$  is the detection efficiency) and  $P_0$  is the laser incident power. The  $\mathbf{M}_p$ -matrix is the Mueller matrix that accounts for the modification of the polarization state of the laser pulse during its propagation in the particles medium and in the air surrounding medium. The particles backscattering signal  $P_p$  corresponds to the first component of the Stokes vector  $\mathbf{St}_p$ , since our detector only measures the total light intensity and is obtained by projecting the  $\mathbf{St}_p$ -vector on the  $[1, 0, 0, 0]^T$  vector, as done by M. Hayman et al. (2012).

#### (a) Mueller matrix $\mathbf{M}_p$ of the particle and surrounding air

Using the Mueller matrix formalism allows to decompose the matrix  $\mathbf{M}_p$  as the product of the successive Mueller matrices encountered by the laser pulse during its propagation from the laser cavity to the detector:

$$\mathbf{M}_p = \mathbf{M}_R \times \mathbf{T}_{air, -k} \times \mathbf{F}_p \times \mathbf{T}_{air, k} \times \mathbf{M}_E \quad (4. 3)$$

The Mueller matrices  $\mathbf{M}_E$  and  $\mathbf{M}_R$  correspond to emitter and receiver optical devices, and include the retro-reflecting PBC and a quarter-wave plate (QWP). In between  $\mathbf{M}_E$  and  $\mathbf{M}_R$ , the particles backscattering is taken into account through the particles scattering phase matrix  $\mathbf{F}_p$  (see Section 2.1). The propagation of the incident laser pulse in the air surrounding medium is described by the  $\mathbf{T}_{air,k}$  and  $\mathbf{T}_{air,-k}$  matrices, where  $\mathbf{k} = 2\pi/\lambda \mathbf{u}$  is the incident laser wavevector represented in Figure 4.1 ( $\mathbf{u}$  is the unit vector in the  $z$ -direction). It is important to note that, by combining Equations (4.1) to (4.3), the scattering matrix  $\mathbf{F}_p$  of the particles ensemble can be determined by varying the  $\mathbf{M}_E$  or / and  $\mathbf{M}_R$  Mueller matrices. To modify  $\mathbf{M}_E$  and  $\mathbf{M}_R$ , we inserted a QWP after the retro-reflecting PBC on the optical pathway from the laser source to the particles. By rotating the angle  $\psi$  between the horizontal ( $x,z$ )-plane and the fast axis of the QWP, we modulate the incident laser linear polarization and measure the corresponding

$T_p$ -signal as a function of  $\psi$  ( $\psi$  is counted counter clockwise when looking in the z-propagation optical axis).

*Mueller matrix  $M_E$  of the emitter*

The Mueller matrix  $\mathbf{M}_E$  of the emitter optics, composed of a PBC and a QWP, has been derived from (Shurcliff, 1962):

$$\mathbf{M}_E = \frac{1}{2} \begin{bmatrix} 1 & 0 & 0 & 0 \\ 0 & \cos^2(2\psi) & \sin(4\psi)/2 & -\sin(2\psi) \\ 0 & \sin(4\psi)/2 & \sin^2(2\psi) & \cos(2\psi) \\ 0 & \sin(2\psi) & -\cos(2\psi) & 0 \end{bmatrix} \begin{bmatrix} T_p & T_p & 0 & 0 \\ T_p & T_p & 0 & 0 \\ 0 & 0 & 2T_s^{1/2} & 0 \\ 0 & 0 & 0 & 2T_s^{1/2} \end{bmatrix} \quad (4.4)$$

The imperfections of the PBC are described by its s-transmission coefficient  $T_s \ll 1$  since a perfect PBC would have  $T_s = 0$  and  $T_p = 1$  and would transmit the incident laser linear polarization corresponding to the Stokes vector  $[1, 1, 0, 0]^T$  without any modification.

*Mueller matrix  $M_R$  of the receiver*

In the backscattering geometry, the same optical components {PBC + QWP} are crossed after the particle backscattering in the opposite direction ( $-\mathbf{k}$ ). As a consequence, the receiver optics Mueller matrix  $\mathbf{M}_R$  can be derived from Equation (4.4) by changing the angle  $\psi$  to its opposite, while using the PBC as a retro-reflector (we hence replace  $T_p$  with  $R_s$  and the retro-reflecting PBC imperfections are now addressed by its p-reflectance coefficient  $R_p \ll 1$ ):

$$\mathbf{M}_R = \frac{1}{2} \begin{bmatrix} R_s & -R_s & 0 & 0 \\ -R_s & R_s & 0 & 0 \\ 0 & 0 & 2R_p^{1/2} & 0 \\ 0 & 0 & 0 & 2R_p^{1/2} \end{bmatrix} \begin{bmatrix} 1 & 0 & 0 & 0 \\ 0 & \cos^2(2\psi) & -\sin(4\psi)/2 & \sin(2\psi) \\ 0 & -\sin(4\psi)/2 & \sin^2(2\psi) & \cos(2\psi) \\ 0 & -\sin(2\psi) & -\cos(2\psi) & 0 \end{bmatrix} \quad (4.5)$$

The use of a second PBC in the detector (see Section 3.2.2) enables to minimize the polarization cross-talk, which is equal to  $R_p \times T_s$ , in the range of  $10^{-5}$ . It follows that only the s-polarization of the backscattering radiation is measured on our detector. The scattering phase matrix  $\mathbf{F}_p$  of the particles scattering medium has been detailed in Equation (2.2) for arbitrary particles in random orientation. As shown by K. Sassen (2005), extinction is not sensitive to the polarization state of the light. Hence, the Mueller matrices  $\mathbf{T}_{\text{air}, \mathbf{k}}$  and  $\mathbf{T}_{\text{air}, -\mathbf{k}}$  associated to the air surrounding medium do not modify the polarization state of the incident

laser pulse and be considered as transmission factor. As a consequence, backscattering from the air surrounding medium is not a main concern and as detailed in Equation (4.1), it can be subtracted to the backscattering signal to extract the particles backscattering signals  $\mathbf{P}_p$ .

*Mueller matrix  $M_p$*

As  $\mathbf{T}_{\text{air}, \mathbf{k}}$  and  $\mathbf{T}_{\text{air}, -\mathbf{k}}$  do not depend on the polarization, we may hence write the  $\mathbf{M}_p$ -Mueller matrix (Equation (4.3)) as follows  $\mathbf{M}_p = \mathbf{M}_R \times \mathbf{F}_p \times \mathbf{M}_E$ . By neglecting any polarization cross-talk (i.e. assuming  $R_p = T_s = 0$ ) and combining Equations (2.2), (4.4) and (4.5), we get for the  $\mathbf{M}_p$ -Mueller matrix:

$$M_p = \frac{1}{4} \begin{bmatrix} R_S & -R_S & 0 & 0 \\ -R_S & R_S & 0 & 0 \\ 0 & 0 & 0 & 0 \\ 0 & 0 & 0 & 0 \end{bmatrix} \begin{bmatrix} 1 & 0 & 0 & 0 \\ 0 & \cos^2(2\psi) & -\sin(4\psi)/2 & \sin(2\psi) \\ 0 & -\sin(4\psi)/2 & \sin^2(2\psi) & \cos(2\psi) \\ 0 & -\sin(2\psi) & -\cos(2\psi) & 0 \end{bmatrix} \begin{bmatrix} F_{11,p} & 0 & 0 & F_{14,p} \\ 0 & F_{22,p} & 0 & 0 \\ 0 & 0 & -F_{22,p} & 0 \\ F_{14,p} & 0 & 0 & F_{11,p} - 2F_{22,p} \end{bmatrix} \begin{bmatrix} 1 & 0 & 0 & 0 \\ 0 & \cos^2(2\psi) & \sin(4\psi)/2 & -\sin(2\psi) \\ 0 & \sin(4\psi)/2 & \sin^2(2\psi) & \cos(2\psi) \\ 0 & \sin(2\psi) & -\cos(2\psi) & 0 \end{bmatrix} \begin{bmatrix} T_p & T_p & 0 & 0 \\ T_p & T_p & 0 & 0 \\ 0 & 0 & 0 & 0 \\ 0 & 0 & 0 & 0 \end{bmatrix} \quad (4.6)$$

### (b) Particles backscattering signal $\mathbf{P}_p$

We have calculated  $\mathbf{P}_p$  for a linearly polarized laser pulse, corresponding to the Stokes vector  $\mathbf{S}_{\text{inc}} = [1, 1, 0, 0]^T$ . By injecting Equation (4.6) into Equation (4.2), then projecting the particles backscattering radiation on the unitary vector  $[1, 0, 0, 0]^T$ , after a few calculations, we get the following expression for  $\mathbf{P}_p(\psi)$ :

$$\mathbf{P}_p(\psi) = \frac{\eta \cdot P_0}{2d^2} \times \left[ F_{11,p} + F_{22,p} + (F_{11,p} - 3F_{22,p}) \times \cos(4\psi) \right] \quad (4.7)$$

$\mathbf{P}_p(\psi)$  hence only depends on  $F_{11,p}$  and  $F_{22,p}$  so that by performing accurate particles backscattering signals measurements for a set of different  $\psi$ -angles, it is possible to accurately evaluate the  $F_{11,p}$  and  $F_{22,p}$ -coefficients to retrieve the particles depolarization  $D_p$  defined in Equation (2.5) for an ensemble of nanoparticles in ambient air, and this, for the first time in the exact backscattering direction.

### 4.1.3 Experimental set-up

The setup developed and built for the exact backscattering measurement is detailed in Figure 4.2. The laser pulses are generated by a tripled-Nd:YAG laser source, delivering 25 mJ energy

at a 10 Hz repetition rate. The laser wavelength ( $\lambda = 355$  nm) has been chosen to increase our sensitivity to nano-sized particles, in the range of a few cents of nanometers (see Figure 2.6). The laser pulse duration  $\tau = 5$  ns is below the time-of-flight  $\Delta t = 2d/c = 40$  ns, and, as in lidar applications, the laser cavity trigger (rise time of 100 ps) is used to fix the time origin. At the exit of the laser cavity, a half-wavelength plate  $\text{HWP}_E$  (HWP-355-100-2, MG) and a polarizing beamsplitter cube  $\text{PBC}_E$  (PBSO-355-050, MG) are used to set the p-polarization of the incident laser pulse, corresponding to the Stokes vector  $\mathbf{St}_{\text{inc}} = [1, 1, 0, 0]^T$ . Moreover the  $\text{HWP}_E$  and  $\text{PBC}_E$  are used to adjust the laser energy without changing the laser alignment. In Figure 4.2, the emitter optics system is composed of the PBC and the QWP, while the three components QWP, PBC and  $\text{PBC}_D$  figure the receiver optics system. The p-polarization of the laser pulse is transmitted through the PBC (PBSO-355-100, MG), also used to retro-reflect, towards the detector, the s-polarization of the backscattering radiation. This air-spaced PBC has an extinction ratio  $T_p/T_s$  greater than 250:1 at  $\lambda = 355$  nm and is 355 nm-AR-coated. A precise alignment procedure has been followed to achieve the backscattering geometry described in Figure 4.1. During this procedure, the 355 nm-laser was also used as an alignment laser, which entered the detector by its exit, so as to precisely position the retro-reflecting PBC on the detector x-optical axis, in exact perpendicular direction to the z-optical axis, materialized by the 355 nm-laser pulses. Moreover by using the Helmholtz reciprocity, the laser entering the detector from its exit is used to visualize the detector field of view. Hence the laser is aligned on the detector field of view to ensure that exact backscattering is observed. The use of a diffuser and the observation of diffraction rings from several irises along the optical paths allowed defining the detector x-axis perpendicular to the z-optical axis, with a maximum deviation of  $1 \text{ mm} \cdot 10^{-1}$ , corresponding to 0.1 mrad.

The laser specifications determine the backscattering volume, which is defined, along the z-axis, by the length  $\ell = c\tau/2 = 0.75$  meter, and in the (x, y) transverse plane, by the waist of the laser (beam-profile measurements led to 9 mm waist for  $z = d = 5$  m). The particles flux enters this volume through a  $1/4''$ -injection nozzle, chosen for injecting all the particles in the backscattering volume, to increase the signal-to-noise ratio. The nanoparticles, generated with a commercial atomizer (TSI, model 3079), are not static but move in a  $4 \text{ L} \cdot \text{min}^{-1}$  particles flow rate. The use of a commercial compressed-clean air nebulizer prevented from particles coagulation. After the diffusion drier (used to remove the water liquid phase), the moving particles enter the scattering volume before leaving the experiment through an exhaust pump. We hence generated water droplets in ambient air, or, alternatively, solid salt particles in

ambient air. According to the manufacturer, their size was in the range of a few hundreds of nanometers. We controlled their number concentration with a TSI particle counter to ensure it is stable during the measurements. The stability of the generated particle number concentration and the role of the QWP are discussed along with the results in Section 4.1.4. Our AR-coated QWP (QWPM-355-10-4, MG) has been tilted from normal incidence by  $\theta_i = 2.5^\circ$  to compensate for some of its imperfections (Poirson et al., 1995). This also helped to minimize the partial reflections on the QWP. The influence of the tilt angle on the retrieved particles depolarization is discussed in Section 4.1.4.

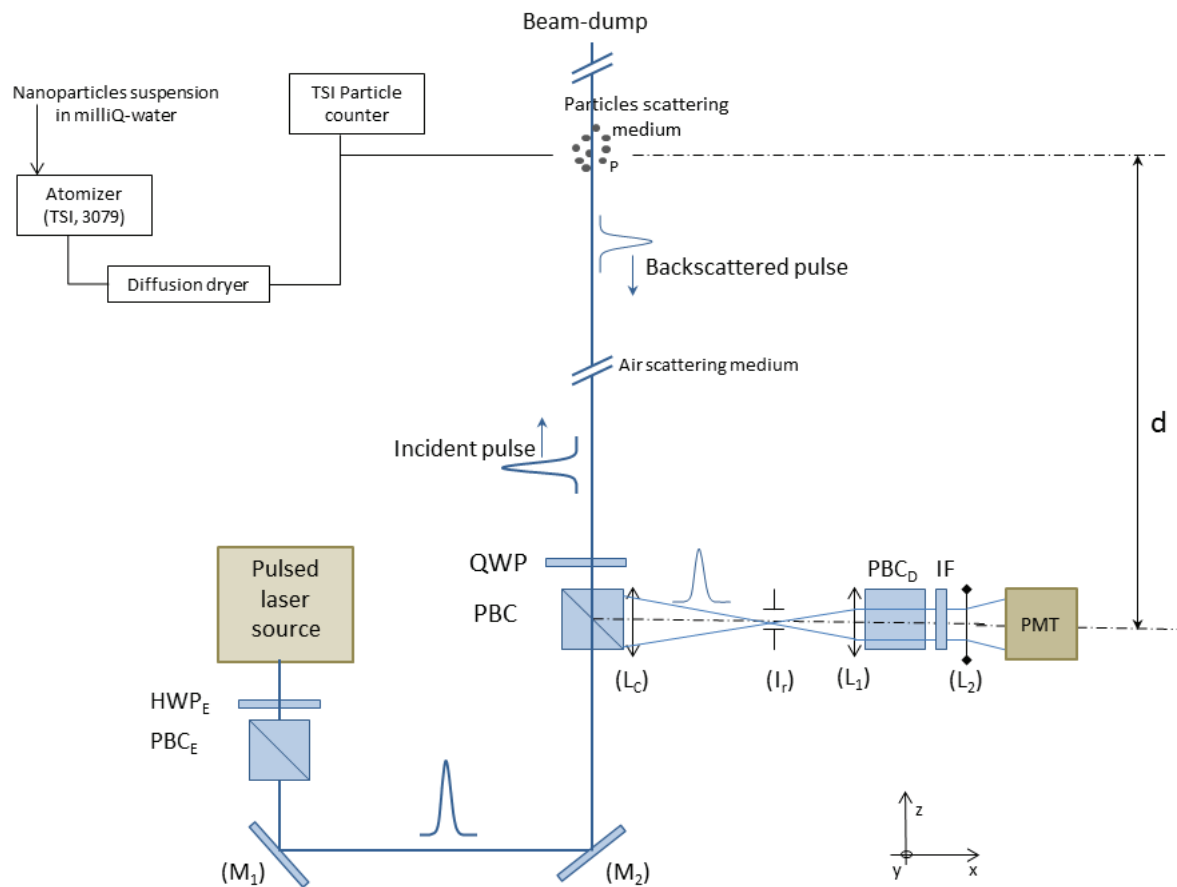


**Figure 4.2** Experimental set-up for measuring the exact backscattering of light pulses by an ensemble of particles in ambient air. The nanosecond time-resolved particles backscattering radiation is collected and detected after retro-reflection on a PBC. The nanoparticles were generated by atomization from a liquid water solution, then dried. An air-cooled 355 nm beam-dump (EKSMA optics) was placed a large distance from the particles to block the laser propagation.

### (a) Detector setup

The whole detector is housed in a secured dark box to minimize stray light. It is composed of a second PBC ( $PBC_D$ ), a collecting lens ( $L_C$ ), two supplementary lenses ( $L_1$ ) and ( $L_2$ ), an interference filter ( $IF$ ) and a photomultiplier tube ( $PMT$ ). The secondary PBC is used to

minimize the polarization cross-talk  $R_p \times T_s$  equal to a few  $10^{-5}$ , which is fully negligible. Accordingly, only the s-polarization of the backscattering radiation is detected. The 355 nm-IF is used to remove the non-elastic contribution from the collected backscattering signal. As shown by David et al. (2012), it also helps minimizing the molecular contribution to the collected backscattering signal, which improves the signal-to-noise ratio of the particles backscattering signal  $P_p$  by minimizing  $P_0$ . At the exit of the Licel PMT (DC-350 MHz electrical bandwidth), the photo-electrons are sampled with a 12 bits digital oscilloscope (Le Croy HDO4054, 300 MHz, 2.5 GS/s), necessary for a time-resolved precise measurement of the low particles backscattering signal  $P_p$ . Special care has been taken to efficiently collect the particles backscattering signal  $P_p$ , which might be low for particles in air, while minimizing the stray light contribution  $P_0$ . The iris  $I_r$  (diameter  $\emptyset$ ) is used for that purpose by limiting the amount of collected stray light. The converging lens ( $L_1$ ) is used to parallelize the backscattering radiation before entering  $PBC_D$  whose acceptance angle is equal to  $2^\circ$ . The diverging lens ( $L_2$ ) is used to focus the backscattered photons on the 6 mm-diameter photocathode of a Licel photomultiplier tube, used as a photo-detector.

### **(b) Collection efficiency optimization**

The collection efficiency of the detector has been numerically evaluated and is here presented. Let us consider a small scattering volume element materialized by a point  $P_V(x, y, z)$  of the particles scattering medium, as represented in Figure 4.3. The scattering radiation induced by  $P_V$ , is collected by the lens ( $L_C$ ) under the solid angle  $\Delta\Omega = 2\pi \times (1 - \cos \gamma)$ , where  $2\gamma$  is the apex angle of the cone defined by the clear aperture of lens ( $L_C$ ) and the distance  $d = OP_V$  from the collecting lens ( $L_C$ ) to the point  $P_V$ . Only a fraction  $\chi$  of this collected light ( $I_{coll}$ ) reaches the PMT, mostly due to the size of the iris  $I_r$  as the finite diameters of  $L_1$  and  $L_2$  have a negligible influence. To optimize the collection of the  $P_p$ -signal, we have built a numerical program, based on matrix geometric optics, to analyze our multi-component optical system. As represented in Figure 4.3, this program considers the optical rays of light scattered by  $P_V$  toward ( $L_C$ ). It then computes the optical paths of these rays through the detector. The fraction  $\chi$  is then computed from the overlap between these rays reaching  $L_C$  and the optical components of the detector. This program evaluates  $\chi$ ,  $\Delta\Omega$  and their product  $\Delta\Omega \times \chi$  as a function of the position of the point  $P_V$  in the scattering volume element.

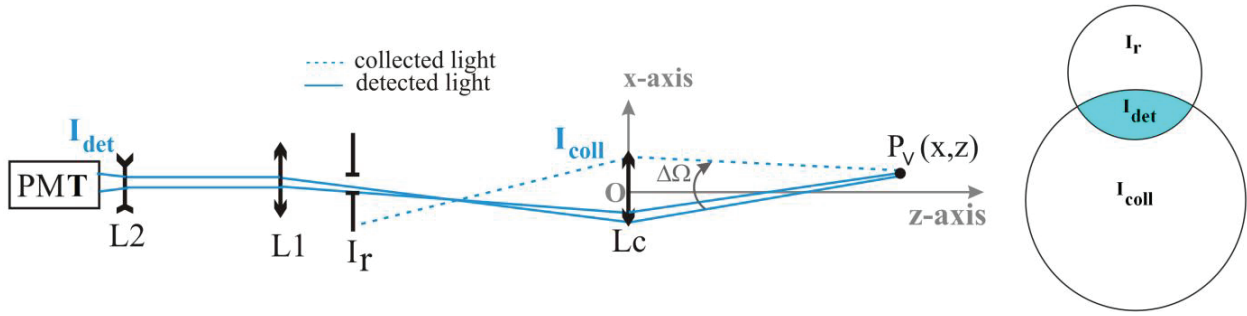


**Figure 4.3** Scheme of the numerical simulation (a). The backscattered light from a point  $P_V(x, y, z)$  is collected by  $(L_C)$  with a  $\Delta\Omega$  solid angle. On ly a fraction  $\chi$  of this collected light is detected. The simulation compute this fraction  $\chi = I_{det}/I_{coll}$ , where  $I_{coll}$  is the light collected by  $(L_C)$  and  $I_{det}$  is the light detected by the PMT.  $I_{det}$  is computed by the overlap between the collected light  $I_{coll}$  and the iris  $I_r$  (b). The finite diameters of the  $(L_1)$  and  $(L_2)$  lens have a negligible effect on  $\chi$ .

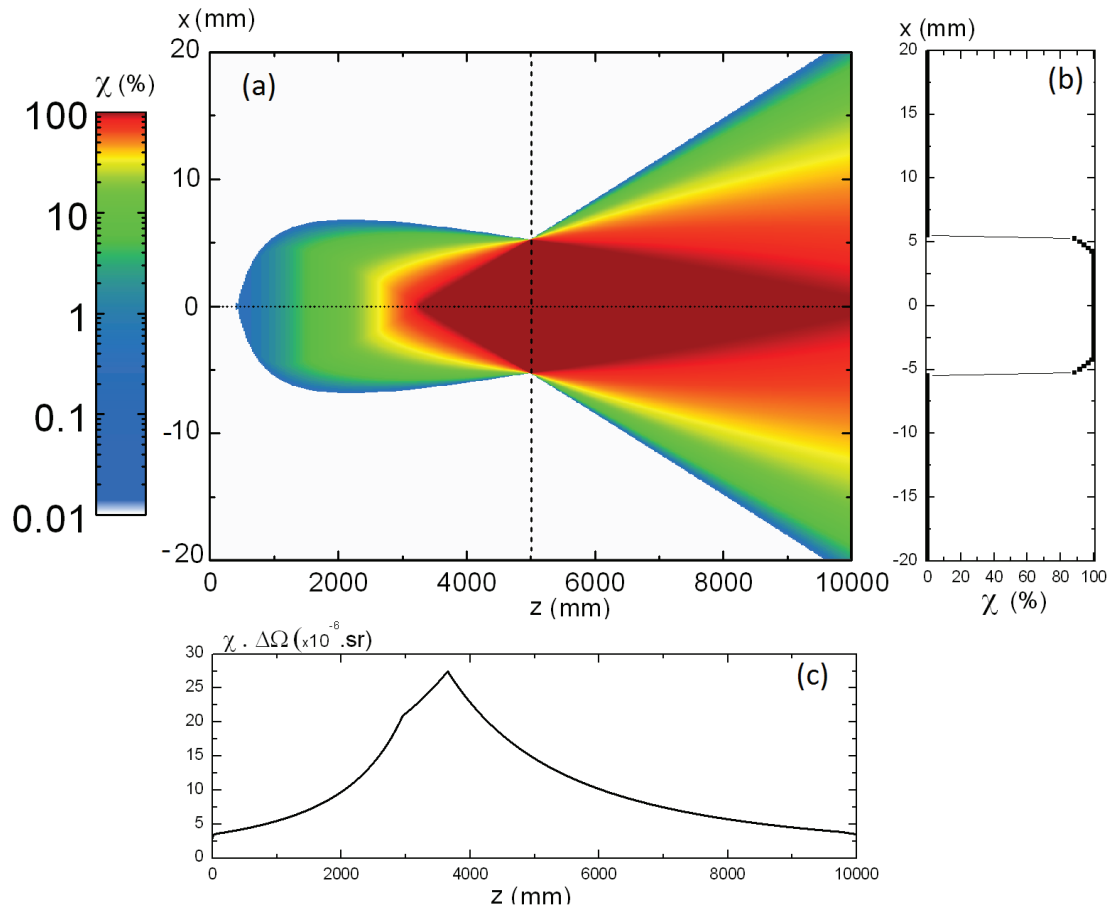
Figure 4.4-a displays the collection efficiency  $\chi$  as function of  $z$  and  $x$  coordinate of  $P_V$ , by taking into account the set of input parameters given in Table 4.2.  $\chi$  is only plotted as a function of  $x$ , as  $\chi$  along  $x$ - or  $y$ -axis are equivalent due to the detector symmetry. As can be seen in Figure 4.4-a, no scattered light is collected ( $\chi = 0\%$ ) as soon as the absolute value of  $x$  ( $|x|$ ) is higher than 20 mm, which in fact strongly reduces the detected stray light. While reducing the stray light,  $\chi$  reaches 100% for  $z > 3.7$  meters.

**Table 4.2** Characteristics of the optical set-up collecting the particles backscattering radiation. The matrix optics numerical program computes the distances  $D$ ,  $D_\emptyset$  and  $D_1$  for the following set of input values:  $\emptyset_c = \emptyset_1 = \emptyset_2 = 25.4$  mm,  $\emptyset = 1$  mm, using a 100 mm distance between  $(L_1)$  and  $(L_2)$ .

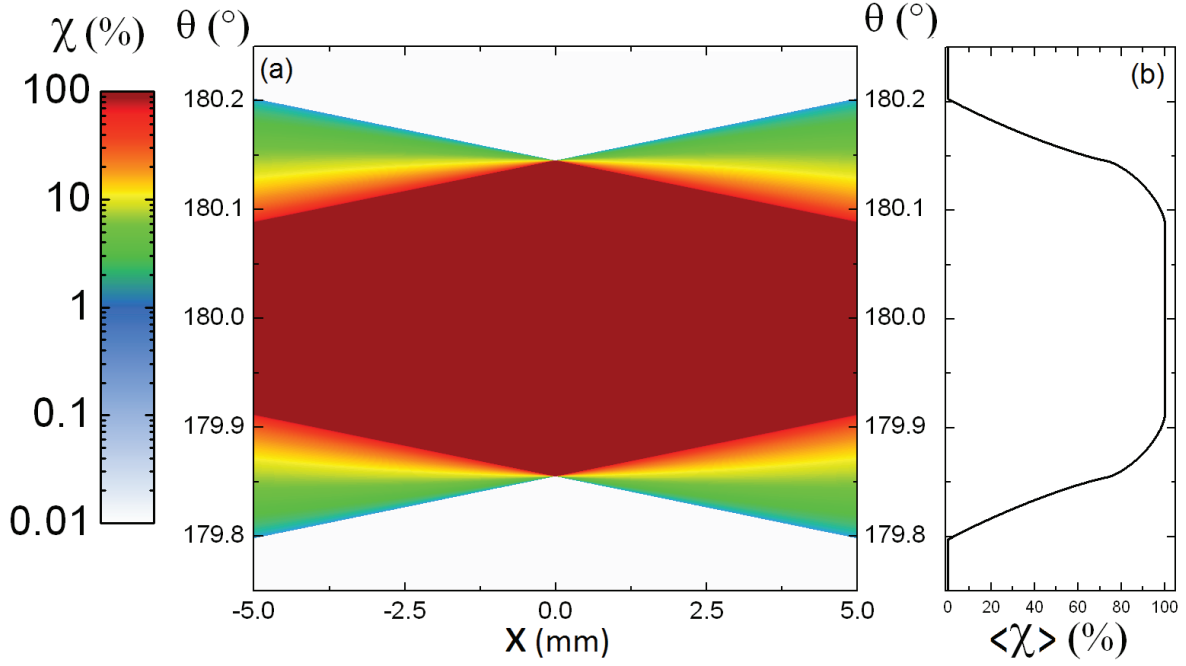
Set-up parameter	Numerical value (mm)
Lens diameter ( $L_C, L_1, L_2$ )	$\emptyset_c = \emptyset_1 = \emptyset_2 = 25.4$
Iris diaphragm	$\emptyset = 1$
$(L_C)$ focal lens	$f_c = 432.7$
$(L_1)$ focal lens	$f_1 = 38.7$
$(L_2)$ focal lens	$f_2 = -29.0$
Distance between the particles group and $(L_C)$	$d = 5000$
Distance $(L_C)$ to iris	$d_\emptyset = 474$
Distance $(L_C)$ to $(L_1)$	$d_1 = 512$

Figure 4.4-c represents  $\Delta\Omega \times \chi$ -value along the optical axis, which is maximum at  $z = 3.7$  meters and is strictly decreasing below and beyond this value. Hence the PBC and the QWP, which induce stray light, should be positioned as close to  $L_C$  as possible to reduce their contribution to the signal. As can be seen in Figure 4.4-a, when the scattering point  $P_V$  deviates from the  $z$ -optical axis by  $\Delta x = \pm 5$  mm, a 100%  $\chi$ -collection efficiency is obtained for  $\emptyset = 1$  mm only if  $z = d = 5$  meters. Figure 4.4-b displays the profile of  $\chi$  at  $z = 5$  meters

and confirms that  $\chi$  reach 100 % for  $\Delta x = \pm 5$  mm while beyond  $\Delta x = \pm 5$  mm  $\chi$  falls to zero. We then set the distance  $d$  to 5 meters. Note that this  $d$ -distance is sufficiently high for the retro-reflecting PBC to operate well-below its acceptance angle of  $2^\circ$ . We then deduced the distances  $d_\theta$  (between  $L_C$  and  $I_r$ ) and  $d_1$  (between  $L_C$  and  $L_1$ ) from geometrical optics. In this way, our experimental set-up operates at the exact backscattering angle  $\theta = 180.0^\circ$ , with a maximum width of scattering angle detected  $\xi$  equal to  $(\Delta x + \varnothing_c/2)/d = 0.2^\circ$ , if  $\varnothing_c$  is the diameter of the collecting lens ( $L_C$ ). Hence, for the first time to our knowledge, our experimental set-up covers the exact backscattering direction with accuracy, namely  $\theta = \pi \pm \xi$  with  $\xi = 3.5 \times 10^{-3}$  rad. A more precise evaluation of the collected scattering angles is displayed in Figure 4.5-a, where  $\chi$  is computed as function of  $\theta$  and  $x$  for  $z = d$ . Figure 4.5-b displays the mean value of  $\chi$  ( $\langle \chi \rangle$ ) as function of  $\theta$ , where  $\langle \chi \rangle$  is averaged over the corresponding row in Figure 4.5-a. Figure 4.5-b hence represents the collection efficiency of our experimental setup as a function of the scattering angle  $\theta$ .



**Figure 4.4** Numerical simulation of the fraction  $\chi$  of the collected light reaching the detector. Panel (a) presents a color plot of  $\chi$  as function  $z$  (along the optical axis direction) and  $x$  (perpendicular to optical axis direction). The dashed line and dotted lines in in panel (a) represent the profiles displayed in panel (b) and (c) respectively. Panel (b) presents the profile of  $\chi$  along  $x$  axis at the particle injection where  $z = d = 5000$  mm. Hence when  $z=d=5000$  mm, the scattered light is detected only if  $x \in [-5,+5]$  mm. Panel (c) displays  $\chi \cdot \Delta\Omega$  along the optical axis ( $x=0$ ) as function of  $z$ , which is proportional to the measured signal.



**Figure 4.5** Numerical simulation of  $\chi$  as function of  $\theta$  and  $x$  (panel (a)). Panel (b) plot the mean value of  $\chi$  ( $\langle\chi\rangle$ ) as function of  $\theta$ , which is average over the corresponding row in panel (a).

### (c) Far-field approximation

As summarized in Table 4.3, the proposed detection set-up fulfills the far-field scattering conditions settled in Section 2.1, corresponding to Equations (9, 10, 51, 71, 73) from Mishchenko et al. (2004), for the following set of numerical values: particle radius  $r = 1 \mu\text{m}$ , distance scattering volume-observation point  $d = 5 \text{ m}$ , wavelength  $\lambda = 355 \text{ nm}$ , maximum linear dimension of the particle volume element  $L_{\text{max}} = 15 \text{ mm}$  (which is voluntarily overestimated), wave number in ambient medium  $k_{\text{air}} = 1.77 \times 10^7 \text{ m}^{-1}$ , diameter of the collecting lens  $\varnothing_C = 25.4 \text{ mm}$  and averaged distance between neighboring particles  $\text{dist}_p = 1.87 \times 10^{-6} \text{ m}$ .

**Table 4.3** Summary of the condition to respect to performed far-field measurement. The equations are extracted from Mishchenko et al. (2004) and (#) indicates the number of the equation in this article. The condition is fulfilled if the ratio of the left term to right term of the equation is much greater than 1. Hence all the conditions are fulfilled with our experimental setup.

Equation	(#)	left term to right term ratio
$d \gg r$	(9)	$5 \times 10^6$
$r \gg k_{\text{air}} r^2/2$	(10)	$5.65 \times 10^6$
$\pi/(2 k_{\text{air}} r) \gg \varnothing_C / (2d)$	(51)	35.5
$r \gg L_{\text{max}} k_{\text{air}} r / \pi$	(71)	59.2
$k_{\text{air}} r \gg 1$	(73)	$8.85 \times 10^7$

Finally, the particles can be assumed as randomly-oriented. Though not easy to check, this assumption can be addressed from the Kolmogorov scale, which determines the smallest scale for observing a vortex in a viscous air flow (Perkins, personal communication). In our experiment, the Kolmogorov scale, fixed by the Reynolds number of our flow and by our geometry, is equal to  $6 \times 10^{-5}$  meters, which is very low and well below the millimeter characteristic dimension of our scattering volume including the particle scattering medium.

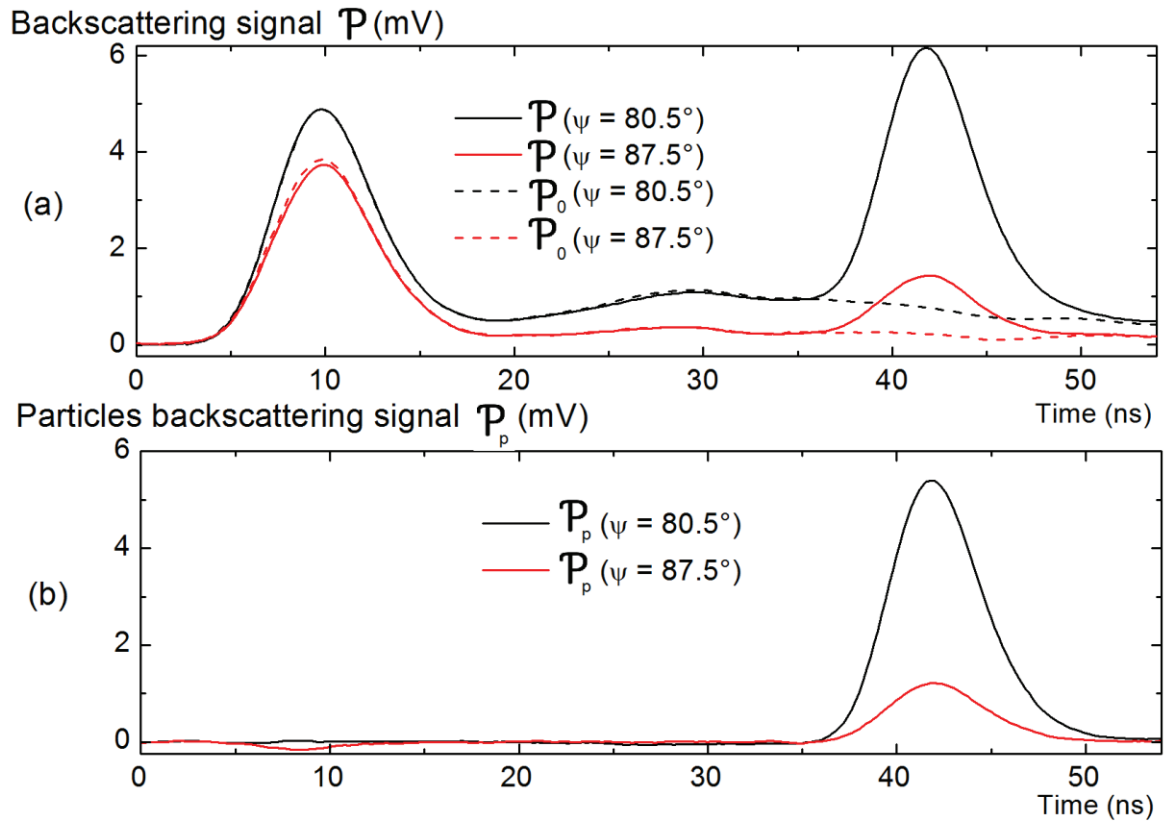
#### 4.1.4 Results and discussion

The first experimental observation of the exact backscattering of light by an ensemble of particles in ambient air has been achieved and is here reported. To test our experimental set-up, we have considered two particles case studies: water droplets suspended in ambient air, as an example of spherical particles, then salt particles in ambient air, as an example of non-spherical particles. As a first result, we present the raw data corresponding to the salt particles backscattering signal induced by UV-laser pulses. The particles UV-depolarization is then precisely evaluated for water droplets and salt crystals in ambient air with accuracy: the error is in the %-range. Finally, the measured depolarization ratios are discussed.

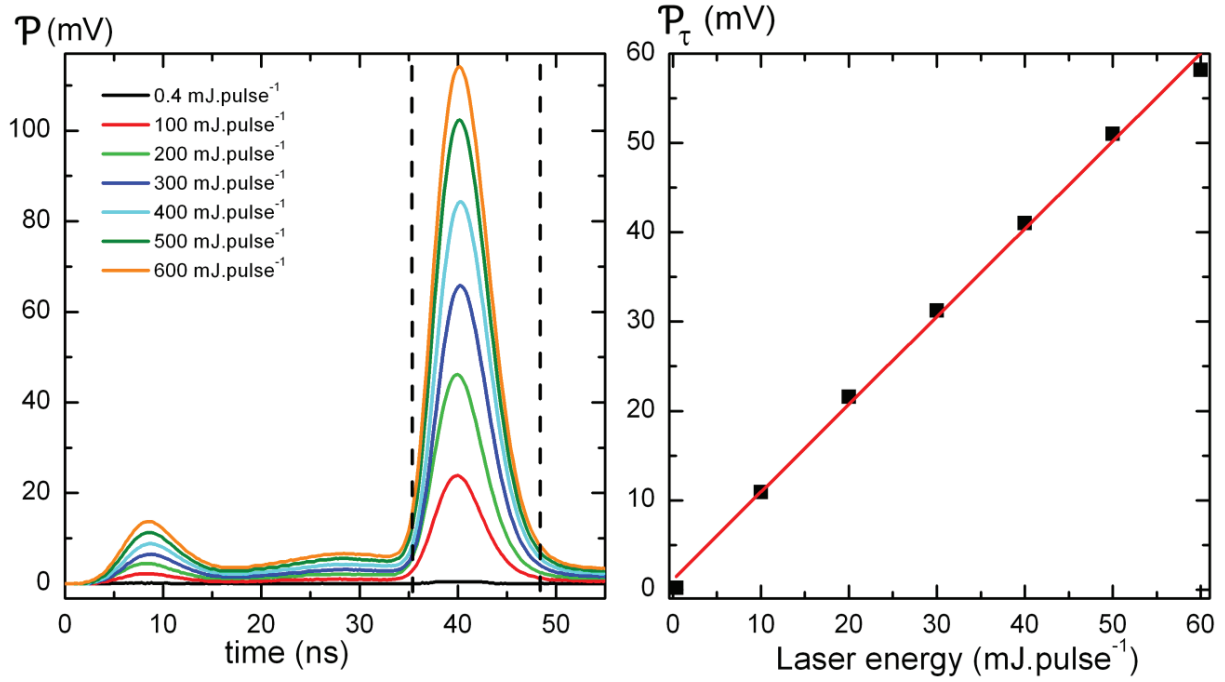
##### (a) UV exact backscattering signals

Figure 4.6-a presents the electrical detected backscattering signal  $\mathcal{P}$ , which is proportional to the UV-backscattered light, as a function of the laser pulse propagation time. Observation has been performed for two values of the angle  $\psi$  between the horizontal plane and the QWP fast axis. For each  $\psi$ -angle, the background signal  $\mathcal{P}_0$  (in dashed lines in the upper panel) has a time evolution showing the partial reflection of the laser pulse on the tilted QWP (to be seen around  $t = 10$  ns) and the air particles backscattering signal, along the optical pathway from the laser source to the detector. As shown in Figure 4.6-a, the background signal  $\mathcal{P}_0$  depends on the angle  $\psi$  and remained constant between the  $\mathcal{P}$  and  $\mathcal{P}_0$ -acquisitions. In the presence of the particles (full lines),  $\mathcal{P}$  differs from  $\mathcal{P}_0$  and this difference is the particles backscattering signal  $\mathcal{P}_p$  as shown by Equation (4.1). As plotted in Figure 4.6-b, the signal  $\mathcal{P}_p$ , which results from the difference of two signals, exhibits no systematic bias as a function of time, which means that the stray light has been efficiently removed from  $\mathcal{P}_p$ . Moreover, the  $\mathcal{P}_p$ -amplitude varies from zero to a few milli-Volts, so that the PMT, connected to a  $50 \Omega$  load resistance, is used in linear regime. The signal has been measured for different laser powers (Figure 4.7-a)

by using the  $\text{HWP}_E$  and  $\text{PBC}_E$  polarization components, to preserve the exact backscattering geometry. The corresponding signal (Figure 4.7-b) remains linear with the incident laser power over two decades. The detected light intensity being proportional to the incident laser power (Equation (4.7)), the measured signal remains linear with respect to the detected backscattered intensity over two decades. We are hence confident that the  $\mathcal{P}_p$ -signal corresponds to the detection of the particles backscattering. Due to the laser pulse duration ( $\tau = 5$  ns), this particles backscattering signal extends over a few nanoseconds.



**Figure 4.6** Observation of exact backscattering of light at 355 nm by an ensemble of particles suspended in air. Case study of salt particles. (a) Backscattering signal  $\mathcal{P}$  as a function of laser pulse propagation time, for two  $\psi$ -angles between the QWP fast axis and the horizontal scattering plane, in the presence (full-lines) and in the absence (dashed-lines,  $\mathcal{P} = \mathcal{P}_0$ ) of the particles. For  $\psi = 80.5^\circ$  (black curve), at times lower than 20 ns, the  $\mathcal{P}$  and  $\mathcal{P}_0$  black curves merge on a unique line. (b) Particles backscattering signal  $\mathcal{P}_p$  as a function of time obtained by applying Equation (1). The sign of the PMT raw data have been changed to obtain a positive voltage and the signals result from an average over 150 laser shots. The time dependence of the signal  $\mathcal{P}$  has been recorded at each time to ensure that the PMT remained in its linear regime (output voltage below 50 mV).



**Figure 4.7** Signals  $P$  for different laser energy (left graph) and signal  $P_\tau$  (signal  $s$  in the left graph integrated between the two dash line) as function of the laser energy.  $P_\tau$  is linear with the laser energy as shown by the linear fit (red line). The responsivity of the detector stays linear from less than 1 mV signal (a few mJ.pulse<sup>-1</sup>) up to at least 100 mV signal (50 mJ.pulse<sup>-1</sup>) and seems to decrease when more than more than 100 mV signal is reach (50 mJ.pulse<sup>-1</sup>). Hence to ensure signal linearity, care has been taken to never obtain signal more than 50 mV signal  $P_\tau$ .

### (b) Particles depolarization in the exact backscattering direction

As shown Figure 4.6-b, the particles backscattering signal  $P_p$  is modified when the angle  $\psi$  of the QWP is varied. Following the methodology presented in Section 4.1.2, we have measured the particles backscattering signal  $P_p$  for a set of 12  $\psi$ -values, by measuring the corresponding signals  $P$  and  $P_0$ . To account for the amount of light backscattered during the whole laser pulse duration, the particles backscattering signal  $P_p = P - P_0$  has been integrated over the time  $\tau$  for each laser shot. Then, to reduce the statistical error, we averaged this time integral over 150 laser shots and plotted the retrieved signal  $P_{p\tau}$  in Figure 4.8 as a function of  $\psi$ . The variations of  $P_{p\tau}$  have been adjusted with the  $\cos(4\psi)$ -curve corresponding to Equation (4.4). The fit retrieves  $(F_{11} - F_{22})$  and  $2F_{22}$  as they respectively correspond to the minimum and maximum values of the signal (see Equation (4.4)). We hence determine the particles depolarization  $D_p = 1 - F_{22,p} / F_{11,p}$ . From the fitting procedure, the water droplets depolarization was found equal to  $D_w = (0.04 \pm 0.08) \%$ , while we got  $D_{\text{salt}} = (8.40 \pm 0.30) \%$  for the generated salt particles (Figure 4.9). These  $D_w$ - and  $D_{\text{salt}}$ -values correspond to the following lidar particles depolarization ratios:  $\delta_w = (0.02 \pm 0.05) \%$  for water droplets and  $\delta_{\text{salt}} = (4.38 \pm 0.16) \%$  for the generated salt particles, in the exact backscattering direction.

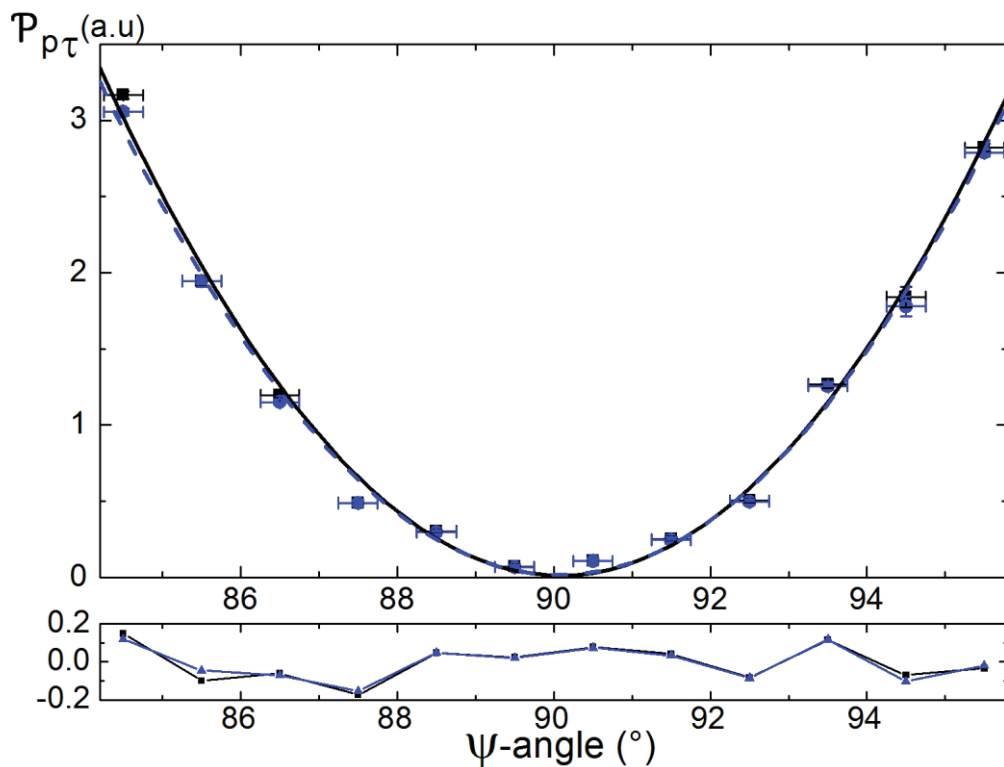


**Figure 4.8** Time integral over the pulse duration of the particles backscattering signal  $s_p$  averaged over 150 laser shots as a function of the angle  $\psi$  between the horizontal scattering plane and the QWP fast axis. Case study of water droplets particles. The error bar on the reading of the  $\psi$ -angle is equal to  $0.5^\circ$ . The plotted error bar on  $P_{p\tau}$  is too low to be visible (it is equal to  $1\sigma$  and calculated from the statistical error obtained by averaging the time integral of  $P_p(t)$  over 150 laser shots). The full-line black curve (dashed-line blue curve) corresponds to the adjustment of the data by using Equation (4) (after particles number normalization). In both cases, no systematic bias is visible on the residue plot plotted in the lower panel.

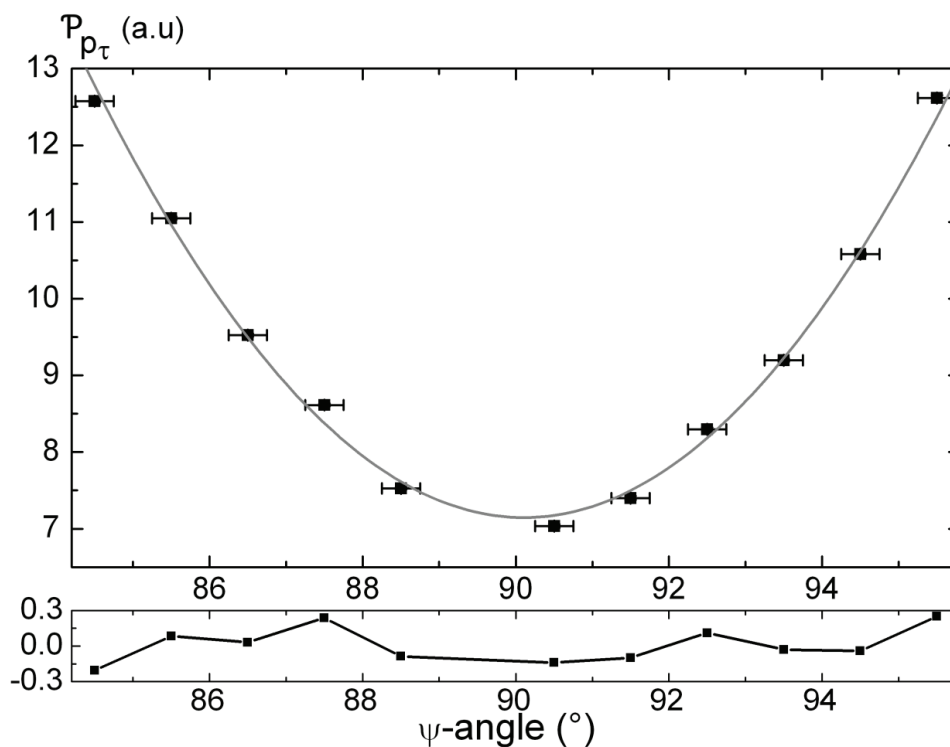


**Figure 4.9** Salt particles signal  $P_{p\tau}$  as function of  $\psi$ , for a NaCl concentration of the atomized solution equal to  $3 \text{ mol.L}^{-1}$ .

### (c) Error analyses

The statistical errors are mainly due to photon noise; thermal and electronic noises are not a major concern. This photon noise corresponds to the shot noise induced by the laser backscattered photons and the detected stray light (any detected light that has not been scattered by the generated particles). The detected stray light has been strongly reduced by building a detector with a narrow field of view. Moreover, by performing time-resolved measurements of the background signal  $P_0$  is also strongly reduced, as any stray light from the QWP and the beam-dump do not contribute to  $P_0$ . Hence, the given statistical error bars on  $D_p$  are very low, as drastically reduced by the experimental set-up, laser shot averaging (150 laser shots), by the 12-bits acquisition and by the 12  $\psi$ -values fitting procedure. The  $D_p$ -measurement is also affected by systematic errors:

- The laser intensity and particles number fluctuations are however very low: over the duration of the experiment, we measured a mean laser energy of  $(24.0 \pm 0.4) \text{ mJ.pulse}^{-1}$  and a mean particles number concentration of  $N_p = (5.23 \pm 0.15) \times 10^6 \text{ part.cm}^{-3}$ . In addition, the acquisition has been performed by choosing the 12  $\psi$ -values in an almost random order, to minimize the systematic error on  $D_p$ , due to possible experimental fluctuations, including  $N_p$ -fluctuations. Hence, the obtained residue plot exhibits no clear structure. As shown in Figure 4.8 in dashed-lines, normalization of the  $P_{pr}$ -signal by the particles number concentration does not noticeably affect the retrieved particles depolarization. In addition, pulse-to-pulse laser mode fluctuations were also minimized by using a Gaussian mirror in the laser cavity, to favor the  $TEM_{00}$  Gaussian mode.
- The exact position of the QWP along the Gaussian beam of the laser is not a main concern (Poirson et al., 1995). However, the QWP is tilted from normal incidence by an angle  $\theta_i = 2.5^\circ$  while Equation (4.4) assumes that the QWP operates at normal incidence. The Jones matrix of a QWP tilted from normal incidence by an angle  $\theta_i$  is given in (Zhu, 1994). The main correction factor is equal to  $1 - (\sin \theta_i / m_o)^2$  where  $m_o$  is the ordinary refractive index. We have expressed the Mueller matrix of a tilted QWP as a function of  $\psi$  and  $\theta_i$ . For our  $\psi$ -values (between  $84^\circ$  and  $96^\circ$ ) and an incidence angle  $\theta_i$  of  $2.5^\circ$ , we calculated that the Mueller matrix elements of the tilted QWP and found a fully negligible relative error of  $10^{-5}$  when compared to the Mueller matrix elements of a QWP at normal incidence.
- Influence of a non-perfect linear polarization of the light emitted in the atmosphere: The incident laser has a high degree of linear polarization, above 100:1. Passing through the

PBC improves this degree with a factor higher than 250:1. Hence the emitted laser has highly linearly polarized with a degree higher than 25000:1.

- Imperfect separation of polarization component, namely polarization crosstalk between  $\perp$  and  $\parallel$ -detection channels: The backscattered light is reflected by the PBC and transmitted by the PBC<sub>D</sub>, leading a polarization cross-talk  $R_p \times T_s$  equal to a few  $10^{-5}$ .
- Transmitter and receiver polarization axes misalignment: As the polarization axes of the emitter and receiver are both defined by the PBC, they cannot be misaligned.

#### (d) Comparison with the literature

Within our error bars, the observed water droplets depolarization  $D_w = (0.04 \pm 0.08) \%$  is compatible with the expected zero-depolarization value for homogeneous spherical particles, which in turn favors our experimental set-up. In addition, the single-scattering approximation, assumed from the very beginning, now appears to be realistic, since multiple scattering would have led to particles depolarization, as shown by Mishchenko et al. (2007). Indeed, the right-hand panel of Figure 5 in Mishchenko et al. (2007) provides specific quantitative evidence that at particle packing densities typically encountered with this laboratory setup, the assumption of the single-scattering regime is quite safe. Moreover, our experimental set-up has the ability to measure non-zero particles depolarization, corresponding to nonspherical particles, as are the generated salt particles. The retrieved salt particles signal  $P_{p\tau}$  are plotted in Figure 4.9 as a function of  $\psi$ . The retrieved salt particles depolarization  $\delta_{\text{salt}} = (4.38 \pm 0.16) \%$  is in the range of what is usually observed in the atmosphere by using a polarization lidar close to the sea-salt particles source region (Murayama et al., 1999). However, sea-salt particles may differ from our generated salt particles and even close to the source region, comparison of our laboratory measurement with field measurements remains difficult, as atmospheric particles are present in the form of a particle external mixture (see Section 3.5). Comparing the obtained value with a laboratory reference literature is also difficult as no apparatus exactly operates in the exact backscattering direction. For the closest value to the exact backscattering direction (Sakai et al., 2010), the observed particles depolarization for salt particles is larger than ours (15 %). However, extrapolation up to  $180.0^\circ$  may lead to quite important errors (Schnaiter et al., 2012) and in our experiment the relative humidity (RH) is probably too high for the particles to depolarize as in Sakai et al.'s experiment (2010), despite the use of a diffusion dryer. Indeed, for a higher relative humidity, we retrieve  $\delta_{\text{salt}} = (1.09 \pm 0.11) \%$  instead of  $\delta_{\text{salt}} = (4.38 \pm 0.16) \%$ , which support the assumption that higher relative humidities lead to less depolarizing particles.

### (e) Influence of the PSD and comparison with numerical model

Moreover, we show in this paragraph that the salt PSD also influence the measured  $\delta_{\text{salt}}$ , so that comparing our measurements with Sakai et al. (2010) is further complicated.  $\delta_{\text{salt}}$  has been measured for four different PSD plotted in Figure 4.10-a. These PSD's have been obtained by using a TSI differential mobility analyzer coupled with a condensation particle counter. Four different PSDs have been obtained by changing the NaCl concentration of the atomized salt solution.

Figure 4.10-b displays the corresponding  $\delta_{\text{salt}}$  as a function of the mean radius  $\langle r \rangle$  of the four PSDs ( $\langle r \rangle = 1/N_p \int r \cdot n_p(r) \cdot dr$ ). When the mean particles radius increases from 37 to 90 nm, the retrieved  $\delta_{\text{salt}}$  increases by a factor five from  $(0.20 \pm 0.05) \%$  to  $(1.09 \pm 0.11) \%$ . T-matrix numerical simulations of  $\delta_{\text{salt}}$  have been achieved for the four generated salt PSD by using a  $m = 1.51 - 0.0004i$  -refractive index at 355 nm. The obtained numerical results for spheroids having a  $\varepsilon = 1.05$  aspect ratio are displayed in Figure 4.10-b where the error bars on the mean particle radius correspond to a  $\pm 10\%$ -uncertainty, as done in Section 2.4.3. A quite good agreement is found between the measured and the simulated  $\delta_{\text{salt}}$ -values, at least for mean particle radii around 100 nm, which shows that, within error bars, the generated salt particles might be simulated with such spheroids.

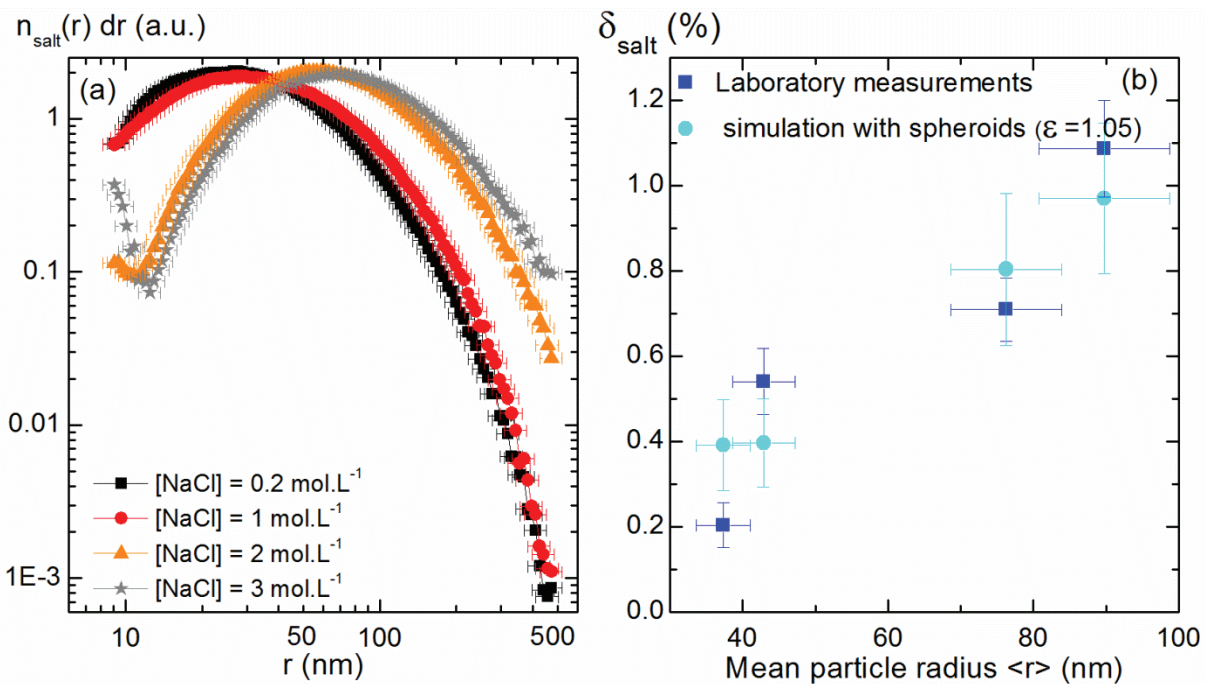


**Figure 4.10** Salt PSDs generated by changing the salt (NaCl) concentration in the atomized solution (a).  $\delta_{\text{salt}}$  measured on the corresponding PSD (blue squares in panel (b)) and  $\delta_{\text{salt}}$  simulated with the same PSD and spheroids with an aspect ratio  $\varepsilon = 1.05$  (cyan circles in panel (b)).

### 4.1.5 Conclusion

In this section, a new experimental set-up has been developed to precisely measure the exact backscattering of light by an ensemble of nanoparticles in ambient air, which may help validating numerical simulations which are never assumption-free and may be also useful in active lidar remote sensing field experiments. A pulsed laser source and a polarizing beamsplitter cube have been used to fulfill the needed requirements of a high angular resolution and a high dynamical range to cover the exact backscattering direction, for the first time for particles in ambient air. The exact backscattering direction is covered with accuracy:  $\theta = \pi \pm \xi$  radians with  $\xi = 3.5 \times 10^{-3}$  radian the maximum width of detected scattering angles. Special care has been taken to optimize the collection of the particles backscattering signal  $\mathcal{P}_p$ , while minimizing the background stray light signal  $\mathcal{P}_0$ , and this in the UV-spectral range, to increase our sensitivity to nano-sized particles. In addition, for the first time to our knowledge, our light-scattering experimental set-up fulfills the far-field single-scattering approximation, which is generally applied in both numerical simulations and field experiments. We also reported on the first experimental observation of backscattering of light by water droplets in ambient air, as an example of spherical particles, then by salt particles in ambient air, as an example of non-spherical particles. The particles backscattering signal  $\mathcal{P}_p$  has been retrieved from the detected signal  $\mathcal{P}$  by subtracting the background signal  $\mathcal{P}_0$  obtained in the absence of the particles, the latter being constant for several minutes. Moreover, by modulating the incident laser polarization, we measured the particles depolarization with accuracy. For polarization lidar remote sensing field applications, this particles depolarization  $D_p$  can be converted into the so-called particles lidar depolarization ratio  $\delta_p$ . We hence have retrieved  $\delta_w = (0.02 \pm 0.05) \%$  for water droplets, which is compatible, within our error bars, with the expected zero-depolarization value for homogeneous spherical particles predicted by Mie. For the generated salt particles, we found  $\delta_{\text{salt}} = (4.38 \pm 0.16) \%$  with a strong dependence on RH and on generated salt particles PSD. At higher RH-values, we retrieve  $\delta_{\text{salt}} = (1.09 \pm 0.11) \%$  instead of  $\delta_{\text{salt}} = (4.38 \pm 0.16) \%$ , which support the assumption that higher relative humidity lead to less depolarizing particles. By changing the NaCl PSD, the corresponding  $\delta_{\text{salt}}$  changed by more than a factor of five (from  $(0.20 \pm 0.05) \%$  to  $(1.09 \pm 0.11) \%$ ). PSD's measurements of the generated salt particles allowed to compare our laboratory measurement with numerical simulations. Using  $m = 1.51 - 0.0004i$  for the NaCl-refractive index at 355 nm, a good agreement has been found when particles are simulated by spheroids having an aspect ratio  $\varepsilon = 1.05$ .

## 4.2 Single nanoparticle experiment

In this section, we present the first absolute measurement of the extinction cross-section of a fixed single aerosol nanoparticle. The absolute extinction cross-section has been measured as a function of the incident light polarization and wavelength by using the spatial modulation spectroscopy technique (SMS), described in (Arbouet et al., 2004) in a work dedicated to metallic nanoparticles. The work presented in this section has been achieved in collaboration with the group headed by N. Del Fatti and F. Vallée at the Institute of Light and Matter (ILM).

### 4.2.1 Introduction

As underlined by Miles et al. (2011), the study of a single particle is necessary to avoid the ambiguity induced by the inherent averaging present in particles ensemble studies, which is necessary to compare optical models with optical properties measurements. Moreover, as shown by Nirmal et al. (1996), the study of single nanocrystals has raised new knowledge on fluorescence intermittence that were never expected from measurements performed on an ensemble of particles). Hence, single particles are often studied to measure their extinction (Butler et al., 2007; Miles et al., 2011; Lombardi et al., 2013), scattering (Person et al., 2013) or fluorescence (Kaye et al., 2005; Heyes et al., 2007; Pan et al., 2012). These fluorescence, scattering or extinction measurements on a single nanoparticle have been performed for single metallic nanoparticles, such as gold (Sönnichsen and Alivisatos, 2005; Lombardi et al., 2012; Li et al., 2013; Kuhlicke et al., 2013), silver (Billaud et al., 2010; Tanabe and Tatsuma, 2012; Lee et al., 2013), or for single semiconducting nanoparticles such as quantum dots (Chung and Bawendi, 2004; Heyes et al., 2005). However, to my knowledge, such measurements have never been performed on a single dielectric nanoparticle, probably due to their lower refractive index, inducing lower scattering or extinction cross-sections (Yurt et al., 2012). In addition, in contrary to metallic nanoparticles, a dielectric nanoparticle, such as a polystyrene latex (PSL) sphere, an ammonium sulphate ((NH<sub>4</sub>)<sub>2</sub>SO<sub>4</sub>) nanoparticle or a mineral dust nanoparticle exhibits a refractive index whose imaginary part is generally weak so that their extinction is dominated by scattering.

Miles et al. (2011) recently reviewed the existing measurements of light extinction, scattering and absorption by single aerosols particle and underlined that *“this review is necessarily*

*limited to measurement on coarse particles and it is crucially important that the new techniques under development aim to push the lower size limit down to the sub-micron range*". Hence, for the first time to my knowledge, we here report the preliminary measurements of the absolute extinction cross-section of a single aerosol or dielectric nanoparticle as a function of the incident light polarization and wavelength, by using the spatial modulation spectroscopy (SMS). The extinction measurement are performed with the SMS technique, which allows measuring the absolute cross-section extinction (Lombardi et al., 2013) in contrary to other measurements, such as dark-field microscopy (Mock et al., 2002; Fan et al., 2012). The extinction cross-sections have been measured for a single polystyrene latex (PSL) sphere having a calibrated size (NIST traceable), for three single  $(\text{NH}_4)_2\text{SO}_4$  nanoparticles and two single mineral dust nanoparticles. PSL spheres (Duke scientific) are NIST traceable, which means that the particles radius is calibrated ( $r = (40.5 \pm 1.5) \text{ nm}$ ), exhibit a spherical shape and have a known refractive index ( $m = 1.59$  at  $559 \text{ nm}$ ). Hence, the measured extinction cross-section of a single PSL can be considered as a reference measurement. Indeed, absolute extinction measurements are commonly validated by using PSL's spheres (Pettersson et al., 2004; Stawa et al., 2006; Khalizov et al., 2009; Butler et al., 2009; Lang-Yona et al., 2009). The single  $(\text{NH}_4)_2\text{SO}_4$  and dust nanoparticles have been studied for environmental and climate purposes as they both are among the predominant atmospheric aerosols (Pöschl et al., 2005). This section is organized as follows. First, we present the experimental methodology. Then, the experimental measurements of the absolute extinction cross-section are presented and discussed.

#### **4.2.2 Experimental methodology**

This subsection aims at describing the methodology used to measure the absolute extinction cross-section  $C_{\text{ext,np}}$  of a single dielectric nanoparticle as a function of the incident laser polarization and wavelength. In addition, the  $C_{\text{ext,np}}$ -measurement is coupled with the observation of the fixed nanoparticle by Transmission Electron Microscopy (TEM) to correlate the optical measurements with the size and shape of the nanoparticle, as done by (Billaud et al., 2008). Hence, this subsection is organized as follows. The single dielectric nanoparticle sampling necessary to operate the SMS and the TEM observation is first presented. Then the size and shape observation of the single nanoparticles is detailed. Finally, the SMS setup and the  $C_{\text{ext,np}}$ -retrieval are presented.

### (a) Nanoparticle sampling

Here, we aim to sample nanoparticles having a chosen size and chemical composition (dust, PSL and  $(\text{NH}_4)_2\text{SO}_4$ ) on a substrate allowing both the TEM observation and the SMS measurements. Absorbing and fluorescing substrate must hence be avoided. Consequently, the nanoparticles are sampled on a TEM-grid having a 40 nanometers thick  $\text{SiO}_2$  substrate (Davletshin et al., 2012). Figure 4.11 presents the scheme of the nanoparticle sampling for dust, PSL and  $(\text{NH}_4)_2\text{SO}_4$  nanoparticles. The dust nanoparticles are generated in a dry nitrogen flux with the dust generator described in (Dupart et al., 2012). Hence, Arizona test dust nanoparticles (ATD) are generated by mechanically mixing them with a magnetic stirrer in a glass bottle continuously purged with a dry nitrogen flow. The PSL and the  $(\text{NH}_4)_2\text{SO}_4$  nanoparticles are generated with the commercial atomizer (TSI, model 3079) from their aqueous solution. These aqueous solutions are obtained by diluting the PSL solution (Duke Scientific,  $r = (40.5 \pm 1.5) \text{ nm}$ ) or dissolving pure  $(\text{NH}_4)_2\text{SO}_4$  solid crystals in milliQ-water. A diffusion dryer is used to reduce RH, except for dust nanoparticles which are already in dry conditions. Mono-sized nanoparticles are obtained by using a commercial differential mobility analyzer (except for PSL, which are already mono-sized), which drift the nanoparticles according to their electrical mobility by using an electric field. These mono-sized (mono-aerodynamic radius) nanoparticles are then deposit on the TEM-grids by using a commercial nano aerosol sampler (NAS), which use an electric field to attract the nanoparticles onto the grid.

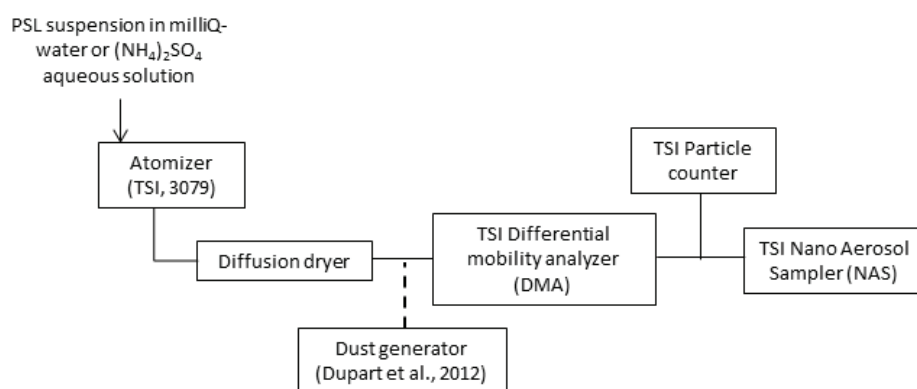


**Figure 4.11** Nanoparticle sampling. The dust nanoparticles are generated in a dry nitrogen flow with the dust generator described in (Dupart et al., 2012). PSL and  $(\text{NH}_4)_2\text{SO}_4$  nanoparticles are generated with an atomizer from an aqueous solution. A diffusion dryer is used to reduce RH (except for dust nanoparticles which are already in dry conditions). Mono-sized nanoparticles are obtained and then deposit on a TEM-grid by using respectively a differential mobility analyzer (except for PSL, which are already mono-sized) and a nano aerosol sampler (NAS). The particle counter is used to ensure depositing the appropriate concentration of nanoparticles on the TEM-grid.

A  $1\mu\text{m}$ -distance between the nanoparticles is necessary to perform SMS measurements on a single nanoparticle (Lombardi et al., 2012). Hence, a particle counter is used to ensure depositing less than  $1\text{ part.}\mu\text{m}^{-2}$  on the TEM-grid. To fix ideas, when the  $100\text{ L.h}^{-1}$  inlet flow of the NAS contains approximately  $1000\text{ part.cm}^{-3}$ , a 1 minute deposition generally provides the appropriate nanoparticles concentration on the TEM-grid.

### (b) Nanoparticle size and shape observation

We here present the single nanoparticle localization and their size and shape observation with TEM-pictures, which are further used to perform and interpret the SMS optical measurements. As shown in Figure 4.12-a, the individual nanoparticles are first selected and localized with TEM with the criterion that the nearest neighbour nanoparticle be located at least at the  $1\mu\text{m}$ -distance necessary to perform the SMS measurements. This selection is performed under low magnification (approximately  $\times 2000$ ) TEM-observation and moderate electron beam illumination, to avoid altering the optical properties of the nanoparticles (Lombardi et al., 2012). As shown in Figure 4.12-b, thanks to the preliminary TEM-observation, the selected nanoparticle can also be localized when applying the SMS-technique. Then, the optical measurements are performed with SMS on the selected nanoparticle. Finally, the nanoparticle is observed with TEM again, this time with a high magnification (approximately  $\times 200\,000$ ) to precisely characterize its size and its shape (Lombardi et al., 2013).

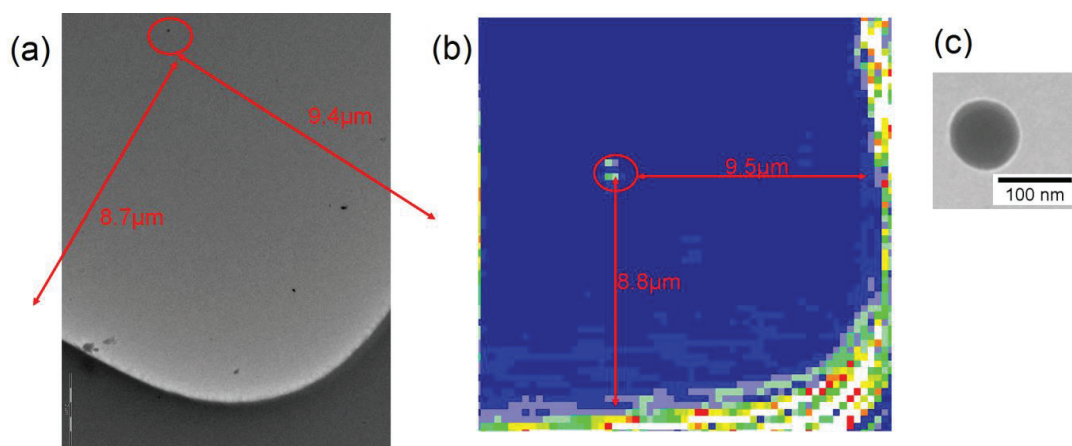


**Figure 4.12** Transmission electron microscope (TEM) observation of the nanoparticle ((a) and (c)) and localization of the corresponding nanoparticle with spatial modulation spectroscopy (b). A low magnitude TEM observation ensures no neighboring nanoparticles are closer than  $1\mu\text{m}$  to the selected single nanoparticle (a). Low magnitude observation and moderate electron illumination are used to preserve the optical properties of the observed nanoparticles. Then the selected nanoparticles is localized with the SMS technique by scanning the TEM grid (b). The distance measured with low magnitude TEM are used to ensure localizing the selected nanoparticle.

### (c) SMS experimental setup

The SMS technique measures the normalized transmission change  $\Delta T/T$  induced by the spatial modulation of a single nanoparticle in the incident light beam (Arbouet et al., 2004), where  $\Delta T/T$  is proportional to  $C_{\text{ext,np}}$  (Lombardi et al., 2012). Here, we present the SMS experimental setup used to measure  $\Delta T/T$ , followed by the  $\Delta T/T$  measurement as a function of the incident light polarization and then as a function of the incident wavelength  $\lambda$ . As shown in Figure 4.13 from Juvé (2011), a 100 $\times$  microscope objective having a 0.75 numerical aperture, focuses the light beam close to the diffraction limit (full width half maximum  $\approx 0.7 \lambda$  in the focal plane) to improve the measured  $\Delta T/T$  signal (Arbouet et al., 2004). The nanoparticle's position is modulated by a piezoelectric translation stage at the frequency  $f \approx 1.5$  kHz along the y-axis. The modulation amplitude  $\Delta y = 380$  nm has been chosen to maximize  $\Delta T/T$  (Arbouet et al., 2004). In addition, by using this piezoelectric translation stage, a (x,y) map of  $\Delta T/T$  is measured to localize the selected single dielectric nanoparticle (see Figure 4.12-b). To measure  $\Delta T/T$ , the modulated transmitted light is then collected by a second identical 100 $\times$  microscope objective, before its detection by a photodiode and its demodulation by a lock-in amplifier at the 2f-frequency. Here, the 2f-demodulation frequency is used to measure the maximum value of  $\Delta T/T$  when the particle is located at the center of the light beam, which adds precision on the localization of the dielectric nanoparticle compared with the f-demodulation (Davletshin et al., 2012).

Moreover, to account for polarization effects induced by the fixed particle,  $\Delta T/T$  has been measured as a function of the orientation of the incident laser linear polarization, which is modulated by coupling a fixed quarter-waveplate (QWP) with a rotatable Glan-Thompson polarizer. As for the experiment performed in Section 4.1, the QWP changes the incident light polarization, here from linear to circular, and the polarizer selects a linear polarization.

In addition,  $\Delta T/T$  has been measured as a function of the laser wavelength with a 10 nm resolution from 440 to 840 nm (the later value may be lower depending on the signal-to-noise ratio of  $\Delta T/T$ ). The spectral range from 690 up to 840 nm is measured by using a tunable Ti:Sa oscillator. A BBO crystal doubled the frequency of the Ti:Sapphire oscillator to cover the spectral range from 440 to 520 nm, while, between 520 and 690 nm, laser pulses are generated by an optical parametric oscillator, pumped by the Ti:Sapphire oscillator.

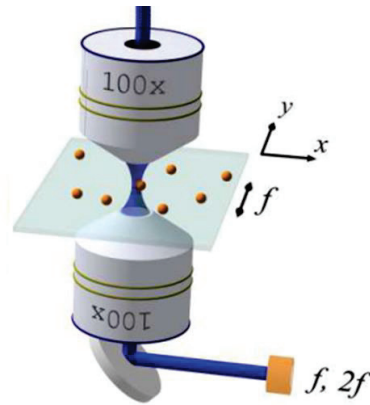


**Figure 4.13** Principle of the spatial modulation spectroscopy (figure from Juvé (2011)). A 100× microscope objective focalize the light on a single nanoparticle, which position is modulated at the frequency  $f \approx 1.5$  kHz. The transmitted light is collected by a second identical 100× microscope objective before being demodulated with a lock-in amplifier at  $2f$ -frequency

#### (d) Retrieval of the absolute extinction cross-section $C_{\text{ext,np}}$ of a single nanoparticle

Here, we present the retrieval of  $C_{\text{ext,np}}$  from the  $\Delta T/T$ -measurement. As  $\Delta T/T$  and  $C_{\text{ext,np}}$  are proportional,  $C_{\text{ext,np}}$  can be derived from  $\Delta T/T$ , if the intensity spatial profile  $I_I(x,y)$  of the light beam is precisely determined (Billaud et al., 2010). As shown in Figure 4.14, we determine  $I_I(x,y)$  from the  $\Delta T/T$  measurement around the single nanoparticle. Along the  $y$ -axis, the  $\Delta T/T$  profile observed is broader than the light beam due to the spatial modulation along this axis (Arbouet et al., 2004). Along the  $x$ -axis however, due to the absence of spatial modulation, the  $\Delta T/T$ -profile follows the light beam intensity. Hence the intensity spatial profile  $I_I(x,y)$  is determined by the Gaussian profile of  $\Delta T/T$  along the  $x$ -axis, as explained in Figure 4.14. Consequently, and as further explained by Billaud et al. (2010),  $C_{\text{ext,np}}$  can be derived from  $\Delta T/T$ .

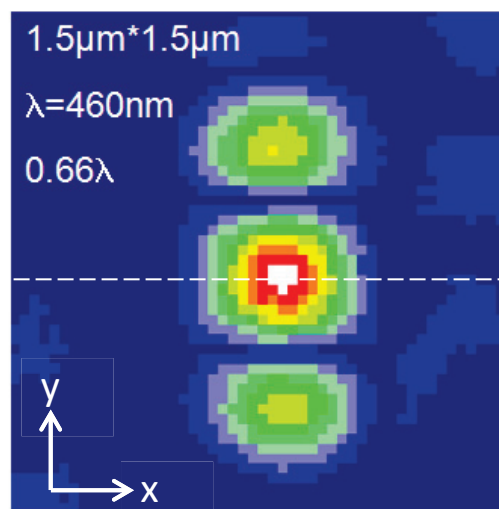


**Figure 4.14**  $\Delta T/T$  measured around a single nanoparticle with  $2f$ -demodulation. Three peak are retrieved as expected from **Erreur ! Source du renvoi introuvable**. The intensity spatial profile  $I_I(x,y)$  of the light beam is determine with the Gaussian profile of  $\Delta T/T$  along the dashed line and a  $0.66\lambda$  full width half maximum is retrieved, corresponding to the diffraction limit of the experimental setup.

### 4.2.3 Results and discussion

Here, we present the absolute extinction cross-section measurement for six single aerosol nanoparticles. These measurements have been performed by applying the SMS technique as a function of the wavelength and the polarization of the incident light beam. Then, these preliminary results are compared with numerical simulations and discussed. Three case studies have been carried out on single dielectric nanoparticles having different chemical compositions, namely:

- (a) PSL sphere with calibrated size (NIST traceable) to obtain a reference measurement
- (b)  $(\text{NH}_4)_2\text{SO}_4$  as an example of common atmospheric aerosols
- (c) Dust nanoparticle as an example of common atmospheric aerosols

#### (a) TEM observation and SMS measurements on a single nanoparticle

Figure 4.15 presents the TEM-observations of six single nanoparticles together with the corresponding SMS-measurements. The six single nanoparticles correspond to one PSL (a), three  $(\text{NH}_4)_2\text{SO}_4$  nanoparticles (b1, b2, b3) and two desert dust nanoparticles (c1, c2). The corresponding TEM-observations show that the (a) and (b1) nanoparticles are spherical, with a respective radius, measured on the TEM-picture, around  $r = 35$  nm and  $r = 38$  nm. The four other nanoparticles (b2, b3, c1, c2) are nonspherical with a respective radius around  $r = 48$  nm,  $r = 65$  nm,  $r = 75$  nm and  $r = 50$  nm. Nonetheless, it is very difficult to measure the volume-equivalent radius of a nonspherical particle on a TEM picture, especially for dust nanoparticles which show internal inhomogeneities.  $\Delta T/T$  has been measured as a function of the orientation of the incident light linear polarization at  $\lambda = 480$  nm for PSL, at  $\lambda = 460$  nm for  $(\text{NH}_4)_2\text{SO}_4$  and at  $\lambda = 490$  nm for dust nanoparticles. For the two spherical nanoparticles,  $\Delta T/T$  is almost independent of the incident linear polarization (less than 2 %-variation). Meanwhile, for the five nonspherical nanoparticles,  $\Delta T/T$  depends on the incident linear polarization with variations of 11.8 %, 13.5 %, 16.5 % and 10.1 % respectively for the (b2, b3, c1, c2)-nanoparticles. Since  $C_{\text{ext,np}}$  and  $\Delta T/T$  are proportional, the same variation with the incident linear polarization is obtained for  $C_{\text{ext,np}}$  and  $\Delta T/T$ . We hence verify that the variation of  $C_{\text{ext,np}}$  and  $\Delta T/T$  as a function of the incident linear polarization indicates the deviation from isotropy of the fixed nanoparticle. In addition for the  $(\text{NH}_4)_2\text{SO}_4$  nanoparticle (b2), the polarization dependence of  $\Delta T/T$  has been studied at  $\lambda = 460$  nm,  $\lambda = 560$  nm and  $\lambda = 700$  nm,

where it varies by respectively 13.5 %, 5.9 % and 11.1 %. Hence, the incident wavelength can have a strong influence on the polarization dependence of  $\Delta T/T$  and  $C_{\text{ext,np}}$ .

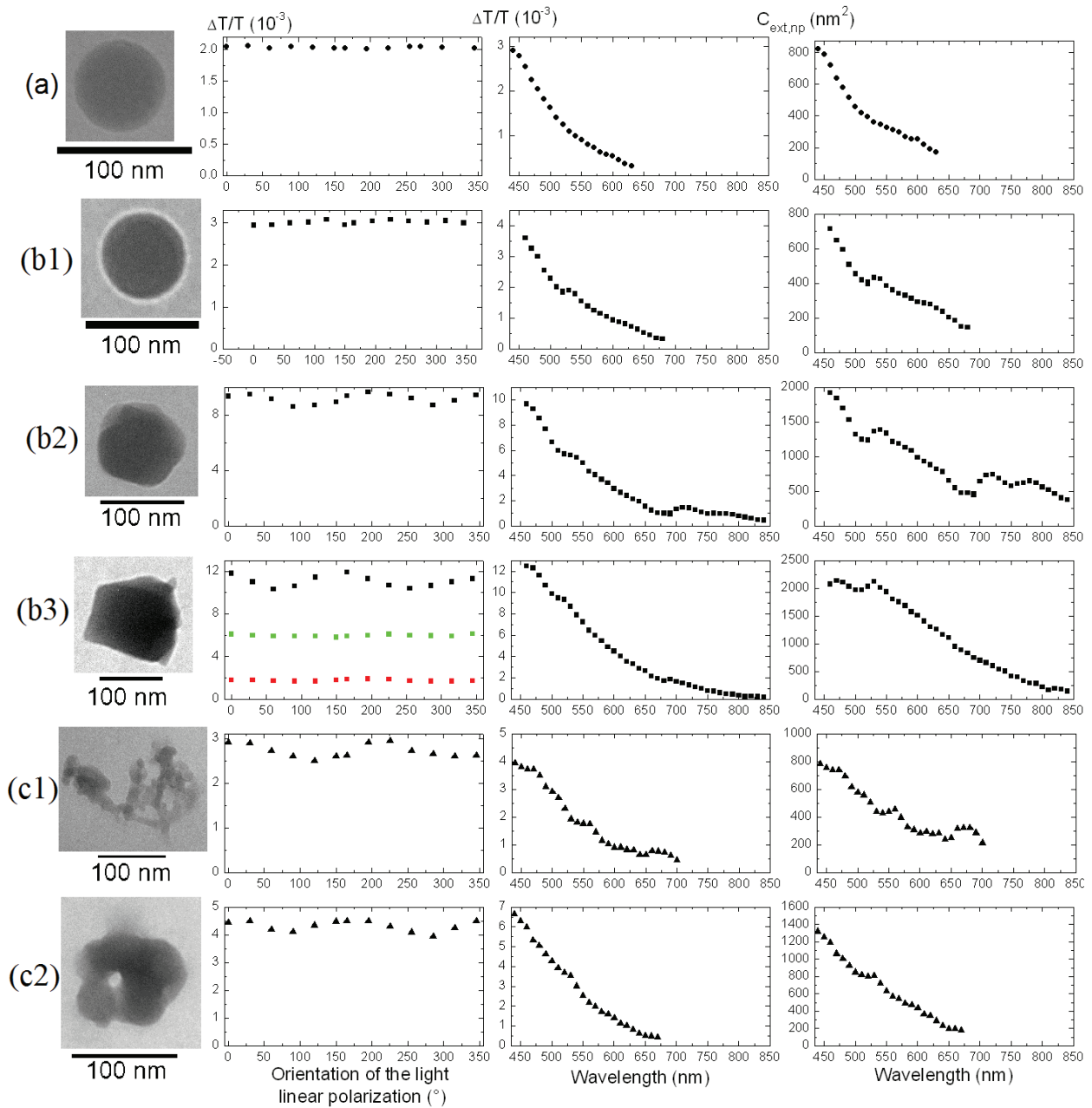


**Figure 4.15** TEM photos and SMS measurements on one PSL (a), three  $(\text{NH}_4)_2\text{SO}_4$  ((b1), (b2) and (b3)) and two dust ((c1) and (c2)) single nanoparticles. The first column corresponds to the TEM observation of the single nanoparticles.  $\Delta T/T$  measured as function of the linear polarization of the incident light (with  $\lambda = 480$  nm for PSL,  $\lambda = 460$  nm for  $(\text{NH}_4)_2\text{SO}_4$  and  $\lambda = 490$  nm for dust nanoparticles) is presented in the second column.  $\Delta T/T$  has been measured as function the linear polarization of the incident light for three different wavelength on particle (b3), namely  $\lambda = 460$  nm (black squares),  $\lambda = 560$  nm (green squares) and  $\lambda = 700$  nm (red squares).  $\Delta T/T$  measured as function of the incident wavelength (with the linear polarization corresponding to the higher  $\Delta T/T$ -value) is presented in the third column. Finally the extinction cross section  $C_{\text{ext,np}}$  deduced from the  $\Delta T/T$  measurement is plotted in the fourth column.

In addition as plotted in Figure 4.15,  $\Delta T/T$  has been measured as function of the wavelength by using the SMS-technique and the corresponding  $C_{\text{ext,np}}$  is retrieved by following the Section 4.2.2-d-methodology. When  $\Delta T/T$  is measured as function of the wavelength, the incident linear polarization is set to correspond to the highest  $\Delta T/T$ -value. The measured  $\Delta T/T$  and  $C_{\text{ext,np}}$  generally decrease when increasing the wavelength. Nonetheless, for a few wavelengths,  $\Delta T/T$  and  $C_{\text{ext,np}}$  are almost constant or even increase with the wavelength, as around 530 and 700 nm for  $(\text{NH}_4)_2\text{SO}_4$  single nanoparticles or around 550 nm and 670 nm for dust nanoparticles. Nonetheless, as can be seen in Figure 4.15, the increase of  $C_{\text{ext,np}}$  around these wavelength is stronger than the  $\Delta T/T$  increase. In addition, for the PSL and  $(\text{NH}_4)_2\text{SO}_4$  nanoparticles, the higher  $\Delta T/T$  and  $C_{\text{ext,np}}$  are the bigger the nanoparticle is. For the dust nanoparticle, the correlation between extinction and size is difficult as they are highly nonspherical and have internal inhomogeneities.

### **(b) Comparison of SMS experimental measurements with numerical simulations**

Figure 4.1 presents the comparison of  $C_{\text{ext,np}}$  measured by SMS with its numerical simulations. As  $C_{\text{ext,np}}$  is not measured on random but static nanoparticles, the numerical simulations are not to be averaged over the different nanoparticle orientations, as are the T-matrix simulations performed in Chapter 2. Hence, the numerical simulations have been performed with Mie theory. For this, the following refractive indices have been used:  $m = 1.59 - 0i$  for the PSL sphere (Duke scientific),  $m = 1.52 - 10^{-7}i$  for  $(\text{NH}_4)_2\text{SO}_4$  nanoparticles (Lang-Yona et al., 2009) and  $m = 1.57 - 0.007i$  for the dust nanoparticles (Kandler et al., 2011). By adjusting the radius of the simulated nanoparticle, a good agreement is found between the simulated and measured  $C_{\text{ext,np}}$ -values, as can be seen in Figure 4.16. However, the  $C_{\text{ext,np}}$  enhancement around 530 and 700 nm for  $(\text{NH}_4)_2\text{SO}_4$  nanoparticles or around 550 nm and 670 nm for dust nanoparticles, is not retraced by the numerical simulation. These enhancements might be due to change in the refractive index of the nanoparticles or to the coupling between the nanoparticle and the substrate, as the  $\text{SiO}_2$  substrate and the nanoparticle refraction indices are very close.

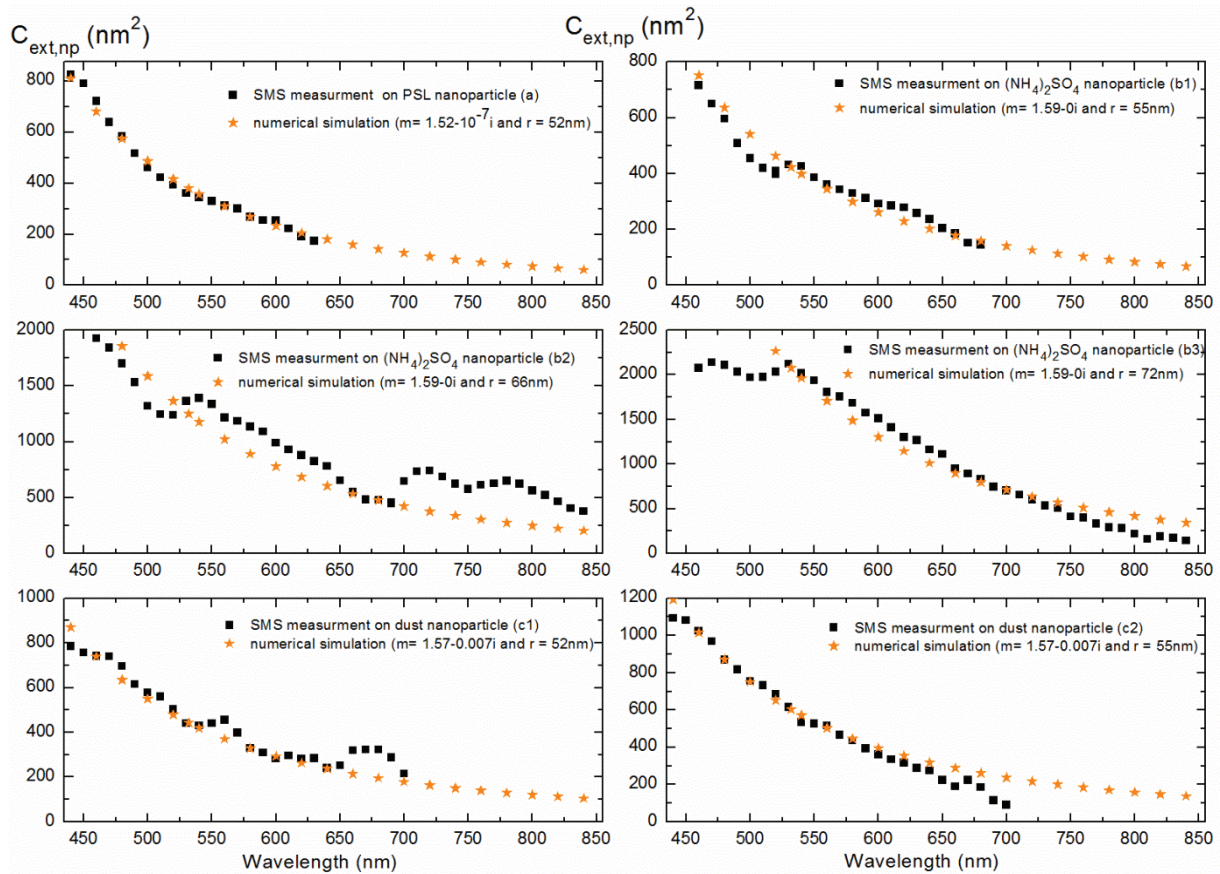


**Figure 4.16** Comparison of  $C_{\text{ext,np}}$  measured with SMS and numerical simulation. The SMS measurements of  $C_{\text{ext,np}}$  are identical to those plotted in to the Figure 4.15. Numerical simulations are performed with the Mie theory and the refractive index and nanoparticle radius are indicated in each subplot.

Table 4.4 summarized the radii measured by TEM and the size retrieved from the Mie numerical simulation. We also note a difference between the PSL radius measured on the TEM picture ( $r = (35 \pm 3.5)$  nm as the TEM calibration has approximately 10 % error) and the PSL NIST traceable radius ( $r = (40.5 \pm 1.5)$  nm), from which we may deduce that the TEM pictures underestimate the size of the nanoparticles. This deduction is further reinforced as the same effect has been observed on several PSL nanoparticles. Hence, we can correct the calibration of the TEM-observation by using the factor  $40.5/35$ . Table 4.4 also presents the measured radius corrected from TEM-calibration by this factor  $40.5/35$ . For the PSL (a) and the  $(\text{NH}_4)_2\text{SO}_4$  nanoparticles (b1) and (b2), the radius retrieved by the numerical simulation is higher than the radius that measured by the TEM-observations. Several hypotheses may explain this discrepancy: i) as these nanoparticles are hygroscopic, water uptake is possible and would enhance the measured extinction cross section for such small nanoparticles. ii) The  $\text{SiO}_2$  substrate and the nanoparticle refraction indices being very close, light scattering may be enhanced by the coupling of the nanoparticle with the  $\text{SiO}_2$ -grid. Such a coupling might be higher for dielectric nanoparticles than for metallic nanoparticles, the extinction of aerosol

nanoparticle such as a PSL, a  $(\text{NH}_4)_2\text{SO}_4$  or a dust nanoparticle being dominated by scattering. iii) The electron beam illumination may have changed the optical properties of the selected nanoparticles, although moderate illumination has been used. iv) Finally,  $C_{\text{ext,np}}$  might be enhanced due to non-linear processes. However the very low power density used ( $\approx 1\mu\text{W}$ ) makes this hypothesis rather unlikely. For  $(\text{NH}_4)_2\text{SO}_4$  nanoparticle (b3) and dust nanoparticles (c1) and (c2), the radius retrieved by numerical simulation is smaller than the one retrieved by TEM-observation. However, as can be seen in Figure 4.15, these three nanoparticles are highly nonspherical, hence their radius can obviously not be retrieved with Mie theory. As an outlook, these experimental results should then be further compared with numerical simulations performed on a fixed non-spherical nanoparticle (Mishchenko et al., 2000).

**Table 4.4** Summary of the particle radius retrieved from the TEM picture, the radius measured by TEM corrected from its calibration and from numerical simulation assuming spherical nanoparticles. The radius measured by TEM can be corrected as the PSL have a calibrated radius  $r = 40.5 \pm 1.5$  nm, hence with a correctly calibrated TEM should indicate the same size. The size measured by TEM is then corrected by a factor  $40.5/35$ .

single nanoparticle	TEM measured radius (nm)	radius corrected from TEM calibration (nm)	radius retrieved from numerical simulation (nm)
PSL (a)	35	40.5	52
$(\text{NH}_4)_2\text{SO}_4$ (b1)	38	44	55
$(\text{NH}_4)_2\text{SO}_4$ (b2)	48	55.5	66
$(\text{NH}_4)_2\text{SO}_4$ (b3)	65	75	72
Dust (c1)	75	87	52
Dust (c2)	50	58	55

### 4.3 Conclusion

In this chapter, the polarization and spectral properties of common atmospheric aerosols have been studied by using two laboratory experiments. The absolute depolarization of an ensemble of nanoparticles in ambient air has been measured for the first time in the exact backscattering direction ( $\theta = 180^\circ \pm 0.2^\circ$ ) in a new laboratory measurement performed at the ILM (David et al., 2013b). In addition, the absolute extinction cross-section of a single aerosol dielectric nanoparticle has been measured as a function of the incident light linear polarization and wavelength by using the spatial modulation spectroscopy (SMS). This last experiment has been performed in collaboration with N. Del Fatti and F. Vallee's group at the ILM.

Exact backscattering measurements may help validating numerical simulations based on T-matrix or DDA-numerical codes and may also be useful in active lidar remote sensing field experiments. Hence an experiment has been developed to measure the exact backscattering of light ( $\theta = \pi \pm 3.5 \times 10^{-3}$  radian) by an ensemble of nanoparticles in ambient air. Special care has been taken to optimize the collection of the particles backscattering signal  $\mathcal{P}_p$ , while minimizing the background stray light signal  $\mathcal{P}_0$ , and this in the UV spectral range, to increase our sensitivity to nano-sized particles. In addition, for the first time to our knowledge, our light-scattering experimental set-up fulfills the far-field single-scattering approximation, which is generally applied in both numerical simulations and field experiments. Moreover, by modulating the incident laser polarization, we measured the particles depolarization ratio  $\delta_p$  with accuracy. We hence retrieved  $\delta_w = (0.02 \pm 0.05) \%$  for water droplets: within our error bars, this value matches the expected zero-depolarization value for homogeneous spherical particles predicted by Mie. For the generated non-spherical salt (NaCl) nanoparticles,  $\delta_{\text{salt}} = (4.38 \pm 0.16) \%$  has been retrieved. The measured  $\delta_{\text{salt}}$ -value strongly depends on the relative humidity RH as well as on the salt particles PSD, respectively by a factor of four and five. Several outlooks are possible: i) The same experiment could be built for another spectral range to address the spectral dependence of  $\delta_p$ , ii)  $\delta_{\text{salt}}$  could be measured for more RH-values and PSD, iii) The depolarization of other nanoparticles, such as volcanic ash or desert dust particles, could be measured and finally, iv) angles around  $\theta = \pi$ , may be used to measure the particles backscattering enhancement. To conclude with, this first experimental achievement of a polarimetric measurement in the exact backscattering direction opens new outlooks in coupling laboratory light scattering matrix measurements with both numerical simulations and field observations.

As underlined by Miles et al. (2011), the study of a single aerosol particle is necessary and optical measurements, such as extinction, on single dielectric aerosol nanoparticle are essential. Hence, in Section 4.2, for the first time to my knowledge, as a preliminary result, the absolute extinction cross-section  $C_{\text{ext,np}}$  of six aerosol nanoparticles has been measured as a function of the incident light linear polarization and wavelength by using the SMS (Arbouet et al., 2004). One PSL sphere has been used to obtain a reference measurement, as its size ( $r = (40.5 \pm 1.5) \text{ nm}$ , NIST traceable), spherical shape and refractive index are known. Then, three  $(\text{NH}_4)_2\text{SO}_4$  and two dust nanoparticles have been studied as one of the predominant atmospheric aerosols (Pöschl et al., 2005). The incident wavelength influences the polarization dependence of  $\Delta T/T$  and  $C_{\text{ext,np}}$ . The spectral dependence of  $\Delta T/T$  and  $C_{\text{ext,np}}$  has

been measured, from 440 to 840 nm. Both  $\Delta T/T$  and  $C_{\text{ext,np}}$  decrease when increasing the wavelength, except around 530 and 700 nm for the  $(\text{NH}_4)_2\text{SO}_4$  nanoparticles or around 550 and 670 nm for the dust nanoparticles, in which case  $\Delta T/T$  and  $C_{\text{ext,np}}$  sometimes increases with the wavelength. This increase might be due to changes in the refractive index of the nanoparticles or to the optical coupling between the nanoparticle and the substrate. For PSL and  $(\text{NH}_4)_2\text{SO}_4$  nanoparticles, the higher  $\Delta T/T$  and  $C_{\text{ext,np}}$  are, the bigger the dielectric nanoparticle is. For dust nanoparticles, the correlation between extinction and size is more difficult to achieve as they are highly nonspherical and have internal inhomogeneities. In addition, the measured  $C_{\text{ext,np}}$  have been compared with numerical simulations, by applying the Mie theory, to adjust the radius of the simulated nanoparticle at a given refractive index. A good agreement is found between the simulated and the SMS-measured  $C_{\text{ext,np}}$ -value (Figure 4.16). However, the  $C_{\text{ext,np}}$  enhancement around 530 and 700 nm for  $(\text{NH}_4)_2\text{SO}_4$  nanoparticles or around 550 nm and 670 nm for dust nanoparticles, is not retrieved by the numerical simulation. In addition, a radius larger than that expected from TEM pictures has been needed for the SMS-measurement to agree with numerical simulations. Several hypotheses have been raised to explain this discrepancy, including particle hygroscopic growth, optical coupling between the nanoparticle and the  $\text{SiO}_2$ -substrate, modifications induced by the electron beam illumination on the nanoparticle optical properties. Meanwhile, for highly nonspherical nanoparticles, the agreement is found for optical simulation performed with smaller radius than the radius observed with TEM pictures. This discrepancy can be explained by the nonspherical shape of these nanoparticles, which cannot be accurately simulated with the Mie theory. Hence, more realistic numerical simulations, performed on a nonspherical fixed dielectric nanoparticle, might be useful. Ideally, these numerical simulations should also account for the potential role of the substrate.

## Chapter 5

### Conclusion and outlooks

As a conclusion, this thesis addresses the optical backscattering properties of an ensemble of dielectric atmospheric nanoparticles, up to three-component particle external mixtures and the extinction of a single dielectric nanoparticle. Backscattering and extinction of light by atmospheric particles is evaluated through numerical simulations (Chapter 2), sensitive and accurate UV-VIS polarization lidar experiments (Chapter 3), as well as laboratory experiments (Chapter 4). Each chapter addresses the spectral and polarization properties of atmospheric aerosols by emphasizing on the potential applications, as for the observation of new particle formation events in Chapter 3.

Hence, in Chapter 1, the scientific context of this thesis has been introduced and especially the remaining high uncertainties on atmospheric particles radiative forcing due to their wide range of size, shape and chemical composition (IPCC report, 2007). In this context, Chapter 1 also explains that the work is dedicated to optical methodologies related to particles having an atmospheric and climate interest.

In Chapter 2, the formalism of this thesis has been presented into details. It includes the particle light extinction, scattering and especially the polarization-resolved backscattering. Then, the optical backscattering of a two-component particle mixture has been analyzed, to address either a {spherical (s), nonspherical (ns)} or a {ns1,ns2} particle external mixture. It has been shown that the depolarization ratio  $\delta_p$  of the particles mixture differs from the nonspherical (ns) particles depolarization ratio  $\delta_{ns}$ , due to the presence of spherical or less depolarizing particles in the mixture. The depolarization ratio of the particles mixture being sensitive to both s and ns-particles, we then identified a tracer for ns-particles, based on the cross-polarized backscattering coefficient  $\beta_{p,\perp}$ . By using this tracer, the optical backscattering partitioning in a two-component particle mixture (OBP2) has been developed to simultaneously retrieve the backscattering coefficients specific to each of the two particle components. In more details, the OBP2-methodology is based on coupling a single wavelength ( $1\lambda$ ) polarization-resolved backscattering measurement ( $1\beta+1\delta$ ) with the  $\delta_{ns}$  of each component.

Moreover, the OBP2-methodology has been extended to the case of a three-component particle external mixture (OBP3), which has been developed to retrieve the backscattering coefficient specific to each of the three particle components (David et al., 2013a). Dual-wavelength ( $2\lambda$ ) polarization-resolved backscattering measurements ( $2\beta+2\delta$ ) are needed, together with optical inputs, specific to each ns-particle component, namely the  $\delta_{ns}$ -ratio and the cross-polarized backscattering Ångstrom exponent  $\mathring{A}_{ns,\perp}$ . Hence, OBP3 allows taking into account the nonsphericity of each of the three particle components, by addressing both the particles spectral and polarization backscattering properties. The chapter ended with the retrieval of the  $\delta_{ns}$  and  $\mathring{A}_{ns,\perp}$ -coefficients, obtained by using laboratory measurements for volcanic ash particles (Muñoz et al., 2004), but also by applying the T-matrix numerical code (Mishchenko et al., 1998) for dust particles, or an extension of this code for particles having a cubic shape, such as sea-salt particles (Kahnert, 2013).

In Chapter 3, the atmospheric particle vertical layering has been studied by using the Lyon UV-VIS polarization lidar (David et al., 2012) to apply the OBP2/OBP3 methodologies, to retrieve particles backscattering coefficients specific to each of the two/three particle components. After analyzing the statistical errors and systematic biases affecting the  $2\lambda$ -polarization lidar, the Lyon UV-VIS polarization lidar performances have been analyzed: the backscattered radiation is efficiently separated with respect to its  $(\lambda, \pi)$ -spectral and polarization optical properties with negligible wavelength and polarization cross-talks, as published in (David et al., 2012).  $\beta_{p,\perp}$ , as low as  $(2.4 \pm 0.5) \times 10^{-8} \text{ m}^{-1} \cdot \text{sr}^{-1}$ , have been measured, corresponding to a  $\delta_p$ -detection limit of 0.6 %, close to the molecular depolarization. Then, the OBP2/OBP3 methodologies have been applied to three case studies, which provided several new outputs:

- The *Ash case*, as an example of a two-component particle mixture, corresponding to the mixing of volcanic ash particles with non-ash particles (nash) (likely to be sulfate) which occurred during the April 2010 Eyjafjallajökull eruption and has been observed above Lyon after more than 2 600 km advection. By applying the OBP2-methodology, we retrieved the ash and nash-particles backscattering coefficients  $\beta_{ash}$  and  $\beta_{nash}$ . Changing the Lidar ratio  $S_p$  and the nash-particles depolarization  $\delta_{nash}$  negligibly influenced the retrieved ash particles backscattering coefficient  $\beta_{ash}$  (Miffre et al., 2011). Moreover, three outputs have been highlighted: i) The retrieved  $\beta_{ash}$  and  $\beta_{nash}$ -variations with altitude were negatively correlated,

as detailed in Section 3.3, which opens new insights on NPF-events ii) The  $\beta_{\text{nash}}$ -vertical profile followed the relative humidity vertical profile, which is interesting as an optical signature of the nash particles hygroscopic growth. iii) Finally, a new methodology has been developed to retrieve range-resolved particles number concentrations specific to one ns-particle component (ash, dust) (Miffre et al., 2011, 2012b). This methodology is robust as it includes the variability in the ns-particles size distribution, sensitivity to water uptake as well as possible sedimentation effects (Miffre et al., 2012b). In addition, from the ash number concentration, the ash mass concentration has been retrieved and found in nice agreement with FLEXPART ash particles numerical dispersion model (Miffre et al., 2012a).

- The *Dust case* (two-component particle mixture), in which desert dust particles mixed with non-dust particles, as observed above Lyon during a Saharan dust outbreak that occurred on July, 09<sup>th</sup> 2010. Applying the OBP2-methodology provided the time-altitude maps of the dust and non-dust (ndust) particles backscattering coefficient  $\beta_{\text{dust}}$  and  $\beta_{\text{ndust}}$ . N dust particles have been observed close to the dust layer. To interpret this observation, numerical simulations of  $\beta_{\text{ndust}}$  corresponding to an NPF event have been performed based on Dupart et al.'s laboratory measurements (2012). Several NPF features have been pointed out from these numerical simulations, which have all been retrieved on the lidar  $\beta_{\text{ndust}}$  measurement: i) NPF leads to a  $\beta_{\text{ndust}}$ -enhancement and UV should be preferably used to observe NPF since the enhancement is two (resp. five) times higher than in the VIS (resp. in the IR). ii) We demonstrated that NPF can be observed within the  $\beta_{\text{ndust}}$ -detection limit of the UV polarization lidar presented in Section 3.2. iii) The number concentration of the formed particles increases with increasing UV-irradiance, as observed by a  $\beta_{\text{ndust}}$ -enhancement with solar UV-irradiance. iv) Dust particles are necessary to initiate this NPF mechanism where they act as a condensation sink: hence,  $\beta_{\text{ndust}}$  is negatively-correlated with  $\beta_{\text{dust}}$  during the NPF event while no negative-correlation is observed before. For all these reasons, we are confident that NPF has been observed with our UV-polarization lidar (Dupart et al., 2012).

- The *Sea-salt/dust case*, as an example of a three-component particle external mixture, occurring in the presence of Saharan dust particles mixed with sea-salt (ss) and water-soluble (ws) particles, as observed above Lyon due to favorable metrological conditions on October, 18<sup>th</sup> 2011. The OBP3-methodology has been applied to simultaneously retrieve the vertical profile of the backscattering coefficient of each distinct particle component (David et al., 2013a), namely  $\beta_{\text{dust}}$ ,  $\beta_{\text{ss}}$  and  $\beta_{\text{ws}}$ . The observed backscattering coefficients clearly indicate that

the newly proposed methodology is able to reveal very complex particle microphysical behaviour. The inherent assumptions of the OBP3-methodology have then been discussed, which demonstrated the performance of this methodology, as variability in the optical inputs induced a less than 24 % uncertainty on the retrieved  $\beta_{\text{dust}}$ ,  $\beta_{\text{ss}}$  and  $\beta_{\text{ws}}$ .

In Chapter 4, a new laboratory experiment is presented, aimed at measuring, with a high precision, the depolarization of an ensemble of randomly-oriented nanoparticles suspended in ambient air for the first time in the exact backscattering direction ( $\theta = 180^\circ \pm 0.2^\circ$ ) (David et al., 2013b). This light-scattering experiment fulfills the far-field single-scattering approximation, which is generally applied in both numerical simulation and field experiments. Special care has been taken to optimize the collection of the particle backscattering signal  $\mathcal{P}_p$ , while minimizing the background stray light signal  $\mathcal{P}_0$ , and this in the UV spectral range, to increase our sensitivity to nano-sized particles. Moreover, by modulating the incident laser polarization, we measured the particles depolarization ratio  $\delta_p$  with accuracy. We hence have retrieved  $\delta_w = (0.02 \pm 0.05) \%$  for water droplets, in agreement with Mie theory, within our error bars. For the generated nonspherical salt (NaCl) particles, we retrieved  $\delta_{\text{salt}} = (4.38 \pm 0.16) \%$ . Moreover, we showed that the measured  $\delta_{\text{salt}}$  strongly depends on RH and on the salt PSD, respectively by a factor of four and five.

In addition, in collaboration with N. Del Fatti and F. Vallee's group, the absolute extinction cross-section  $C_{\text{ext,np}}$  of six single dielectric aerosol nanoparticles has been measured as a function of the incident light linear polarization and wavelength by using the spatial modulation spectroscopy (SMS). PSL sphere has been used as a reference measurement, as its size ( $r = (40.5 \pm 1.5) \text{ nm}$ , NIST traceable), shape and refractive index are known. Three  $(\text{NH}_4)_2\text{SO}_4$  and two dust nanoparticles have also been studied as examples of common atmospheric particles. The normalized transmission change  $\Delta T/T$  and the absolute extinction cross section  $C_{\text{ext,np}}$  of each single nanoparticle have been measured by using the SMS-technique. We hence experimentally verify that the variation of  $C_{\text{ext,np}}$  and  $\Delta T/T$  as a function of the incident linear polarization indicates the deviation from isotropy of the fixed dielectric nanoparticle (less than 2 % variation for the spherical nanoparticles and more than 10 % variation for the non-spherical nanoparticles). We also showed that the incident wavelength can have a strong influence on this polarization dependent variation of  $C_{\text{ext,np}}$  and  $\Delta T/T$ . In addition,  $\Delta T/T$  and  $C_{\text{ext,np}}$  have been measured as a function of the wavelength from 440 to 840 nm, depending on the  $\Delta T/T$  signal-to-noise ratio. A good agreement has been found

between the  $C_{\text{ext,np}}$  experimental measurement and its numerical simulation using Mie theory. However, the  $C_{\text{ext,np}}$ -enhancement around 530 and 700 nm for  $(\text{NH}_4)_2\text{SO}_4$  nanoparticles or around 550 and 670 nm for dust nanoparticles, is not retrieved by the numerical simulation. These enhancements might be due to changes in the nanoparticles refractive index, or to the optical coupling between the nanoparticle and the substrate. Moreover, a radius larger than that expected from TEM pictures has been needed for the SMS-measurement to agree with numerical simulations. Several hypotheses have been raised to explain this discrepancy, including particle hygroscopic growth, optical coupling between the  $\text{SiO}_2$ -substrate of the TEM grids or modifications in the nanoparticle optical properties induced by the electron beam illumination. Meanwhile, the extinction of a highly nonspherical particle  $C_{\text{ext,np}}$  cannot be accurately simulated with Mie theory.

The work performed on the interaction of light with atmospheric dielectric particulate matter has allowed increasing the knowledge on the particles content of the atmosphere and its scattering properties in the UV and visible spectral ranges, by including the polarization in the analysis. Because the work was guided by high precision and accurate experimental achievements, the discussion on the results could open several outlooks on novel experiments, as well as closure experiments. Several of them are given below as possible outlooks of this thesis:

- (a) Validation of the OBP3-methodology
- (b) Extension of the OBP2/OBP3 methodology
- (c) Extension to the OBP4 methodology
- (d) Extension of the  $\delta_p$ -measurement in the exact backscattering direction
- (e) Measurement of the angular dependence of  $\delta_p$  and backscattering enhancement
- (f) Numerical simulation on a fixed non-spherical dielectric nanoparticle
- (g) Measuring the same observable on a single and an ensemble of nanoparticles
- (h) Observation of new particle formation during the Eyjafjallajökull volcanic eruption

#### **(a) Validation of the OBP3-methodology**

The retrieved backscattering coefficients obtained by applying the OBP2/OBP3-methodology now need to be validated in the atmosphere by independent co-located measurements. For instance, an airborne aerosol mass spectrometer (AMS) would be a very interesting independent measurement as it provides the PSD and the chemical composition of atmospheric particles (Muller et al. 2011; Favez et al. 2010). AMS enables to retrieve the PSD

as a function of the chemical composition of the particles. However, this apparatus is not range-resolved so that an airborne measurement is required to retrieve the vertical profile of the particles chemical composition and the PSD. Hence the OBP2/OBP3-methodology could be validated by performing co-located AMS measurements, despite a few difficulties which would rise from the difference of the time resolution to retrieve the vertical profile of atmospheric particles that is much longer for airborne measurement than for Lidar remote sensing.

### **(b) Extension of the OBP2/OBP3-methodology**

By applying the T-matrix numerical code from Mishchenko et al. (1998) and Kahnert for cubes (2013), numerical simulation of  $\delta_{ns}$  and  $\mathring{A}_{ns,\perp}$  have been performed to apply the OBP2/OBP3 methodologies. However, the numerical simulation of  $\delta_{ash}$  with spheroids led to a  $\delta_{ash}$ -underestimation. Hence a DDA-approach (Darine and Flatau, 1994) might be a fruitful complementary approach to account for some more complex and realistic shapes or / and including porosity effects (Lindqvist et al., 2011).

Moreover, optical properties of internally-mixed particles can be simulated with DDA, such as soot mixed with sulfate (Kahnert et al., 2013). Hence the OBP2/OBP3 methodologies could address internally-mixed particles in the atmosphere.

### **(c) Extension to the OBP-methodology to N-particle external mixtures**

The optical backscattering partitioning in a four-component particle mixture (OBP4) could be developed and applied by performing triple-wavelength polarization backscattering measurements ( $3\beta+3\delta$ ). Indeed, the 6 retrieved backscattering coefficients [ $\beta_{p,\parallel}(\lambda)$ ,  $\beta_{p,\perp}(\lambda)$  with  $\lambda = \{\lambda_1, \lambda_2, \lambda_3\}$ ], could be used in combination with 18 retrieved quantities [ $\delta_{ns1}(\lambda)$ ,  $\delta_{ns2}(\lambda)$ ,  $\delta_{ns3}(\lambda)$ ,  $\delta_{n12}(\lambda)$ ,  $\mathring{A}_{ns1,\perp}(\lambda_1, \lambda_2)$ ,  $\mathring{A}_{ns2,\perp}(\lambda_1, \lambda_2)$ ,  $\mathring{A}_{ns3,\perp}(\lambda_1, \lambda_2)$ ,  $\mathring{A}_{ns1,\perp}(\lambda_1, \lambda_3)$ ,  $\mathring{A}_{ns2,\perp}(\lambda_1, \lambda_3)$ ,  $\mathring{A}_{ns3,\perp}(\lambda_1, \lambda_3)$ ], to determine the 24 ns-particles backscattering coefficients  $\beta_{p,\pi}(\lambda)$ , with  $(p) = \{ns1, ns2, ns3, n12\}$ ,  $\pi = \{\parallel, \perp\}$  and  $\lambda = \{\lambda_1, \lambda_2, \lambda_3\}$ . In this case, the optical inputs are very numerous (18), hence their determination has to be very accurate.

In summary, by using  $N\beta+N\delta$ -measurements, a  $(N+1)$ -component particle mixture can be addressed to simultaneously retrieve the backscattering coefficient specific to each particle component (the  $2N-\beta_{p,\pi}(\lambda)$  measured coefficients are coupled with  $N(N+1)$   $\delta_{ns}$ -values and  $N(N-1)$  to retrieve  $2N(N+1)$  backscattering coefficient).

**(d) Extension of the  $\delta_p$ -measurement in the exact backscattering direction**

An experiment measuring the absolute depolarization of an ensemble of nanoparticles in ambient air ( $\theta = 180^\circ \pm 0.2^\circ$ ) in the exact backscattering direction has been built in the UV spectral range and measurements have been performed on salt (NaCl) for different PSD and RH.  $\delta_{\text{salt}}$  could be measured for more RH-values and PSDs to determine the appropriate numerical model to simulate them as function of RH and the PSD.

In addition, this measurement could be used to determine  $\delta_{\text{ash}}$  in the exact backscattering direction, which appears interesting as volcanic ash particles are difficult to simulate (Lindqvist et al., 2011) and the state-of-the-art measurement on ash particles (Muñoz et al., 2004) do not operate in the exact backscattering direction. Hence, we may cooperate with O. Muñoz to perform measurement on ash particles in the exact backscattering direction. We may also cooperate with C. George's group to measure  $\delta_{\text{dust}}$  in the exact backscattering direction.

The same experiment could also be built in another spectral range to address the spectral dependence of  $\delta_p$  required to apply the OBP3.

**(e) Measurement of the angular dependence of  $\delta_p$  and backscattering enhancement**

The measurement could also be performed for scattering angles around the exact backscattering direction ( $\theta = 180^\circ$ ), which may be used to measure the angular dependence of  $\delta_p$  or the backscattering enhancement. In this context, this experimental set-up has been used to simultaneously measure the backscattering ratio at  $\theta = 180^\circ$  and around it (preliminary results have been performed at  $\theta = 179.5^\circ$ ). As shown in Figure 5.1, a second incident laser has been created by splitting the incident laser with the emission polarization beamsplitter cube (PBC<sub>E</sub>), which, by using a delay line, can be used to measure the backscattering at  $\theta = 180^\circ$  and  $(180 - \Delta\theta)^\circ$  on the same detector within a few tens of nanoseconds. By applying the same methodology as that described in Section 4.1.2, the signal  $\Lambda$  is obtained for  $\theta = (180 - \Delta\theta)^\circ$ :

$$\Lambda_p = \frac{\eta \cdot P_0}{2d^2} \cdot \begin{bmatrix} 1 \\ 0 \\ 0 \\ 0 \end{bmatrix} \cdot \begin{bmatrix} 1 & -1 & 0 & 0 \\ -1 & 1 & 0 & 0 \\ 0 & 0 & 0 & 0 \\ 0 & 0 & 0 & 0 \end{bmatrix} \cdot \begin{bmatrix} 1 & 0 & 0 & 0 \\ 0 & \cos^2(2\psi) & -\sin(4\psi)/2 & \sin(2\psi) \\ 0 & -\sin(4\psi)/2 & \sin^2(2\psi) & \cos(2\psi) \\ 0 & -\sin(2\psi) & -\cos(2\psi) & 0 \end{bmatrix} \cdot \begin{bmatrix} F_{11,p} & F_{12,p} & 0 & 0 \\ F_{12,p} & F_{22,p} & 0 & 0 \\ 0 & 0 & F_{33,p} & F_{34,p} \\ 0 & 0 & -F_{34,p} & F_{44,p} \end{bmatrix} \cdot \begin{bmatrix} 1 \\ 1 \\ 0 \\ 0 \end{bmatrix} \quad (5.1)$$

$$\Lambda_p(\psi) = \frac{\eta \cdot P_0}{2d^2} \cdot \left[ F_{11,p} - \frac{F_{22,p}}{2} + \frac{F_{12,p}}{2} - \frac{(F_{22,p} + F_{12,p})}{2} \cdot \cos(4\psi) \right] \quad (5.2)$$

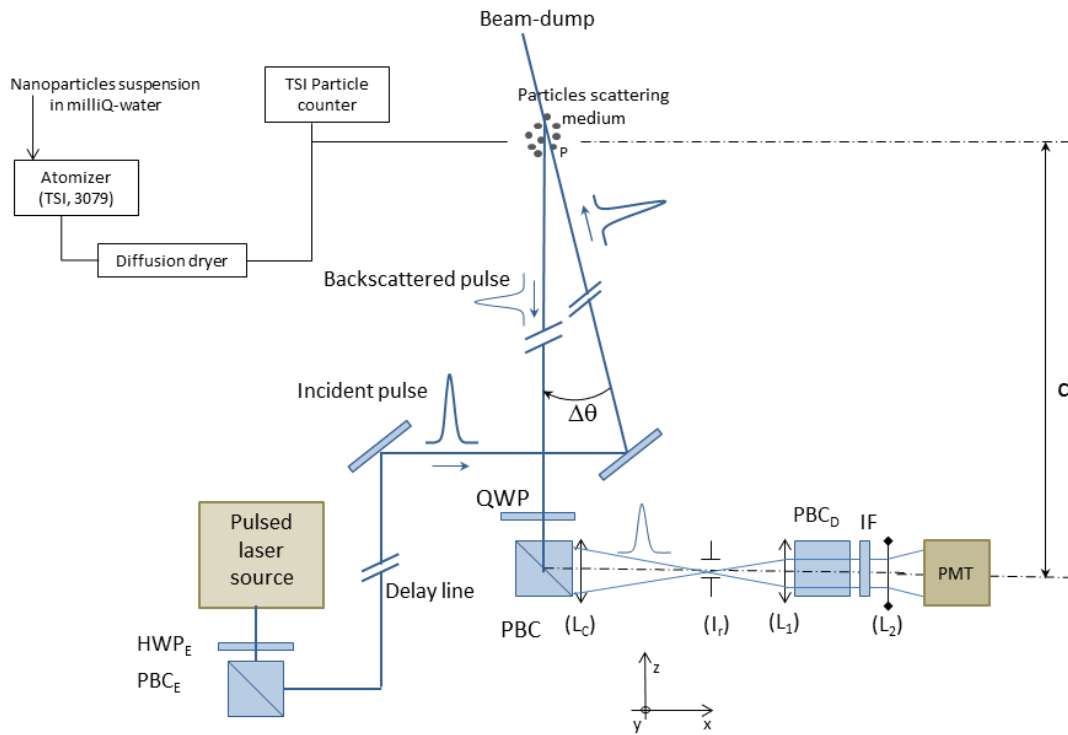


**Figure 5.1** Principle of the measurement close to the backscattering direction. The detected scattered light has a scattering angle  $\theta = ((180^\circ - \Delta\theta) \pm \xi)$ , where  $\xi$  is the width of the detected scattering angles.

A preliminary result at  $\theta = 179.5^\circ$  has been obtained on water droplets, as presented in Figure 5.2. By fitting Equation (5.2) in Figure 5.2, we retrieve  $F_{11,p} - F_{22,p}$  and  $F_{11,p} + F_{12,p}$  from which  $\delta_p(179.5^\circ) = (F_{11,p} - F_{22,p}) / (F_{11,p} + 2F_{12,p} + F_{22,p})$  (Schnaiter and al., 2012) can be deduced. We hence retrieved  $\delta_w(179.5^\circ) = (0.16 \pm 0.05)\%$ , which, within error bars, do not agree with Mie theory, in contrary to the corresponding simultaneous measurement in the exact backscattering direction ( $\delta_w(180^\circ) = (0.02 \pm 0.05)\%$ ). Such a small discrepancy may be explained by a systematical error, such as a non-perfect linear polarization of the emitted light or a misalignment between the emitted polarization and receiver polarization axes.

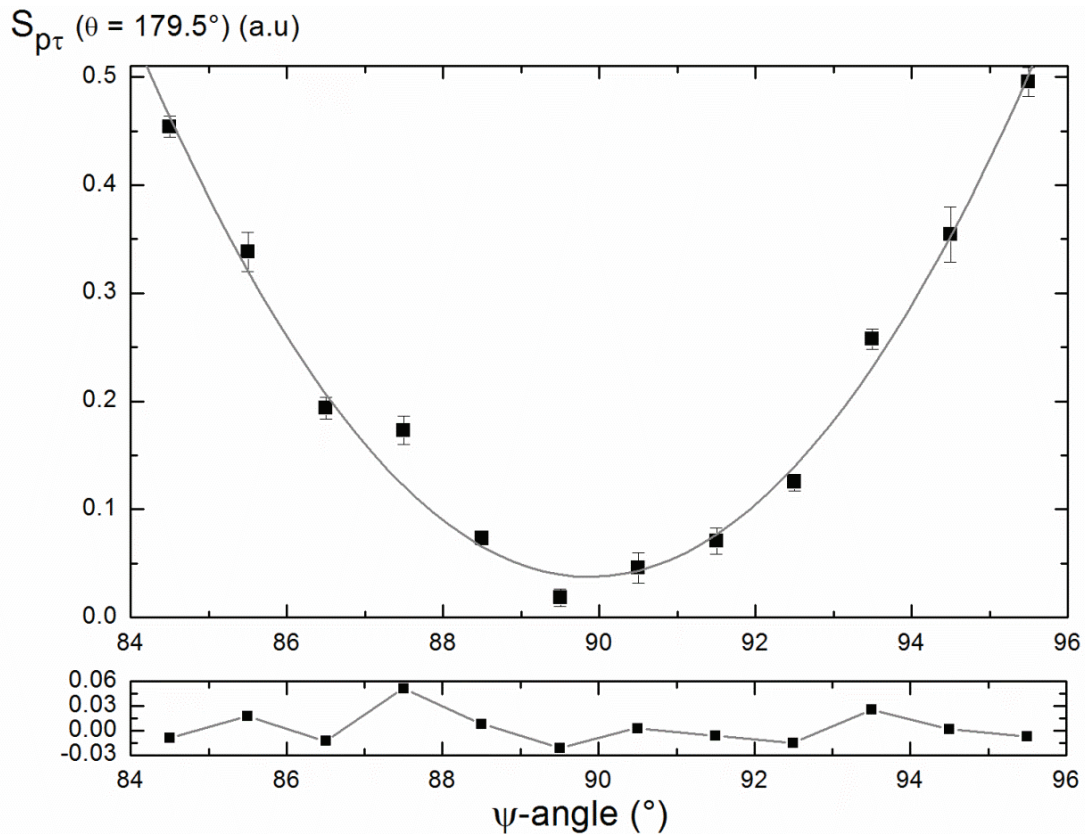


**Figure 5.2** Time integral over the pulse duration of the particles backscattering signal  $s_p$  averaged over 150 laser shots as a function of the angle  $\psi$  of the QWP used to modulate the incident laser linear polarization. Case study of water droplets particles.

**(f) Numerical simulation on fixed non-spherical dielectric nanoparticle**

Numerical simulations of the extinction of a nonspherical fixed nanoparticle may be useful to interpret the SMS  $C_{\text{ext,np}}$  measurements when the single nanoparticle is highly irregularly shaped.

**(g) Measuring the same observable on a single and an ensemble of nanoparticles**

Finally, higher knowledge could be gathered if the same physical value (extinction or backscattering) could be observed on a single and on an ensemble of particles of the same shape and size. For this, a novel experiment should be proposed like cavity ring-down spectroscopy (CRDS) on an ensemble of particles or SMS on optical backscattering. In this context, preliminary measurements have been performed with CRDS as shown in Figure 5.3, however due to the laser cavity mismatch, the achieved sensitivity does not allow the comparison with the SMS measurement.

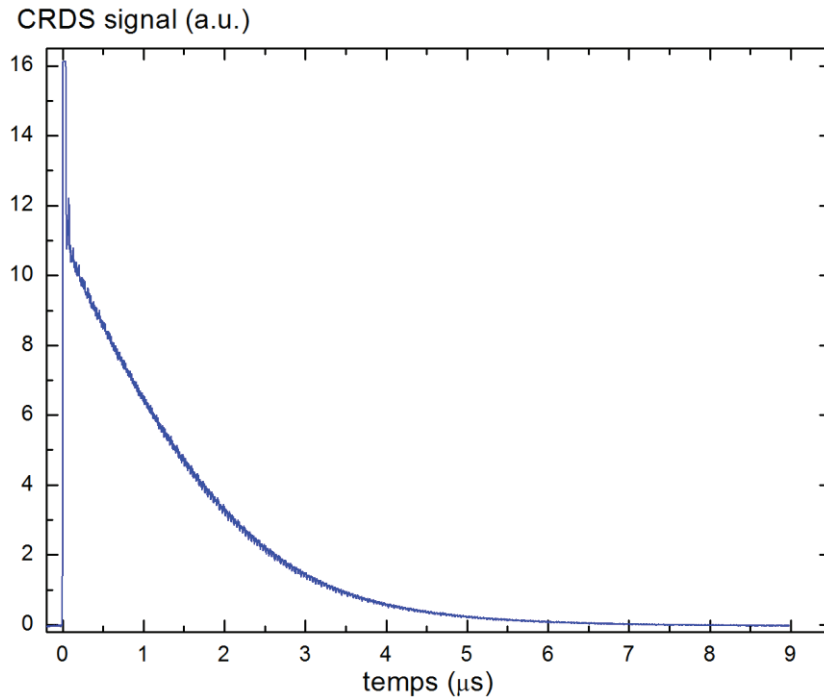


**Figure 5.3** Preliminary signal of CRDS at  $\lambda = 355$  nm.

**(h) Observation of new particle formation during the Eyjafjallajökull volcanic eruption**

We are confident that NPF event has been observed during a dust outbreak with the Lyon UV-polarization lidar. During this NPF event,  $\beta_{\text{ndust}}$  and  $\beta_{\text{dust}}$  were negatively correlated. A negative correlation between  $\beta_{\text{ash}}$  and  $\beta_{\text{nash}}$  has also been observed during the Eyjafjallajökull eruption, as shown in Figure 3.12, which is recall here for the sake of clarity. In addition, NPF has already been observed during this eruption (Boulon et al., 2011). Hence this negative correlation might be due to NPF. This hypothesis requires further investigation, such as coupling our observation with numerical simulations and/or laboratory experiments during such events, as it has been done for desert dust in Section 3.4.

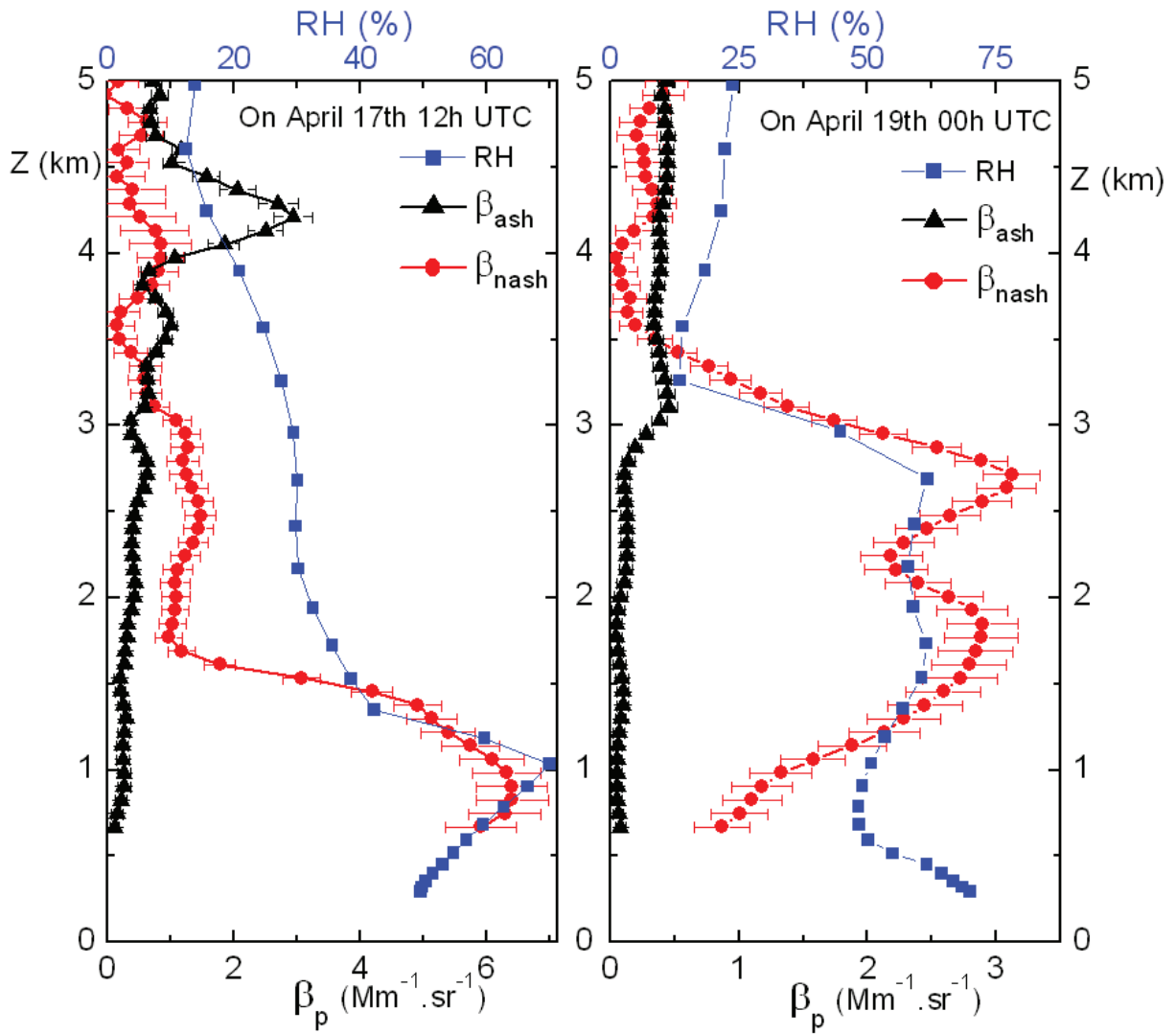


**Figure 5.4** (recall of **Figure 3.29**) Vertical profiles of  $\beta_{\text{ash}}$  (black triangles),  $\beta_{\text{nash}}$  (red circles) and RH (blue squares) on April 17<sup>th</sup> at 12 h UTC (left panel) and April 19<sup>th</sup> at 0 h UTC (right panel).

## Appendix A

### Atmospheric gases

In this appendix, we present the methodology developed to measure the spatial and temporal distribution of atmospheric trace gases, which is extensively described in (Thomas et al., 2012, 2013a, b). This methodology is based on coupling lidar with optical correlation spectroscopy (OCS) (for the principle of the lidar technique see Section 1.3).

Atmospheric gases, such as ozone, carbon dioxide, methane and sulfur dioxide, play a key role in the global warming process (Lashof and Ahuja, 1990; IPCC, 2007), health hazard (Tsen et al., 2012; Fann and Risley, 2013). The most important gases in these processes are not the most concentrated ones, for instance the three most effective warming gases are the water vapor (mixing ratio around 1-2% volume), the carbon dioxide (mixing ratio around 380 part per million volume (ppmv)) and the methane (approximately 1.8 ppmv). In addition, new particle formation (NPF) may be initiated by gas-to-particle conversion as observed for volatile organic compound (VOC) (O'Dowd et al., 2002) or SO<sub>2</sub> (Dupart et al., 2012).

In this appendix, the lidar technique and its inherent methodologies (Raman, DIAL) are first recalled.

#### A.1 Optical remote sensing methods to monitor atmospheric gases

Lidar is used to study the atmospheric gases, such as water vapor (Bösenberg et al., 1998; Whiteman et al., 2011; Di Girolamo et al., 2012), ozone (Browell et al., 1998; Gheusi et al., 2011), CO<sub>2</sub> (Gibert et al., 2008; Ishii et al., 2010) or methane (Ikuta et al., 1999; Ehret et al., 2008). Raman scattering lidar (RSL) (Whiteman et al., 2011; Di Girolamo et al., 2012) and differential absorption lidar (DIAL) (Bösenberg et al., 1998; Ehret et al., 2008) are appropriate for range-resolved remote sensing of atmospheric trace gases and water vapor. RSL uses the Raman frequency shift of the scattered light due to inelastic interaction of the photon with the gas. However, due to the weakness of Raman scattering cross sections

(Measures, 1992), the RSL methodology is often limited to the remote sensing detection of highly concentrated gases such as water vapor (Whiteman et al., 2011). DIAL is based on the differential absorption of two closed wavelengths by the target gas. These two wavelengths are chosen as only one is strongly absorbed by the target gas. Hence to achieve accurate DIAL measurements, a tunable laser, having a narrow spectral line width, is required, even for high-energy pulses (in the millijoule range) and with a high spectral resolution detector. Consequently when applying the DIAL methodology, limitations may occur when the spectral width of the emission laser does not match the target gas absorption line (Burlakov, 2010). Finally other methodologies measure the atmospheric gases with a broadband differential absorption lidar of a few nanometers width instead of a few picometers (Minato et al. 1999; Georgieva et al. 2011 Penchey et al. 2012).

## **A.2 Methodology**

Here, to measure the spatial and temporal distribution of atmospheric gases, a methodology has been developed (Thomas et al., 2012, 2013a, b) and is based on coupling lidar with optical correlation spectroscopy (OCS) (hereafter called OCS-lidar). OCS is a robust methodology for in-situ gas sample concentration measurements (Dakin et al. 2003; Lou et al. 2010, 2012a, b). Pioneering work in this field has been done by Ward and Zwick (1975), who developed the so-called GASPEC instrument. In a few words, the OCS instrument involves two broadband light sources with identical spectral distributions: one beam passes through a reference cell (non-correlated beam) containing the target gas (TG) of interest, before entering the cell where the measurement is achieved, while the second light beam (correlated beam) only passes through the measurement cell. Then, the difference of optical extinction induced on the two beams by the measurement cell is used to measure the TG concentration in the measurement cell. The coupling of GASPEC with a lidar has been first proposed by Edner et al. (1984), who performed a laboratory experiment in a remote open-ended chamber, simulating a Hg-containing atmosphere. Laser pulses, emitted at the 253.7-nm wavelength Hg-absorption line, were retro-reflected by a solid target back to the lidar telescope, hence simulating backscattering from the simulated Hg atmosphere. The spectral correlation was then achieved by inserting a highly concentrated Hg-reference gas cell in the light pathway. However, no field measurements were performed and no other species, such as greenhouse gases, were considered.

## A.2.1 OCS-Lidar principle

The OCS-lidar principle, presented in Figure A.1, consists in retrieving range-resolved trace gas concentrations from the difference in optical absorption experienced by two lidar signals. More precisely, at a wavelength  $\lambda$ , the power spectral density  $P_0(\lambda)$  of a broadband laser pulse is spectrally shaped to correlate with the trace gas extinction cross section  $C_{\text{ext}}$ , giving rise to the correlated OCS-signal  $P_C$  (subscript C for correlated), while a second broadband laser pulse is spectrally shaped to be non-correlated  $P_{\text{NC}}$  (subscript NC for non-correlated). This spectral shaping of a broadband laser pulse is achieved by amplitude modulation functions, hereafter noted  $M_C(\lambda)$  and  $M_{\text{NC}}(\lambda)$  for the correlated and the non-correlated functions, respectively. The presence of the atmospheric gas is then retrieved using the two OCS-lidar signals.

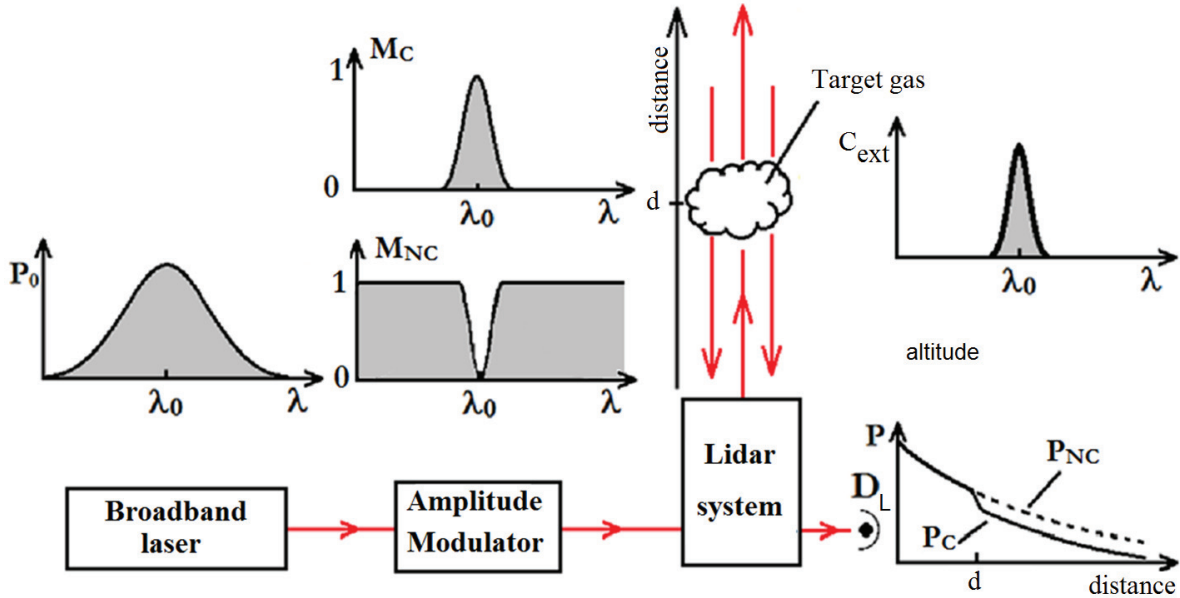


**Figure A.1** Scheme of the OCS-lidar principle: a broadband laser pulse  $P_0$ , centered on an absorption line of the TG gas (wavelength  $\lambda_0$ ) is shaped by applying the amplitude modulation  $M_C(\lambda)$  (correlated with the TG absorption) or  $M_{\text{NC}}(\lambda)$  (non-correlated with the TG absorption). By applying the lidar technique, two range-resolved OCS-lidar signals are generated on the lidar detector  $D_L$ , one for the correlated signal ( $P_C$ ), one for the non-correlated signal ( $P_{\text{NC}}$ ). The TG concentration is retrieved at altitude  $r$  from the observed difference in absorption between the two OCS-lidar signals.

At a distance  $d$  from the lidar receiver station, the measured optical power  $P_i(d)$  is given by the OCS-lidar equation, based on the lidar equation (Equation (1.1))

$$P_i(d) = \frac{O(d)}{d^2} \cdot \int_{\Delta\lambda} \eta(\lambda) \cdot P_0(\lambda) \cdot M_i(\lambda) \cdot \beta(\lambda, d) \cdot T^2(\lambda, d) \cdot d\lambda + P_F(\lambda) \quad (1.10)$$

where the subscript  $i$  refers to either correlated (C) or non-correlated (NC). The signal is integrated over an effective wavelength spectral range  $\Delta\lambda$ , defined from the effective width of the amplitude modulation function; therefore, the OCS-lidar methodology does not require a spectrally resolved detector, which would make either the laser source or the detector (or even both of them) much more complex. From the two OCS-lidar signals  $P_C$  and  $P_{NC}$ , a calculus detailed in Thomas et al. (2012) is then performed to retrieve absolute range-resolved atmospheric gas concentrations, with statistical and systematic error assessment. It is important to note that this OCS-lidar methodology does not require a permanent gas calibration as in regular optical correlation spectroscopy (Dakin et al., 2003).

### A.2.2 Experimental and numerical assessment of OCS-Lidar

The OCS-lidar methodology has been assessed both numerically and experimentally. This methodology has four main inputs: the water vapor absorption cross-section spectrum plotted in Figure A.2, based on the HITRAN database (Rothman et al., 2009), the two amplitude modulation functions  $M_C(\lambda)$  and  $M_{NC}(\lambda)$ , also presented in Figure A.2, and the laser power density  $P_0(\lambda)$ . The right panel of Figure A.2 plots the experimental results of  $P_0(\lambda) \times M_C(\lambda)$  and  $P_0(\lambda) \times M_{NC}(\lambda)$ .

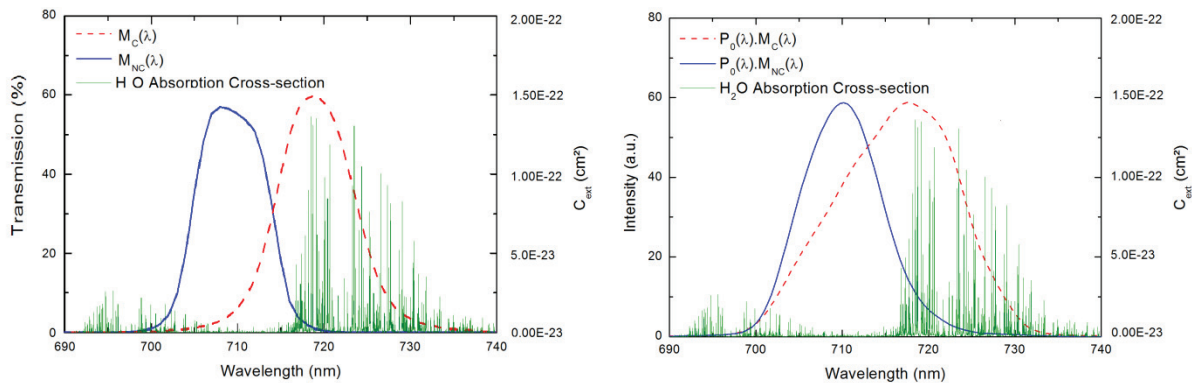


**Figure A.2** Simulation (left panel) and experimental measurement (right panel) of the amplitude modulation function  $M_C(\lambda)$  (red dash line) and  $M_{NC}(\lambda)$  (blue line) together with the water vapor extinction cross-section spectrum derived from the HITRAN database (Rothman et al., 2009).

Before the OCS-lidar measurement itself, a bias control experiment has been performed by setting  $M_C(\lambda) = M_{NC}(\lambda)$  to ensure that the two OCS-lidar signals probe the same atmospheric volume and do not undergo any range-dependent bias. Hence, during this control experiment, the ratio  $P_C/P_{NC}$  remains constant within error bars. While by setting  $M_C(\lambda)$  and  $M_{NC}(\lambda)$  as in Figure A.2, the simulated and measured ratio  $P_C/P_{NC}$  decreases with  $d$  due to the water vapor

content of the atmosphere, as can be seen in Figure A.3. Such a behavior reveals the range-dependent water vapor mixing-ratio to be seen in Figure A.3-c. Error bars on the retrieved water vapor mixing-ratios are evaluated thanks to a Monte Carlo simulation on the OCS-lidar numerical simulation based on the signal-to-noise ratio of experimental OCS-lidar signals (Thomas et al., 2012). The mixing-ratio detection limit is evaluated from this error bar taken at  $2\sigma$ . This approach leads to a range-dependent sensitivity equal to  $3 \times 10^5$  ppm.m at a 2-km distance, corresponding to a detection limit of 3,000 ppm with a 200-m spatial resolution.

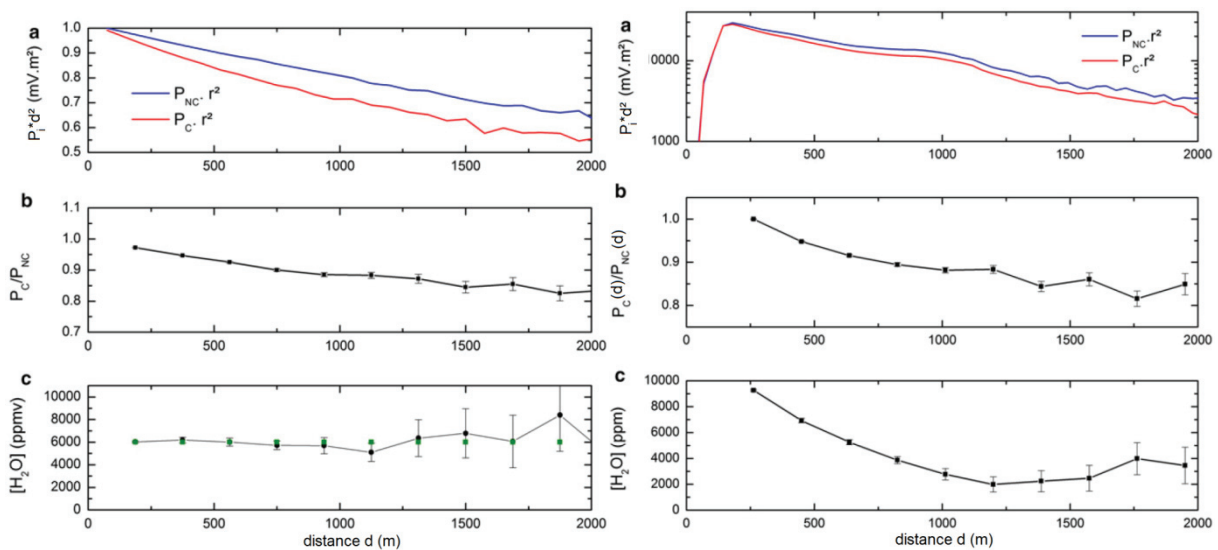


**Figure A.3** Simulation (left column) and experimental (right column) results for correlated and non-correlated range-corrected OCS-lidar signals  $P_i(d) \times d^2$  (a), ratio of both OCS-lidar signals (b) and retrieved water vapor mixing-ratio (black dots) and model input mixing-ratio (green squares) (c)

Hence for the first time, we experimentally demonstrate the ability of OCS-lidar methodology to measure the water vapor content in the lower atmosphere. In addition, numerical simulation have been performed to show that other atmospheric trace gases remote sensing is feasible with OCS-lidar, especially for methane greenhouse gas (Thomas et al., 2012). Finally, as shown in (Thomas et al., 2013b), the OCS-lidar signal is moderately affected by pressure and temperature broadening of an individual absorption line, since OCS relies on signals spectrally integrated over a broadband light. Hence we believe that the OCS-lidar methodology offers great possibilities for atmospheric trace gases remote sensing.

## Appendix B

### Sky background contribution to the polarized Lidar signal

In this appendix, the sky background contribution to the Lyon polarization lidar signal is analyzed. Scattering of sunlight by atmospheric molecules and particles is detected with the Lidar as a sky background intensity, noted  $I_{sb}$  in Equation (B.1). Geophysical factors contribute to  $I_{sb}$  such as the local meteorological conditions or the relative positioning between the Sun and the Earth. Sun sky scattering can drastically limit the range accessible to the perpendicular backscattering coefficient  $\beta_{p,\perp}$  and induce photon noise.

We here studied the polarization components of the sky background intensity vector  $\mathbf{I}_{sb}$ . These p and s-sunlight polarization components are defined with respect to the solar scattering plane, represented in Figure B.1-a, together with the Lidar station (source and detector). The scattering angle is the solar zenith angle  $\theta_s$ , whose cosine is equal to  $\cos(\theta_s) = \sin(L)\sin(\delta_s) + \cos(L)\cos(\Delta_s)\cos(h)$ , where  $L$  is Lidar station latitude,  $\Delta_s$  is the solar declination angle and  $h$  is the local hour angle of the Sun. The p and s-polarization components of the sky intensity have been calculated by assuming a standard molecular atmosphere. In the presence of aerosols, the ratio of p-polarized component to s-polarized component will increase (if these aerosols are spherical) or both polarized components will increase (if some aerosols are non-spherical). In the presence of cirrus clouds, the perpendicular sky background intensity will increase, due to cirrus clouds depolarization (in the range of 30-40 % at mid-latitudes, according to Del Guasta and Vallar (2003)), which may limit the range of the polarization Lidar measurements. However, as recently shown by B. Barja and J.C. Antuña (2011), who quantified the cirrus clouds radiative forcing, the UV-VIS sky background intensity will be lower than under clear sky conditions so that the range of the polarization Lidar measurements should not be drastically affected, even in the presence of cirrus clouds. By assuming an unpolarized sunlight, the ratio between p and s-polarization components of  $\mathbf{I}_{sb}$  can be expressed by using the molecular differential scattering cross-sections dependence on the scattering angle  $\theta_s$  (Miles et al., 2001):

$$\frac{I_{sb,p}}{I_{sb,s}} = \rho_0 + (1 - \rho_0)\cos^2(\theta_s) \quad (\text{B.1})$$

where  $\rho_0$  is the depolarization factor of the standard molecular atmosphere (Bucholtz, 1995). Hence, the p-polarized component  $I_{sb,p}$  is always smaller than the s-component  $I_{sb,s}$ . We then projected these polarization components on the  $\{\parallel, \perp\}$ -polarization Lidar axes by using Figure B.1-a to obtain:  $I_{sb,\parallel} = \sin^2(h)I_{sb,s} + \cos^2(h)I_{sb,p}$  and  $I_{sb,\perp} = \cos^2(h)I_{sb,s} + \sin^2(h)I_{sb,p}$ . Hence, from sunrise to sunset, the two polarization sky background components cross twice during daytime.

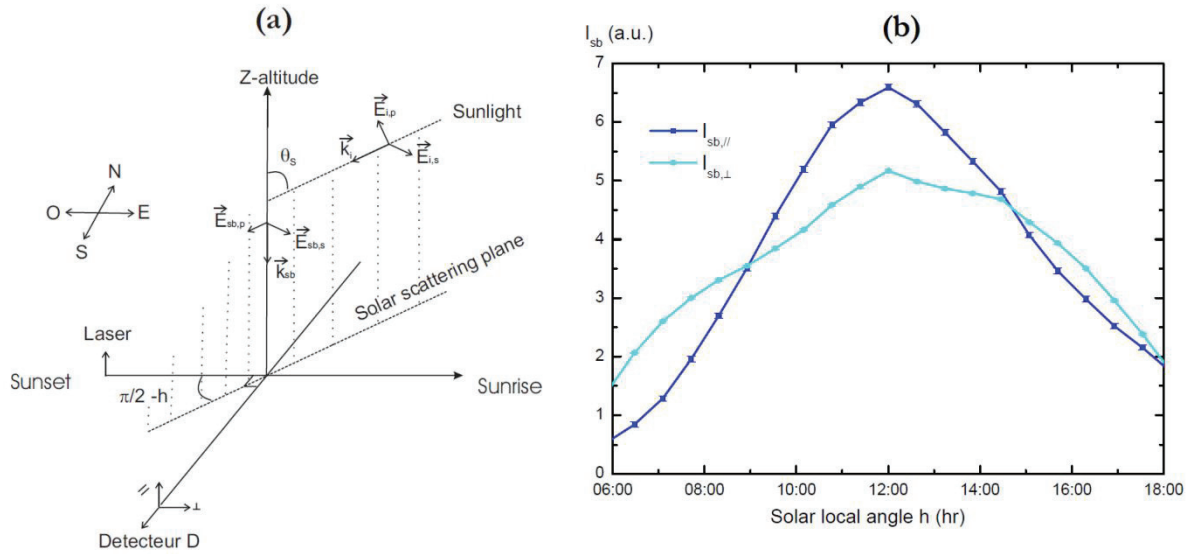


**Figure B.1** Sky background contribution to the Lidar intensity. (a) Sun scattering plane geometry and orientation with respect to the Lidar laser source and the detector polarization  $\{\parallel, \perp\}$ -axes. The emission laser is oriented to the East, and the angle between the solar scattering plane and the East is  $\pi/2 - h$ . (b) Measured sky background intensity  $I_{sb}$  on each polarization  $\{\parallel, \perp\}$ -axis as a function of the solar local angle on July 3<sup>rd</sup> 2011 at Lyon.

To achieve sensitive and accurate Lidar particle depolarization measurements in the percent range, the perpendicular Lidar signal, which is approximately 100 times lower than the parallel Lidar signal, must be accurately measured. This task is difficult to achieve during daytime as the sky background intensity  $I_{sb}$  reaches its maximum. From sunrise to sunset, figure 2b displays the sky background intensity  $I_{sb}$  measured on July 3<sup>rd</sup> in the UV-polarization channels with our vertically pointing Lidar. These observations agree with the above  $I_{sb,\parallel}$  and  $I_{sb,\perp}$ -expressions and between 9h and 15h,  $I_{sb,\perp}$  is lower than  $I_{sb,\parallel}$ . As shown in Figure B.1-b, the laser linear polarization has been chosen to match the perpendicular Lidar signal with the sky background intensity  $I_{sb,\perp}$  at noon ( $h = 0$ ), in agreement with the above projections equations. Hence, thanks to our geometry and to this polarization matching, the sky background contribution to the perpendicular Lidar signal has been lowered during

daytime, which preserves the range of the polarization Lidar measurement and the signal-to-noise ratio.

## Appendix C

### Depolarization ratio $\delta^*$ in the presence of a dichroic beamsplitter misalignment

In this appendix, we investigate the effect of a misalignment of the dichroic beamsplitter on the measured depolarization ratio  $\delta^*$ . To parameterize the magnitude and the direction of this misalignment, we introduce an offset angle  $\theta_0$  as the angle between the parallel laser linear polarization and the p-axis of the dichroic beamsplitter (defined with respect to the dichroic beamsplitter plane of incidence) (see Figure (3.1-d)). The aim of this appendix is to derive the relationship between the measured depolarization  $\delta^*$  and the atmosphere depolarization  $\delta$  as a function of the  $\theta_0$  offset angle and the  $R_p$ ,  $R_s$ -reflectivity coefficients of the dichroic beamsplitter, hence justifying Equation (3.5).

The incident electric field  $\mathbf{E}_i$  on the dichroic beamsplitter can be written in the two involved mathematical bases, namely the ( $//$ ,  $\perp$ )-Lidar polarization basis and the (p,s)-dichroic beamsplitter basis. As shown by Figure 3.1-d, a  $\theta_0$ -rotation angle enables to change from one basis to the other. We projected the incident electric field vector  $\mathbf{E}_i$  of backscattered photons on the (p, s)-polarization basis to express the electric field vector  $\mathbf{E}_r$  of the reflected wave:

$$\begin{bmatrix} E_{r, //} \\ E_{r, \perp} \end{bmatrix} = \begin{bmatrix} \sqrt{R_p} \cos(\theta_0) & -\sqrt{R_s} \sin(\theta_0) \\ \sqrt{R_p} \sin(\theta_0) & \sqrt{R_s} \cos(\theta_0) \end{bmatrix} \begin{bmatrix} E_{i,p} \\ E_{i,s} \end{bmatrix} \quad (\text{C.1})$$

where  $\sqrt{R_p} = E_{r,p}/E_{i,p}$  and  $\sqrt{R_s} = E_{r,s}/E_{i,s}$  with  $E_{i,p}$  and  $E_{i,s}$  are the components of  $\mathbf{E}_i$  in the (p,s)-dichroic beamsplitter basis (the same notations are used for the reflected field  $\mathbf{E}_r$ ). Then, by projecting the incident electric field in the ( $//, \perp$ )-polarization basis, Equation (C.1) becomes:

$$\mathbf{E}_r = \mathbf{m}_{DB} \mathbf{E}_i \quad \text{with} \quad \mathbf{m}_{DB} = \begin{bmatrix} B - A \sin^2 \theta_0 & A \cos \theta_0 \sin \theta_0 \\ A \cos \theta_0 \sin \theta_0 & B - A \cos^2 \theta_0 \end{bmatrix} \quad (\text{C.2})$$

where the  $\mathbf{m}_{\text{DB}}$ -matrix relates the incident and reflected electric fields in the ( $//, \perp$ )-polarization basis and the two coefficients  $A = \sqrt{R_p} - \sqrt{R_s}$  and  $B = \sqrt{R_p}$  are determined by the dichroic beamsplitter  $R_p, R_s$ -reflectivity coefficients. Hence, reflection (or symmetrically transmission) on the dichroic beamsplitter induces a rotation of the linear polarization state of the light. In the ideal case, the dichroic beamsplitter is vertical, so that the p-axis is horizontal and  $\theta_0$  is zero. If we exchange the  $//$  and  $\perp$ -polarization channels,  $\theta_0$  is then  $\pi/2$ . In both cases ( $\theta_0 = 0$  or  $\pi/2$ ), the  $\mathbf{m}_{\text{DB}}$ -matrix is diagonal so that no cross-talk is induced. To derive the measured depolarization ratio  $\delta^*$  as a function of  $\delta$ , we now introduce intensities, proportional to the square of the electric field. Hence, Equation (C.2) can be written for laser intensities vectors  $\mathbf{I}_r$  and  $\mathbf{I}_i$ . By removing proportionality constants (which disappear in the  $\delta^*$ -calculation), we get:

$$\mathbf{I}_r = [\mathbf{M}_{\text{DB}}] \mathbf{I}_i \quad \text{with} \quad \mathbf{M}_{\text{DB}} = \begin{bmatrix} (B - A \sin^2 \theta_0)^2 & A^2 \cos^2 \theta_0 \sin^2 \theta_0 \\ A^2 \cos^2 \theta_0 \sin^2 \theta_0 & (B - A \cos^2 \theta_0)^2 \end{bmatrix} \quad (\text{C.3})$$

by noting that the ( $//, \perp$ )-polarization basis is orthogonal. As expected, the  $\mathbf{M}_{\text{DB}}$ -matrix is diagonal in the absence of offset angle  $\theta_0$  (i.e. if  $\theta_0 = 0$  or  $\pi/2$ ). By noting that  $\delta^* = I_{r,\perp}/I_{r,//}$  while  $\delta = I_{i,\perp}/I_{i,//}$ , we get the following relationship between  $\delta, \delta_0$  and  $\theta_0$ , which is identical to equation (9):

$$\delta^* = \frac{A^2 \cos^2 \theta_0 \sin^2 \theta_0 + \delta_0 (B - A \cos^2 \theta_0)^2}{(B - A \sin^2 \theta_0)^2 + \delta_0 A^2 \cos^2 \theta_0 \sin^2 \theta_0} \quad (\text{C.4})$$

where the two coefficients  $A = \sqrt{R_p} - \sqrt{R_s}$  and  $B = \sqrt{R_p}$  are determined by the dichroic beamsplitter  $R_p, R_s$ -reflectivity coefficients.

## List of personal publications:

David G., A. Miffre, B. Thomas and P. Rairoux: Sensitive and accurate dual-wavelength UV-VIS polarization detector for optical remote sensing of tropospheric aerosols, *Appl. Phys. B*, 108, 197–216, 2012.

David G., B. Thomas, T. Nousiainen, A. Miffre and P. Rairoux: Retrieving simulated volcanic, desert dust, and sea-salt particle properties from two / three-component particle mixtures using UV-VIS polarization Lidar and T-matrix, *Atmos. Chem Phys.*, 13, 6757-6776, 2013a.

David G., B. Thomas, E. Coillet, A. Miffre and P. Rairoux: Polarization-resolved exact light backscattering by an ensemble of particles in air, *Opt. Express*, 21, 16, 18624-18639, 2013b.

Dupart Y., S.M. King, B. Nekat, A. Nowak, A. Wiedensohler, H. Herrmann, G. David, B. Thomas, A. Miffre, P. Rairoux, B. D'Anna, and C. George: Mineral dust photochemistry induces nucleation events in the presence of SO<sub>2</sub>, *Proc. Natl. Acad. Sci. U.S.A.*, [www.pnas.org/cgi/doi/10.1073/pnas.1212297109](http://www.pnas.org/cgi/doi/10.1073/pnas.1212297109), 2012.

Miffre A., G. David, B. Thomas and P. Rairoux: Characterization of Iceland volcanic aerosols by UV-polarization Lidar at Lyon, SW Europe, *Proceedings of SPIE*, 7832, 2010b.

Miffre A., G. David, B. Thomas and P. Rairoux: Atmospheric non-spherical particles optical properties from UV-polarization lidar and scattering matrix, *Geophys. Res. Lett.*, 38, L16804, 2011.

Miffre A., G. David, B. Thomas, P. Rairoux, A.M. Fjaeraa, N.I. Kristiansen and A. Stohl: Volcanic aerosol optical properties and phase partitioning behavior after long-range advection characterized by UV-Lidar measurements, *Atm. Env.* 48, 76-84, 2012a.

Miffre A., G. David, B. Thomas, M. Abou Chacra, and P. Rairoux,: Interpretation of accurate UV-Polarization Lidar measurements: Application to volcanic ash number concentration retrieval, *J. Atm. Ocean. Tech.*, 29, 2012b.

Thomas B., A. Miffre, G. David, J-P. Cariou and P. Rairoux: Remote sensing of trace gases with optical correlation spectroscopy and Lidar: Theoretical and numerical approach, *Appl. Phys. B*, 108, 689, 2012.

Thomas B., G. David, C. Anselmo, J-P. Cariou, A. Miffre and P. Rairoux: Remote sensing of atmospheric gases with optical correlation spectroscopy and lidar: first experimental result on water vapor profile measurements, *Appl. Phys. B*, doi: 10.1007/s00340-013-5468-4, 2013a.

Thomas B., G. David, C. Anselmo, E. Coillet, A. Miffre, J. P. Cariou, P. Rairoux, Remote sensing of methane with broadband laser and optical correlation spectroscopy on the Q-branch of the 2v<sub>3</sub> band, *Jour. Mol. Spectrom.*, doi: 10.1016/j.jms.2013.05.015, 2013b.

## References:

- Abou Chacra M.: Télédétection résolue en polarisation dans l'ultraviolet des particules atmosphériques; thèse, Université Claude Bernard Lyon1, 2009.
- Adam de Villiers R., G. Ancellet, J. Pelon, B. Quennehen, A. Scharwzenboeck, J. F. Gayet, and K. S. Law: Airborne measurements of aerosol optical properties related to early spring transport of mid-latitude sources into the Arctic, *Atm. Chem. Phys.* 9, 27791–27836, 2009.
- Alvarez J.M., M. A. Vaughan, C. A. Hostelier, W. H. Hunt and D. M. Winker: Calibration technique for polarization-sensitive Lidars, *J. Atm. Ocean. Tech.*, 23, 683-699, 2006.
- Ansmann, A., A. Petzold, K. Kandler, I. Tegen, M. Wendisch, D. Muller, B. Weinzierl, T. Muller and J. Heintzenberg: Saharan Mineral Dust Experiments SAMUM-1 and SAMUM-2: what have we learned ?, *Tellus*, 63B, 403–429, 2011.
- Ansmann A., P. Seifert, M. Tesche and U. Wandinger: Profiling of fine and coarse particle mass: case studies of Saharan dust and Eyjafjallajökull/Grimsvötn volcanic plumes, *Atmos. Chem. Phys.*, 12, 9399–9415, 2012.
- Arbouet, A., D. Christofilos, N. Del Fatti, F. Vallée, J. Huntzinger, L. Arnaud, P. Billaud and M. Broyer: Direct Measurement of the Single-Metal-Cluster Optical Absorption, *Phys. Rev. Lett.*, 93, 127401, 2004.
- Attwood A.R. and M.E. Greenslade: Optical Properties and Associated Hygroscopicity of Clay Aerosols, *Aerosol Sci. Technol.*, 45, 1350–1359, 2011.
- Barja B. and J. C. Antuña: The effect of optically thin cirrus clouds on solar radiation in Camagüey, Cuba, *Atmos. Chem. Phys.*, *Atmos. Chem. Phys.*, 11, 8625–8634, 2011, 8625–8634, 2011.
- Baumgardner D., R. Newton and N. Boyouk,: The Aerosol Particle Spectrometer with Polarization Detection (APSPD) Part I: laboratory studies, *Atmos. Chem. Phys. Special Issue*, in preparation, 2012.
- Behrendt A. and T. Nakamura: ‘Calculation of the calibration constant of polarization lidar and its dependency on atmospheric temperature’, *Opt. Exp.*, 10, 805-817, 2002.
- Bell C. L., G. Hancock, R. Peverall, G. A. D. Ritchie, J. H. van Helden and N. J. van Leeuwen: Characterization of an external cavity diode laser based ring cavity NICE-OHMS system, *Opt. Express*, 17, 9834–9, 2009.
- Berden, G. and R. Engeln: *Cavity ring-down spectroscopy*, Chichester: Wiley, 2009.
- Billaud P., S. Marhaba, E. Cottancin, L. Arnaud, G. Bachelier, C. Bonnet, N. Del Fatti, J. Lermé, F. Vallée, J.-L. Vialle, M. Broyer, and M. Pellarin: Correlation between the Extinction Spectrum of a Single Metal Nanoparticle and Its Electron Microscopy, *J. Phys. Chem. C*, 112, 978–982, 2008.
- Billaud P., S. Marhaba, N. Grillet, E. Cottancin, C. Bonnet, J. Lermé, J.L. Vialle, M. Broyer and M. Pellarin: Absolute optical extinction measurements of single nano-objects by spatial modulation spectroscopy using a white lamp, *Rev. Sci. Instrum.*, 81, 043101, 2010.
- Bohren C. F. and D. R. Huffman: *Absorption and scattering of light by small particles*, Wiley New York, 1983.

- Bösenberg J.: Ground-based differential absorption lidar for water-vapor and temperature profiling: methodology, *Appl. Opt.*, 37, 3845-3860, 1998.
- Boulon J., K. Sellegri, M. Hervo, and P. Laj: Observations of nucleation of new particles in a volcanic plume, *Proc. Natl. Acad. Sci. U.S.A.*, [www.pnas.org/cgi/doi/10.1073/pnas.1104923108](http://www.pnas.org/cgi/doi/10.1073/pnas.1104923108), 2011.
- Bourcier, L., K. Sellegri, P. Chausse, J.M. Pichon and P. Laj: Seasonal variation of water-soluble inorganic components in aerosol size-segregated at the puy de Dome station (1,465 m a.s.l.), France, *J. Atm. Chem.*, 69, 47-66, 2011.
- Browell E. V., S. Ismail and W. B. Grant: Differential absorption lidar (DIAL) measurements from air and space, *Appl. Phys. B*, 67, 399-410, 1998.
- Bucholtz A.: Rayleigh-scattering calculations for the terrestrial atmosphere, *Appl. Opt.* 34, 2765-2773, 1995.
- Burg T. P., M. Godin, S. M. Knudsen, W. Shen, G. Carlson, J. S. Foster, K. Babcock and S. R. Manalis: Weighing of biomolecules, single cells and single nanoparticles in fluid, *Nature*, 446, 1066-1069, 2007.
- Burlakov V. D., S. I. Dolgii, A. P. Makeev, A. V. Nevzorov, O. A. Romanovskii and O. V. Kharchenko: A differential-absorption lidar for ozone sensing in the upper atmosphere-lower stratosphere, *Instrum. Exp. Tech.*, 53, 886-889, 2010.
- Butler, T. J., J. L. Miller and A. J. Orr-Ewing: Cavity ring-down spectroscopy measurements of single aerosol particle extinction. I. The effect of position of a particle within the laser beam on extinction. *J. Chem. Phys.*, 126, 174302, 2007.
- Butler T. J., D. Mellon, J. Kim, J. Litman and A. J. Orr-Ewing: Optical-Feedback Cavity Ring-Down Spectroscopy Measurements of Extinction by Aerosol Particles, *J. Phys. Chem. A*, 113, 3963-3972, 2009.
- Cairo F., G. Di Donfrancesco, A. Adriani, L. Pulvirenti and F. Fierli: Comparison of various depolarization parameters measured by lidar, *Appl. Optics*, 38, 4425-4432, 1999.
- Chen, H., J. Winderlich, C. Gerbig, A. Hofer, C. W. Rella, E. R. Crosson, A. D. Van Pelt, J. Steinbach, O. Kolle, V. Beck, B. C. Daube, E. W. Gottlieb, V. Y. Chow, G. W. Santoni, and S. C. Wofsy: High-accuracy continuous airborne measurements of greenhouse gases (CO<sub>2</sub> and CH<sub>4</sub>) using the cavity ring-down spectroscopy (CRDS) technique. *Atm. Meas. Tech.*, 3, 375-386, 2010.
- Chung, I., and M. G. Bawendi: Relationship between single quantum-dot intermittency and fluorescence intensity decays from collections of dots, *Phys. Rev. B*, 70, 165304, 2004.
- Chylek P. and J. Wong: Effect of absorbing aerosols on global radiation budget, *Geophys. Res. Lett.*, 22, 929-931, 1995.
- Crosson E. R.: A cavity ring-down analyzer for measuring atmospheric levels of methane, carbon dioxide, and water vapour, *Appl. Phys. B*, 92, 403-8, 2008.
- Cziczo D.J and J.P. Abbatt: Infrared Observations of the Response of NaCl, MgCl<sub>2</sub>, NH<sub>4</sub>HSO<sub>4</sub>, and NH<sub>4</sub>NO<sub>3</sub> Aerosols to Changes in Relative Humidity from 298 to 238 K, *J. Phys. Chem. A*, 104, 2038-2047, 2000.

Dakin J.P., M.J. Gunning, P. Chambers and Z.J. Xin: Detection of gases by correlation spectroscopy, *Sens. Actuators B*, 90, 124 2003.

David G., A. Miffre, B. Thomas and P. Rairoux: Sensitive and accurate dual-wavelength UV-VIS polarization detector for optical remote sensing of tropospheric aerosols, *Appl. Phys. B*, 108, 197–216, 2012.

David G., B. Thomas, T. Nousiainen, A. Miffre and P. Rairoux: Retrieving simulated volcanic, desert dust, and sea-salt particle properties from two / three-component particle mixtures using UV-VIS polarization Lidar and T-matrix, *Atmos. Chem Phys.*, 13, 6757-6776, 2013a.

David G., B. Thomas, E. Coillet, A. Miffre and P. Rairoux: Polarization-resolved exact light backscattering by an ensemble of particles in air, *Opt. Express*, 21, 16, 18624-18639, 2013b.

Davletshin Y. R., A. Lombardi, M. F. Cardinal, V. Juvé, A. Crut, P. Maioli, L. M. Liz-Marza, F. Valleée N. Del Fatti and J. C. Kumaradas: A Quantitative Study of the Environmental Effects on the Optical Response of Gold Nanorods, *Acs Nano*, 6, 8183-8193, 2012.

de Gouw, J. and C. Warneke: Measurements of volatile organic compounds in the earth's atmosphere using proton-transfer-reaction mass spectrometry, *Mass Spectrometry Reviews*, 26, 223-257, 2007.

Del Guasta M., M. Morandi, L. Stefanutti, B. Stein, J. Kolenda, P. Rairoux, J. P. Wolf, R. Matthey and E. Kyro: Multiwavelength lidar observation of thin cirrus at the base of the Pinatubo stratospheric layer during the EASOE Campaign, *Geophys. Res. Lett.*, 21, 1339-1342, 1994.

Del Guasta M. and E. Valla: In-cloud variability of LIDAR depolarization of polar and midlatitude cirrus, *Geophys. Res. Lett.*, 30, No. 11, 1578, 2003.

Del Guasta M., E. Vallar, O. Riviere, F. Castagnoli, V. Venturi and M. Morandi: Use of polarimetric lidar for the study of oriented ice plates in clouds, *Appl Opt.*, 45, 4878-4887, 2006.

Delmelle P., F. Villi eras and M. Pelletier: Surface area, porosity and water adsorption properties of fine volcanic ash particles, *Bull. Volcanol.* 67, 160-169, 2005.

Di Girolamo P., D. Summa, R. Bhawar, T. Di Iorio, M. Cacciani, I. Veselovskii, O. Dubovik, and A. Kolgotin: Raman lidar observations of a Saharan dust outbreak event: characterization of the dust optical properties and determination of particle size and microphysical parameters, *Atmos. Env.* 50, 66-78, 2012.

Dinar E., A. Abo Riziq, C. Spindler, C. Erlick, G. Kiss and Y. Rudich: The complex refractive index of atmospheric and model humic-like substance (HULIS) retrieved by cavity ring down aerosol spectrometer, *Faraday Discuss.*, 137, 279-295, 2008.

Dockery D. W. and C. A. Pope: Acute respiratory effects of particulate air pollution. *Annual review of public health*, 15, 107-132, 1994.

Draine B.T. and P.J. Flatau: Discrete-dipole approximation for scattering calculations, *J Opt Soc Am* 11, 1491–9, 1994.

Dubovik O., A. Sinyuk, , T. Lapyonok, , B. N. Holben, , M. I. Mishchenko, P. Yang, , T. F. Eck, H. Volten, O. Mu oz, B. Veihelmann, W. J. van der Zande, J.-F. Leon, M. Sorokin, and I. Slutsker: Application of spheroid models to account for aerosol particle nonsphericity in remote sensing of desert dust, *J. Geophys. Res.*, 111, D11208, 2006.

Dupart Y., S.M. King, B. Nekat, A. Nowak, A. Wiedensohler, H. Herrmann, G. David, B. Thomas, A. Miffre, P. Rairoux, B. D'Anna, and C. George: Mineral dust photochemistry induces nucleation events in the presence of SO<sub>2</sub>, *Proc. Natl. Acad. Sci. U.S.A.*, [www.pnas.org/cgi/doi/10.1073/pnas.1212297109](http://www.pnas.org/cgi/doi/10.1073/pnas.1212297109), 2012.

Edner, H., S. Svanberg, L. Unéus and W. Wendt: Gas-correlation lidar. *Opt. Lett.*, 9(11), 493-495, 1984.

Eickenscheidt N. and R. Brumme: NO<sub>x</sub> and N<sub>2</sub>O fluxes in a nitrogen-enriched European spruce forest soil under experimental long-term reduction of nitrogen depositions, *Atm. Env.*, 60, 51-58, 2012.

Engeln R., G. Berden, R. Peeters and G. Meijer: Cavity enhanced absorption and cavity enhanced magnetic rotation spectroscopy. *Rev. Sci. Instrum.*, 69, 3763-3769, 1998.

Engelstaedter S., I. Tegen and R. Washington: North African dust emissions and transport, *Earth-Science Reviews*, 79, 73-100, 2006.

Ehret G., C. Kiemle, M. Wirth, A. Amediek, A. Fix and S. Houweling: Space-borne remote sensing of CO<sub>2</sub>, CH<sub>4</sub>, and N<sub>2</sub>O by integrated path differential absorption lidar: a sensitivity analysis, *Appl. Phys. B*, 90, 593-608, 2008.

Fan J. A., K. Bao, J. B. Lassiter, J. Bao, N. J. Halas, P. Nordlander and F. Capasso: Near-Normal Incidence Dark-Field Microscopy: Applications to Nanoplasmonic Spectroscopy, *Nano Lett.*, 12, 2817-2821, 2012.

Fann, N. and D. Risley: The public health context for PM<sub>2.5</sub> and ozone air quality trends, *Air Qual. Atmos. Health*, 6, 1-11, 2013.

Favez O., I. El Haddad, C. Piot, A. Boréave, E. Abidi, N. Marchand, J.L. Jaffrezo, J.L. Besombes, M.B. Personnaz, J. Sciare, H. Wortham, C. George and B. D'Anna. Inter-comparison of source apportionment models for the estimation of wood burning aerosols during wintertime in an Alpine city (Grenoble, France), *Atmospheric Chemistry and Physics* 10, 5295e5314, 2010.

Finlayson-Pitts, B. J., J. N. Pitts Jr: *Chemistry of the upper and lower atmosphere: theory, experiments, and applications*, Academic Press., San Diego, 2000.

Fraikin J. L., T. Teesalu, C. M. McKenney, E. Ruoslahti and A. N. Cleland: A high-throughput label-free nanoparticle analyser, *Nature Nanotechn.*, 6, 308-313, 2011.

Freudenthaler V., M. Esselborn, M. Wiegner, B. Heese, M. Tesche, A. Ansmann, D. Müller, D. Althausen, M. Wirth, A. Fix, G. Ehret, P. Knippertz, C. Toledano, J. Gasteiger, M. Garhammer and M. Seefeldner: Depolarization ratio profiling at several wavelengths in pure Saharan dust during Samum 2006, *Tellus*, 61B, 165–179, 2009.

Gasteiger, J., S. Groß, V. Freudenthaler and M. Wiegner: Volcanic ash from Iceland over Munich: mass concentration retrieved from ground-based remote sensing measurements, *Atmos. Chem. Phys.*, 11, 2209–2223, 2011.

Gayet J. F., O. Crépel, J. F. Fournol, S. Oshchepkov: A new airborne polar Nephelometer for the measurements of optical and microphysical cloud properties, Part I: Theoretical design, *Ann. Geophysicae*, 15, 451-459, 1997.

Georgieva E. M., W. S. Heaps and W. Huang: New Broadband LIDAR for Greenhouse Carbon Dioxide Gas Sensing in the Earth's Atmosphere, SPIE, Conference on Lidar Technologies Techniques and Measurements for Atmospheric Remote Sensing, Proceedings of SPIE, 8182, 2011.

Gheusi F., F. Ravetta, H. Delbarre, C. Tsamalis, A. Chevalier-Rosso; C. Leroy, P. Augustin, R. Delmas, G. Ancellet, G. Athier, P. Bouchou, B. Campistron, J.M. Cousin, M. Fourmentin, Y. Meyerfeld, Pic 2005, a field campaign to investigate low-tropospheric ozone variability in the Pyrenees, *Atm. Res.*, 101, 640, (2011).

Gibert, F., P. H. Flamant, J. Cuesta and D. Bruneau: Vertical 2- $\mu$  m Heterodyne Differential Absorption Lidar Measurements of Mean CO<sub>2</sub> Mixing Ratio in the Troposphere, *J. Atm. Ocean. Tech.*, 25, 1477-1497, 2008.

Glen A. and S.D. Brooks: A new method for measuring optical scattering properties of atmospherically relevant dusts using the Cloud Aerosol Spectrometer Polarization (CASPOL) instrument, *Atmos. Chem. Phys.* 13, 1345-1356, 2013.

Gimmestad G.: Reexamination of depolarization in lidar measurements, *Appl. Opt.*, 47, 3795-3802, 2008.

Ghosh N., M.F.G. Wood, I.A. Vitkin: Polarimetry in turbid, birefringent, optically active media: A Monte Carlo study of Mueller matrix decomposition in the backscattering geometry *J. Appl. Phys.* 105, 102023, 2009.

Gobbi, G. P., F. Barnaba and L. Ammannato: The vertical distribution of aerosols, Saharan dust and cirrus clouds in Rome (Italy) in the year 2001, *Atm. Chem. Phys.*, 4, 351-359, 2004.

Gurlit W., R. Zimmermann, C. Giesemann, T. Fernholz, V. Ebert, J. Wolfrum, U. Platt and J. P. Burrows: Lightweight diode laser spectrometer CHILD (compact high-altitude in-situ laser diode) for balloonborne measurements of water vapor and methane, *Appl. Opt.*, 44, 91-102, 2005.

Hadar, I., G. B. Hitin, A. Sitt, A. Faust and U. Banin: Polarization Properties of Semiconductor Nanorod Heterostructures: From Single Particles to the Ensemble, *The Journal of Physical Chemistry Letters*, 4, 502-507, 2013.

Hallquist M., J. C. Wenger, U. Baltensperger, Y. Rudich, D. Simpson, M. Claeys, J. Dommen, N. M. Donahue, C. George, A. H. Goldstein, J. F. Hamilton, H. Herrmann, T. Hoffmann, Y. Iinuma, M. Jang, M. E. Jenkin, J. L. Jimenez, A. Kiendler-Scharr, W. Maenhaut, G. McFiggans, Th. F. Mentel, A. Monod, A. S. H. Prévôt, J. H. Seinfeld, J. D. Surratt, R. Szmigielski, and J. Wildt: The formation, properties and impact of secondary organic aerosol: current and emerging issues, *Atmos. Chem. Phys.*, 9, 5155-5236, 2009.

Halmer MM., et al.: The annual volcanic gas input into the atmosphere, *J. Volc. Geotherm. Res.*, 115, 511-528, 2002.

Hamburger T., G. McMeeking, A. Minikin, W. Birmili, M. Dall'Osto, C. O'Dowd, H. Flentje, B. Henzing, H. Junninen, A. Kristensson, G. de Leeuw, A. Stohl, J. F. Burkhart, H. Coe, R. Krejci and A. Petzold: Overview of the synoptic and pollution situation over Europe during the EUCAARI-LONGREX field campaign. *Atmospheric Chemistry and Physics*, 11, 1065-1082, 2011.

Harris-Hobbs R.L. and W.A. Cooper: Field evidence supporting quantitative predictions of secondary ice production rates, *J. Atmos. Sci.*, 44, 1071-1082, doi:10.1175/1520-0469, 1987.

Hasager C. B., W. Birmili, G. Pappalardo and F. Prata: Atmospheric implications of the volcanic eruptions of Eyjafjallajökull, Iceland 2010, *Eyjafjallajökull Special Issue, Atmos. Chem. Phys.*, 2012.

Hayman M., S. Spuler, B. Morley and J. VanAndel: Polarization lidar operation for measuring backscatter phase matrices of oriented scatterers, *Opt. Exp.*, 20, 29553-29567, 2012.

- Haywood J.M. and O. Boucher: Estimates of the direct and indirect radiative forcing due to tropospheric aerosols: A review, *Rev. Geophys.*, 38, 513–543, 2000.
- Herich H., T. Tritscher, A. Wiacek, M. Gysel, E. Weingartner, U. Lohmann, U. Baltensperger and D.J. Cziczo: Water uptake of clay and desert dust aerosol particles at sub- and supersaturated water vapor conditions, *Phys. Chem. Chem. Phys.*, 11, 7804–7809, 2009.
- Hervo M., B. Quennehen, N. I. Kristiansen, J. Boulon, A. Stohl, P. Fréville, J.-M. Pichon, D. Picard, P. Labazuy, M. Gouhier, J.-C. Roger, A. Colomb, A. Schwarzenboeck and K. Sellegri: Physical and optical properties of 2010 Eyjafjallajökull volcanic eruption aerosol: ground-based, Lidar and airborne measurements in France, *Atmos. Chem. Phys.*, 12, 1721–1736, 2012.
- Hess M., P. Koepke and I. Schult: Optical Properties of Aerosols and Clouds: The Software Package OPAC, 79, 831-844, 1998.
- Heyes C. D., A. Y. Kobitski, V. V. Breus and G. U. Nienhaus: Effect of the shell on the blinking statistics of core-shell quantum dots: A single-particle fluorescence study, *Phys. Rev. B*, 75, 125431, 2007.
- Hovenier J.W., H. Volten, O. Muñoz, W.J. van der Zande and L.B.F.M. Waters: Laboratory studies of scattering matrices for randomly oriented particles: potentials, problems and perspectives, *J. Quant. Spec. Rad. Transf.* 79-80, 741-755, 2003.
- Hummel, J. R., E. P. Shettle and D. R. Longtin: A New Background Stratospheric Aerosol Model for Use in Atmospheric Radiation Models, AFGL-TR-88-0166, Air Force Geophysics Laboratory, Hanscom AFB, MA, 1988.
- Ikuta K., N. Yoshikane, N. Vasa, Y. Oki, M. Maeda, M. Uchiumi, Y. Tsumura, J. Nakagawa, and N. Kawada: Differential absorption lidar at 1.67  $\mu\text{m}$  for remote sensing of methane leakage, *Jap. J. Appl. Phys.*, 38, 110, 1999.
- Ilyinskaya, E., V.I. Tsanev, R.S. Martin, C. Oppenheimer, J. Le Blond, G.M. Sawyer and M.T. Gudmundsson: Near source observations of aerosol size-distribution in the eruptive plumes from Eyjafjallajökull volcano, March-April 2010, *Atm. Env.*, 45, 3210-3216, 2011.
- Ishii S., K. Mizutani, H. Fukuoka, T. Ishikawa, B. Philippe, H. Iwai, T. Aoki, T. Itabe, A. Sato, and K. Asai: Coherent 2  $\mu\text{m}$  differential absorption and wind lidar with conductively cooled laser and two-axis scanning device, *Appl. Opt.*, 49, 1809-1817, 2010.
- Jacobson, M. Z.: Strong radiative heating due to the mixing state of black carbon in atmospheric aerosols, *Nature*, 409, 695-697, 2001.
- Juvé V.: Spectroscopie Linéaire et Ultra-rapide de Nanoparticules Métalliques : de l'ensemble au nano-objet individuel Université Claude Bernard Lyon1, 2011.
- Kaaden, N., A. Massling, A. Schladitz, T. Müller, K. Kandler, L. Schütz, B. Weinzierl, A. Petzold, M. Tesche, S. Leinert, C. Deutscher, M. Ebert, S. Weinbruch, and A. Wiedensohler: State of mixing, shape factor, number size distribution, and hygroscopic growth of the Saharan anthropogenic and mineral dust aerosol at Tinfou, Morocco, *Tellus* 61B, 51–63, 2009.
- Kacenelenbogen M. et al.: An accuracy assessment of the CALIOP/CALIPSO version 2/version 3 daytime aerosol extinction product based on a detailed multi-sensor, multi-platform case study, *Atm. Chem. Phys.*, 11, 3981-4000, 2011.

- Kahnert M., T. Nousiainen and B. Veihelmann: Spherical and spheroidal model particles as an error source in aerosol climate forcing and radiance computations: a case study for feldspar aerosols, *J Geophys Res*, 110:D18S13, 2005.
- Kahnert M., T. Nousiainen, H. Lindqvist, and M. Ebert: Optical properties of light absorbing carbon aggregates mixed with sulfate: assessment of different model geometries for climate forcing calculations, *Opt. Express*, 20, 9, 10042-10058, 2012.
- Kahnert M.: The T-matrix code Tsym for homogeneous dielectric particles with finite symmetries. *J. Quant. Spec. Rad. Transf.*, 123, 62–78, 2013.
- Kahnert M., T. Nousiainen, and H. Lindqvist: Models for integrated and differential scattering optical properties of encapsulated light absorbing carbon aggregates, *Opt. Express*, 21, 7974-7993, 2013.
- Kaplan D. and P. Tournois: Theory and performance of the acousto-optic programmable dispersive filter used for femtosecond laser pulse shaping, *J. Phys. IV France*, 12, 69, 2002.
- Kandler K., K. Lieke, N. Benker, C. Emmel, M. Küpper, D. Müller-Ebert, M. Ebert, D. Scheuven, A. Schladitz, L. Schütz, and S. Weinbruch: Electron microscopy of particles collected at Praia, Cape Verde, during the Saharan Mineral Dust Experiment: particle chemistry, shape, mixing state and complex refractive index, *Tellus 63B*, 475–496, 2011.
- Kasparian J., E. Frejafon., P. Rambaldi, J. Yu, B. Vezin, J.P. Wolf: Characterization of urban aerosols using SEM-microscopy, X-ray-analysis and Lidar measurement. *Atmos. Environ.* 32 (17), 2957-2967, 1998.
- Katanoda K., T. Sobue, H. Satoh, K. Tajima, T. Suzuki, H. Nakatsuka, T. Takezaki, T. Nakayama, H. Nitta, K. Tanabe and S. Tominaga: An association between long-term exposure to ambient air pollution and mortality from lung cancer and respiratory diseases in Japan, *J Epidemiol.*, 21, 132-43, 2011.
- Kaye P., W. R. Stanley, E. Hirst, E. V. Foot, K. L. Baxter and S. J Barrington: Single particle multichannel bio-aerosol fluorescence sensor. *Optics express*, 13(10), 3583-3593, 2005.
- Kirkby J. et al.: Role of sulphuric acid, ammonia and galactic cosmic rays in atmospheric aerosol nucleation, *Nature*, 476, 429-433, 2011.
- Khalizov A. F., H. Xue, L. Wang, J. Zheng and R. Zhang.: Enhanced light absorption and scattering by carbon soot aerosol internally mixed with sulfuric acid, *J. Phys. Chem. A*, 113, 1066-1074, 2009.
- Klaassen, M. and H. Biebach: Flight altitude of trans-Sahara migrants in autumn: a comparison of radar observations with predictions from meteorological conditions and water and energy balance models, *J. Avian Biology*, 31, 47-55, 2000.
- Klein H. , S. Nickovic, W. Haunold, U. Bundke, B. Nillius, M. Ebert, S. Weinbruch, L. Schuetz, Z. Levin, L. A. Barrie and H. Bingemer: Saharan dust and ice nuclei over central Europe, *Atmos. Chem. Phys.*, 10, 10211-10221, 2010.
- Klett J.D.: Lidar inversion with variable backscatter/extinction ratios, *Appl. Opt.*, 24, 1638-1643, 1985.
- Kuga Y. and A. Ishimaru: Retroreflectance from a dense distribution of spherical particles, *J. Opt. Soc. Am. A* 1, 831-835, 1984.
- Kuhlicke A., S. Schietinger, C. Matyssek, K. Busch and O. Benson: In Situ Observation of Plasmon Tuning in a Single Gold Nanoparticle during Controlled Melting, *Nano Lett.*, 13, 2041–2046, 2013.

- Kulmala M., H. Vehkamäki, T. Petäjä, M. Dal Maso, A. Lauri, V.-M. Kerminen, W. Birmili and P.H. McMurry: Formation and growth rates of ultrafine atmospheric particles: a review of observations, *J. Aerosol Sci.*, 35, 143–176, 2004.
- Kulmala M., T. Petäjä, T. Nieminen, M. Sipilä, H. E. Manninen, K. Lehtipalo, M. Dal Maso, P. P. Aalto, H. Junninen, P. Paasonen, I. Riipinen, K. E. J. Lehtinen, A. Laaksonen and V. M. Kerminen: Measurement of the nucleation of atmospheric aerosol particles, *Nat. Protoc.*, 7, 9, 1651, 2012.
- Kyrö E. M., V. M. Kerminen, A. Virkkula, M. D. Maso, J. Parshintsev, J. Ruíz-Jimenez, L. Forsström, H. E. Manninen, M.-L. Riekkola, P. Heinonen and M. Kulmala: Antarctic new particle formation from continental biogenic precursors, *Atmos. Chem. Phys.*, 13, 3527–3546, 2013.
- Lang-Yona N., Y. Rudich, E. Segre, E. Dinar and A. Abo-Riziq: Complex refractive indices of aerosols retrieved by continuous wave-cavity ring down aerosol spectrometer. *Anal. Chem.*, 81, 1762–1769, 2009.
- Lashof D. A. and D. R. Ahuja: Relative contributions of greenhouse gas emissions to global warming, *Nature*, 344, 529–531, 1990.
- Latham T. L., P. Kumar, A. Nenes, J. Dufek, I. N. Sokolik, M. Trail and A. Russell: Hygroscopic properties of volcanic ash, *Geophys. Res. Lett.*, 38, L11802, doi:10.1029/2011GL047298, 2011.
- Lee K. J., L. M. Browning, P. D. Nallathamby, and X. N. Xu: Study of Charge-Dependent Transport and Toxicity of Peptide-Functionalized Silver Nanoparticles Using Zebrafish Embryos and Single Nanoparticle Plasmonic Spectroscopy, *Chem. Res. Toxicol.*, 26, 904–917, 2013.
- Lesins G., P. Chylek and U. Lohmann: A study of internal and external mixing scenarios and its effect on aerosol optical properties and direct radiative forcing, *J. Geophys. Res.*, 107, 4094, 2002.
- Levenson M. D., B. A. Paldus, T. G. Spence, C. C. Harb, J. S. Harris Jr and R. N. Zare: Optical heterodyne detection in cavity ring-down spectroscopy, *Chem. Phys. Lett.*, 290, 335–40, 1998.
- Li J., J. G. D. Wong, J. S. Dobbie and P. Chylek: Parameterization of the Optical Properties of Sulfate Aerosols, *J. Atmospheric Sci.*, 58, 193–209, 2001.
- Li L., T. Hutter, U. Steiner and S. Mahajan: Single molecule SERS and detection of biomolecules with a single gold nanoparticle on mirror junction, *Analyst*, 138, 4574–4578, 2013.
- Lindqvist H., T. Nousiainen, E. Zubko, O. Munoz: Optical modeling of vesicular volcanic ash particles, *J. Quant. Spec. Rad. Transf.* 112, 1871–1880, 2011.
- Liu L., M.I. Mishchenko, J.W. Hovenier, H. Volten and O. Muñoz: Scattering matrix of quartz aerosols: comparison and synthesis of laboratory and Lorenz-Mie results, *J. Quant. Spec. Rad. Transf.* 79–80, 911–920, 2003.
- Loftfield N., H. Flessa, J. Augustin and F. Beese: Automated gas chromatographic system for rapid analysis of the atmospheric trace gases methane, carbon dioxide, and nitrous oxide, *Journal of Environmental Quality*, 26, 560–564, 1997.
- Lombardi A., M. Loumagne, A. Crut, P. Maioli, N. Del Fatti, and F. Vallée: Surface Plasmon Resonance Properties of Single Elongated Nanoobjects: Gold Nanobipyramids and Nanorods, *Langmuir*, 28, 9027–9033, 2012.

- Lou X.T., G. Somesfalean, B. Chen, Y.G. Zhang, H.S. Wang, Z.G. Zhang, S.H. Wu and Y.K. Qin: Simultaneous detection of multiple-gas species by correlation spectroscopy using a multimode diode laser, *Opt. Lett.*, 35, 1749, 2010.
- Mallet, M., J. C. Roger, S. Despiaud, J. P. Putaud and O. Dubovik: A study of the mixing state of black carbon in urban zone, *J. Geophys. Res.*, 109, D04202, 2004.
- Marenco F. and R.J. Hogan, Determining the contribution of volcanic ash and boundary layer aerosol in backscatter lidar returns: A three-component atmosphere approach, *J. Geophys. Res.*, 116, doi: 10.1029/2010JD015415, 2011
- Markowicz K.M., T. Zielinski, A. Pietruczuk, M. Posyniak, O. Zawadzka, P. Makuch, I.S. Stachlewska, A.K. Jagodnicka, T. Petelski, W. Kumala, P. Sobolewski, T. Stacewicz: Remote sensing measurements of the volcanic ash plume over Poland in April 2010, *Atm. Env.*, 48, 66-75, 2012.
- Mather T.A., Pyle, D.M., and Oppenheimer, C.: Tropospheric Volcanic Aerosol, Volcanism and the Earth's Atmosphere, *Geophys. Monograph* 139, 10.129/139GM12, 189-212, 2003.
- Measures R.M.: *Laser Remote Sensing, Fundamentals and Applications*, Krieger Melbourne, 1992.
- Mejean G., J. Kasparian, J. Yu, S. Frey, E. Salmon, JP Wolf: Remote detection and identification of biological aerosols using a femtosecond terawatt lidar system, *App. Phys. B*, 78, 535-537, 2004.
- Merikallio S., H. Lindqvist, T. Nousiainen and M. Kahnert: Modelling light scattering by mineral dust using spheroids: assessment of applicability, *Atmos. Chem. Phys.*, 11, 5347–5363, 2011.
- Mie G.: Beiträge zur Optik trüber Medien, speziell kolloidaler Metallösungen, *Annalen der Physik* 330, 377-445 (1908).
- Miffre A., M. Abou Chacra, S. Geffroy, P. Rairoux, L. Soulhac, R.J. Perkins and E. Frejafon: Aerosol load study in urban area by Lidar and numerical model, *Atm. Env.*, 44, 1152-1161, 2010a.
- Miffre A., G. David, B. Thomas and P. Rairoux: Characterization of Iceland volcanic aerosols by UV-polarization Lidar at Lyon, SW Europe, *Proceedings of SPIE*, 7832, 2010b.
- Miffre A., G. David, B. Thomas and P. Rairoux: Atmospheric non-spherical particles optical properties from UV-polarization lidar and scattering matrix, *Geophys. Res. Lett.*, 38, L16804, 2011.
- Miffre A., G. David, B. Thomas, P. Rairoux, A.M. Fjaeraa, N.I. Kristiansen and A. Stohl: Volcanic aerosol optical properties and phase partitioning behavior after long-range advection characterized by UV-Lidar measurements, *Atm. Env.* 48, 76-84, 2012a.
- Miffre A., G. David, B. Thomas, M. Abou Chacra, and P. Rairoux,: Interpretation of accurate UV-Polarization Lidar measurements: Application to volcanic ash number concentration retrieval, *J. Atm. Ocean. Tech.*, 29, 2012b.
- Miles R.B., W.R. Lempert, and J.N. Forkey: Laser Rayleigh scattering, *Meas. Sci. Tech.*, 12, R33-R51, 2001.
- Miles R.E.H., A.E Carruthers and J.P. Reid: Novel optical techniques for measurements of light extinction, scattering and absorption by single aerosol particles. *Laser & Photon. Rev.*, 5, 534–552, 2011.
- Minato A, M.A. Joarder, S. Ozawa, M. Kadoya and N. Sugimoto: Development of a Lidar System for Measuring Methane Using a Gas Correlation Method, *Jap. J. Appl. Phys.*, 38, 6130, 1999.

Mishchenko M.I. and J. W. Hovenier: Depolarization of light backscattered by randomly oriented non spherical particles, *Opt. Lett.*, 20, 1356–1359, doi:10.1364/OL.20.001356, 1995.

Mishchenko M.I. and L.D. Travis: Capabilities and limitations of a current Fortran implementation of the T-matrix method for randomly oriented rotationally symmetric scatterers, *J. Quant. Spectrosc. Radiat. Transf.*, 60, 309-324, 1998.

Mishchenko M. I. and K. Sassen: Depolarization of lidar returns by small ice crystals: An application to contrails, *Geophys. Res. Lett.*, 25, 309-312, 1998.

Mishchenko M.I.: Calculation of the amplitude matrix for a nonspherical particle in a fixed orientation, *Appl. Opt.*, 39, 1026-1031, 2000.

Mishchenko M.I., J. W. Hovenier and L. D. Travis: *Light scattering by nonspherical particles: theory, measurements, and applications*, SanDiego Academic Press, 2000.

Mishchenko M.I., L.D. Travis and A.A. Lacis: *Scattering, absorption and emission of Light by small particles*, 3<sup>rd</sup> edition, Cambridge University Press, UK, 2002.

Mishchenko M. I., J. W. Hovenier, and D. W. Mackowski: Single scattering by a small volume element, *J. Opt. Soc. Am. A*, 21, 71–87, 2004.

Mishchenko M. I., L. Liu, and G. Videen: Conditions of applicability of the single-scattering approximation, *Opt. Express*, 15, 12, 7522–7527, 2007a.

Mishchenko, M. I., B. Cairns, G. Kopp, C. F. Schueler, B. A. Fafaul, J. E. Hansen, J. E. Hansen, R. J. Hooker, T. Itchkawich, H. B. Maring and L. D. Travis: Accurate monitoring of terrestrial aerosols and total solar irradiance: introducing the Glory Mission, *Bull. Amer. Meteor. Soc.*, 88, 677-691, 2007b.

Mishchenko M.I.: Electromagnetic scattering by nonspherical particles: A tutorial review, *J. Quant. Spec. Rad. Transf.*, 110, 808–832, 2009.

Mock J. J., M. Barbic, D. R. Smith, D. A. Schultz and S. Schultz: Shape Effects in Plasmon Resonance of Individual Colloidal Silver Nanoparticles, *J. Chem. Phys.*, 116, 6755–6759, 2002.

Muñoz O., H. Volten, J. W. Hovenier, B. Veihelmann, W. J. van der Zande, L. B. F. M. Waters, and W. I. Rose: Scattering matrices of volcanic ash particles of Mount St Helens, Redoubt, and Mount Spurr volcanoes. *J. Geophys. Res.*, 109, D16201, 2004.

Munoz O.: Laboratory measurements for small particles in single-scattering conditions, *ELS XII*, 2010.

Muñoz O. and J.W. Hovenier: Laboratory measurements of single light scattering by ensembles of randomly oriented small irregular particles in air. A review, *J. Quant. Spec. Rad. Transf.*, 112, 1646-1657, 2011.

Muller M., C. George and B. D'Anna, Enhanced spectral analysis of C-TOF Aerosol Mass Spectrometer data: iterative residual analysis and cumulative peak fitting, *Int. J. Mass. Spectrom.*, 306:1–8 (2011).

Müller T., M. Laborde, G. Kassell and A. Wiedensohler, Design and performance of a three-wavelength LED-based total scatter and backscatter integrating nephelometer, *Atmos. Meas. Tech.*, 4, 1291–1303, 2011.

- Murayama T., H. Okamoto, N. Kaneyasu, H. Kamataki and K. Miura: Application of lidar depolarization measurement in the atmospheric boundary layer: Effects of dust and sea-salt particles, *J. Geophys. Res.*, 104, No. D24, 1999.
- Muskens O. L. and A. Lagendijk: Broadband enhanced backscattering spectroscopy of strongly scattering media, *Opt. Exp.*, 16, 1222-1231, 2008.
- Neumann, N., M. Ebermann, S. Kurth, and K. Hiller: Tunable infrared detector with integrated micromachined Fabry-Perot filter, *J. Micro/Nanolith., MEMS MOEMS*, 7(2), 021004, 2008.
- Nirmal M., B. O. Dabbousi, M. G. Bawendi, J. J. Macklin, J. K. Trautman, T. D. Harris and L. E. Brus: Fluorescence intermittency in single cadmium selenide nanocrystals, *Nature*, 383, 802-804, 1996.
- Nishizawa T., N. Sugimotoa, I. Matsui, A. Shimizu and H. Okamoto: Algorithms to retrieve optical properties of three component aerosols from two-wavelength backscatter and one-wavelength polarization lidar measurements considering nonsphericity of dust, *J. Quant. Spec. Rad. Transf.*, 112, 254-267, 2011.
- Nousiainen T.: Optical modeling of mineral dust particles: a review, *J. Quant. Spec. Rad. Transf.*, 110, 1261-1279, 2009.
- Nousiainen T., E. Zubko, H. Lindqvist, M. Kahnert and J. Tyynel,: Comparison of scattering by different nonspherical, wavelength-scale particles, *J. Quant. Spec. Rad. Transf.*, 113, 2391-2405, 2012.
- O'Dowd C., M. H. Smith, I. E. Consterdine and J. A. Lowe: Marine aerosol, sea salt, and the marine sulfur cycle: a short review, *Atm. Env.*, 31, 73-80, 1997.
- O'Dowd C. D., J. L. Jimenez, R. Bahreini, , R. C. Flagan, J. H. Seinfeld, K. Hämeri, L. Pirjola, M. Kulmala, S. G. Jennings and T. Hoffmann: Marine aerosol formation from biogenic iodine emissions, *Nature*, 417, 632-636, 2002.
- O'Keefe A.: Integrated cavity output analysis of ultra-weak absorption. *Chem. Phys. Lett.*, 293, 331-336, 1998.
- Onasch T.B., R.L. Siefere, S.D. Brooks, A.J. Prenni, B. Murray, M.A. Wilson and M.A. Tolbert: Infrared spectroscopy study of the deliquescence and efflorescence of ammonium sulfate aerosol as a function of temperature, *J. Geophys. Res.* 104, D17, 21317-21326, 1999.
- Ovadnevaite J., D. Ceburnis, K. Plauskaite-Sukiene, R. Modini, R. Dupuy, I. Rimselyte, R. Ramonet, K. Kvietkus, Z. Ristovski, H. Berresheim and C. O'Dowd: Volcanic sulfate and arctic dust plumes over the North Atlantic Ocean, *Atm. Env.*, 43, 4968-4974, 2009.
- Palmer K. F. and D. Williams: Optical constants of sulfuric acid: Application to the clouds of Venus? *Appl. Opt.* 14, 208- 219, 1975.
- Pan Y. L., H. Huang and R. K. Chang: Clustered and integrated fluorescence spectra from single atmospheric aerosol particles excited by a 263-and 351-nm laser at New Haven, CT, and Adelphi, MD. *J. Quant. Spec. Rad. Transf.*, 113, 2213-2221, 2012.
- Park, J. H., A. H. Goldstein, J. Timkovsky, S. Fares, R. Weber, J. Karlik and R. Holzinger: Active Atmosphere-Ecosystem Exchange of the Vast Majority of Detected Volatile Organic Compounds, *Science*, 341, 643-647, 2013.

Patterson B. A., J. P. Lenney, W. Sibbett, B. Hirst, N. K. Hedges and M. J. Padgett: Detection of benzene and other gases with an open-path, static Fourier-transform UV spectrometer. *Appl. Opt.*, 37, 3172-3175, 1998.

Paul J. B., L. Lapson and J. G. Anderson: Ultrasensitive absorption spectroscopy with a high-finesse optical cavity and off-axis alignment, *Appl. Opt.*, 40, 4904-4910, 2001.

Penchev S., V. Pencheva and S. Naboko, *Compte Rendus de l'Academie Bulgare des Sciences* 56, 669, 2012.

Penner J.E. et al.: Aerosols, their direct and indirect effects. In: *Climate Change 2001: The Scientific Basis. Contribution of Working Group I to the Third Assessment Report of the Intergovernmental Panel on Climate Change* [Houghton, J.T., et al. (eds.)]. Cambridge University Press, Cambridge, United Kingdom and New York, NY, USA, pp. 289– 348, 2001.

Perkins R.J., LMFA, Ecole Centrale Lyon, France, personal communication, 2012.

Person S., M. Jain, Z. Lapin, J. J. Sáenz, G. Wicks and L. Novotny: Demonstration of zero optical backscattering from single nanoparticles. *Nano Lett.*, 13, 1806-1809, 2013.

Petters M.D. and S. M. Kreidenweis: A single parameter representation of hygroscopic growth and cloud condensation nucleus activity, *Atmos. Chem. Phys.*, 7, 1961–1971, 2007.

Pettersson A., E. R. Lovejoy, C. A. Brock, S. S. Brown and A. R. Ravishankara: Measurement of aerosol optical extinction at 532nm with pulsed cavity ring down spectroscopy, *J. Aerosol Sci.*, 35, 995-1011, 2004.

Platt U. and J. Stutz: *Differential Optical Absorption Spectroscopy: Principles and Applications*, Berlin Springer, 2008.

Poirson J., T. Lanternier, J.C.Cotteverte, A. Le Floch and F. Bretenaker: Jones matrices of a quarter-wave plate for Gaussian beams, *Appl. Opt.* 34, 6806-6818, 1995.

Pope III C. A., M. Ezzati and D. W. Dockery: Fine particulate air pollution and life expectancies in the United States: The role of influential observations, *J. Air. Waste. Manage.*, 63(2), 129-132, 2013.

Pöschl U.: Atmospheric aerosols: Composition, transformation, climate and health effects. *Angew. Chem. Int. Ed.*, 44, 7520-7540, 2005.

Prata, A.J. and A. Tupper: Aviation hazards from volcanoes: the state of the science, *Nat. Hazards*, 51, 239-244, 2009.

Punger E. M. and J. J. West,: The effect of grid resolution on estimates of the burden of ozone and fine particulate matter on premature mortality in the USA, *Air Qual. Atmos. Health*, 1-11, 2013.

Quirantes A. and S. Bernard: Light scattering by marine algae: two-layer spherical and nonspherical models, *J. Quant. Spec. Rad. Transf.*, 89, 311-321, 2004.

Ramaswamy V. et al.: Radiative forcing of climate change. In: *Climate Change 2001: The Scientific Basis. Contribution of Working Group I to the Third Assessment Report of the Intergovernmental Panel on Climate Change* [Houghton, J.T., et al. (eds.)]. Cambridge University Press, Cambridge, United Kingdom and New York, NY, USA, 349– 416, 2001.

- Randriamiarisoa H., P. Chazette, P. Couvert, J. Sanak and G. Mégie: Relative humidity impact on aerosol parameters in a Paris suburban area, *Atm. Chem. Phys.*, 6, 1389–1407, 2006.
- Ravishankara, A. R.: Heterogeneous and multiphase chemistry in the troposphere. *Science*, 278, 1058–1065, 1997.
- Reichardt J. et al.: Optical properties of PSC Ia-enhanced at UV and visible wavelengths: Model and observations, *Geophys. Res. Lett.*, 27, 201-204, 2000.
- Revuelta M.A., M. Sastre, A.J. Fernández, L. Martín, R. García, F.J. Gómez-Moreno, B. Artíñano, M. Pujadas and F. Molero: Characterization of the Eyjafjallajökull volcanic plume over the Iberian Peninsula by lidar remote sensing and ground-level data collection, *Atm Env.*, 48, 46-55, 2012.
- Riemer N., M. West, R. Zaveri and R. Easter: Estimating black carbon aging time-scales with a particle-resolved aerosol model, *Aerosol Science*, 41, 143-158, 2010.
- Riley C.M., W.I. Rose and G.J.S. Bluth: Quantitative shape measurements of distal volcanic ash, *Journ. Geophys. Res.* 108, 2504, 2003.
- Riccobono F., L. Rondo, M. Sipilä, P. Barmet, J. Curtius, J. Dommen, M. Ehn, S. Ehrhart, M. Kulmala, A. Kürten, J. Mikkilä, P. Paasonen, T. Petäjä, E. Weingartner, and U. Baltensperger: Contribution of sulfuric acid and oxidized organic compounds to particle formation and growth, *Atm. Chem. Phys.* 12, 20, 9427-9439, 2012.
- Robock A.: Volcanic eruptions and climate, *Rev. Geophys.*, 38, 191-219, 2000.
- Rothman L.S., I.E. Gordon, A. Barbe, D. ChrisBenner, P.F. Bernath, M. Birk, V. Boudon, L.R. Brown, A. Campargue, J.-P. Champion, K. Chance, L.H. Coudert, V. Dana, V.M. Devi, S. Fally and J.-M. Flaud: The HITRAN 2008 molecular spectroscopic database, *J. Quant. Spec. Rad. Transf.*, 110, 533, 2009.
- Roy G., X. Cao and R. Bernier: On linear and circular depolarization LIDAR signatures in remote sensing of bioaerosols: experimental validation of the Mueller matrix for randomly oriented particles. *Opt. Engineering*, 50, 126001, 2011.
- Sakai T., Nagai T., Zaizen Y., and Mano Y.: Backscattering linear depolarization ratio measurements of mineral, sea-salt, and ammonium sulfate particles simulated in a laboratory chamber, *Appl. Opt.* 49, Vol. 23, 4441-4449, 2010.
- Sasano Y., and E. V. Browell: Light scattering characteristic of various aerosol types derived from multiple wavelength lidar observations, *Appl. Opt.*, 28, 1670-1679, 1989.
- Sassen K., “Polarization in Lidar”, in *Lidar, Range-Resolved Optical Remote Sensing of the Atmosphere*, C. Weitkamp, Springer, 2005.
- Sassen K., J. Zhu, P. Webley, K. Dean and P. Cobb: Volcanic ash plume identification using polarization lidar: Augustine eruption, Alaska, *Geophys. Res. Lett.*, 34, L08803, 2007
- Schiff H. I., G. I. Mackay and J. Bechara: The use of tunable diode laser absorption spectroscopy for atmospheric measurements *Air Monitoring by Spectroscopic Techniques*, ed M. W. Sigrist (New York: Wiley) chapter 5, 1994.
- Schnaiter M., H. Horvath, O. Möhler, K.-H. Naumann, H. Saathoff and O.W. Schöck: UV-VIS-NIR spectral optical properties of soot and soot containing aerosols. *Aerosol Sci.* 34, 1421-1444, 2003.

Schnaiter M., S. Büttner, O. Möhler, J. Skrotzki, M. Vragel and R. Wagner: Influence of particle size and shape on the backscattering linear depolarization ratio of small ice crystals – cloud chamber measurements in the context of contrail and cirrus microphysics, *Atmos. Chem. Phys.*, 12, 10465–10484, 2012.

Schumann U., B. Weinzierl, O. Reitebuch, H. Schlager, A. Minikin, C. Forster, R. Baumann, T. Sailer, K. Graf, H. Mannstein, C. Voigt, S. Rahm, R. Simmet, M. Scheibe, M. Lichtenstern, P. Stock, H. Rüba, D. Schäuble, A. Tafferner, M. Rautenhaus, T. Gerz, H. Ziereis, M. Krautstrunk, C. Mallaun, J.-F. Gayet, K. Lieke, K. Kandler, M. Ebert, S. Weinbruch, A. Stohl, J. Gasteiger, S. Groß, V. Freudenthaler, M. Wiegner, A. Ansmann, M. Tesche, H. Olafsson and K. Sturm: Airborne observations of the Eyjafjalla volcano ash cloud over Europe during air space closure in April and May 2010, *Atm. Chem. Phys.*, 11, 2245-2279, 2011.

Seinfeld J.H. and S.N. Pandis: *Atmospheric chemistry and physics: from air pollution to climate change*, John Wiley & Sons, 2006.

Shen Y.R.: *The principles of nonlinear optics*, ed. Wiley-Interscience, 2003.

Shettle E. P. and R. W. Fenn: *Models for the Aerosols of the Lower Atmosphere and the Effects of Humidity Variations on Their Optical Properties*, AFGL-TR-79-0214, 1979.

Shimizu A., N. Sugimoto, I. Matsui, K. Arao, I. Uno, T. Murayama, N. Kagawa, K. Aoki, A. Uchiyama and A. Yamazaki: Continuous observations of Asian dust and other aerosols by polarization lidars in China and Japan during ACE-Asia. *J. Geophys. Res.*, 109, D19S17, 2004.

Shurcliff W.A.: *Polarized light*, Harvard University Press, 1962.

Silverman M.P., W. Strange, J. Badoz and I.A. Vitkin: Enhanced optical rotation and diminished depolarization in diffusive scattering from a chiral liquid, *Opt. Commun.*, 132, 410-416, 1996.

Sönnichsen C. and A. P. Alivisatos: Gold nanorods as novel nonbleaching plasmon-based orientation sensors for polarized single-particle, *Nano Lett.*, 5, 301–304, 2005

Strawa, A. W., R. Elleman, A. G. Hallar, D. Covert, K. Ricci, R. Provencal, T. W. Owano, H. H. Jonsson, B. Schmid, A. P. Luu, K. Bokarius and E. Andrews: Comparison of in situ aerosol extinction and scattering coefficient measurements made during the Aerosol Intensive Operating Period. *J. Geophys. Res.*, 111, D05S03, 2006.

Stohl A., G. Wotawa, P. Seibert and H. Kromp-Kolb: Interpolation errors in wind fields as a function of spatial and temporal resolution and their impact on different types of kinematic trajectories. *J. Appl. Meteor* 34, 2149e2165, 1995.

Sugimoto N. et al.: Observation of dust and anthropogenic aerosol plumes in the Northwest Pacific with a two-wavelength polarization lidar on board the research vessel Mirai, *Geophys. Res. Lett.* 29, 2002.

Sugimoto N. and C. H. Lee: Characteristics of dust aerosols inferred from lidar depolarization measurements at two wavelengths, *Appl. Opt.*, 45, 2006.

Tanabe I. and T. Tatsuma: Plasmonic manipulation of color and morphology of single silver nanospheres, *Nano Lett.*, 12, 5418-5421, 2012.

Tatarov B., T. Trifonov, B. Kaprielov and I. Kolev: Dependence of the lidar signal depolarization on the receiver's field of view in the sounding of fog and clouds, *Appl. Phys. B* 71, 593–600, 2000.

Tesche M., A. Ansmann, D. Müller, D. Althausen, R. Engelmann, V. Freudenthaler and S. Groß: Vertically resolved separation of dust and smoke over Cape Verde using multiwavelength Raman and polarization lidars during Saharan Mineral Dust Experiment 2008, *J. Geophys. Res.*, 114, D13202, 2009.

Thomas B., A. Miffre, G. David, J-P. Cariou and P. Rairoux: Remote sensing of trace gases with optical correlation spectroscopy and Lidar: Theoretical and numerical approach, *Appl. Phys. B*, 108, 689, 2012.

Thomas B., G. David, C. Anselmo, J-P. Cariou, A. Miffre and P. Rairoux: Remote sensing of atmospheric gases with optical correlation spectroscopy and lidar: first experimental result on water vapor profile measurements, *Appl. Phys. B*, doi: 10.1007/s00340-013-5468-4, 2013a.

Thomas B., G. David, C. Anselmo, E. Coillet, A. Miffre, J. P. Cariou, P. Rairoux, Remote sensing of methane with broadband laser and optical correlation spectroscopy on the Q-branch of the 2v<sub>3</sub> band, *Jour. Mol. Spectrom.*, doi: 10.1016/j.jms.2013.05.015, 2013b.

Tsanev, V. I. and T. A. Mather: MicrotopsII inverse.NERC Field Spectroscopy Facility. [Available online at <http://fsf.nerc.ac.uk/resources/software/MicrotopsInverse.shtml>.], cited 2007.

Tseng, C. Y., Y. C. Huang, S. Y. Su, J. Y. Huang, C. H. Lai, C. C. Lung, C. C. Ho and Y. P. Liaw: Cell type specificity of female lung cancer associated with sulfur dioxide from air pollutants in Taiwan: An ecological study, *BMC public health*, 12, 4, 2012.

Tritscher T., Z. Juranyi, M. Martin, R. Chirico, M. Gysel, M. F Heringa, P. F DeCarlo, B. Sierau, A. S. H. Prévôt, E. Weingartner and U. Baltensperger: Changes of hygroscopicity and morphology during ageing of diesel soot, *Environ. Res. Lett.*, 6, 034026 (10pp), 2011.

Twomey, S.A.: The influence of pollution on the shortwave albedo of clouds, *J. Atmos. Sci.*, 34, 1149–1152, 1977.

Van de Hulst H. C.: *Light Scattering by Small Particles*, Wiley, New York, 1957.

Veselovskii I., O. Dubovik, A. Kolgotin, T. Lapyonok, P. Di Girolamo, D. Summa, D. N. Whiteman, M. I. Mishchenko and D. Tanré: Application of randomly oriented spheroids for retrieval of dust particle parameters from multiwavelength lidar measurements, *J. Geophys. Res.*, 115, D21203, 2010.

Vester B. P., M. Ebert, E. B. Barnert, J. Schneider, K. Kandler, L. Schütz and S. Weinbruch: Composition and mixing state of the urban background aerosol in the Rhein-Main area (Germany), *Atm. Env.*, 41, 6102-6115, 2007.

Von Glasow R., N. Bobrowski and C. Kern: The effects of volcanic eruptions on atmospheric chemistry, *Chemical Geology* 263, 131-142, 2009.

Wang Y., G. Zhuang, Y. Sun and Z. An: Water-soluble part of the aerosol in the dust storm season—evidence of the mixing between mineral and pollution aerosols, *Atm. Env.*, 39, 7020-7029, 2005.

Wang X., J. Lai, Z. Li, Harshman, T. K. Gustafson and P. Kelley: Polarization studies for backscattering of RBC suspensions based on Mueller matrix decomposition *Opt. Expr.* 20, 20771-20182, 2012.

Wehner B., H. Siebert, A. Ansmann, F. Ditas, P. Seifert, F. Stratmann, A. Wiedensohler, A. Apituley, R. A. Shaw, H. E. Manninen, and M. Kulmala: Observations of turbulence-induced new particle formation in the residual layer, *Atmos. Chem. Phys.*, 10, 4319–4330, 2010.

- Weitkamp C.: Lidar range-resolved optical remote sensing of the atmosphere, Springer, 455, 2005.
- Whiteman D.N., D.Venable, and E. Landulfo: Comments on “Accuracy of Raman lidar water vapor calibration and its applicability to long-term measurements”, *Appl. Opt.*, 50, 2170-2176, 2011.
- Wiegner M., J. Gasteiger, K. Kandler, B. Weinzierl, K. Rasp, M. Esselborn, V. Freudenthaler, B. Heese, C. Toledano, M. Tesche, and D. Althausen: Numerical simulations of optical properties of Saharan dust aerosols with emphasis on lidar applications, *Tellus*, 61B, 180–194, 2009.
- Wiegner M., J. Gasteiger, S. Groß, F. Schnell, V. Freudenthaler and R. Forkel: Characterization of the Eyjafjallajökull ash-plume: Potential of lidar remote sensing, *Phys. Chem. Earth*, 45–46, 79–86, 2012.
- Wiersma D.S., M.P. Van Albada and A. Lagendijk: An accurate technique to record the angular distribution of backscattered light, *Rev. Sc. Instrum.* **66**, 5473-5476, 1995.
- Wiersma D.S., P. Bartolini, A.Lagendij and R. Righini: Localization of light in a disordered medium, *Nature*, 390, 671-673, 1997.
- Winchester, L. W., Determination of the complex refractive index of samples of volcanic ash, contract report S01394-G, NASA, Washington, D. C, 1998.
- Winker D.M., and M.T. Osborn: Preliminary analysis of observations of the Pinatubo volcanic cloud with a polarization-sensitive lidar. *Geophys. Res. Lett.*, 19, 171-174, 1992.
- Winker D. M., J. L. Tackett, B. J. Getzewich, Z. Liu, M. A. Vaughan, and R. R. Rogers: The global 3-D distribution of tropospheric aerosols as characterized by CALIOP, *Atmos. Chem. Phys.*, 13, 3345–3361, 2013.
- Wise M. E., G. Biskos, S. T. Martin, L. M. Russell, and P. R. Buseck: Phase Transitions of Single Salt Particles Studied Using a Transmission Electron Microscope with an Environmental Cell, *Aerosol Sc. and Tech.*, 39, 849–856, 2005.
- Whitby K. T. and B. Cantrell: Fine particles, in *Proc. Int. Confe. Environmental Sensing and Assessment*, Las Vegas, NV, Institute of Electrical and Electronic Engineers, (1976).
- Worringen A., M. Ebert, T. Trautmann, S. Weinbruch and G. Hela: Optical properties of internally mixed ammonium sulfate and soot particles e a study of individual aerosol particles and ambient aerosol populations. *Appl. Opt.*, 47, 21, 3835-3845, 2008.
- Yurt A., G. G. Daaboul, , J. H. Connor, , B. B. Goldberg and M. S. ÜnlüSingle nanoparticle detectors for biological applications, *Nanoscale*, 4, 715-726, 2012.
- Zhang D.: Effect of sea salt on dust settling to the ocean, *Tellus*, 60B, 641–646, 2008.
- Zhu X.: Explicit transformation matrix for a tilted birefringent plate with its optic axis parallel to the plate surface, *Appl. Opt.* 33, 3502-3506, 1994.